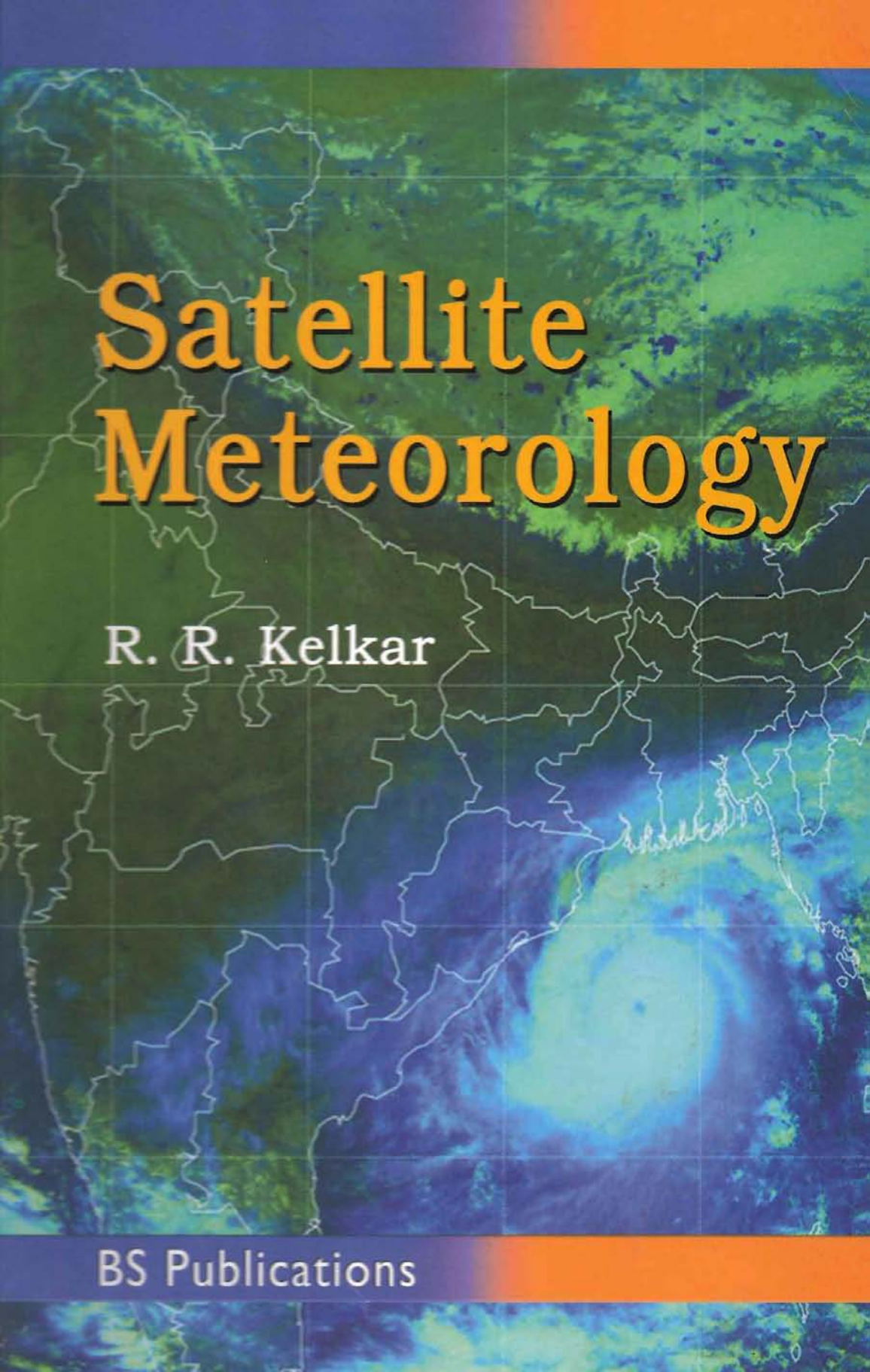
Satellite Meteorology
R. R. Kelkar
BS Publications

Satellite Meteorology

R. R. Kelkar
M.Sc, Ph.D.

ISRO Space Chair Professor
Department of Atmospheric and Space Sciences
University of Pune
and
Former Director General of Meteorology
India Meteorological Department

BSP **BS Publications**
Hyderabad, India

Published by :

BS Publications
4-4-309, Giriraj Lane, Sultan Bazar,
Hyderabad - 500 095 - A.P.
Phone : 040 - 23445677, 23445688
e-mail : contactus@bspublications.net
www.bspublications.net

Printed at
Sanat Printers
Kundli, Haryana

ISBN : 978-817800-137-1

ISBN : 81-7800-137-3

Contents

Chapter 1

Fundamentals

Fifty years ago, satellite meteorology did not exist except perhaps in science fiction. Today, satellite images of the world's weather, animated sequences of tropical storms, 5-day weather forecasts, are all being beamed through satellite channels into our television sets every hour or half-hour. Anyone, not just meteorologists, can access the latest images scanned by meteorological satellites around the world, on home PCs connected to the internet. The fascinating origin of satellite meteorology as an independent branch of the science of meteorology, and its phenomenal growth, have indeed had a touch of fantasy. What satellite meteorology happens to be today, is the result of an interplay of science on one hand, and the technology of satellites, computers and communications on the other. Limitations of technology have been overcome by scientific ingenuity, and the requirements of science have driven technology to the cutting edge.

After the successful launch of the first weather satellite in 1960 and the growth of satellite coverage of the earth's atmosphere and oceans within just a decade afterwards, meteorologists were in fact overwhelmed by the new satellite data that became available to them. Prior to the satellite era, meteorologists had laid the greatest emphasis on atmospheric pressure. Lows and highs showing up in synoptic isobaric analysis were of their main interest and many other weather elements including cloud cover, although observed, were not analysed on a synoptic scale in a similar manner. With the availability of satellite images, however, the accent shifted to observing and examining clouds and cloud patterns in the imagery, from which the state of the atmosphere could be directly observed or inferred. Images received from geostationary and orbiting satellites together revealed the presence of a wide spectrum of atmospheric phenomena across individual cumulus cells, thunderstorms, tropical cyclones and jet streams, just at a glance. So much so, that ground weather observation stations began to face the risk of redundancy and closure. Competition from satellite imagery forced many national meteorological services to take a re-look at their network configurations and trim them, particularly the upper air stations which are expensive to operate and maintain.

While the question whether meteorological satellites can give us all that we want for weather analysis and forecasting has been a subject of debate, the

answer as of now at least, appears to be firmly in the negative. In spite of the limitations of conventional data and the clear advantages of satellites, the global ground observing network can not just be done away with. Over land, the atmospheric pressure at the surface is measured most accurately with barometers and automatic instruments. This is the data on which all synoptic weather charts are constructed. Over the sea, pressure data is very sparse. However, as of now, atmospheric pressure can not be retrieved from satellites, except that low pressure areas can be identified in a qualitative sense from certain cloud patterns in satellite imagery. It has not so far been possible to re-create a synoptic weather chart with remote sensing data alone.

The greatest help from weather satellites comes in observing weather over oceans, mountains, deserts, and unpopulated places where conventional data is either sparse or just unavailable. Here again, satellite data may not be able to replace the functions of an observing network for various reasons. For example, ship observations of sea surface temperature are made within the upper 1 m layer of the sea, while only the ocean skin temperature is retrieved from satellites, and it has errors associated with it due to the presence of clouds and atmospheric moisture. On ground, temperature measurement is made at 1.4 m height above the ground in a Stevenson Screen. It is extremely difficult to get this from satellites as the emissivity of land is highly variable and is not accurately known.

Over land, accurate measurements can be made with anemometers and automatic instruments and over sea, ships and buoys provide surface wind data. The popularly used cloud drift technique applied to satellite imagery cannot be used at the surface, but sea surface winds can be obtained from scatterometers.

An observer on the ground looks up to the sky and estimates visually how much of the sky above is occupied by clouds (expressed in 1/8ths of the hemisphere or oktas). Cloud amount has a different meaning when seen from a satellite looking down and becomes the fraction of an area covered by cloud within a prescribed area as seen from the satellite. From the ground, it is the height of the cloud base that can be estimated by an observer or determined by instrumental methods and vertical growth of cloud cannot be visualized. On the contrary, satellites can give the height of the cloud top and help in seeing the vertical growth of clouds from fall in temperature over time.

Rainfall is measured over land with raingauges and automatic instruments, is a point measurement and areal averages are difficult to obtain. Over sea, rainfall measurements are rarely available. From satellite data, large-scale rainfall can be estimated from the type of cloud, its persistence and assumed

rain rate and areal averaging is easy. A space-borne precipitation radar can make direct measurements of rainfall over the sea.

Upper level winds are routinely measured with pilot balloons, radiosondes, wind profilers and radars. Balloon ascents are taken at the most 2-4 times a day due to the high cost of consumables. By using successive cloud imageries, winds can be estimated from the movement of cloud tracers. Here, the availability of suitable tracers determines whether the winds can be derived or not and different types of errors are involved in the derivation process.

Temperature and humidity profiles of the atmosphere are routinely obtained from the global radiosonde network. It is becoming increasingly expensive to run upper air stations, and over the sea only a few ships make radiosonde measurements. Vertical profiles of temperature and humidity are bring made globally with sounders on NOAA and GOES satellites, but the retrieval is a complex process and there are many problems particularly over hot and humid tropics.

In essence, the practices of weather analysis and forecasting currently in vogue employ a judicious combination of conventional and remotely sensed data, so as to compensate for the deficiencies of one source of data with the advantages of the other. The capability of weather satellites to observe and monitor weather systems is determined by various factors such as the number, type and resolution of spectral channels of the radiometer, the period of the satellite orbit which determines its revisit time, its height above the earth, the inclination of the orbit that delineates the geographical coverage, and so on.

1.1 Principles of Meteorological Remote Sensing

Remote sensing has been defined in various ways, but it is basically the process of observing an object in wavelengths that the human eye cannot perceive. The term has also developed a strong association with satellites, although aircrafts can be used for the same purpose. Remote sensing has applications in many diverse areas, ranging from monitoring of earth resources to medical diagnosis, but the basic principles are the same. In the forthcoming sections we shall discuss various aspects of remote sensing as applied to the area of satellite meteorology.

1.1.1 Absorption, Emission, Reflection and Scattering

It is quite a paradox that the radiative and thermal equilibrium of the earth-atmosphere system is not controlled by the two major constituents of the atmosphere, nitrogen and oxygen, but by some of the miscellaneous and numerous gases that all put together make up for 1 % of its volume. The behaviour of gases like water vapour, carbon dioxide, ozone, methane and other trace gases, and also particulate matter floating in the atmosphere, is what alters the radiation from the sun traversing the atmosphere and the radiation returned to the sun by the earth. Since satellite remote sensing is essentially the measurement of the returned radiation, it is important to know how the gases in the atmosphere influence the radiative processes in the atmosphere.

Atoms and molecules in a gas have electronic, rotational or vibrational energy, and absorption or emission of radiation takes place when there is a transition from one energy state to another. Absorption spectra of atoms, such as atomic oxygen and nitrogen, are associated with electronic transition and occur in the ultra-violet (UV) region of the electromagnetic spectrum. Tri-atomic molecules like those of water vapour, carbon dioxide and ozone, have additional rotational and vibrational transitions, which occur mainly in the infra-red (IR) region. In the visible (VIS) region, gases in the atmosphere account for very little absorption. The main absorption bands are those of three atmospheric gases: water vapour at 6.7 μ, carbon dioxide 15 μ and ozone 9.6 μ (1 μ or micron = 10^{-6} m). There are other minor absorption bands attributable to methane, nitrous oxide, and other gases.

Radiation from the sun gets reflected when it strikes a plane surface such as the ground or cloud tops and its direction gets altered. Depending upon the albedo or reflectivity of the surface, some part of the radiation will be reflected and the remaining amount will get absorbed by the medium or be transmitted through it. Snow and cumulonimbus cloud tops have high albedo values while the ocean surface reflects very little of the radiation falling upon it.

Air molecules and suspended particles or aerosols scatter radiation in the VIS wavelengths. When the size of the scattering particles is small compared to the wavelength of the incident radiation, the scattering is said to be of the Rayleigh type. In Rayleigh scattering, the intensity is inversely proportional to the 4th power of the wavelength, and the distribution of scattered radiation intensity is symmetric in both the forward and backward directions. When the sizes of the scattering particles become comparable to the wavelength of the incident radiation, the scattering processes is said to be of the Mie type, in which the angular distribution of the scattered radiation intensity is

complex and does not remain symmetric. Rayleigh scattering by air molecules is what gives the blue colour to the sky, while Mie scattering by the larger sized particles and aerosols gives it a grayish appearance.

1.1.2 Black Body and Radiation Laws

Many fundamental laws governing the absorption and emission of electromagnetic radiation are commonly based on the concept of what is termed as a black body. This is largely a theoretical concept as ideal or perfect black bodies can be said to be almost non-existent. A black body is defined as an object that absorbs all radiation incident upon it, does not reflect any of it, and emits all energy at full efficiency for all wavelengths as per the following equation

$$B(\lambda,T) = 2hc^2 \lambda^{-5} / (e^{hc/\lambda kT} - 1)$$

where B is the energy in w m^{-2} μ^{-1},
T is the temperature of the black body in °K,
λ is the wavelength in μ,
h is Planck's constant 6.625 x 10^{-27} erg sec,
k is Boltzmann constant 1.38 x 10^{-16} erg $°K^{-1}$,
c is the velocity of light 3 x 10^{10} cm sec^{-1}

This relationship of the black body emission to its temperature is known as Planck's Law. For any given temperature, Planck's Law gives a distribution of emitted energy or a characteristic spectrum of electromagnetic radiation that peaks at a certain wavelength. This peak shifts to shorter wavelengths for higher temperatures and the area under the curve grows rapidly with increasing temperature.

Wien's Displacement Law describes the temperature dependence of the black body radiation curves derived from Planck's Law and it states that the wavelength λ_{max} at which the black body radiation is the maximum is inversely proportional to the temperature T of the black body (in °K), or

$$\lambda_{max} = c / T$$

where c is a constant whose value is 2898 μ °K.

Stefan-Boltzmann's Law gives the total energy E emitted at all wavelengths by the black body at temperature T,

$$E = \sigma T^4$$

where σ is the Stefan-Boltzmann constant which has a value of 5.6705×10^{-5} erg cm^{-2} sec^{-1} $°K^{-4}$.

E is in fact the area under the Planck's Law curve. Thus, as the temperature of a black body increases, the shift of the peak emission to shorter wavelengths is governed by Wien's Law while the increase in the height of the curve is explained by Stefan-Boltzmann's Law. This increase in E with temperature is not linear, since it varies with the fourth power of the temperature.

There is another important law called Kirchhoff's Law which states that the ratio ε of emitted radiation to absorbed radiation is the same for all black bodies at the same temperature. This law forms the basis for the definition of emissivity. The emissivity of a perfect black body is 1 and that of a perfect reflector is 0.

Strictly speaking, the laws mentioned above are applicable only to a black body, but they are important in the real world as they can be applied as a close approximation to other bodies which have a very weak interaction with the surrounding environment and can be considered to be in a state of equilibrium. In the earth-atmosphere system, the earth's sea surface and thick clouds can be regarded as acting very similar to a black body.

1.1.3 Solar and Terrestrial Radiation

The radiation laws described in the previous section help us to understand the nature of an object and identify some of its thermal properties by interpreting the pattern of radiation emitted by it in different wavelengths. The spectrum of the solar radiation received at the top of the earth's atmosphere matches very well the spectrum of a black body having a surface temperature of about 5700 °K. This is called solar radiation and it has a peak at about 0.5 μ (Figure 1.1.3.1). The radiation emitted by a black body at the same temperature as the average temperature of the earth's surface which is 283 °K, peaks at about 10 μ (Figure 1.1.3.2). We therefore have to deal with two different radiation regimes, the radiation received by the earth from the sun, called solar or shortwave radiation and the radiation returned to space by the earth-atmosphere system, called terrestrial or longwave radiation. The intensity of terrestrial radiation is far less than that of solar radiation.

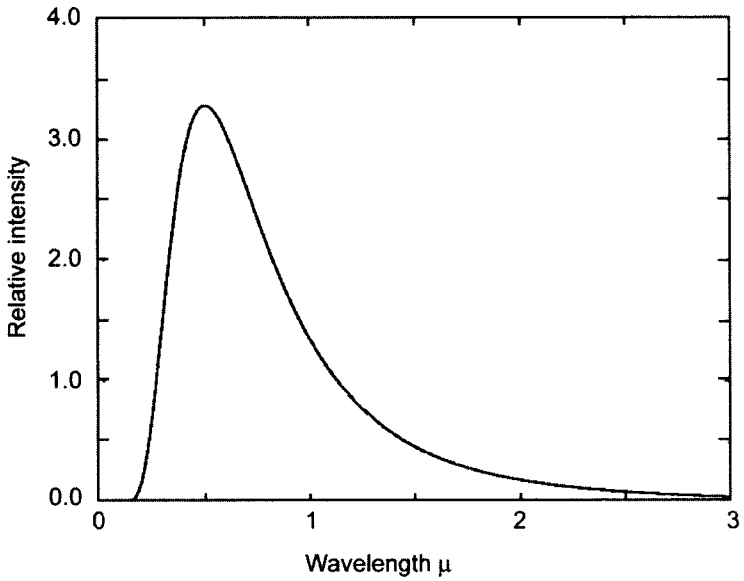

Figure 1.1.3.1 Variation of the relative intensity of black body radiation with wavelength (μ) at temperature 5700 °K, peaking at a wavelength of 0.5 μ in the visible region (Solar radiation)

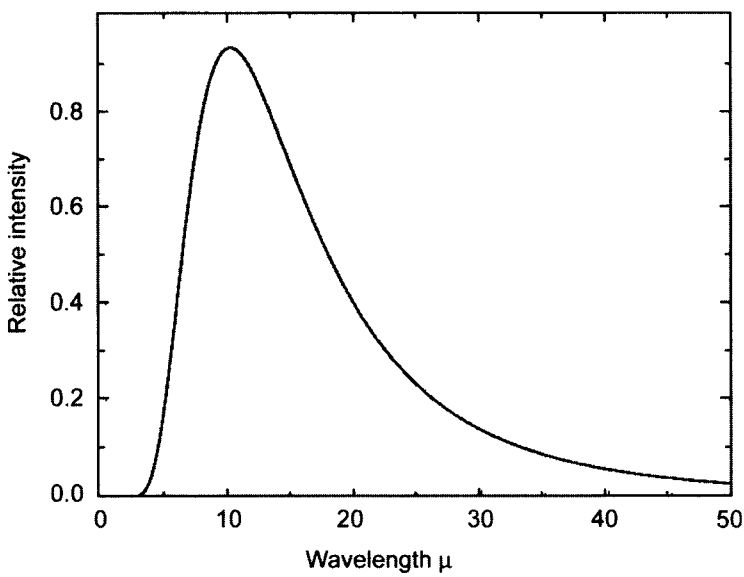

Figure 1.1.3.2 Variation of the relative intensity of black body radiation with wavelength (μ) at temperature 283 °K, peaking at a wavelength of 10 μ in the infra-red region (Terrestrial radiation)

1.1.4 Sun-Earth-Atmosphere Radiation Budget

The solar constant is defined as the annual average solar radiation received outside the earth's atmosphere on a plane normal to the incident radiation at the mean sun-earth distance and has a value close to 2 cal cm^{-2} min^{-1} or 1370 W m^{-2}. The actual solar irradiance varies by 3-4% of this value during the year due to the eccentricity of earth's orbit about the sun.

If we consider the incoming solar radiation at the top of the atmosphere as made of 100 units, 30 units are reflected back to space (6 by the atmosphere, 20 by clouds and 4 by the earth's surface). 19 units are absorbed by the atmosphere (16 by gases and 3 by clouds). The remaining 51 units are absorbed by the earth's surface.

Out of these 51 units, 6 are lost to space directly and 45 are returned upwards and absorbed by the atmosphere and clouds (7 by convection and conduction, 23 by evaporation as latent heat and 15 by longwave radiation). The atmosphere and clouds have already absorbed 19 units from the solar radiation, making a total of 64 units which are returned to space as longwave radiation. The budget is thus balanced at the top of the atmosphere.

At the earth's surface and at any level in the atmosphere, the net radiation is the balance of four radiative fluxes, downward solar radiation, downward longwave radiation, upward solar radiation and upward longwave radiation. These can be measured with special instruments installed on the ground or flown on balloons as radiometersondes. The prime factors involved in the radiation budget of the earth-atmosphere system are the albedo or reflectance properties of land, ocean and cloud tops, scattering properties of aerosols, dust and particulate matter in the atmosphere, and vertical profiles of temperature and concentration of gases which absorb longwave radiation (water vapour, CO_2, ozone). Data on these variables if available can be used to compute the radiation budget components indirectly.

1.1.5 Electromagnetic Spectrum

By the term spectrum, we commonly mean the seven colours of visible light, like in the rainbow. In scientific parlance, it refers to the entire range of wavelength or frequency of electromagnetic radiation, visible light being just a small portion of it (Table 1.1.5.1). The characteristic spectrum of a given object is the pattern of electromagnetic radiation that it absorbs, transmits and emits. The product of the wavelength λ and frequency ν of electromagnetic waves is equal to c, the velocity of light. The associated

energy $E = h.\nu = h.c / \lambda$ where h is Planck's constant. This means that as the wavelength of electromagnetic radiation increases, its frequency decreases and the associated energy gets reduced.

The region of the electromagnetic spectrum with which we are most concerned in real life is the region of visible light, to which the human eye is very sensitive and in which the sun and stars emit the strongest radiation. In recent times, we are getting familiar with other wavelength regions as FM radio stations, mobile phones, satellite television or microwave ovens become more and more a part of our daily life.

Table 1.1.5.1 Electromagnetic Spectrum

<table>
<tr><th>Wavelength</th><th></th><th>Wavelength</th><th></th></tr>
<tr><td>10^{-6} nm</td><td rowspan="4">Gamma Rays (MeV)</td><td>1 mm</td><td>Millimetre Waves (mm)</td></tr>
<tr><td>10^{-5} nm</td><td>1 cm</td><td rowspan="3">Microwaves (cm, GHz)</td></tr>
<tr><td>10^{-4} nm</td><td>10 cm</td></tr>
<tr><td>10^{-3} nm</td><td>1 m</td></tr>
<tr><td>10^{-2} nm</td><td rowspan="3">X-Rays (Å)</td><td>10 m</td><td rowspan="6">Radio Waves (MHz, kHz)</td></tr>
<tr><td>10^{-1} nm</td><td>100 m</td></tr>
<tr><td>1 nm</td><td>1 km</td></tr>
<tr><td>10 nm</td><td>Ultra-violet (nm), Visible, Near Infra-red (μ)</td><td>10 km</td></tr>
<tr><td>100 nm</td><td></td><td>100 km</td></tr>
<tr><td>1 μ</td><td></td><td>10^3 km</td></tr>
<tr><td>10 μ</td><td>Thermal Infra-red (μ)</td><td>10^4 km</td></tr>
<tr><td>100 μ</td><td>Far Infra-red (μ)</td><td>10^5 km</td></tr>
</table>

Table 1.1.5.2 Wavelength Range of Visible Colours

Colour	Wavelength	
	(nm)	(μ)
Violet	380-430	0.38-0.43
Indigo	430-500	0.43-0.50
Blue	500-520	0.50-0.52
Green	520-565	0.52-0.565
Yellow	565-590	0.565-0.59
Orange	590-625	0.59-0.625
Red	625-740	0.625-0.740

The visible spectrum consists of the seven colours familiar to us which are identified by their wavelength in nm (1 nanometre = 10^{-9} m) or in μ (1 micrometre or micron = 10^{-6} m) as given in Table 1.1.5.2. The visible wavelength region is, however, an extremely small part of the whole spectrum. Radiation of wavelengths shorter than violet is called ultra-violet (UV) radiation. This has very high energy that can break chemical bonds, ionize molecules, damage skin cells or cause cancer. However, most of the UV radiation coming from the sun is absorbed by the layer of atmospheric ozone which resides in the stratosphere, and shields life on earth from its harmful effects.

X-rays have wavelengths that are even shorter than UV, which are expressed in Å (Angstrom Units or 10^{-10} m). Gamma rays have wavelengths that could be as short as 10^{-15} m and it is more convenient to express their magnitude in terms of their energy levels which are of the order of keV (kilo electron volts) or MeV (Million electron Volts). X-rays and gamma rays have great penetration power and have applications in astronomy, radioactivity and other fields.

Towards the other end of the visible spectrum, radiation which has wavelength higher than red is called infra-red (IR). The IR region of the spectrum can be further sub-divided into near (NIR), short-wave (SWIR), middle (MIR), and thermal (TIR) with increasing wavelength.

Radiation with still longer wavelengths are called millimetre waves, followed by microwaves and radio waves. These again are further classified with respect to their frequency as given in Tables 1.1.5.3 and 1.1.5.4.

1.2 Satellite Orbits

The design of an optimum orbit around the earth for a meteorological satellite is a complex process. There are two main classes of orbits, polar orbiting and geostationary, and they are complementary to each other. However, many new types of orbits have now come into use or are being considered. The following sections describe the fundamental principles behind orbit design, technical considerations and the operational implications.

Table 1.1.5.3 Nomenclature of Microwave and Radio Wave Frequencies

Abbreviation	Full Form	Frequency	Wavelength
EHF	Extremely high frequency (Microwaves)	30-300 GHz	1 mm-1 cm
SHF	Super high frequency (Microwaves)	30-3 GHz	1 cm-10 cm
UHF	Ultra-high frequency	3 GHz-300 MHz	10 cm-1 m
VHF	Very high frequency	300-30 MHz	1 m-10 m
HF	High frequency	30-3 MHz	10 m-100 m
MF	Medium frequency	3 MHz-300 kHz	100 m-1 km
LF	Low frequency	300-30 kHz	1-10 km
VLF	Very low frequency	30-3 kHz	10-100 km
VF	Voice frequency	3 kHz-300 Hz	100-10^3 km
ELF	Extremely low frequency	300-30 Hz	10^3-10^4 km

Table 1.1.5.4 Microwave Bands

Band	Wavelength	Frequency
mm-Band	1-7.5 mm	40-300 GHz
Ku-K-Ka- Band	0.75-2.5 cm	12-40 GHz
X-Band	2.5-4 cm	8-12 GHz
C-Band	4-8 cm	4-8 GHz
S-Band	8-15 cm	2-4 GHz
L-Band	15-30 cm	1-2 GHz

1.2.1 Gravitational and Astronomical Laws

There are certain classical laws that were originally formulated to explain the motion of planets in the solar system and their orbits around the sun. They are, however, very fundamental and general in nature and we now know that they are equally applicable to the orbits of artificial satellites placed around the earth and other planets or moons in the solar system.

Kepler's laws of motion state that: (i) A planet moves around the sun in an elliptical orbit, with the sun at one focus, (ii) The vector joining the sun's centre to the planet sweeps out equal areas in equal time, and (iii) The square of the period of revolution of the planet is proportional to the cube of its

semi-major axis. As mentioned above, these laws also hold good for artificial satellites orbiting the earth.

Kepler's laws have to be considered in conjunction with another fundamental physical law. As per Newton's law of gravitation, the gravitational force between two bodies of mass m_1 and m_2 is proportional to the product of m_1 and m_2 and inversely proportional to the square of the distance r between them, or

$$F = G\, m_1\, m_2 / r^2$$

where G is the universal gravitational constant having a value of 6.67×10^{-8} $cm^3\, g^{-1}\, sec^{-2}$.

The forces acting on a satellite around the earth are the gravitational force and the centripetal force, which should balance for the satellite to attain a stable orbit. So we must have

$$m_s\, v^2 / R = GM_e m_s / R^2$$

where M_e and m_s are the masses of the earth and satellite respectively, R is the mean distance between them and v is the velocity of the satellite. The term m_s appears on both sides of the equation and can be cancelled out. We then have

$$v^2 = GM_e / R$$

For a circular orbit, the velocity v can be expressed as $2\, \pi\, R / T$ where T is the time period of revolution of the satellite, which is inversely related to its mean distance from the earth and is given by the equation

$$T^2 = 4\, \pi^2\, R^3 / GM_e$$

This means that the time period, speed and acceleration of an artificial satellite orbiting the earth are not dependent upon its mass. So theoretically speaking we can put into orbit as big a satellite as we wish, the only practical constraint being that of lifting it into space with the rockets that we have.

We can evaluate T for a given R as

$$T = (4\, \pi^2\, R^3 / GM_e)^{1/2}$$

R can be expressed as $R_e + h$, where R_e is the radius of the earth and h is the height of the satellite above the earth. For the limiting case of $h = 0$, and using $M_e = 5.98 \times 10^{24}$ kg, and $R_e = 6370$ km, T works out to be 84 min. In reality of course it is not possible to have a satellite grazing the earth. For $h = 200$ km, T will work out to be 88 min. For $h = 1000$ km, T will be 105 min, and this is a popular choice for meteorological satellites.

If T is set at 24 hr, the height of the satellite will work out to be about 35,840 km above the earth's surface. Such an orbit is called geosynchronous as the satellite matches the angular velocity of the earth at this height.

1.2.2 Orbital Elements

As depicted in Figure 1.2.2.1, the satellite's orbit is specified by the following parameters (Kelkar et al 1980):

(a) a - the semi-major axis of the orbit (defines the size of the orbit)
(b) e - the eccentricity of the orbit (defines the shape of the orbit)
(c) I - the inclination of the orbit (with respect to the earth's equatorial plane)
(d) Ω - the right ascension of the ascending node (longitude of the north-bound equatorial crossing)
(e) ω - the argument of the perigee
(f) f - true anomaly
(g) T_e - epoch time

For a given orbit, all the above fixed parameters are fixed, except f which specifies the position of a satellite at a given time.

The semi-major axis a of the ellipse is the maximum height of the satellite above the earth's surface. As per Kepler's third law, satellites move faster when they are close to the earth and slowly when they are further away. The semi-major axis is thus an indirect measure of the average speed or mean motion of the satellite.

The satellite orbit is generally an ellipse. The eccentricity e is an indicator of the shape of the ellipse. A circular orbit is a special case of an ellipse when e is 0, and as e increases towards the limiting value of 1, the ellipse becomes more and more eccentric or elongated.

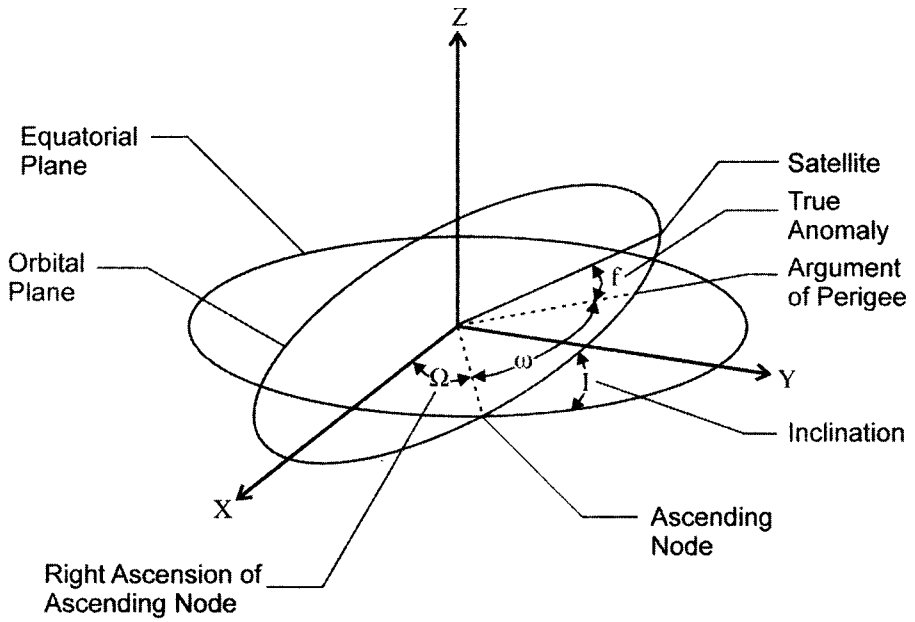

Figure 1.2.2.1 Orbital elements of a satellite in orbit around the earth

For a geostationary satellite the inclination is 0°. For a satellite in a perfectly polar orbit, it would be 90°. The intersection of the equatorial plane and the orbital plane is known as the line of nodes.

The point where the satellite is closest to the earth is called the perigee, and the point where it is farthest from earth is called the apogee. The major axis of the ellipse is thus the line joining the perigee and the apogee. The argument of perigee ω helps to define the orientation of the orbital ellipse within the orbital plane. It is the angle measured at the centre of the earth from the ascending node to the perigee.

For a given inclination, there can be an infinite number of orbital planes. The right ascension of the ascending node along with the inclination uniquely specifies the orbital plane. The ascending node is the longitude at which the satellite crosses the equator while going from south to north. The descending node is where the satellite crosses the equator while going from north to south. Since the earth is spinning, we cannot use the common latitude/longitude coordinate system to specify where the line of nodes points. Instead, we use an astronomical coordinate system, known as the right ascension/declination coordinate system, which does not spin with the earth. Right ascension is an angle measured in the equatorial plane from a reference point in the sky where right ascension is defined to be zero, which

is the vernal equinox. Thus the right ascension of the ascending node Ω denotes an angle, measured at the centre of the earth, from the vernal equinox to the ascending node (see Section 1.3.6).

The true anomaly f is the angle at the centre of the earth, measured in the orbital plane, between the perigee and the satellite at any given time. If the satellite is in a circular orbit and hence moving at a constant speed, this angle would point directly to the satellite.

A satellite orbit is subject to several small perturbations due to various reasons such as non-sphericity of the earth's geoid leading to gravitational anomalies, gravitation effects of other celestial bodies like the sun, moon or stars, atmospheric drag, solar radiation pressure and tides. The order of magnitude of these perturbations would depend on the nature of the satellite orbit. For example, geostationary satellites at 36,000 km height would be less prone to atmospheric drag, but more sensitive to the pressure of solar radiation, whereas the reverse would be true in the case of polar orbiting satellites. Geostationary meteorological satellites like GOES or INSAT which have large solar panels on one side of the spacecraft, are provided a long solar sail on the other side for maintaining balance (Figure 1.2.2.2).

1.2.3 Satellite Attitude

While the altitude of a satellite is its height above the earth, the term satellite attitude refers to its orientation in space. Altitude and attitude are two equally important characteristics of a satellite and they together determine the kind of mission that the satellite can best perform. In the case of a meteorological or remote sensing satellite, the antennas must always remain in ground contact for communications and data transfer, and its imaging sensors must always view the earth as intended. Any deviation from the nominal attitude would result in an improper functioning of the satellite. Satellite attitude therefore demands to be carefully controlled and the two ways of doing it are through spin-stabilization and three-axes stabilization.

A spin-stabilized satellite rotates around its own vertical axis, spinning like a top and resisting external perturbation forces. Here the orientation of the satellite spin vector in space defines its attitude. Spin-stabilized satellites are equipped with thrusters which can be fired occasionally to bring about desired changes in the spin rate and to restore the spin vector orientation. The early GOES and Meteosat satellites had a cylindrical design and rotated at the rate of one revolution per second during which the earth's disc would be scanned. A disadvantage in spinning satellites is that they cannot have large

solar arrays and require to be supported by battery power. Another inconvenient factor is that instruments or antennas are required to de-spin so that the antennas and radiometers maintain their desired orientation relative to the earth.

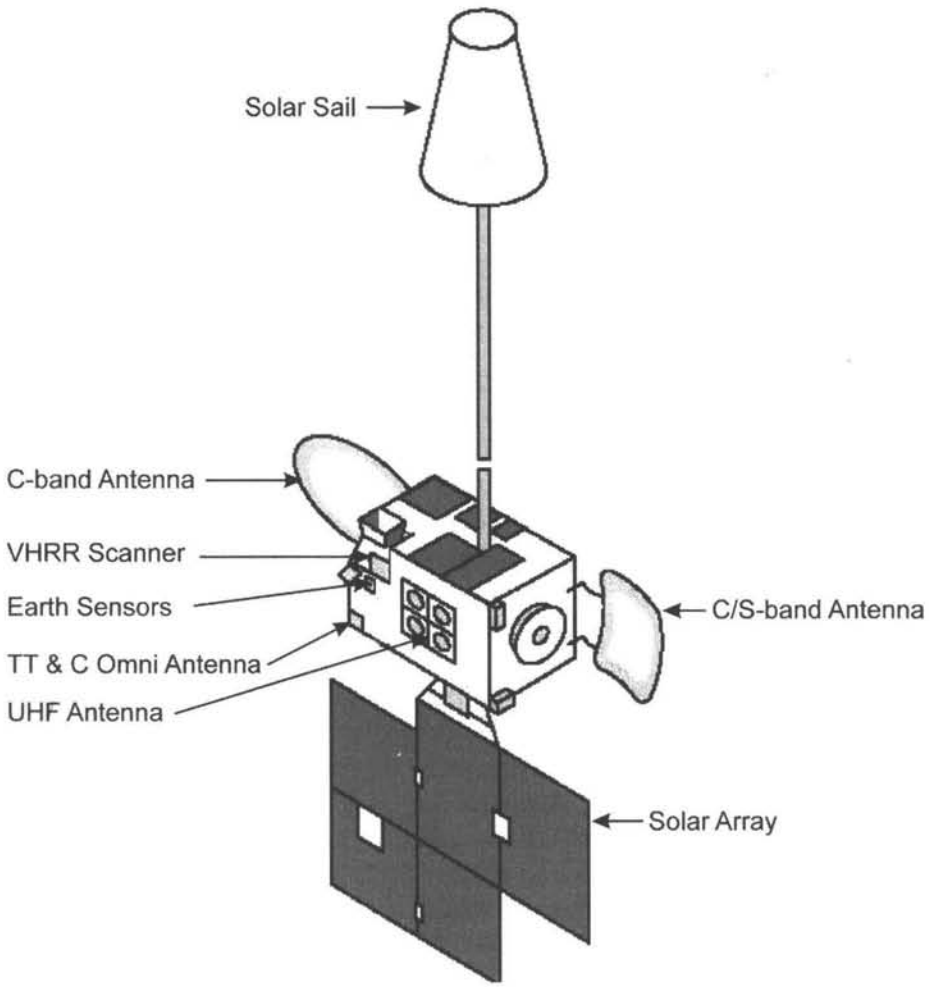

Figure 1.2.2.2 A schematic of the INSAT-1 spacecraft
(Source: IMD)

The design of the first Indian National Satellite, INSAT-1A, launched in 1982, was a major departure from that of the U. S. and European satellites operating at that time, in that it was a non-spinning satellite. This INSAT design has since been adopted by many other countries including the U. S. In a non-spinning satellite, the attitude is defined in terms of the deviations from the nominal orientations of its roll, pitch and yaw axes. The terms roll, pitch and yaw are applied to a satellite in the same manner as they are used in the case of ships or aircrafts. Roll is the rotation of the spacecraft around the direction of its forward movement. Yaw is its rotation around the axis looking at the nadir. Pitch is the rotation around an axis normal to the roll and yaw axes. The three axes can be envisaged as lines running through the satellite's centre of gravity and intersecting at right angles.

The attitude of non-spinning satellites is controlled by minimizing the roll, pitch and yaw. This is called three-axis stabilization, and achieved through the deployment of electrically powered spinning wheels called momentum or reaction wheels. These wheels are mounted in three orthogonal axes on the spacecraft and allow a transfer of angular momentum back and forth between the spacecraft and wheels. If the satellite is found to be deviating from its desired attitude, the appropriate spinning wheels are speeded up or slowed down to restore the correct attitude. Spacecrafts may also have propulsion system thrusters to apply the required torque. An advantage of three-axis stabilization is that radiometers and antennas can always be made to point at the desired targets without having to perform de-spin maneuvres.

In three-axes stabilized geostationary meteorological satellites, the scanning radiometers have to alternate their scans between east-west and west-east directions until the earth's disc gets fully scanned. The polar-orbiting NOAA satellites are also three-axes stabilized but the scanning is required to be done only in the east-west direction as the north-south progression of the scan is taken care of by the movement of the satellite in its orbit.

Attitude errors result in a distortion of the satellite image and the scene viewed looks slightly different from the nominal view. Yaw errors will result in the image getting rotated around the sub-satellite point in a clockwise or anticlockwise manner. With roll and pitch errors, the image will not be centred at the nominal sub-satellite point but a little away from it. When the attitude errors are large, the sub-satellite point of a geostationary satellite is seen to meander in a figure-of-eight pattern around its nominal position on the equator.

1.2.4 Types of Orbits

Figure 1.2.4.1 shows the relative orientations of polar, geostationary and tropical orbits around the earth. A satellite in a polar orbit crosses the equator twice a day, but views the poles in every orbit. With every orbital revolution, a new region of the earth comes under its view because of the earth's rotation. A global picture thus emerges over a period of time.

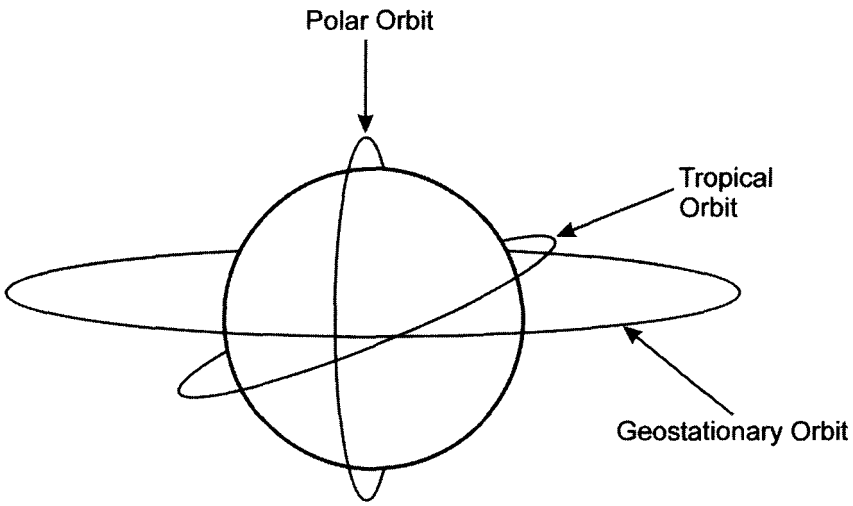

Figure 1.2.4.1 Relative orientations of polar, geostationary and tropical orbits around the earth

The earth is not a perfect sphere and the surface mass is not uniformly distributed, leading to gravitational anomalies. Other bodies in the solar system also exert their gravitational influences on a spacecraft in orbit around the earth. It is possible to choose the parameters of a spacecraft's orbit so as to take advantage of these gravitational influences to induce precession or a slow movement of the satellite orbital plane with respect to fixed inertial space. A special case of a polar-orbiting satellite is a sun-synchronous satellite which is designed in such a manner that the precession of the satellite orbit matches the earth's revolution around the sun. In other words, the satellite crosses the equator at the same local time (there are AM and PM orbits) and views any given place under comparable lighting conditions. The orbit does not go exactly over the poles but has an inclination of about 100° and a height of 700-1000 km. Occasional orbit maneuvres may be required to maintain the sun-synchronous characteristics of the orbit.

When a satellite is placed in a circular orbit with a radius of 42,400 km or a height of 36,000 km above the earth's surface, it will circle round the earth with the same angular velocity as that of the earth. At that specific height, it will complete its orbit in 24 hours. Such a satellite is called a geosynchronous satellite. A special case of a geosynchronous satellite is one in which its orbit is in the equatorial plane. In a relative sense, such a satellite will appear to remain stationary above a given point on the equator and is called a geostationary satellite. A geostationary satellite provides a continuous earth view from about 60° N to 60° S, but it will not be able to see the polar regions. A constellation of 5 or 6 geostationary satellites spaced around the equator, is needed to complete the near-global picture. Geostationary satellites are ideal for communications purposes and continuous monitoring of the weather over the region within their view. Considerations of orbit stability demand that a geostationary satellite be placed only over a point on the equator and not above any other latitude. To maintain the geostationary satellite within the permissible limits of altitude and inclination, station-keeping maneuvres have to be carried out periodically.

When the direction in which a satellite is moving in its orbit around the earth is the same as that of the rotation of the earth, the orbit is called direct or prograde. If the satellite is moving in a direction that is opposite to that of the earth's rotation, the orbit is called retrograde. A geostationary satellite is a special case of a prograde orbit in the equatorial plane, while polar-orbiting satellites are generally placed in a retrograde orbit with an inclination of about 100°. An inclination of 180° would mean a retrograde equatorial orbit.

Kelkar et al (1982) had envisaged a non-geostationary satellite orbiting around the equator and providing frequent meteorological coverage of the entire tropical belt but not observing the higher latitudes. Tropical orbits have now become a reality with the TRMM satellite and the proposed Megha-Tropiques mission (see Sections 4.1 and 6.5.1). The GPM mission which will succeed the TRMM mission is going to have satellites in an orbit of 65° inclination with respect to the equatorial plane so that they will cover the tropics as well as the extra-tropical regions of the earth (see Section 6.4). There are also new innovations like the A-Train which has a series of satellites in the same orbit following one after another in a formation (see Sections 4.2.4)

1.3 Satellite Payloads

The payload carried by the TIROS-1 satellite in 1960 was just a television camera that relayed to the ground whatever it saw of land, ocean and clouds.

With every successive meteorological satellite launched over the last four decades by different countries, there have been rapid advances in satellite instrumentation and technology, serving various areas of application, which will be described in the next few sections and the following chapters of this book.

1.3.1 TV Cameras

Historically speaking, the U. S. satellite, Vanguard 2, launched on 17 February 1959 was the world's first satellite designed to observe the earth's cloud cover, but because of a poor axis of rotation, it could not collect much useful data.

The world's first meteorological satellite to be considered a success, was the Television and Infra-Red Observation Satellite, TIROS-1, which was launched by the U. S. on 1 April 1960. TIROS-1 was operational for only 78 days, but it demonstrated beyond doubt the tremendous potential use of satellites for surveying global weather conditions from space and paved the way for future advanced weather satellites.

TIROS-1 had two television cameras housed in the spacecraft, one low-resolution and one high-resolution. The pictures were transmitted directly to ground receiving stations. Each camera had a magnetic tape recorder for storing photographs taken when the satellite was out of range of ground stations. The spacecraft was spin-stabilized but not earth-oriented. Therefore, the cameras were only operated while they were pointing at the earth when that portion of the Earth was in sunlight. The video systems relayed thousands of pictures containing cloud cover views of the earth that provided information about large scale cloud regimes for the first time.

TIROS-2 was launched on 23 November 1960 and was operational for over a year. Besides TV cameras, it also carried two experimental infra-red radiation sensors which were successfully used. The TV cameras used 500 scan-line, 1.27 cm vidicons. The tape recorders could store up to 32 frames of pictures. Transmission of the 32-frame sequence was accomplished in 100 sec by a 3 watt FM transmitter. Pictures taken from the satellite altitude of about 700 km by the wide angle camera covered a 1200 × 1200 km area with a spatial resolution of 2.5 to 3.0 km at nadir. The narrow angle camera covered a 120 × 120 km area and had a resolution of 0.3 to 0.8 km. The experiment was capable of producing daytime cloud cover pictures for the region between 55 °S and 55 °N latitudes. Deposits accumulated on the lens of the wide angle camera caused all its pictures to be of very poor quality.

The other camera operated normally until 1 February 1961 and sporadically thereafter until 27 September 1961, but it transmitted more than 25,000 usable pictures.

Five more satellites in the TIROS series were launched during the years 1961 to 1963. TIROS-8 was the first satellite to be equipped with the Automatic Picture Transmission (APT) capability that made satellite pictures available the world over to meteorological agencies in real time as the satellite passed over their region. It was launched on 21 December 1963 and 50 ground stations including one at Mumbai (Colaba) in India, participated in the APT experiment, which was terminated by the end of April 1964 due to degradation of the APT camera. In addition to the APT camera system, the satellite carried a wide angle TV camera which transmitted useful data until 12 February 1966. The satellite was deactivated on 1 July 1967.

TIROS-10, which was the last of the experimental satellite series, was launched on 2 July 1965 and had a life of two years.

The successor satellite programme was named after the U. S. agency, the Environmental Science Services Administration (ESSA), which operated it. The ESSA series was initiated in 1966 as an extension of the TIROS programme and its primary objective was to acquire higher resolution cloud cover images. Over the next four years, nine satellites in the ESSA series transmitted thousands of images that helped to predict weather patterns including hurricanes. By the end of the programme, more than 300 APT reception stations had come up in 45 countries (Datar et al 1971, Das Gupta 1971).

In 1964, the U. S. National Aeronautics and Space Administration (NASA) launched a parallel satellite programme named Nimbus, to develop observation systems aimed at meeting the research requirements of atmospheric and earth sciences. Between 1964 and 1978, NASA launched seven Nimbus satellites which had very advanced on-board instruments for mapping ozone, sea ice, radiation budget components, coastal zone properties and sea surface temperature, However, Nimbus satellites also continued to carry an improved vidicon camera system for daylight coverage of local cloud conditions which were transmitted through the APT system.

Another APT service was provided parallelly by the Russian Meteor series of satellites. However, the early satellites in this series were not sun-synchronous and the images were received at different times of the day in each pass.

1.3.2 Scanning Radiometers

After the end of the TIROS satellite series, TV cameras were given up as a means of observing the earth's cloud cover and replaced by scanning radiometers which have become more and more advanced in recent times. Scanning radiometers do not give snapshot pictures but images are constructed from the digital data transmitted by them over a span of time required to complete the scan. In brief, a meteorological satellite measures only radiation. What you see in the satellite image depends upon the spectral band in which the satellite radiometer has received radiation, the sensitivity and response of the sensor, the height from which the satellite is viewing the earth, the time of the scan and such other factors.

1.3.2.1 NOAA AVHRR

The TIROS Next Generation satellite programme, named TIROS-N, was aimed at providing higher resolution imaging, and more quantitative environmental data on local and global scales for both day and night than with the earlier TIROS satellites. TIROS-N was launched on 13 October 1978, and followed by many more satellites in the series, which were later renamed as NOAA satellites, after the operating U. S. agency, the National Oceanic and Atmospheric Administration. The NOAA satellite series is still in operation, the latest satellite in the series, NOAA-18, having been launched on 20 May 2005.

All NOAA satellites are placed in a near-circular polar orbit, and they carry on board an instrument called the Advanced Very High Resolution Radiometer (AVHRR). This was at first a 4-channel radiometer, but it was subsequently improved to a 5-channel instrument (AVHRR/2) beginning with NOAA-7 which was launched on 23 June 1981. The latest instrument version is AVHRR/3, which views the earth in 6 channels, and was first carried on NOAA-15, launched on 13 May 1998.

The AVHRR/3 radiometer scans the earth in 6 channels, one in visible (VIS), two in near infra-red (NIR), one in mid-wave infra-red (MIR) and two in thermal infra-red (TIR) wavelength regions (Table 1.3.2.1.1). All the channels have a resolution of 1.09 km at the sub-satellite point.

The instrument utilizes a 20.32 cm diameter collecting telescope. Cross-track scanning across the earth from one horizon to another is accomplished by a continuous 360° rotation of a flat scanning mirror directly driven by a motor.

The scan lines are oriented normal to the satellite's direction of movement and the speed of rotation of the scan mirror is selected so that adjacent scan lines are contiguous at the sub-satellite point. Complete strip maps of the earth from pole to pole are thus obtained as the spacecraft travels in orbit at an altitude of approximately 833 km.

Channels 1 and 2 use silicon detectors, channels 3A and 3B use InGaAs and InSb detectors respectively, while channels 4 and 5 have HgCdTe detectors. The IR detectors are cooled to 105 °K by a two-stage passive radiant cooler. Although AVHRR/3 is a 6-channel radiometer, at any given time, data of only 5 channels can be transmitted to the ground. Another constraint is that out of the two channels 3A and 3B, only one can operate at a time. All six spectral channels of the AVHRR/3 are well-registered with one another, which means that they all receive radiation from the same spot on the earth at the same time.

Table 1.3.2.1.1 NOAA AVHRR/3 Channel Characteristics

Channel Number	Spectral Band	Wavelength Range (μ)	Applications
1	VIS	0.58 - 0.68	Daytime cloud and surface mapping
2	NIR	0.725 - 1.00	Land-water boundary delineation
3A	NIR	1.58 - 1.64	Snow and ice detection
3B	MIR	3.55 - 3.93	Night-time cloud mapping, sea surface temperature retrieval
4	TIR	10.3 - 11.3	Night cloud mapping, sea surface temperature retrieval
5	TIR	11.5 - 12.5	Sea surface temperature retrieval

(Source: http://noaasis.noaa.gov/NOAASIS/ml/avhrr.html)

A scanning radiometer very similar to the NOAA AVHRR is currently flying on the TRMM satellite in a tropical orbit (see Sections 1.2.4 and 4.1.1). The TRMM Visible and InfraRed Scanning Radiometer (VIRS) measures radiances in five channels centred at 0.63, 1.6, 3.75, 10.80, and 12.0 μ, similar to channels 1, 3A, 3B, 4 and 5 of the NOAA AVHRR, at a ground resolution of 2.1 km.

1.3.2.2 SMS VISSR and GOES Imager

The first two geostationary meteorological satellites were SMS-1 and SMS-2, launched by the U. S. on 17 May 1974 and 6 February 1975 respectively. SMS-1 was placed on the equator at 45 °W over the central Atlantic and SMS-2 at 135 °W over the east-Central Pacific. Both spacecrafts were spin-stablilised at 100 revolutions per minute. The principle instrument on board was the Visible Infrared Spin-Scan Radiometer (VISSR) which provided day and night imagery of cloud conditions over the earth's disc. The VISSR instrument consisted of a scanning system, a radiometer telescope and VIS and IR sensors, a mirror that was mechanically positioned to provide north-south viewing, while the 100 rpm rotation of the satellite provided for west-east scanning.

The first U. S. Geostationary Operational Environmental Satellite (GOES) was launched on 16 October 1975. GOES-1 to -7 were spin-stabilized satellites and carried the VISSR instrument. GOES-8, the first of a new generation of GOES satellites, was launched on 13 April 1994. Since then, GOES-9 to -12 have been launched. Currently, GOES-12 (or GOES-East) is positioned at 75 °W longitude, while GOES-10 (or GOES-West) is positioned at 135 °W longitude.

The new GOES satellites are 3-axis stabilized. The current GOES imager is a 5-channel imaging radiometer. The imager multi-spectral channels can simultaneously sweep an 8 km north-south swath along an alternating east-west and west-east path, at a rate of 20° east-west scan per second. This translates into covering the full earth disc in 26 minutes.

The spectral channels of the scanning radiometers on geostationary satellites are not quite the same as those of the scanning radiometers on polar orbiting channels. The choice of wavelengths in the VIS, IR and WV bands is made on the basis of several different considerations which apply to the two different classes of meteorological satellites. Polar orbiting satellites give a composite global mosaic over a course of time and are useful for retrieving the global distribution of parameters like sea surface temperature or vegetation index. They cover the polar regions and are useful for ice cover monitoring. Hence they have near IR and split window TIR channels as described in the previous section. Geostationary satellites are specially suited for continuous monitoring of weather phenomena and large scale

atmospheric flows, so they carry a broader VIS channel and a WV channel instead (Table 1.3.2.2.1).

Table 1.3.2.2.1 GOES Imager Channels Characteristics

Channel Number	Spectral Band	Wavelength Range (μ)	Resolution (km)
1	VIS	0.55 - 0.75	1
2	SWIR	3.80 - 4.00	4
3	WV	6.50 - 7.00	8
4	TIR	10.20 - 11.20	4
5	TIR	11.50 - 12.50	4

(Source: http://noaasis.noaa.gov/NOAASIS/ml/imager.html)

1.3.2.3 INSAT VHRR

The Indian satellites INSAT-1A to -1D, and INSAT-2A and -2B carried a 2-channel Very High Resolution Radiometer (VHRR). The two channels were visible (VIS) 0.55-0.75 μ and thermal infra-red (TIR) 10.5-12.5 μ. Their resolutions at the sub-satellite point were 2.75 and 11 km respectively for INSAT-1A to 1D, and 2 and 8 km respectively for INSAT-2A and 2B. The INSAT-2E satellite, for the first time carried a 3-channel VHRR with a water vapour channel (WV) 5.7-7.1 μ added to the VIS and TIR channels. The ground resolution of the WV channel was 8 km.

Full details of the INSAT-2A and -2B VHRR instrument have been described by Joseph et al (1994) and subsequent improvements and additions made to the INSAT-2E VHRR have been discussed by Iyengar et al (1999). The VHRR optics assembly basically consists of a telescope, dichroic beam splitter, IR collimating lens, IR relay optics and VIS band optical elements. The incoming radiation is reflected onto an 8 inch (20.32 cm) diameter primary mirror of the reflective telescope by a two-axis gimbal-mounted beryllium scan mirror. A gold film dichroic beam-splitter placed in the converging beam from the secondary mirror of the telescope bifurcates the radiant energy. The VIS energy is transmitted through the dichroic while combined WV and TIR energy is reflected at right angles to the original direction. This allows the radiation from the earth to be channelled to visible and combined IR focal planes simultaneously with high optical efficiency.

The detector configuration for the VIS band consists of two staggered arrays of four silicon photodiodes each. For WV and TIR bands, the detector package contains two sets of dual mercury-cadmium-telluride (HgCdTe) photoconductive detector elements in close proximity to band defining filters. The IR detectors are operated nominally at a precisely controlled low temperature in the range of 105-115 °K to limit thermally generated noise. A passive radiant cooler is used to cool the IR detector package. One of the detectors in each band is energized, while the other set provides the on-board redundancy. Both sets are identical in function and can be switched on or off from through ground command.

The image of the earth is generated by sweeping the instantaneous geometric field of view of the detectors by rotation of the scan mirror-gimbals in two orthogonal axes. For every east-west sweep of the mirror, four contiguous lines of VIS band and one line each of WV and TIR bands are generated. At the end of the sweep, the mirror is stepped south through an angle equivalent to 8 km on the ground and data collection is resumed in the reverse west-east sweep.

Three modes of operation are provided to allow trade-off between area and frequency of coverage. The full frame mode scans the entire earth disc and some space around (20° × 20°) in about 33 min. The normal frame mode coverage in the east-west direction is the same as in the full frame mode, but in the north-south direction, the scan is limited to only 14°, covering the region between 50 °N and 40 °S latitudes in 23 min. In the sector scan mode, the east-west coverage is the same as in the full frame and normal frame modes, but is further limited to a 4.5° scan in the north-south direction which can be completed in about 7 min. The sector can be positioned, through ground command, anywhere in the full scan field in steps of 0.5° in the north-south direction. This mode is particularly suited for rapid repetitive coverage during severe weather conditions.

The dark and cold space views at the east and west ends are used for establishing reference radiance for all the three bands. A full end-to-end calibration of WV and TIR bands is provided by swinging the mirror to view a black body cavity fitted on the inner side of north plate of the instrument. The physical temperature of the black body is accurately monitored by platinum resistance thermometers at five locations and is telemetered through the VHRR data stream. The system response for black body view is available in the video data slot.

The detector outputs of all the three channels are individually amplified, band limited and digitized to 1024 grey levels by A/D converters. The

digitized data along with other housekeeping information and calibration data, are formatted, randomized and transmitted serially in extended C band to the INSAT Meteorological Data Processing System at the India Meteorological Department, New Delhi.

The design of the VHRR systems on the currently operational Indian satellites, INSAT-3A and Kalpana-1, are similar to the INSAT-2E VHRR.

The INSAT-3D satellite to be launched in 2007, will carry a 6-channel imager with two new SWIR and MWIR channels and two split TIR channels. There will be a higher resolution of 1 km in VIS and SWIR, and 4 km in TIR channels (Table 1.3.7.1). The WV channel will be the same as before.

1.3.2.4 Radiometers of Other Geostationary Satellites

In the two decades between 1977 and 1997, the European Space Agency ESA and EUMETSAT had launched seven geostationary meteorological satellites of the Meteosat series. The prime Meteosat spacecraft is usually kept positioned at 0° longitude on the equator. In the spring of 1998, METEOSAT-5 was moved to 63° E to cover the Indian Ocean to support the INDOEX programme. The Meteosat has a spinning radiometer which has 3 spectral bands, VIS, WV and TIR, with a wavelength range of 0.45-1.0, 5.7-7.1 and 10.5-12.5 μ respectively. The resolution of the VIS channel is 2.5 km and that of the other two channels is 5 km.

EUMETSAT's Meteosat Second Generation (MSG) satellite (Schmetz et al 2002) carries a 12-channel spinning radiometer called SEVIRI, with a 1 km resolution for the VIS band and 3 km resolution for the IR bands. MSG is capable of providing full-disc images every 15 minutes. The 12-channel configuration of SEVIRI includes a new channel in the ozone absorption band, a triple TIR window and three WV channels to serve various new applications (Table 1.3.2.4.1). The MSG-1 satellite was successfully launched on 28 August 2002. When MSG-1 became operational in 2004, it was renamed METEOSAT-8. The MSG-2 satellite was launched on 21 December 2005.

The Japanese geostationary meteorological satellite is known as GMS, or Himawari in Japanese. The last operational satellite in this series, GMS-5, was launched in 1995. After its end of life in 2003, it was replaced at 140°E by the U. S. satellite GOES-9. The spin-scan radiometer on GMS-5 carries a visible channel, two TIR (11 and 12 μ) channels and a WV (6.5 μ) channel.

The VIS channel has a resolution of 2.5 km while the other three channels have a resolution of 5 km.

MTSAT (Multi-purpose Transportation Satellite) is a Japanese three-axes stabilized geostationary satellite which currently serves meteorological as well aeronautical communication requirements. MTSAT-1R was successfully launched on 26 February 2005 at 140 °E and MTSAT-2 was launched on 24 February 2006 as a standby. The MTSAT radiometer has 5 channels, VIS 0.55-0.80 μ, IR1 10.3-11.3 μ, IR2 11.5-12.5 μ, IR3 6.5-7.0 μ and IR4 3.5-4.0 μ with a resolution of 1 km for VIS and 4 km for IR channels.

Table 1.3.2.4.1 MSG SEVIRI Channel Characteristics

Channel Number	Spectral Band	Wavelength Range (μ)	Applications
1	HRV	0.6-0.9	Cloud texture, winds
2	VIS	0.56-0.71	Cloud over land, winds
3	VIS	0.74-0.88	Cloud over water, vegetation
4	NIR	1.50-1.78	Cloud over snow
5	MIR	3.48-4.36	Low cloud
6	IR 6.2	5.35-7.15	High level water vapour
7	IR 7.3	6.85-7.85	Middle level water vapour
8	IR 8.7	8.30-9.10	Total water vapour
9	IR 9.7	9.38-9.94	Total ozone
10	TIR 10.8	9.8-11.8	Surface and cloud top temperature, winds
11	TIR 12.0	11.0-13.0	Surface temp. correction
12	TIR 13.4	12.0-13.4	Higher clouds

Russia launched its first Geosynchronous Operational Meteorological Satellite (GOMS-1), also known as Elektro-1, on 31 October 1994. It was located at 77° E and had a scanning radiometer with two spectral channels, VIS 0.47-0.70 μ with 1.25 km spatial resolution, and TIR 10.5-12.5 μ with 6.25 km spatial resolution.

China's geostationary meteorological satellites are all called Feng-Yun-2 (meaning Wind-Cloud), and are very similar to the Japanese GMS and the U.S. GOES-7 spin-stabilized satellites. The main payload of FY-2 is a Visible and Infrared Spin Scan Radiometer (VISSR) which obtains hourly

full-disc images of the earth, through step action of the scan mirror, in three channels: VIS 0.55-1.05 μ, TIR 10.5-12.5 μ and WV 6.2-7.6 μ. The sub-satellite point resolution is 1.25 km for VIS and 5 km for the other channels. The FY-2C satellite was launched on 19 October 2004 and placed over 105° E longitude. Processed FY-2C images and animated sequences covering China and west Pacific Ocean are posted on the internet by the Hong Kong Observatory at www.hko.gov.hk.

1.3.2.5 Along Track Scanning Radiometer

The Along Track Scanning Radiometer (ATSR) is an instrument that has been innovatively designed for achieving exceptional sensitivity and stability of calibration, which has enabled the accurate measurement of sea surface temperature to an accuracy of 0.3 °K. The primary objective of the ATSR mission is to generate a 10-year global SST data with the accuracy required for climate research. Its second objective is to develop quantitative remote sensing of land surface parameters, particularly vegetation, by means of the improved atmospheric correction that is achievable with AATSR's two-angle view.

The first ATSR instrument, ATSR-1, was launched in July 1991 on board the European Remote Sensing Satellite (ERS-1) of the European Space Agency (ESA) as part of its Earth Observation Programme. An enhanced version, ATSR-2, was launched on board the ERS-2 spacecraft on 21 April 1995. ATSR-2 is equipped with additional visible channels for vegetation monitoring. The AATSR (Advanced Along Track Scanning Radiometer) instrument has been launched on board the ENVISAT spacecraft on 1 March 2002.

The ATSR has one visible channel (1.6 μ) and three thermal IR channels (3.7, 11 and 12 μ) and achieves a resolution of 1 km. As will be discussed later (see Section 3.5.4), satellite measurements of the temperature of the earth's surface are always vitiated because of the partial absorption of the radiation as it passes through the atmosphere, particularly by water vapour. The ATSR employs a dual view design in order to estimate and correct for these atmospheric effects. The two views result from the instrument's conical scanning mechanism. Each scan takes readings from the nadir position and then sweeps round to take measurements from a point about 900 km along the satellite's track. A few minutes after acquiring the forward view, the satellite passes over the same spot and takes readings for the nadir view. As the two views of the same scene are taken through different atmospheric path

lengths, it is possible to calculate a correction for the effect of atmospheric absorption (Stricker et al 1995).

Mathur et al (2002) have made a validation study of sea surface temperature derived from ERS-1/ATSR observations over the Indian seas.

1.3.3 CCD Cameras

While the use of Charge Coupled Devices (CCDs) has been common in remote sensing satellites for land resources applications, India was the first country to fly a 3-band CCD-based imager in geostationary orbit on its INSAT-2E satellite to complement the VHRR. A similar instrument is currently flying on the INSAT-3A satellite. It provides co-registered images of the earth in VIS 0.62-0.68 μ, NIR 0.77-0.86 μ and SWIR 1.55-1.69 μ regions of the spectrum. The ground resolution of these images at the sub-satellite point is 1 × 1 km for all the three bands. The spectral bands as well as dynamic range and saturation radiance set points are so selected that the images can be used for meteorological applications as well as vegetation mapping and other earth resources applications. A complete technical description of the INSAT CCD imager has been given by Iyengar et al (1999).

The CCD imager is similar to the VHRR as far as the basic telescope design and scan mechanism are converned. The separation of the three bands is achieved by two dichroic beam splitters. The first dichroic reflects SWIR energy and transmits VIS and NIR energy, while the second one reflects NIR energy and transmits VIS energy. The VIS and NIR band linear silicon detector arrays are placed directly in the split focal plane of the telescope, whereas an auxiliary lens doublet refocuses the telescope beam to a secondary focus where the SWIR charge coupled photodiode (CCPD) array detector is placed. This optical configuration is designed for achieving identical footprints on the ground while accommodating two different sizes of detector elements. Ground processing is further facilitated by selecting a unidirectional scanning in fast scan direction in view of hybrid scan concept used for this payload. In this type of scanning, mechanical scanning and electronic scanning are simultaneously carried out in two orthogonal axes. This scan geometry generates a three-band image strip of 300 km width (north-south) and 6300 km length (west-east) for each west-east sweep of the scan mirror in 1 minute.

Flexible programmable scan modes allow generation of images with up to 24 contiguous strips covering an area of 6300 × 6300 km on earth. Again, a

positioning mechanism enables this image field to be positioned anywhere in a scan field of 20° × 20° covering the full earth disc.

The scan mechanism consists of a gimballed scan mirror which sweeps the composite detector field of view in two orthogonal axes to generate wide-field 2-dimensional imagery. The fast scan sweep of the mirror generates 300 video lines over 6300 km east-west scan every minute. The stepping of the mirror to the south by about 0.4° after each west-east scan helps to generate successive image strips. Earth imaging is done only during west-east scan of the mirror. Scan efficiency is very high as the retrace time is only about 1.25% of active line time. The total scan field of the mirror is ± 13° east-west and ± 10° north-south, while the active image field is ± 5° east-west and a maximum of ± 5° north-south. This active image field can be positioned anywhere in the total scan field to generate imagery of any part of the visible earth disc.

The detectors used for VIS and NIR bands are 2048-element linear silicon CCD arrays. The outputs of three consecutive detector array elements are added together. Thus 900 pixels of each array are utilized to construct 300 image pixels for each band.

The SWIR detector consists of a 300-element linear CCPD array. This is a hybrid assembly where InGaAs photodiodes are coupled to silicon CCD readout shift registers. As the pixel sizes of VIS/NIR and SWIR CCD arrays are different, effective focal lengths are adjusted by auxiliary optics in SWIR band to give identical ground resolution of better than 1 km x 1km for all the three bands.

Padmanabhan et al (2004) have discussed the complex nature of CCD image processing and the distortions that can arise in the images. They have described the technique of removing the distortions due to the scan imaging, and mosaicing the corrected strips to generate geocoded images of India and the surrounding region. Their method can be used to generate geocoded images of any area imaged by any satellite of the same type. The accuracy of the absolute earth location calculated by considering some ground control points, is found to be about 5 pixels, both in the N–S and E–W directions.

Bhatia et al (1999) have described the wide variety of applications that are possible because to the fine resolution and continuous temporal coverage provided by the INSAT CCD camera.

1.3.4 Spectroradiometers

Precision spectroradiometers are usually based on a monochromator with a diffraction grating. A concave mirror collimates the radiation and the diffraction grating reflects the radiation while dispersing it into its spectral components. A second concave mirror focusses the radiation on a detector. Scanning of the spectrum is accomplished by rotating the grating while recording the electrical signal at the detector.

A satellite-based spectroradiometer can provide extremely high spectral sensitivity with exceptionally low out-of-band response. One such instrument called the Moderate Resolution Imaging Spectroradiometer (MODIS) was flown aboard the Terra and Aqua satellites launched on 18 December 1999 and 4 May 2002 respectively by NASA. Terra's orbit around the Earth is timed so that it passes from north to south across the equator in the morning, while Aqua passes south to north over the equator in the afternoon.

Terra MODIS and Aqua MODIS are viewing the entire earth's surface every 1 to 2 days, acquiring data in 36 spectral bands ranging in wavelength from 0.4 to 14.4 μ. The responses are tailored to meet the needs of several applications (Table 1.3.4.1). The resolution at nadir is 250 m for bands 1-2, 500 m for bands 3-7 and 1 km for bands 8-36. A ± 55° scanning pattern at an orbital altitude of 705 km achieves a 2,330 km swath.

The scan mirror assembly uses a continuously rotating double-sided scan mirror and is driven by a motor encoder built to operate at 100 percent duty cycle throughout the 6-year instrument design life. The optical system consists of a two-mirror off-axis telescope, which directs energy to four refractive objective assemblies; one for each of the VIS, NIR, SWIR/MWIR and LWIR spectral regions to cover a total spectral range of 0.4 to 14.4 μ.

1.3.5 Resolution

The term resolution as applied to meteorological satellites assumes a different meaning in different contexts: spatial, spectral, radiometric and temporal, but in each case it is a critical design consideration. While the highest possible resolution is desirable, it is not always possible to attain it and what is realized is a trade-off between several competing factors. A higher resolution also requires extremely high rates of data transfer and an increasingly complex design of both space and ground systems.

Table 1.3.4.1 MODIS Spectral Bands and their Applications

Band	Spectral Range (μ)	Primary Applications
1	0.620 – 0.670	Land/Cloud/Aerosols Boundaries
2	0.841 – 0.876	
3	0.459 – 0.479	Land/Cloud/Aerosols Properties
4	0.545 – 0.565	
5	1.230 – 1.250	
6	1.628 – 1.652	
7	2.105 – 2.155	
8	0.405 – 0.420	Ocean Colour/ Phytoplankton/ Biogeochemistry
9	0.438 – 0.448	
10	0.483 – 0.493	
11	0.526 – 0.536	
12	0.546 – 0.556	
13	0.662 – 0.672	
14	0.673 – 0.683	
15	0.743 – 0.753	
16	0.862 – 0.877	
17	0.890 – 0.920	Atmospheric Water Vapour
18	0.931 – 0.941	
19	0.915 – 0.965	
20	3.660 - 3.840	Surface/Cloud Temperature
21	3.929 - 3.989	
22	3.929 - 3.989	
23	4.020 - 4.080	
24	4.433 - 4.498	Atmospheric Temperature
25	4.482 - 4.549	
26	1.360 - 1.390	Cirrus Clouds Water Vapour
27	6.535 - 6.895	
28	7.175 - 7.475	
29	8.400 - 8.700	Cloud Properties
30	9.580 - 9.880	Ozone
31	10.780 - 11.280	Surface/Cloud Temperature
32	11.770 - 12.270	
33	13.185 - 13.485	Cloud Top Altitude
34	13.485 - 13.785	
35	13.785 - 14.085	
36	14.085 - 14.385	

What a scanning radiometer views at any instant is called the Instantaneous Field Of View (IFOV) and it is generally considered as the spatial resolution of the imaging sensor. The size of an individual pixel or picture element also depends mainly on the sampling rate and the forward motion of the spacecraft. In a meteorological satellite, the spatial resolution of the radiometer will decide the smallest cloud that can be seen in the image.

The spectral resolution of the sensor is inversely related to the channel bandwidth. A higher spectral resolution and an accurate spectral signature can be obtained by having a large number of narrow bands, rather than one continuous broad band.

The term radiometric resolution is used to indicate the smallest perceptible change in the radiance of various targets that the sensor can discriminate. It is a measure of the signal-to-noise ratio of the sensor. It can also be defined in terms of the ability to resolve temperature difference between targets.

The temporal resolution is an important consideration in operational meteorology because it determines what kind of meteorological phenomena can be viewed by the satellite, as they have different lifetimes. Temporal resolution refers to the elapsed time interval between two successive satellite scans of a given region. This is also called the repeat cycle or repetivity of the orbit.

The temporal resolution is decided by the design of the scanning radiometer as well as the nature of the spacecraft orbit and it has to have a significant trade-off with the spatial resolution. For achieving a finer spatial resolution, the scan has to be made slower and the temporal resolution will get reduced. INSAT imagery can be obtained at an interval of 40 minutes for the full earth disc, 30 minutes for the reduced scan, and 10 minutes for the rapid scan. Satellites meant for monitoring of earth resources or for cartographic applications can have an extremely high spatial and spectral resolution because they can afford to have a long repeat cycle.

1.3.6 Navigation and Gridding

Navigation and gridding are two basic steps in meteorological satellite data processing. The term navigation is used in its conventional sense and implies the use of landmarks for determination and prediction of orbit and attitude. By this process, it is possible to relate points on the earth, defined by latitude and longitude, to point on the image, given by line and element numbers and vice versa.

By gridding we mean the superposition of grid points, political boundaries or latitude-longitude lines on the navigated image. If geostationary satellite images produced at 30 min interval are viewed in quick succession, the landmarks should appear to be stationary. The removal of apparent earth motion from an animated sequence of images is called registration.

Briefly speaking, the navigation process involves transformations among five different coordinate systems: (a) inertial system, having its origin at the centre of the dynamical earth, and the x-axis pointing to the vernal equinox and z-axis normal to the equatorial plane, (b) rotating system, similar to the inertial system but with the z-axis passing through the Greenwich meridian, (c) local vertical system, having its origin at the centre of the satellite, (d) body-centred system, defined in terms of the pitch, roll and yaw angles, and (e) picture frame system, defined in terms of line and element number (Kelkar et al 1980).

The degree of sophistication of the navigation process determines the accuracy with which the latitude-longitudes of pixels are derived (Prakash et al 1996). This has a very important bearing in quantitative product derivation like cloud motion winds in which the positions of the pixels have to be known very precisely. A poor navigation also shows up as a mismatch between the superimposed grid and the geographical features on the image.

Navigation errors may result in image distortions in various forms such as a vertical compression or expansion of the image, non-vertical alignment of the north and south poles, and multiple representations or omissions of image pixels.

1.3.7 INSAT, METSAT and Kalpana Satellites

The evolution of the Indian space programme and its meteorological component has been described in many reviews (Kelkar 1994, Pandey et al 1994, Joshi et al 2003). In India, the need to have a national meteorological and remote sensing satellite programme to monitor its weather and vast natural resources was realized way back in the sixties by great pioneers and visionaries like Vikram Sarabhai and Satish Dhawan. The successful launches of the first Indian satellite Bhaskara-I in 1979 and its follow-on Bhaskara-II in 1981 were followed by the launch of INSAT-1A in 1982 and INSAT-1B in 1983. The first Indian remote sensing satellite IRS-1A was launched in 1988.

Table 1.3.7.1 Meteorological Payloads of INSAT, METSAT and Kalpana Satellites

Name of Satellite	Launch Date	Meteoro-logical Payload	Channel	Spectral Range (μ)	Reso-lution (km)
INSAT-1A	10 April 1982	VHRR Very High Resolution Radiometer	VIS	0.55-0.75	2.75
INSAT-1B	30 August 1983	VHRR	IR	10.5-12.5	11
INSAT-1C	21 July 1988	VHRR			
INSAT-1D	12 June 1990	VHRR			
INSAT-2A	10 July 1992	VHRR	VIS	0.55-0.75	2
INSAT-2B	23 July 1993	VHRR	IR	10.5-12.5	8
INSAT-2C	7 December 1995	None			
INSAT-2D	4 June 1997	None			
INSAT-2E	3 April 1999	VHRR	VIS	0.55-0.75	2
			IR	10.5-12.5	8
			WV	5.7-7.1	8
		CCD Charge Coupled Device Camera	VIS	0.62-0.68	1
			NIR	0.77-0.86	1
			SWIR	1.55-1.69	1
INSAT-3B	22 March 2000	None			
INSAT-3C	24 January 2002	None			
Metsat/ Kalpana-1	12 September 2002	VHRR	VIS	0.55-0.75	2
			IR	10.5-12.5	8
			WV	5.7-7.1	8

Table 1.3.7.1 Contd...

Name of Satellite	Launch Date	Meteoro-logical Payload	Channel	Spectral Range (μ)	Reso-lution (km)
INSAT-3A	10 April 2003	VHRR	VIS	0.55-0.75	2
			IR	10.5-12.5	8
			WV	5.7-7.1	8
		CCD	VIS	0.62-0.68	1
			NIR	0.77-0.86	1
			SWIR	1.55-1.69	1
INSAT-3E	28 September 2003	None			
INSAT-4A	22 December 2005	None			
INSAT-3D	To be launched in 2007	VHRR	VIS	0.52-0.72	1
			SWIR	1.55-1.70	1
			MWIR	3.80-4.00	4
			WV	6.50-7.10	8
			TIR	10.2-11.2	4
			TIR	11.5-12.5	4
		Sounder	SWIR	3.67-4.59 6 channels	10
			MWIR	6.38-11.33 . 5 channels	10
			LWIR	11.66-14.85 7 channels	10
			VIS	0.67-0.72 1 channel	

1. Satellites in the INSAT-1 series were built in the U.S. as per Indian design and launched from abroad.
2. Satellites in the INSAT-2 series were built indigenously but launched from abroad.
3. INSAT-2C was India's first exclusive communications satellite.
4. INSAT-2E was the first geostationary meteorological satellite to have a CCD payload.
5. Metsat, India's first exclusive meteorological satellite, was launched from Sriharikota by ISRO's PSLV-C4
6. Metsat was renamed Kalpana-1 on 5 February 2003 in memory of Dr Kalpana Chawla, the India-born American astronaut who died in the U.S. space shuttle Columbia disaster on 1 February 2003.
7. Kalpana-1 located at 74 °E and INSAT-3A located at 93.5 °E are the current operational satellites.
8. INSAT-3D will be the first Indian meteorological satellite to have a sounder.

INSAT is India's unique domestic satellite system which was conceptualized to bring in satellite-based services in as many fields as possible in the quickest possible time. The multi-purpose concept of INSAT led to the realization of the full potential of the geostationary satellite system in one stroke. Thus while other countries had dedicated satellites for different purposes, INSAT-1A ushered in a new era in communications, television and radio broadcasting, and meteorology at the same time. While the first APT station had been established in India in 1965, it had given Indian weather forecasters only limited access to satellite imagery. Satellite meteorology may be said to have truly come of age in India with the launch of the first INSAT satellite in 1982.

Table 1.3.7.1 is a detailed chart of the milestones in the history of evolution of the INSAT meteorological programme. While the INSAT-1 series consisted of multi-purpose satellites, some of the later satellites did not have a meteorological component. On the other hand, METSAT, launched in 2002, and later renamed Kalpana-1, is exclusively dedicated to meteorological services. INSAT-3D to be launched in 2007, will be the first Indian satellite to carry a sounder.

1.3.8 Microwave Passive Sensors

Microwave remote sensing has always been recognized as a powerful tool for meteorological and oceanographic applications, because of its ability to measure water vapour and liquid water even in the presence of most clouds. However, it did not come into popular use due the poor ground resolution of microwave images and because of the fact that land surface emissivity in the microwave region was high and variable. Moreover, microwave sensors have to be flown on low earth orbiting satellites and it has not been possible so far to place them on geostationary platforms because of the weak microwave signal strength. The principles of satellite-borne microwave radiometry have been reviewed by Pandey (1995).

Seasat, Nimbus-5, Nimbus-7 and India's Bhaskara-II, were the earliest satellites to carry passive scanning microwave radiometers and clearly demonstrated the potential of microwave measurements in the retrieval of atmospheric and oceanographic parameters.

Bhaskara-II, which was launched in 1981, carried a Satellite Microwave Radiometer (SAMIR) that had three channels at 19.35, 22.235 and 31.4 GHz, with vertical polarization. The observations were taken close to nadir at angles of 2.8° and 5.6° along the satellite ground trace during each spin of the satellite. The footprint had a size of 240 km. Pathak et al (1992) used SAMIR

data for the period January 1982 to June 1983 to derive the latitudinal variation of monthly mean values of atmospheric water vapour content over the Arabian Sea and Bay of Bengal and studied its seasonal and geographical variations. Gohil et al (1982) had earlier derived atmospheric water content from Bhaskara SAMIR data.

Nimbus-5 had the Electrically Scanning Microwave Radiometer (ESMR) operating at a frequency of 19.35 GHz and Nimbus-7 carried the Scanning Multichannel Microwave Radiometer (SMMR).

The Defense Meteorological Satellite Programme (DMSP) is a long-term U. S. Air Force effort in space to monitor the meteorological, oceanographic and solar-geophysical environment of the earth. In December 1972, DMSP data was declassified and made available to the civilian and scientific community. The Special Sensor Microwave Imager (SSM/I), was first flown on the DMSP satellites in June 1987. The U. S. maintains an operational constellation of two DMSP satellites, each in a 101 minute, sun-synchronous near-polar orbit at an altitude of 830 km above the surface of the earth. The Special Sensor Microwave Imager (SSM/I) is a 7-channel, 4-frequency, linearly-polarized, passive microwave radiometric system which measures atmospheric, ocean and terrain microwave brightness temperatures at 19.35, 22.235, 37.0 and 85.5 GHz. The footprint sizes vary from 13 x 15 km at 85 GHz to 43 x 69 km at 19 GHz.

SSM/I data are used to derive a variety of geophysical parameters such as, ocean surface wind speed, ice cover, cloud liquid water, integrated water vapor, precipitation over water, soil moisture, land surface temperature, snow cover and sea surface temperature. Most of the retrieval algorithms in vogue are in the form of statistical correlations between the brightness temperatures of various channels or differences between channels, with these parameters.

The TRMM Microwave Imager (TMI) on board the Tropical Rainfall Measuring Mission (TRMM) satellite, is a passive sensor operating at 5 microwave frequencies of 10.65, 19.35, 22.235, 37.0 and 85.5 GHz. These frequencies are very similar to those of SSM/I, but TMI has an additional 10.7 GHz channel designed to provide a more linear response for the high rainfall rates in the tropics. All TMI channels have horizontal and vertical polarizations, except the 21 GHz channel which has only vertical polarization. There is 53° conical scanning and the footprints vary in size from 5 km at 85 GHz to 45 km at 10 GHz. TMI has an improved ground resolution resulting from the lower altitude of TRMM (see Section 4.1).

The Indian Remote Sensing Satellite IRS-P4 (also known as Oceansat-1) launched on 26 May 1999, carried a Multi-channel Scanning Microwave Radiometer (MSMR) operating at 6.6, 10, 18 and 21 GHz frequencies in both H and V polarizations.

1.4 Satellite Imagery

As satellite images started becoming available to meteorologists around the world in the early sixties, the skills of satellite image interpretation developed very rapidly. Until then, knowledge about clouds had been documented into cloud atlases on the basis of what had been observed from the ground or aircrafts. The view from satellite altitudes was, however, completely different and clouds seen by satellites had to be interpreted in an altogether different manner.

It must also be remembered that in the early days of the satellite era, the picture technology was primitive. APT pictures received directly from satellites flying overhead were produced on facsimile chart paper, mostly of inferior quality and liable to fading in a short time. The images many times lacked clarity and hence they had to be examined with great care. However, the technology improved really fast and even photographic paper was mostly done away with, when interactive computer image processing systems like McIDAS became common. Now of course, there are web sites on the internet on which anyone can access satellite imagery in near real time.

1.4.1 Characteristics of Satellite Imagery

Most of the early interpretation schemes used six characteristics to identify clouds in satellite images (Conover 1962), which were:

(1) Cloud brightness relating particularly to the depth and composition,
(2) Texture - whether smooth, fibrous, opaque, or mottled,
(3) Form of elements - whether regular or irregular,
(4) Pattern of elements - associated with topography, air flow, vertical and horizontal wind shear,
(5) Size - both of the patterns and the individual elements, and
(6) Vertical structure - for example shadows thrown below.

In addition, cloud classification schemes were developed on the basis of cloud patterns (Hopkins 1967):

(1) Vertical features:
    (a) Circular or spiral bands,

(b) Crescent-shaped or comma-shaped cloud masses,
(c) Quasi-circular cloud masses, and
(d) Curved or linear bands.

(2) Major cloud bands, in which the length is much greater than the width,
(3) General features:
(a) Minor bands like cloud streets, jet stream bands, lee waves,
(b) Cumuliform features, polygonal cells, and
(c) Stratiform features, fog areas.

Although nowadays most of the picture interpretation work is carried out on image processing computers, and various interpretation aids are available to the analysts, it is necessary to have a basic knowledge of the fundamental characteristics mentioned above and their importance.

It is also important to remember that interpretation of individual satellite images should never be done in isolation, as may happen for example, when one sees a satellite image flashed on a television channel. The day and time of the image, the geographical area covered, the gray scale and enhancement used, must all be known and given due consideration. Other available observational data and synoptic weather charts should also always be referred to. Continuity in time is essential and earlier images should be compared for detecting changes or confirming the interpretation. Images from all available channels should also be compared. The information derived from the VIS, IR, WV and microwave channels is not redundant but complementary, and when all channels are considered together, they help to remove uncertainties or ambiguities in the interpretation process and to identify clouds and surface features uniquely.

1.4.1.1 Visible Channel Imagery

Clouds which appear brighter in VIS imagery are those which have a large albedo because of great depth, high cloud water/ice content and small cloud-droplet size. Clouds which appear gray are those having shallow depth, low cloud water/ice content and large cloud droplet size. Thus vertically grown cumulonimbus clouds appear most prominently in VIS images whereas thin cirrus cannot be clearly seen (Figure 2.2.1.1).

Small cumulus clouds usually take the form of open hexagonal cells while stratocumulus clouds appear as closed cells. Low level stratus clouds or areas covered by fog can be identified by their uniform brightness and sharp boundaries (Figure 2.5.3). Tall Cb cloud tops some times throw shadows on lower cloud layers.

Since convection is the main source of rainfall in the global tropics, in the early years of satellite observation, the distribution of highly reflective clouds (HRC) was considered important and extensively documented (Garcia 1985). Efforts were also made to use the HRC data for estimating precipitation. Mahajan et al (1991) found a good correlation between the monthly HRC frequency and monthly rainfall data over the island stations in Arabian Sea and Bay of Bengal.

1.4.1.2 Infra-red Channel Imagery

The most important advantage of IR imagery is that it is available at any time unlike VIS imagery which is available only in daylight hours. Secondly, IR radiances are a measure of the temperature of the radiating surface. Clouds which appear white in IR imagery are those which have cold cloud top temperatures such as Cb and cirrus clouds. A mature Cb cloud can be further recognized by its sharp edge on the windward side and a fuzzy edge on the other side resulting from the the cirrus plume. The plume may get blown downwind over several hundred kilometres and give an indirect indication of the upper level wind speed and direction (Figure 2.3.5.3).

Clouds in IR imagery do not have the kind of texture that is seen in VIS imagery. IR images cannot discriminate between low clouds and the sea surface or between fog and land surface, because of the absence of sufficient temperature difference.

1.4.1.3 Water Vapour Channel Imagery

Like IR imagery, WV imagery is also available at all times. While IR images are produced from radiances received by the radiometer in the thermal window region, water vapour channel imagery is produced from radiances received in the water absorption band centred at 6.7 μ. The stronger the absorption, the higher is the originating level of the emission that ultimately reaches the satellite. As the atmospheric moisture content decreases with height, the main contribution to the radiance received by the satellite comes from levels in the lower and middle and troposphere. So in WV imagery, the brighter regions are those with high upper tropospheric humidity and the dark regions are those where the upper troposphere is very dry.

While in IR imagery, the brightness of a pixel depends upon its temperature, there is no such simple relationship between moisture and brightness for a WV image as. Since clouds also emit some radiation in the WV band, high

and deep clouds and Cb anvils show up with equal prominence in VIS, IR and WV imageries (Figures 2.2.1.1 to 2.2.1.3).

Bhatia et al (1999) have described the characteristic features and many potential applications of water vapour imagery in the INSAT 6.7 μ (5.7-7.1μ) channel.

Generally speaking, WV images have a different appearance from that of VIS and IR images. WV images are characterized by the presence of extensive and continuous structures (Figure 2.3.1.2). Cloud patterns which appear distinct from each other in the VIS and IR images can be recognized as being a part of the same air mass in corresponding WV images. The band structures also provide some indication of prevailing large scale wind patterns like jet stream cores. This information is important over cloudfree regions where cloud motion winds cannot be derived.

WV images show moisture boundaries in the form of plumes, or tongues or streams of moisture. These can be of great help in the prediction of heavy rainfall and resultant flash floods.

WV imagery has been found to be useful in understanding the processes that govern the movement of tropical cyclones. It is generally understood that the recurvature of a north-westward moving tropical cyclone occurs under the influence of an approaching upper air trough. WV imagery is able to capture such interactions, and the possibility of recurvature becomes evident through a northward expansion of the moisture envelope of the cyclone as it approaches this trough. On the contrary, if the imagery shows a significant moisture dissipation on the northern side, the cyclone is likely to keep a westward track.

1.4.1.4 Microwave Channel Imagery

Microwave channel images give important clues about weather phenomena that may be missed out in VIS or IR pictures. SSM/I 85 GHz products can observe the eye in tropical cyclones since the cirrus overcast is transparent at this frequency, while IR and VIS images of tropical cyclones are usually covered by abundant cirrus. In the case of weakening cyclones, SSM/I can clearly bring out the cloud formations which in other channels have no contrast with the sea surface.

1.4.2 Gray Scale, Enhancement and Pseudocolour Imagery

In satellite images, the brightness of a pixel is usually assigned a value on a scale of 256 points ranging from 0 to 255, which is called the gray scale. The number 0 on the gray scale stands for pure black and the number 255 stands for pure white. This scale is shown as a strip of continuously increasing brightness at the top or bottom of a satellite image for reference. In a VIS image, lower values on the gray scale are seen over oceans because of their high absorption of solar radiation and the value 0 is assigned to the darkest pixels. The higher gray scale values are seen over snow covered regions and thunderstorm cloud tops, with the value 255 corresponding to the brightest pixels. In an IR image, the lower end of the gray scale corresponds to high temperatures and the higher end of the gray scale to low temperatures. In a WV image, lower values of the gray scale correspond to dry regions and higher values to moist regions.

When satellite images taken at different times or by different satellites, or pictures reproduced by different photographic machines, need to be compared, a reference has to be made to their gray scale wedges to avoid drawing unrealistic conclusions.

While the gray scale is basically linear, in order to improve the contrast between individual pixels, a non-linear gray scale may at times be applied to the image. This procedure is called enhancement, as it effectively enhances the original gray scale in some parts and brings out desired features that may have been masked out in the original image. Of course, stretching the gray scale in one part implies that it will get compressed in another part. Thus enhancement of any feature is always at the cost of some other feature. Various enhancement curves can be designed and used for meeting different requirements. For example, in Dvorak's technique (see Section 2.4.4), a step-cum-linear enhancement curve (Figure 1.4.2.1) can be applied to cyclone images to enhance the outer cloud features and separate the class boundaries (Figure 1.4.2.2 and 1.4.2.3).

Pseudocolour imagery is produced by a special kind of enhancement in which parts of the gray scale are not stretched but assigned different colours or shades to bring out the essential features. For example, tall cloud tops can be made to appear as red (Figure 1.4.2.4 - Colour Plate-1), or clear ocean as blue. In pseudocolour images, the possible enhancement choices are much greater and can be effectively used to draw attention to the desired features. Another way of generating false colour images is by combining VIS and IR images. Here as the common features get added and others get subtracted, the combined colour image can be made to highlight the essential features or give a natural look (Figure 1.4.2.5 - Colour Plate-1).

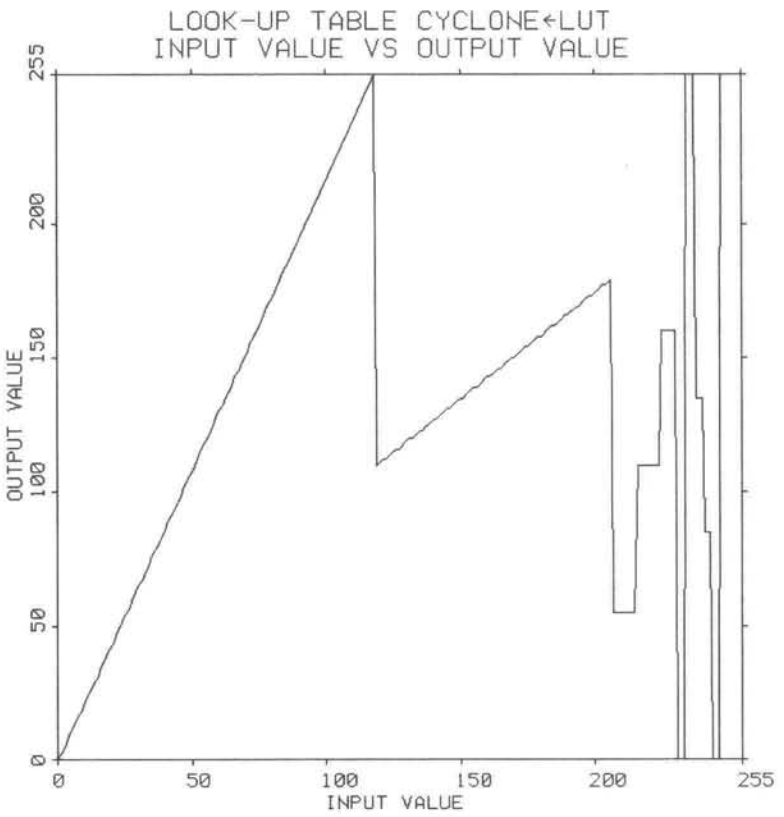

Figure 1.4.2.1 Gray scale enhancement curve for tropical cyclone (Source: IMD)

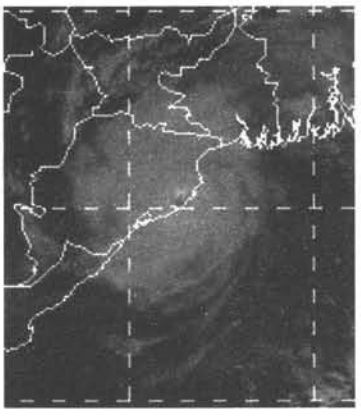

Figure 1.4.2.2 Cyclone image without enhancement (Source: IMD)

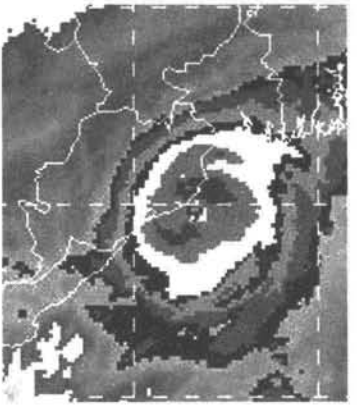

Figure 1.4.2.3 Cyclone image with enhancement (Source: IMD)

1.4.3 Appearance of Surface Features

The VIS channel helps to discriminate between land and sea areas and between different types of clouds. Oceans, rivers, lakes and small water bodies can be easily identified as dark areas. However, snow cover and bright clouds may be difficult to differentiate. Cloud-free land regions appear in various shades of gray depending upon the type of soil and vegetation.

Because of the larger amplitude of the diurnal cycle of temperature over land than over sea, coastlines show up clearly in IR images only when there is strong contrast between land and sea surface temperatures. They may not be recognizable at those hours when there is no temperature contrast.

The reflection of the sun's disc that may some times be seen in VIS channel satellite images of large water bodies is referred to as sunglint. It is particularly observed in noon time images of tropical oceanic regions taken by geostationary meteorological satellites. A smooth water surface acts like a mirror and produces a small bright reflection (Figure 1.4.3.1) while a rough water surface produces a weaker reflection over a larger area. Although scatterometers now give us direct measurement of the sea surface winds, in the very early years of satellite meteorology, attempts were made to estimate the sea surface wind from the area of sunglint and its brightness as seen in VIS satellite pictures (Gokhale 1971).

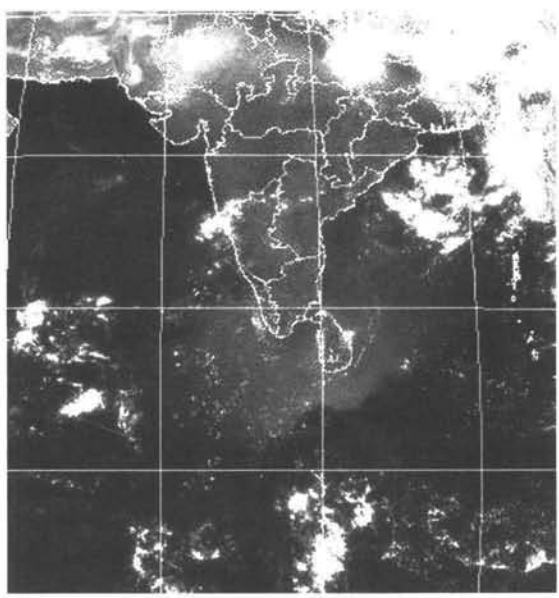

Figure 1.4.3.1 Kalpana-1 VIS image of 10 May 2006 showing a large area of sunglint over the ocean (Source: IMD)

1.5 References

Bhatia R. C., Brij Bhushan and Rajeswara Rao V., 1999, "Applications of water-vapour imagery received from INSAT-2E satellite", *Current Sci.*, 76, 1448-1450.

Bhatia, R. C. and Gupta, H. V., 1999, "Use of charged coupled device payload on INSAT-2E for meteorological and agricultural applications", *Curr. Sci.*, 1999, 76, 1444–1447.

Conover J. H., 1962, "Cloud interpretation from satellite altitudes", *Air Force Cambridge Res. Lab., Res. Note No. 81*, 77 pp.

Das Gupta J., 1971, "A stacked Yagi antenna for APT reception", *Indian J. Meteor. Geophys.*, 22, 381-384.

Datar S. V. and Joseph C. P., 1971, "A satellite automatic picture transmission (APT) system ground receiving station", *Indian J. Meteor. Geophys.*, 22, 377-380.

Garcia O., 1985, "*Atlas of highly reflective clouds over the global tropics: 1971-83*", NOAA-ERL, Boulder, Colorado.

Gohil B. S. and coauthors, 1982, "Remote sensing of atmospheric water content from Bhaskara SAMIR data", *Int. J. Remote Sensing*, 3, 235-241.

Gokhale M. N., 1971, "Surface wind estimate from satellite pictures of sunglint", *Indian J. Meteor. Geophys.*, 22, 443-446.

Hopkins M. M., 1967, "An approach to the classification of meteorological satellite data", *J. Appl. Meteor.*, 6, 164-178.

Iyengar V. S. and coauthors, 1999, "Meteorological imaging instruments on-board INSAT-2E", *Current Sci.*, 76, 1436-1443.

Joseph G. ad coauthors, 1994, "INSAT-2 very high resolution radiometer for meteorological observations", *J. Spacecraft Technol.*, 4, 183-208.

Joshi P. C., Narayanan M. S., Bhatia R. C., Manikiam B., Kirankumar A. S. and Jayaraman V., 2003, "Evolution of Indian satellite meteorological programme", *Mausam*, 54, 1-12.

Kalsi S. R., 2006, "Orissa supercyclone – a synopsis", *Mausam*, 57, 1-20.

Kelkar R. R., Sant Prasad and Ellickson J., 1980, "Image navigation and gridding for three-axis stabilised geostationary satellites", *NOAA/NESDIS Report*, Washington DC, 32 pp.

Kelkar R. R., Sant Prasad and Khanna P. N., 1982, "Conception of an equatorial orbiting meteorological satellite for the tropics", *Mausam*, 33, 507-508.

Kelkar R. R., 1994, "Satellite meteorology in India – an overview", *Indian J. Radio Space Phys.*, 23, 235-245.

Mahajan P. N. and Ghanekar S. P., 1991, "Assessment of satellite-observed HRC data for rainfall estimates over the Indian Ocean", *Mausam*, 42, 347-352.

Mathur A., Agarwal V. K. and Panda T. C., 2002, "Validation of ERS-1/ATSR derived SST in Indian waters", *Int. J. Remote Sensing*, 23, 5155-5163.

Padmanabhan N., Ramakrishnan R. and Gurjar S. B., 2004, "Geometric modelling of INSAT-2E CCD payload and multistrip mosaicking for geocoding large areas", Current Sci., 86, 1113-1121.

Pandey P. C. and Kelkar R. R., 1994, "Space Meteorology in India", *Advances in Space Research in India,* Indian National Sci. Acad.

Pandey P. C., 1995, "Satellite-borne microwave radiometry for atmospheric studies", *Indian J. Radio Space Phys.*, 24, 245-254.

Pathak P. N. and Gautam N., 1992, "Latitudinal distribution of water vapour over the Arabian Sea and Bay of Bengal using Bhaskara-II SAMIR data", *Mausam*, 43, 385-394.

Prakash W. J. and Bhandari S. M., 1996, "An algorithm to overlay continental boundaries and latitude-longitude grids over INSAT-VHRR images", Computers Geosci., 22, 443-440.

Schmetz J. and coauthors, "An introduction to Meteosat Second Generation (MSG)", *Bull. Amer. Meteor. Soc.*, 83, 977-992.

Stricker N. C. M and coauthors, 1995, "ATSR-2: The evolution in its design from ERS-1 to ERS-2", *ESA Bull., No. 83*, 32-37.

Chapter 2

Weather Systems Observed in Satellite Imagery

The complexity of atmospheric motion arises from the rich variety and coexistence of atmospheric phenomena having space scales ranging from less than a metre to thousands of kilometres, and time scales shorter than a minute to longer than a week. They are manifested in various appearances, as tiny eddies and dust devils, short-lived thunderstorms and tornadoes, diurnal sea and land breezes, fronts, jet streams, tropical cyclones and long waves encircling the globe (Table 2.1). These varied atmospheric phenomena not only coexist, but also influence, modify and interact with those of smaller and larger scales. Our knowledge of the atmospheric phenomena is therefore limited by the number of times in a day that we take weather observations at a given place, and the distance between adjacent stations where these observations are made.

Operational global weather analysis and forecasting has conventionally been done on the synoptic scale, and over the years, the global observing network has evolved in such a manner as to meet the necessary and sufficient requirements of synoptic scale forecasting. Comparatively, observations on other scales, especially mesoscale observations, have received much lesser importance in the observational scheme. The global synoptic network has also remained essentially a land network supplemented by ships making some limited weather observations, because of the obvious difficulties in operating weather stations over the ocean that are difficult to overcome.

Meteorological satellite imagery provides an additional means of monitoring the state of the atmosphere by visually examining clouds and cloud patterns. Images received from geostationary and orbiting satellites reveal directly or indirectly the presence of the wide spectrum of atmospheric phenomena mentioned above, just at a glance. The value addition of satellite imagery is the highest over the vast expanse of the world's oceans and inhospitable regions where conventional observations are not available.

Table 2.1 Space and Time Scales of Atmospheric Phenomena

Classification	Examples	Space Scale	Time Scale
Global or Planetary Scale	Long waves, subtropical anticyclones, tropical easterly waves	5000-10000 km	Days to a week or longer
Synoptic Scale	Fronts, extratropical cyclones, anticyclones, cloud clusters, monsoon depressions, tropical cyclones	500-5000 km	Days to a week
Mesoscale	Lee waves, gravity waves, squall lines, land and sea breeze, mesoscale convective elements	20-500 km	Hours to days
Convective Scale or Small Scale	Thunderstorms, tornadoes, convective cells	1-20 km	Minutes to hours
Microscale	Boundary layer eddies, dust devils	100 m - 1 km	Seconds to minutes

Note: The dimensions given above are indicative and approximate, and may have some overlap. Tropical and extra-tropical regions may have systematic differences.

2.1 ITCZ

A very conspicuous and prominent feature of geostationary satellite images or global mosaics constructed from successive passes of polar orbiting meteorological satellites is the Inter-Tropical Convergence Zone (ITCZ). Satellite imagery shows up the ITCZ as a complex cloud band encircling the earth. Of course, long before the satellite era began, the ITCZ was well-known as a zone of convergence of air masses between the two hemispheres. In the lower troposphere there is a wind discontinuity with horizontal velocity convergence and net upward motion. This results in an east-west

band of cloud and rain which oscillates north-south as per the position of the sun.

Asnani (2005a) has given a detailed description of the characteristic features of the ITCZ and the large geographical and seasonal variations in its location. Over regions of eastern Pacific and Atlantic Ocean, it remains north of the equator throughout the year. In other regions, it oscillates between latitudes north of the equator in the northern summer and south of the equator in the southern summer.

From west Africa to southeast Asia, the discontinuity is between the westerlies in the near-equatorial region and the easterly trade winds on either side of it. The westerlies are largely the southeast trade winds which have changed direction after crossing the equator. Over the Atlantic and Pacific Oceans, the discontinuity is between the northeast and southeast trades of the two hemispheres.

Since the ITCZ has a tendency to be located over the warmest regions of land or sea, it is also sometimes called the thermal equator. The ITCZ is an important mechanism that transports heat from the tropical planetary boundary layer to the middle and upper troposphere. The upper limb of the Hadley cell carries it to the sub-tropical latitudes from where it gets further transported to higher latitudes.

Although the ITCZ is broadly regarded as the region of convergence of the trade winds from the northern and southern hemispheres, it must be understood that the air masses on either side of it are not always from the respective hemispheres. As a case in point, during the Indian southwest monsoon season, the origin of the air mass just south of the ITCZ cannot be always be traced back to the southern hemisphere.

The cloud band characteristic of the ITCZ does not appear permanently around the equator, nor does is it take the form of a continuous belt. Due to associated easterly waves and mesoscale circulations, the ITCZ appears in satellite pictures as a series of cloud clusters interspersed with clear areas, as for example, in the Kalpana-1 full disc image of 1 May 2005 (Figure 2.1.1).

In one of the earliest satellite-based studies of equatorial cloudiness over the Indian Ocean, Saha (1971) observed many typical features. The equatorial Indian Ocean within 5° of the equator, has much more clouding east of the 60 °E longitude than to its west throughout the year. Clouds in the equatorial Indian Ocean tend to form in clusters rather than bands. The cloud clusters are randomly distributed with respect to the equator, but occasionally there are two major cloud bands one on either side of the equator. During the

northern summer, the cloud band may be located as far north as 20-25 °N, while in other times of the year, the bands are within 10-15° of the equator. These observed features can be explained in terms of the boundary level convergence due to the thermal wind effect.

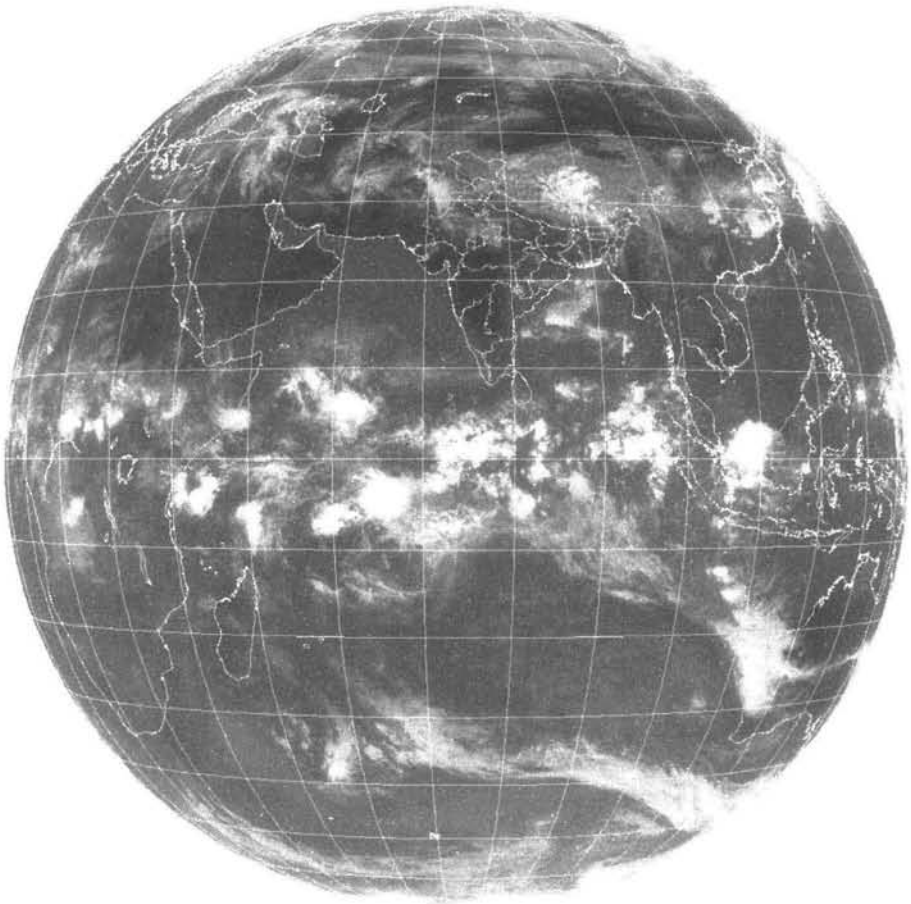

Figure 2.1.1 Kalpana-1 IR image of 1 May 2005 showing the ITCZ clouds extending across the Indian Ocean (Source: IMD)

A satellite-derived climatology of the ITCZ based upon satellite VIS and IR channel data from 1971 to 1987 has been compiled by Waliser et al (1993). It gives global monthly mean positions of the ITCZ as well as its structural characteristics. The ITCZ clouding is characterized by a narrower well-defined band over the Atlantic and eastern Pacific Oceans, while it occupies a broader latitude belt over the Indian and western Pacific Oceans. It is broad and also irregular over land regions of the tropics. An interesting feature of

the satellite climatology is that cloudfree areas over the equator are not always associated with colder waters, and even with high sea surface temperature, deep convection does not necessarily develop.

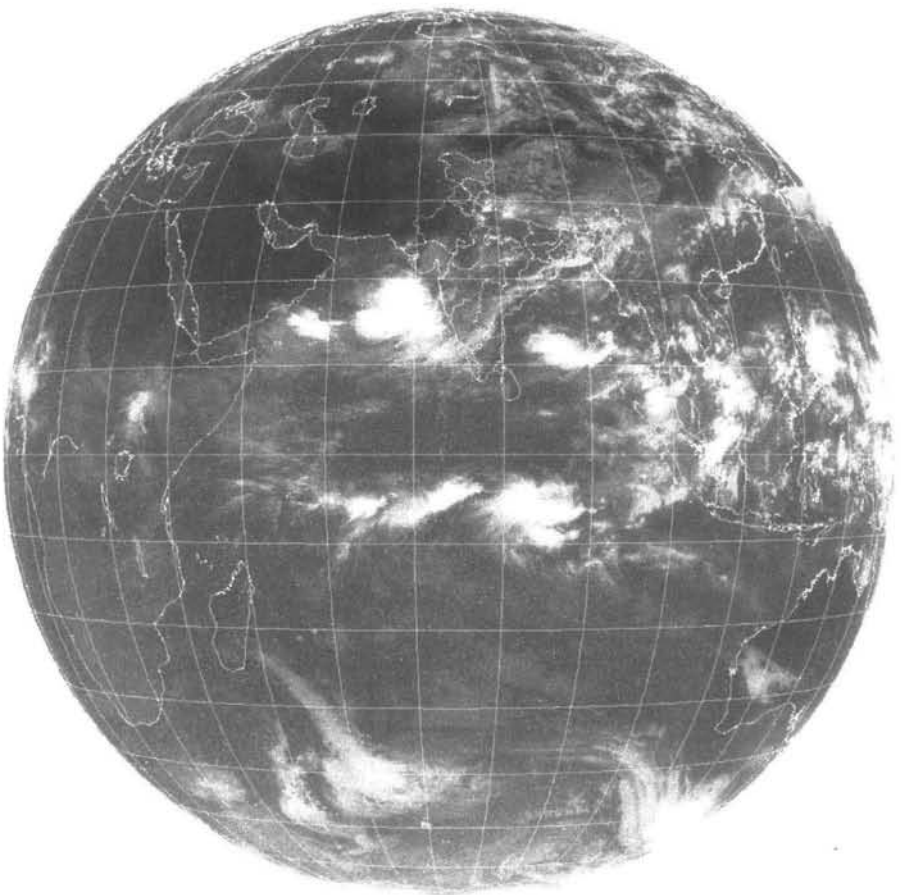

Figure 2.1.2 Kalpana-1 IR image of 24 June 2006 showing double cloud band of the ITCZ over the Indian Ocean (Source: IMD)

The ITCZ related clouding occasionally takes the form of a double cloud band on either side of the equator, as seen for example, over the Indian Ocean on 24 June 2006 (Figure 2.1.2). This type of double cloud band and the causes of subsidence near the equator have been the subject of an extensive analysis and discussion by Asnani (2005b). He regards the equator not just as a geometric line, but as having dynamical effects on the flow of a fluid crossing it. He has postulated that air approaching the equator from north or south suffers horizontal velocity divergence, and air going away

from the equator towards north or south suffers horizontal velocity convergence. When this occurs in the lower troposphere, the air approaching the equator descends, while the air leaving the equator ascends. The equator thus acts like a dynamical valley. This is borne out by the observed tendency of highly reflecting clouds to avoid the geographical equator. According to Asnani, the ancient perception that the equator is a region of abundant cloudiness and perpetual rain is now obsolete, and it would be more correct to look upon the equator as a region of minimum cloudiness instead.

2.2 Mesoscale Systems

The time and space scales of atmospheric phenomena have been given in Table 2.1. It must be understood here that every scale of motion contains within itself a smaller scale of motion and there is an interaction amongst them. To get a reasonable picture of a weather system, it is generally accepted that there should be at least 10 observations per wavelength. Present observational networks are designed for analysis of synoptic scale systems and not mesoscale systems for which special observational networks are required to be set up. Satellites are therefore most useful in observing and monitoring mesoscale systems that synoptic networks are unable to resolve.

The several types of mesoscale convective systems like thunderstorms, hailstorms, dust-storms and tornadoes are discussed in subsequent sections.

2.2.1 Thunderstorms

There are three basic conditions for the development of a thunderstorm: moisture, instability and a lifting mechanism. Air is considered unstable if it continues to rise when given an upward push. An unstable air mass is characterized by warm moist air near the surface and cold dry air aloft. As a rising parcel of air cools, some of the water vapour will condense, forming a cumulonimbus cloud that is commonly called the thunderstorm.

For a thunderstorm to develop, what is needed is an initial trigger or a mechanism that will give a start to the process of upward motion. The temperature of the lowest layers of the atmosphere increases rapidly in the afternoon or evening because of land heating and the warmest air tends to rise. Lifting is also provided by fronts, particularly cold fronts, and dry lines. Terrain may also be a cause for lifting, as when air currents encounter a mountain barrier, they are forced to rise up the slope of the terrain.

The basic building block of all thunderstorms is the thunderstorm cell. The thunderstorm cell has a distinct life cycle that lasts typically for about 30 minutes. The life cycle of a thunderstorm can be described a consisting of three stages:

(a) In the towering cumulus stage, a cumulus cloud begins to grow vertically, to a height of up to 6 km. Air within the cloud is dominated mostly by updrafts with some turbulent eddies around the edges.

(b) In the mature stage of the thunderstorm, the cloud can grow to a considerable height, often up to 12 km or above. Satellite pictures show occasional evidence of overshooting cloud tops which have even penetrated the tropopause. Rain is produced and the downward frictional drag force exerted by the falling rain drops on the surrounding air produces downdrafts. Cooling of the air due to evaporation of the rain drops further increases the speed of the downdrafts. Updrafts and downdrafts are both relatively weak, of the order of 10 m/sec, and they can interfere with each other.

(c) In the dissipating stage, rain spreads throughout the cloud and the downdraft becomes extensive. The updraft gets exhausted, the storm ceases to have the supply of warm moist air that is necessary to maintain itself, and the cloud dissipates. Light rain and weak outflow winds may remain for a while during this stage, before leaving behind just a remnant anvil top.

When the vertical wind shear is weak, single-cell thunderstorms occur. They last for about 30 minutes and get carried by the low-level wind. When there is moderate wind shear, multi-cell storms develop. Here, the individual storms have a life of about 45 minutes, but a group of cells can exist for several hours with new cells forming and replacing old dissipating cells.

A severe thunderstorm has a life of a few hours and it produces very heavy rain, sometimes large hail, and strong squalls on the ground. The rain may be so intense as to cause flash floods. There is high vertical wind shear, both updrafts and downdrafts are very strong, up to 50 m/sec, and they co-exist without interference. Warm moist air enters the cloud from the front and rises. This results in strong updrafts which produce rain and support the formation of large hail. Dry air at the middle level enters the cloud from behind. Rain falls into it, and evaporation of rain cools the air, resulting in strong downdrafts.

The upper portion of thunderstorm finally reaches such a high level that it is influenced by the strong winds in the upper troposphere. These carry the updrafts large distances away from the cloud, forming what is known as the

thunderstorm anvil. A severe thunderstorm is 10-20 km wide and 12-18 km tall, while the anvil may extend horizontally up a distance of up to 100 km. Several such storms may get organized along a line called a squall line. Severe thunderstorms are of the multi-cell or super-cell type. In the super-cell type, the entire storm behaves as if it is a single cell. It may evolve into a rotation circulating, called a meso-cyclone, which can generate a tornado.

There are different motions associated with a thunderstorm: the updrafts and downdrafts within it, the motion of the thunderstorm cloud itself, the motion of the anvil relative to the thunderstorm, the squall speed and the motion of the gust front. Each of these has its own dynamics and scales. The speed and direction of motion of the thunderstorm are functions of the ambient wind in a deep layer. The speed and direction of movement of the anvil away from its parent thunderstorm is a function of the wind at the anvil level. In a jet stream situation the anvil may get blown off more than 200 km away from the parent cloud. There have been instances over Kolkata when the anvil of a Cb cloud associated with a nor'wester has arrived some hours before the arrival of the actual nor'wester itself (see Section 2.2.3).

Although a thunderstorm may consist of just one ordinary cell that goes through the various stages of its life cycle and dissipates, thunderstorms very often form in clusters with numerous cells in various stages of development merging together. Unlike ordinary single cells, cluster storms can last for several hours producing large hail, damaging winds, flash flooding and isolated tornadoes.

If the air is conditionally unstable and there is a strong trigger, a line of several Cb cells, 150-250 km long, develops and is clearly seen in satellite images. This is called a squall line, because there are squalls ahead of it. Along this line, new storms may be forming and older storms may be existing at different stages of their life cycle. The rain-cooled air or gust front spreads out from underneath the squall line and acts as a mini cold front, continually lifting warm moist air to maintain the storm activity. Gusty winds flow out and spread horizontally along the ground. Squall lines are common over north and northeast India during winter and pre-monsoon months. Super-cell thunderstorms are a special kind of single cell thunderstorm that can persist for many hours. They are responsible for nearly all of the significant tornadoes produced in the U.S. and for the formation of giant hailstones.

Although thunderstorm distribution over India is generally well-known, Manohar et al (2003, 2004 and 2005) have recently produced a comprehensive climatology of thunderstorms over the Indian region

including their spatial distribution, the number of thunderstorm days, the number of rainy days, etc. During the pre-monsoon months of March-May, conditions are favourable for occurrence of thunderstorms as there is availability of moisture in the lower levels, and cold sub-tropical westerlies prevail in the upper levels. There are two prominent zones of thunderstorm activity, having 10-12 storms a month, one over the hills of northeast India and another over Kerala. Pre-monsoon thunderstorms are also common over other parts of northeast India (see Section 2.2.3), over northwest India (see Section 2.2.2), and to a lesser extent over the central and southern peninsula. During the monsoon season, the zone of thunderstorm activity shifts to the north and lies in the vicinity of the monsoon trough. During the post-monsoon and winter seasons, the number of thunderstorms over India is very small except over Kerala and the northeast.

Thunderstorms appear bright white in all channels of satellite imagery. In IR images, thunderstorm anvils can be seen as bright white oval-shaped cloud masses blown away in the direction of the upper winds. In a VIS image, the tall clouds may sometimes cast a shadow on the lower level clouds.

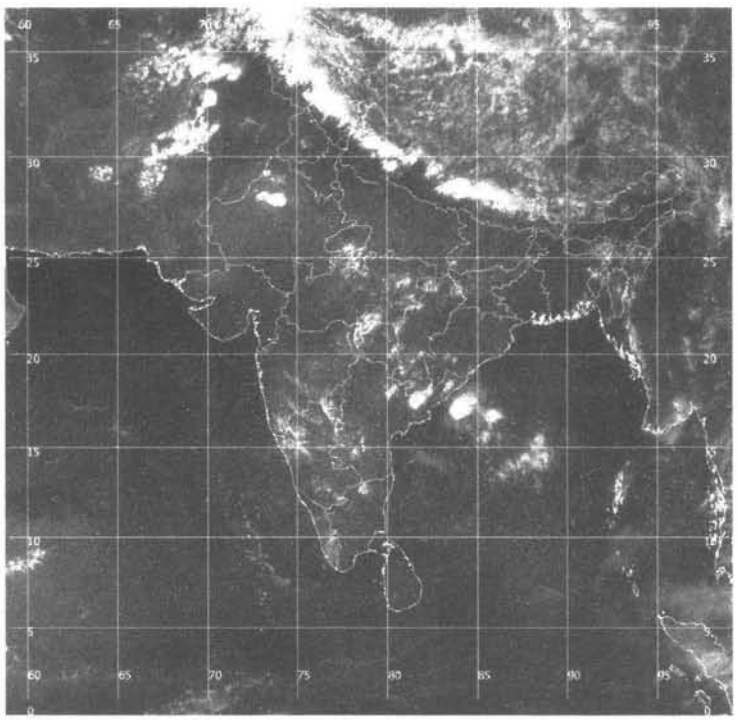

Figure 2.2.1.1 Kalpana-1 VIS image of 1 May 2006 showing the development of afternoon thunderstorms (Source: IMD)

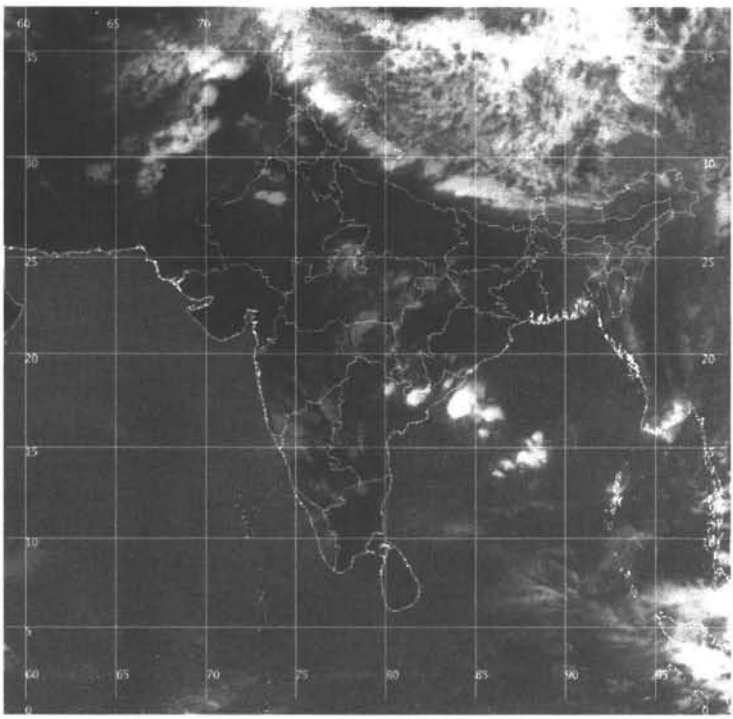

Figure 2.2.1.2 Kalpana-1 IR image of 1 May 2006 showing the development of afternoon thunderstorms (Source: IMD)

Figures 2.2.1.1 to 2.2.1.3 show the development of thunderstorms on a typical summer afternoon over the Indian sub-continent. Notice how the mature thunderstorms appear bright white in the VIS, IR and WV images because of the strong reflection from the Cb tops, low cloud top temperature and high moisture content respectively.

Hail is a solid form of precipitation that is formed when updrafts in thunderstorms carry raindrops high up to extremely cold levels. Hailstones grow by collision with super-cooled water drops. In wet growth, the hailstone nucleus or an ice particle is in a region where the air temperature is just below freezing point. With dry growth, the air temperature is well below freezing and the water droplet immediately freezes as it collides with the nucleus. The stronger the updrafts within the thunderstorm, the larger the size to which a hailstone can grow. However, there eventually comes a stage when the updrafts can no longer match the weight of the hailstones and the precipitation falls to the ground in the form of hail.

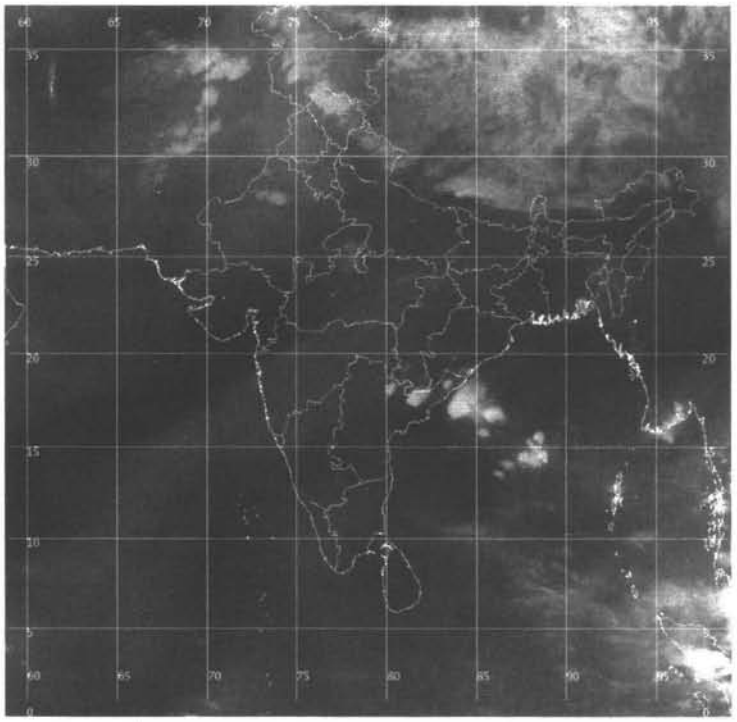

Figure 2.2.1.3 Kalpana-1 WV image of 1 May 2006 showing the development of afternoon thunderstorms (Source: IMD)

There are only a few countries in the world that experience hailstorms frequently and India happens to be one of them. Hailstones comparable in size to lemons, mangoes or cricket balls have been reported in many instances of hailstorms in India. Hailstorms are predominant in the pre-monsoon and winter months over north and northeast India and Bangladesh, but they do not occur during the monsoon. Hailstones can destroy standing crops and may cause damage to vulnerable structures. Some of the hailstorms may be so intense that people and animals could even get killed if exposed directly to falling hail.

A cloudburst is a devastating weather phenomenon in which very heavy rainfall gets concentrated over a small area for a short time, leading to flash floods, structural collapses and human casualties. Although the mechanism of cloudbursts is not yet fully understood, it is generally believed that they are the manifestations of intense vortices which generate strong convective currents. These currents rapidly lift up the moisture laden air to form Cb clouds, particularly in mountain regions where cloudbursts occur more commonly.

Himachal Pradesh in India is one such region prone to cloudburst particularly in the monsoon season. Bhan et al (2004) have documented 36 cases of cloudbursts in Himachal Pradesh during the period 1990-2001. A majority of them occurred in July-August, and Kullu and Shimla districts were the most vulnerable. A possible explanation is that some monsoon lows or cyclonic circulations after moving in a northwestward direction, recurve over Rajasthan or northwest Madhya Pradesh, and move on to Himachal Pradesh resulting in cloudbursts and landslides. Ray et al (2001) have reported 12 landslide situations between 1983 and 1988 in Himachal Pradesh. The orography of the region is such that rain water from the cloudbursts rushes downslope, carrying debris, boulders and uprooted trees at great speeds and causing loss of life and property.

2.2.2 Dust-storms or *Andhis*

When it has not rained over a place for a prolonged period, the soil becomes dry and the particles of the top soil layer get detached. In this situation, the occurrence of a thunderstorm results in large amounts of dust and sand getting thrown up into the air before the commencement of rain. If the area is excessively hot and dry, rain drops may get evaporated on their way down and may not even reach the surface, the result being a dust-storm.

Dust-storms are of two types, pressure gradient type and convective type. Over northwest India, particularly Rajasthan, convective dust-storms which are locally called "*aandhi*"s, commonly occur in the summer months of March to June prior to the arrival of the southwest monsoon rains (Joseph et al 1980, Joseph 1982). These storms are characterized by downdrafts of thunderstorms or squall lines that are so intense that they throw up dust walls on the ground as far as 30 km distance from the main thunderstorm. Even after a dust-storm has ended, dust particles may remain suspended in the atmosphere for quite a long time, reducing visibility and producing haze. The horizontal visibility may get significantly reduced, even to 100 m. Dust-storms also result in a cooling of the atmosphere and give some respite from the summer heat. In India, dust-storms are classified as light, moderate or severe according to the wind speed and visibility level. Dust-storms usually occur in the afternoons, but they are not uncommon in the evening or night in which case they last for a longer duration. After the southwest monsoon has advanced into Rajasthan and the monsoon showers have moistened the soil, the frequency of dust-storms comes down drastically.

Dust-storms cannot be seen in IR images because of the lack of temperature difference between the surface and the dust layer. However, with a suitable enhancement, dust-storms can be detected in VIS images from geostationary satellites if they are of sufficient horizontal extent. MODIS images give an extremely clear view of the dust raised by dust-storms but only if there is a satellite pass at the time the storm has occurred.

2.2.3 Nor'westers or *Kal-Baisakhi*s

In the pre-monsoon months, particularly April and May, violent thunderstorms develop regularly over the eastern and northeastern regions of India and Bangladesh. Strong afternoon heating of the landmass initiates convection which intensifies as it extends towards the southeast and encounters warmer moist air. These thunderstorms are called nor'westers because they appear to arrive at a place from the northwesterly direction or locally as "*kal-baisakhi*"s, meaning calamity during the month of Baisakh of the Indian calendar.

Nor'westers have their origin over Jharkhand, Chhatisgarh or west Orissa and move eastwards or southeastwards towards Gangetic West Bengal at a speed of 50-60 km/hr. They do not advance much into the sea. Nor'westers are generally accompanied by squalls with wind speeds reaching even up to 150 km/hr.

Although the nor'wester is a mesoscale phenomenon, the realisation of instability depends upon the large scale flow and the prevailing synoptic situation. During April-May, there is a shallow layer of moist southerlies and southeasterlies extending from the Bay of Bengal into Gangetic West Bengal. In the upper troposphere, however, there are cold and dry westerly winds associated with the sub-tropical jet stream or trough. This combination of moist southerlies below and cold westerlies aloft, results in the generation of the violent nor'westers.

Karmakar et al (2005) have studied the different energy components of the troposphere prior to the occurrence of nor'westers over Bangladesh. Their study covered more than a hundred nor'westers that occurred over Bangladesh during the period 1990-1995. They found that on the days the nor'westers occurred, both the sensible heat and latent heat increased significantly from the surface to 200 hPa level.

2.2.4 Tornadoes

A tornado is a highly concentrated vortex of very small horizontal dimensions. It has a violent speed of rotation with wind speeds of the order of 300-400 km/hr around a vertical or near-vertical axis, a strong updraft and a very high pressure deficit within it, even 50-100 hPa. It has an extremely short life cycle of barely 10-20 minutes. The tornado is visible in the sky as a narrow funnel tapering from the base of a thundercloud. The end of the funnel may touch the ground or it may remain suspended in the sky. When the funnel is over a water body, it raises water vertically in the form of a pillar, and it is then known as a water spout. Over land, it can cause extreme devastation. About one thousand tornadoes strike the U. S. each year. Oklahoma City has been one particular place that has been the worst hit. In the biggest outbreak of tornadoes, 147 tornadoes touched down in 13 U. S. states on 3 and 4 April 1974. Hurricanes are also known to generate tornadoes within their outer bands.

Tornadoes are relatively rare over the Indian sub-continent (Gupta et al 1982). During the 160-year period from 1839 to 1999, only 64 tornadoes are known to have occurred (Golder et al 2001). On 17 March 1978, in the northern suburbs of New Delhi, near the University, 28 people were killed and 700 were injured by a tornado that cut a path 5 km long and 50 m wide (Gupta et al 1980). On 24 March 1998, a violent tornado killed 160 people and injured 2000 when it tracked through 20 coastal villages in the eastern states of West Bengal and Orissa. As tornadoes are extremely localised events, it is quite possible that some cases could not even have got reported. The area of northeast India and Bangladesh is prone to the development of tornadoes. They generally occur in the pre-monsoon months of March-May, and more commonly in April. The favourable time of occurrence is afternoon or evening.

Tornado development can be spotted in satellite images by continuous monitoring especially when the synoptic situation is known to be favourable, but otherwise they can be missed because of their short life.

2.2.5 Mountain Waves

When the wind is blowing perpendicular to a mountain range, and the atmosphere has thermally stable layers, waves get formed on the leeward side of the mountains producing strong turbulence and vertical air currents. After the winds cross over the mountain tops, air in the lower layers descends into the valley, and rises again to form what is called a rotor cloud. At the higher levels, an internal lee wave builds up above the rotor cloud

(Figure 2.2.5.1). The character of the wave varies with the prevailing wind profile. When the jet stream is favourably aligned to the mountains, the stronger winds may give rise to more intense waves.

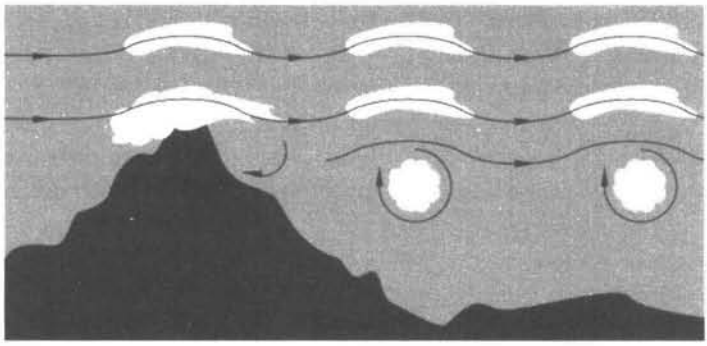

Figure 2.2.5.1 Schematic of formation of mountain waves

If there is sufficient moisture supply, orographic clouds also develop and are identifiable in satellite images as a series of gray or white cloud bands with intervening clear areas running parallel to the mountains, some times even up to several hundred kilometres (Figure 2.2.5.2).

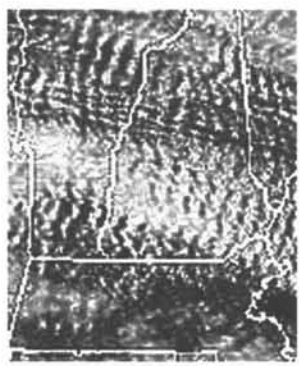

Figure 2.2.5.2 Satellite image of cloud bands in association with mountain lee waves (Source: http://rst.gsfc.nasa.gov/)

Mountain waves have been a subject of considerable study particularly because they are a potential aviation hazard. They create strong turbulence and downdrafts on the leeward side of the mountains which can be dangerous to flying. There have also been several studies in which lee waves identified in satellite images have been compared with theoretical computations of their

wavelengths. De (1970, 1971) reported satellite evidence of lee waves over northeast India and compared the observed wavelengths with theoretical estimates using a two-dimensional steady state linear model.

In the winter season, the air stream over northwest India is stably stratified and is favourable for the formation of lee waves provided the air flow has an appreciable component normal to the mountains. Sinha Ray (1988) who used NOAA satellite imagery for the years 1982-85 for the western Himalayas, found that the wavelengths were between 10 and 30 km and their computed values were in good agreement with those observed in satellite images.

2.3 Monsoons

Monsoons have been defined in various ways in terms of alternating distinct wet and dry seasons during the year, a seasonal reversal of wind direction and the north-south oscillation of the ITCZ, which itself is a region of wind discontinuity. The monsoon is essentially an annual oscillation of the state of the atmosphere in response to the changing position of the sun between the tropic of Cancer and the tropic of Capricorn. The traditional view of the Asian monsoon was that of a giant land-sea breeze phenomenon caused by the differential heating between the Asian land mass and the Indian Ocean.

The monsoon region was originally considered to be restricted to south and south-east Asia, northern Australia and tropical Africa. Around the 1980's, the summer rains in Mexico and south-west U. S. also came to be classified as monsoon rains. The current thinking is that the monsoons are an important part of the global large-scale circulation and the whole tropical region and adjoining sub-tropical region is considered as the monsoon region, which includes parts of north, central and south America, China and east Asia.

This does not mean, however, that the ITCZ moves to 40° N, but there are changes in the intensity and position of the sub-tropical trough lines which are associated with the monsoon in China and east Asia, south Pacific Ocean and south Atlantic Ocean. Then there are some regions like sub-tropical south America which exhibit monsoonal characteristics during winter rather than in summer.

In essence, the monsoon is where the ITCZ is (Asnani 2005c). The monsoon is a fast shift of the ITCZ away from the equator. As far as the south Asian monsoon is concerned, the monsoon oscillation is stronger in the northern hemisphere than in southern hemisphere and it is stronger over south and south-east Asia than elsewhere in the northern hemisphere. This can be attributed to the Himalayan mountains and elevated Tibetan plateau

producing diabatic heating over a large area of the middle troposphere, the Indian Ocean to the south providing abundant moisture supply and the strong meridional gradients of temperature.

Rajeev et al (2006) have constructed monthly mean fields of fractional cloudiness observed by INSAT and NOAA satellites over the years 1996 to 2003. The annual north-south march of the ITCZ, the intense cloudiness over south Asia during the southwest monsoon months of June-September, and its near absence in other seasons, are clearly brought out in the monthly cloudiness fields. The intra-seasonal behaviour of the monsoon is, however, equally important, and satellite observations have been of great help in understanding it as will be explained in the following sections.

2.3.1 Onset and Advance of Southwest Monsoon

The onset of the southwest monsoon over Kerala is a part of a large-scale circulation event and it is associated with slowly evolving as well as sudden changes in many atmospheric and oceanic parameters like low level winds, moisture, upper level temperature and SST (Joshi et al 1994, Joseph et al 1994, Khole et al 2004). In early April, the tropical north Indian Ocean and adjoining west Pacific Ocean begins to warm rapidly and by the end of May, it becomes the warmest tropical ocean area. After the onset of the monsoon, it gets cooled by the strong monsoon westerlies. Convective activity over north Indian Ocean and cyclogenesis over west Pacific Ocean are components of the 30-50 day cycle observed over the areas and there is a see-saw variation between the two, which influences the onset of monsoon over Kerala (Joseph 1990).

The onset of monsoon over Kerala has been the subject of numerous investigations (Joseph et al 2003, Pearce et al 1984, Shenoi et al 1999, Soman et al 1993) and of particular interest has been the generation of the so-called onset vortex that develops over southeast Arabian Sea (Mishra et al 1991, Krishnamurti et al 1984, Rao 1990, Rao et al 1999). However, it is the arrival of the monsoon rains over Kerala which is the prime consideration in defining the onset, because it paves the way for their further advance into the interior parts of India. The monsoon onset in south Bay of Bengal and Myanmar takes place in May. In June, monsoon covers the Bay of Bengal, and extends into southwest China, Arabian Sea and the South China Sea (Wang et al 2004). By the end of June, the whole rain belt in the area stretching from the Arabian Sea to the South China Sea and further eastward, is well entrenched. The mean onset date over Kerala is 1 June with a standard deviation of a week. The earliest ever onset has occurred on 11 May (1918,

1955) and has been as late as on 18 June (1972). The standard deviation of the onset dates over other places in India is also about 6 to 8 days.

There have been many attempts to arrive at an objective definition of the onset of monsoon over Kerala (Ananthakrishnan et al 1988, Fassulo et al 2003, Joseph et al 2006) but there is no unique definition and there is a divergence among meteorologists on this issue. In the pre-satellite years, the onset over Kerala was defined in terms of a detectable change in the pentad rainfall pattern over Kerala. This approach does not always determine a clear onset since there is considerable thunderstorm rainfall before the monsoon onset. There are other precursors of the onset such as a steady increase of convection over an area bounded by 0-15°N and east of 60°E about 3 pentads before onset and a steady acceleration of the cross-equatorial Findlater Low Level Jet (LLJ) in response to this heat source. There is an increase in the depth (600 hPa) and strength of the westerlies in the LLJ just prior to onset. The axis of the LLJ also moves from the equatorial Arabian Sea to higher latitudes in the 3 pentads before onset.

The characteristic features associated with the onset over Kerala are generally known, but all of them may not always be present. It is even more difficult to define the monsoon onset or advance into interior areas of India. For the common people, particularly farmers, onset must signify sustained rains. Very often the onset of monsoon over Kerala is accompanied with thunder, heavy rain, strong winds, rough seas, etc. Westerlies are strong and surface wind speeds are of the order of 20 knots. The westerlies extend aloft up to 6 km and rainfall is of the order of 10 cm in a day. In some years, the onset is of a subdued nature.

The north-south sea level pressure gradient over India exhibits an annual see-saw oscillation. Between November and April, the pressure decreases from north to south. Between May and October, the pressure increases from north to south. In the transition months, the gradient is almost zero.

In the pre-monsoon season (March-May), there is considerable thunderstorm activity over the country. Kerala and northeast India have on an average 10-12 thunderstorm days per month during March-May. The first storms may be dust-storms due to the rising of loose soil particles after a long period of dry weather. Some thunderstorms may have squally winds and hail. After the monsoon has established itself, the number of thunderstorms reduces considerably.

The best precursors of monsoon onset over Kerala are observed in satellite imagery such as that provided by INSAT. In many years, INSAT images show convective clouds along the west coast of India, indicative of a trough

in the westerly winds over the Arabian Sea. Figure 2.3.1.1 shows a Kalpana-1 image of a weak and delayed onset on 5 June 2005 with no clouds over the country except over the southern tip. Figure 2.3.5.1 shows the satellite image for 26 May 2006 when there was an early and strong monsoon onset over Kerala with an associated onset vortex. WV imagery vividly brings out the onset over Kerala and shows the distinctly moist air of the monsoon with dry regions to its south and north (Figure 2.3.1.2).

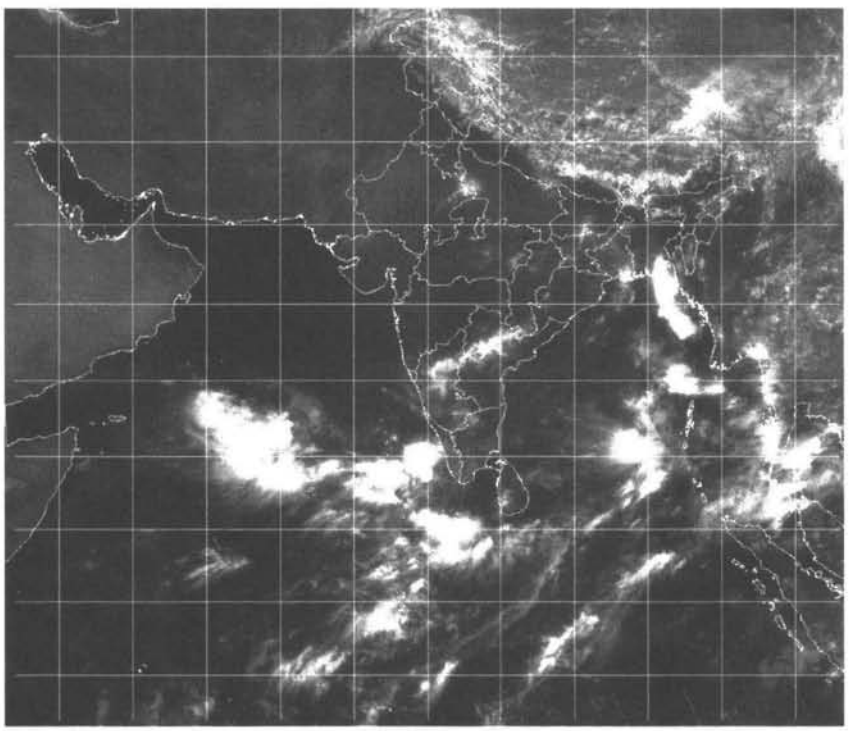

Figure 2.3.1.1 Kalpana-1 VIS image of 5 June 2005 showing a weak and delayed onset of the southwest monsoon over Kerala (Source: IMD)

Weekly data of Oceansat-1 MSMR for the pre-monsoon season of the year 2000 showed that as the monsoon progressed towards the Indian sub-continent, the area of maximum moisture content and wind speed moved northwards. There was a sharp increase in water vapour over western Indian Ocean about three weeks prior to the onset over Kerala and a rise in the wind speed over western Arabian Sea just prior to the onset (Simon et al 2001).

The subsequent advance of the monsoon into the interior parts of the country is a slow process and the monsoon covers the entire country by 15 July.

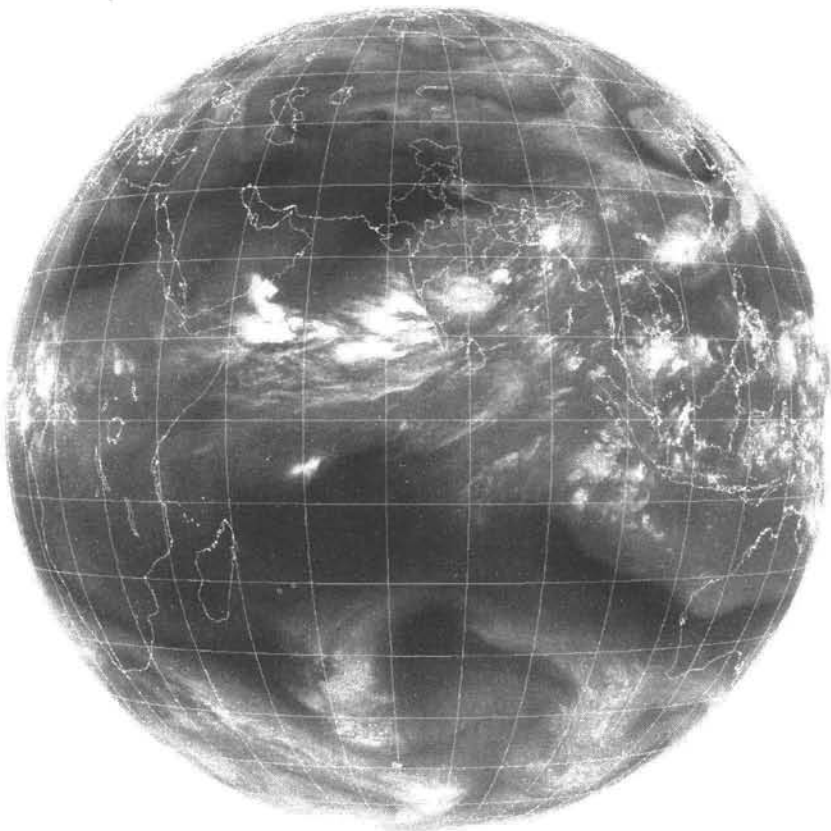

Figure 2.3.1.2 Kalpana-1 full disc WV image of 27 May 2006 showing the onset of the southwest monsoon, and the distinctly moist air of the monsoon with dry regions to its south and north (Source: IMD)

2.3.2 Low Level Jet

By definition, a jet stream in the atmosphere is a strong narrow current, running across thousands of kilometres, with a width of a few hundred kilometres and a depth of at least a kilometre (Berggren et al 1958). Jet streams have wind speeds greater than 60 knots concentrated along a quasi-horizontal axis and the show strong wind shears of the order of 10-20 knots/km in the vertical direction and 10 knots/km in the horizontal direction. They are generally characterized by one or two vorticity maxima. There are, however, some currents in the atmosphere which do not strictly meet these criteria but still qualify to be called jet streams. One such current is the Low

Level Jet (LLJ) which develops along the east African coast in association with the Indian southwest monsoon. This phenomenon, which was first reported by Bunker (1965) and fully explained afterwards by Findlater (1966, 1969), has since come to be called the Findlater Jet. Some characteristic features of the LLJ have been discussed by Pant (1982) and Joseph et al (2004).

The LLJ which accumulates moisture from the sea surface is now regarded as a significant factor in the cross-equatorial moisture transport that is important to monsoon dynamics. It has its origin in the southern hemisphere and in the month of July, the current flows from Mauritius over the northern tip of Malagasy into the coast of Kenya in east Africa at around 3 °S. Thereafter it penetrates inland into Kenya, Ethiopia and Somalia and emerges into the southwest Arabian Sea at 9 °N and moves towards the west coast of India. The LLJ remains a narrow stream along the African coast because of the mountains there, but orography also helps the wind to intensify near the surface and run parallel to the coasts of Somalia, Yemen, and Oman.

The LLJ is remarkable for its steadiness of direction but not necessarily in its strength. At the 850-900 hPa level, speeds of 30 knots are generally observed over Malagasy and 35 knots near the Somali coast in July and August. However, much higher speeds are occasionally encountered, Findlater (1974) having reported an extreme value of 126 knots.

The Somali current off the Somali coast, is an inertial boundary current forced by the atmospheric LLJ. As the LLJ interacts with the waters off the Somalia coast, it produces intense upwelling and cold water rich in nutrients is brought up to the surface. This leads to convergence and downwelling in the central and eastern part of the Arabian Sea. In response to the southwest monsoon, the surface mixed layer in the central Arabian Sea deepens and cools during the summer. The cross-equatorial LLJ is a major component of the lower limb of the monsoon circulation connecting the southern Indian Ocean and the south-east Asian region. Intensification of the LLJ usually leads to an increase in the monsoon activity over west coast of India (Ngara et al 1978).

Generally, low level jets are strongly influenced by factors such as orography, friction, diurnal heating cycle and variations of pressure gradient. As they have limited horizontal and vertical extent, they may not always show up in mean climatological charts. Using aircraft flight data gathered during Monex-79, Grossman et al (1986) have demonstrated that the structure of the east African LLJ can be explained by a combination of the geostrophic wind shear or the thermal wind, above the wind maximum and turbulent momentum transfer below it.

Joseph (2006) has attributed the LLJ with two main functions. One, it acts as a conduit carrying the moisture generated by the trade winds over the south Indian Ocean and the evaporative flux from the Arabian Sea to the areas of monsoon rainfall production over south Asia. Two, the cyclonic vorticity north of the LLJ axis in the atmospheric boundary layer serves as a dynamic forcing for the generation of upward air motion, convective clouds and associated rainfall and for the generation of monsoon depressions in the north Bay of Bengal. During an active monsoon, the core of the LLJ passes eastward across peninsular India, while during monsoon breaks, the LLJ axis moves southwards from the central Arabian Sea, skirts India and passes eastward.

Satellite cloud motion winds over the Indian Ocean, particularly those derived with low level clouds using VIS imagery, clearly brings out the LLJ (Figure 3.1.3.1).

2.3.3 Tropical Easterly Jet

During the summer monsoon season, marked north-south temperature and pressure gradients develop between the Indian Ocean and the Tibetan plateau. In the lower troposphere, pressure increases equatorward and in the middle and upper troposphere, pressure increases poleward. As the Coriolis parameter is small in the lower latitudes, even a slight pressure gradient can give rise to strong easterly flow with speeds going up to 60 knots at 100-300 hPa levels. This is manifested as the Tropical Easterly Jet (TEJ). TEJ extends from southeast Asia to north Africa in the latitude belt 10-15 °N. The strongest winds occur just to the west of the southern tip of India, over the Arabian Sea at about 150 hPa. The TEJ is very stable in direction but the wind speed is variable. The vertical wind shear is of the order of 10 knots/km and the horizontal wind shear is very weak, 10 knots/500 km in contrast with the sub-tropical westerly jet (10 knots/100 km).

The TEJ is an important feature of the southwest monsoon and is easily identifiable in satellite imagery (Figure 2.3.5.3). Singh et al (1982) made one of the earliest studies of TEJ using satellite pictures during June 1977. The TEJ is more evident in IR images than in VIS images because of the associated cold cirriform clouds. Extended cirrus bands parallel to the jet axis are observed, some times with a sharp equatorward edge indicative of descending air over the equatorial region (Koteswaram 1958). Transverse lines were also observed over the Arabian Sea. The monsoon was seen to be active in the right entrance sector of the jet clouds.

The strong winds of the TEJ are also seen in high level satellite cloud motion winds (Figure 3.1.3.2).

2.3.4 Monsoon Depressions and MTCs

During the monsoon season, a series of depressions form over the north Bay of Bengal. They generally move in a west-northwesterly direction across the country and often merge into the seasonal low over northwest India. Some of them take a westerly course and in rare cases even emerge into the Arabian Sea. Some may take a north-northeasterly course and dissipate over the mountain slopes, causing flooding of rivers which originate there. If depressions linger over central India, it is the peninsular rivers which get flooded.

Generally, 4 to 6 monsoon depressions form every year but the number is highly variable. In the 2005 monsoon season, there were 11 low pressure systems, 5 of which intensified into a depression and 1 into a marginal cyclonic storm. There were other years when only a single depression had formed. The number of monsoon depressions is also seen to have a decreasing trend in recent years.

The time interval between two successive depressions is also variable. Depressions may follow in quick succession or may be after a long interval, which may signal the end of a break in the monsoon.

Most of the monsoon depressions typically have a life of 3 to 5 days, but some may last even for a week. When the seasonal trough intensifies and a closed low appears, a monsoon depression is likely to grow out of it. The development may occur because of the arrival of an easterly wave or in situ. In a day or two, the low intensifies into a depression with winds of 22-33 knots. Depressions move at about 4° latitude or longitude per day but after recurvature, they move very fast. In many years, the advance of the monsoon over northeast India takes place is in association with a depression.

Unlike tropical cyclones, there is considerable asymmetry in the wind field of a monsoon depression. Winds are stronger to the south of the depression centre, due to the superimposition of the depression perturbation over the westerlies south of it. Winds are strongest at 700 hPa level. The system has a cold core below 700 hPa and a warm core aloft. The vertical axis of the depression slopes southwestwards with height. The heaviest rainfall occurs over the southwest quadrant because of convergence. Rainfall amounts are generally of the order of 10-20 cm per day and could even be as high as 30 cm per day in isolated cases. Rainfall in the southwest sector of the

depression has considerable diurnal variation, with the heaviest falls occurring in the early morning hours.

There are three factors which are responsible for causing upward motion and rainfall in the southwest sector of a monsoon depression, (i) boundary layer frictional effects in areas of cyclonic vorticity which is maximum in the south sector, (ii) warm air advection in the lower troposphere and (iii) vorticity advection in the lower troposphere which contributes to upward motion in the left forward sector and descending motion in the rear sector.

In its early stages, a monsoon depression induces a low level trough along the Konkan coast, where there is enhanced rainfall activity, which decreases as the depression moves inland. Rainfall activity is high to the west of the depression, but less over southern India and northeast India. When the depression is over central India, Gujarat and Saurashtra get good rainfall because of fresh moisture supply from the Arabian Sea.

A monsoon depression in its formative stage is seen in satellite imagery as a dense amorphous cloud mass over the Bay of Bengal. As it develops further, convective cloud lines tend to get organized and there are pronounced curved cumulus lines at the edge of the dense overcast mass. In the mature stage, the dense overcast gets ragged edges surrounded by curved cumulus lines (Figure 2.3.4.1 and 2.3.4.2).

Characteristic features of monsoon depressions have been described by Srinivasan et al (1971), Chowdhury et al (1983) and Sarkar et al (1988).

Chowdhury et al (1985) prepared a mean cloudiness pattern of a monsoon depression by examining 40 case histories during 1977-1981. A moving $20^{\circ} \times 20^{\circ}$ lat/long grid was overlaid around the depression centre in the satellite picture and the cloudiness information picked up at each 2.5° grid point which was then averaged to draw isopleths of cloudiness and coefficient of variation. The mean pattern shows a zone of maximum cloudiness $3\text{-}4^{\circ}$ southwest of the depression centre which could be identified as the principal area of heavy rainfall. The north and southeast extremity of the depression field is an area of suppressed cloudiness. The most distinct feature in all cases is the bright central dense overcast southwest of the depression centre and consisting mainly of stratiform clouds. In 50 % of the cases, the centre lay within this amorphous mass, but in the remaining cases the centre was located in the cloudfree zone indicative of a highly sheared environmental flow.

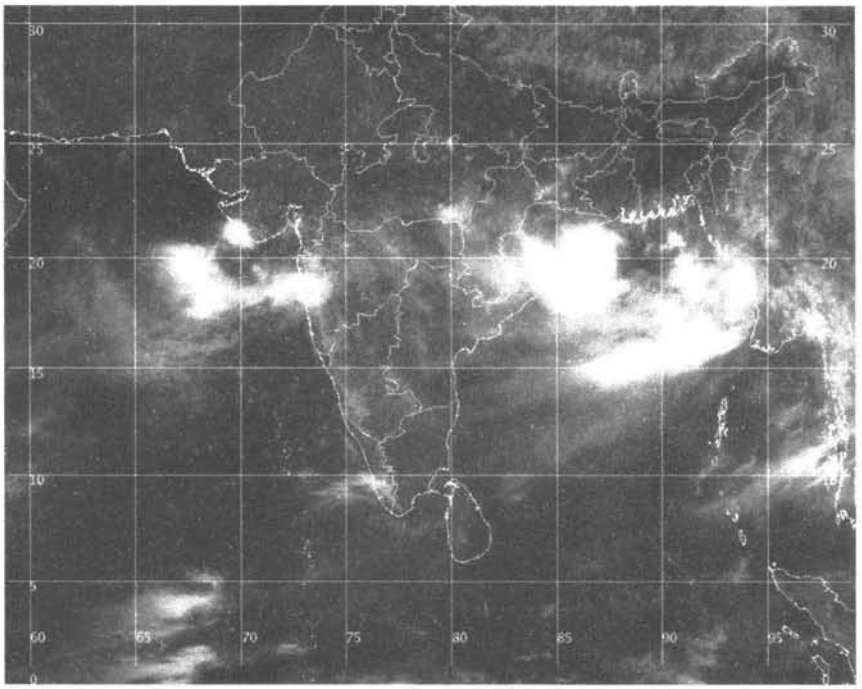

Figure 2.3.4.1 Kalpana-1 VIS image of 1 July 2006 showing the formation of a monsoon depression over the Bay of Bengal (Source: IMD)

Prasad et al (1990) used 3-hourly INSAT images and other data to construct a composite wind and cloud structure of a monsoon depression. They have also described the cloud features seen in satellite images at different stages of development of the depression. The genesis stage which could be called a well-marked low, is characterized by a long east-west band south of the evolving vortex. In the intermediate stage at which the system becomes a depression, this zonal cloud band reorganizes itself suggesting a rotation of the cloud mass, while cumulus lines appear in the northern sector in the region of low level easterlies and define the centre. The centre could be 1-2° away from the centre fixed on the surface chart. In the intense or deep depression stage, the cumulus lines become more curved and the centre comes closest to the northern edge of the dense overcast. The vertical tilt of the system is the least at this stage. The dense overcast will have a 3-5° diameter with sharp edges and embedded overshooting cloud tops that penetrate the tropopause. The system begins to decay 24 hours later.

Mahajan (2003) and Mahajan et al (2004) have used a variety of satellite data from DMSP SSM/I and Oceansat-1 MSMR and cloud motion winds for studying the development of monsoon disturbances. They found that prior to

the formation of a monsoon depression, there is a strengthening of surface winds to the south of the low pressure area over the Bay of Bengal. Highest values of geophysical parameters like integrated water vapour (6-8 gm cm^{-2}), integrated cloud liquid water (50-60 mg cm^{-2}) and precipitation rate (20-25 mm/hr) and lowest values of OLR (120 w m^{-2}) are associated with the southwest sector of a monsoon depression.

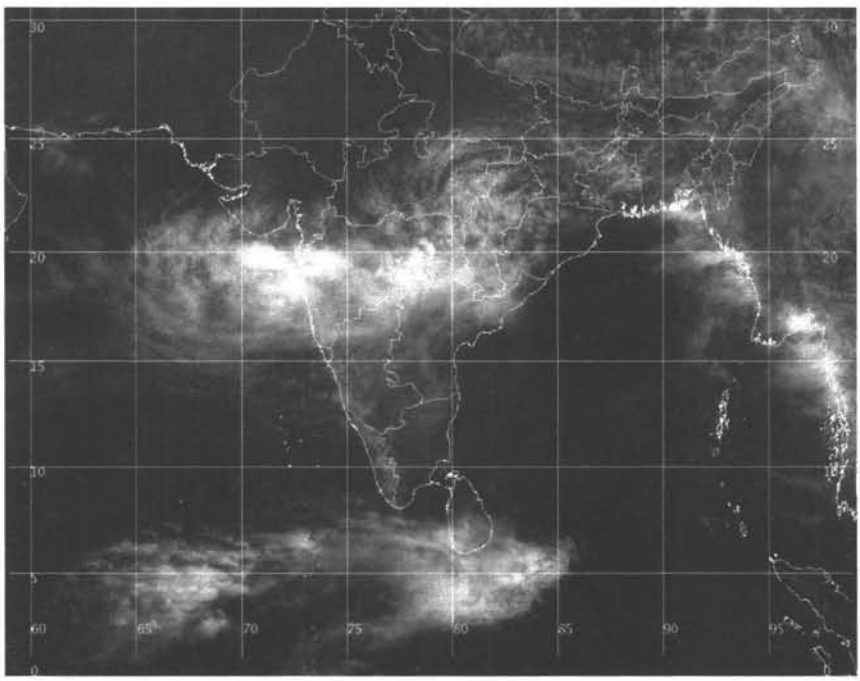

Figure 2.3.4.2 Kalpana-1 VIS image of 4 July 2006 showing a monsoon depression which has crossed from the Bay of Bengal into Orissa. The curved cumulus lines are seen. (Source: IMD)

Rajeevan et al (2001) examined ten cases of monsoon depressions during 1989-1999 using SSM/I microwave data on daily water vapour, cloud liquid water and rain rate on a 25 × 25 km resolution. However, these data are available only on the ocean. They prepared a composite average pattern for a monsoon depression with respect to a common origin which confirmed the asymmetric distribution of precipitation. While atmospheric water vapour did not show any preferred maxima, there was high cloud liquid water (> 1 mm) in the southwest sector about 200 km from the common centre, which indicated the presence of very deep convective clouds. There the precipitation rate exceeded 12-14 mm/hr, equivalent to 30 cm rain in 24 hours. A secondary maximum was located in the northeast sector with

rain rate of 6 mm/hr. Two case studies using TMI data revealed similar features.

A Mid-tropospheric Cyclone (MTC) is a synoptic system that is observed over South Asia during the summer monsoon months. An MTC is a low pressure system having a vorticity maximum in the middle tropospheric levels between 700 and 500 hPa, with much smaller values at the surface or at 200 hPa. It is, therefore, barely noticeable on surface weather charts, but produces heavy rainfall. MTCs are mostly warm core above 600 hPa, but a little cold core below (Miller et al 1968, Krishnamurti et al 1970). Bhagat (2005) computed some aspects of kinetic energy for the average MTC derived from 27 cases during 1985-1980.

Compared with monsoon depressions, MTCs are not that common. Some MTCs form *in situ* over the northeast Arabian Sea and adjoining land areas of Saurashtra. Others form out of monsoon depressions that have travelled from the Bay of Bengal across the country and emerged into the Arabian Sea. MTCs are relatively more frequent in the first half of the monsoon season. They have a tendency to remain quasi-stationary for several days or drift slowly westwards, unlike monsoon depressions which move as fast as 300-500 km per day.

2.3.5 Active and Weak Phases

During the southwest monsoon season, rain does not keep falling continuously all over the Indian subcontinent, but there are spells of vigorous monsoon rainfall interspersed by dry spells or periods of weak rainfall activity. This strong intra-seasonal oscillation that the monsoon exhibits is also referred to as the active-break cycle. In the active monsoon phase, which may last for 2 to 4 weeks, most parts of India receive good rainfall. During the break phase, however, rainfall is highly deficient except over the Himalayan foothills and extreme southern parts of India. In the most recent paper on this subject, Rajeevan et al (2006) have made an analysis of the active-break spells of the monsoon using the newly available high-resolution daily gridded rainfall data of the Indian region.

In one of the earliest studies of the monsoon based upon satellite imagery, Sikka et al (1980) studied daily variations of the maximum cloud zone (MCZ) and the 700 hPa trough over the region covering the Indian longitudes 70-90 °E from the equator to 35 °N in the months of April to October during the years 1973-1977. They observed that in the monsoon months of June-September, two MCZs exist in the region, one over the

continent and another over the ocean. Both the MCZs exhibit alternating episodes of strong and weak intensity, but the strength of the two MCZs is oppositely correlated. Both the MCZs show a northward propagation, and there is a period of 3 to 4 weeks between successive generations of the northward moving cloud bands.

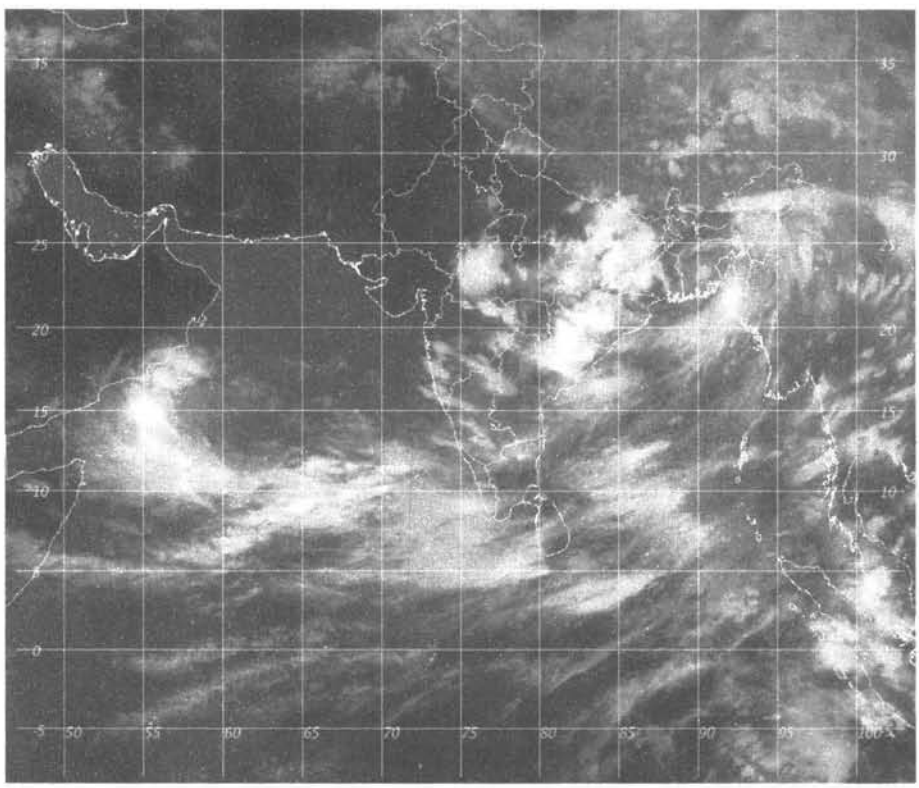

Figure 2.3.5.1 Kalpana-1 IR image of 26 May 2006 showing an early and strong onset of the southwest monsoon over Kerala (Source: IMD)

The monsoon trough is the only synoptic scale system that contributes to the rainfall activity over India. In satellite images the presence of cloud clusters helps to identify areas of heavy rainfall. Satellite images clearly bring out the weak phases of the monsoon followed by a revival and build-up. Figure 2.3.5.1 shows the satellite image for 26 May 2006 showing an early and strong monsoon onset over Kerala with an associated onset vortex. There was, however, a mid-way halt to its progression beyond the peninsula and a weakening of the monsoon current, and on 21 June there was a subsequent revival.

Satellite pictures have confirmed that the cross-equatorial flow over the Indian Ocean has a predominant influence on the monsoon activity. Mishra et al (1991) and Gupta et al (1991) have highlighted the importance of the southern hemisphere equatorial trough (SHET) in regulating the cross-equatorial flow thereby leading to the development of the active-break cycle. They found an inverse relationship between the SHET clouding and the monsoon activity over India and persistence of the SHET cloud band beyond the pre-monsoon months could be a signal of an impending drought. Figure 2.3.5.2 shows the lack of clouding over the Indian sub-continent and the reappearance of the SHET in the satellite image of 11 June 2006 during the weak phase of the monsoon.

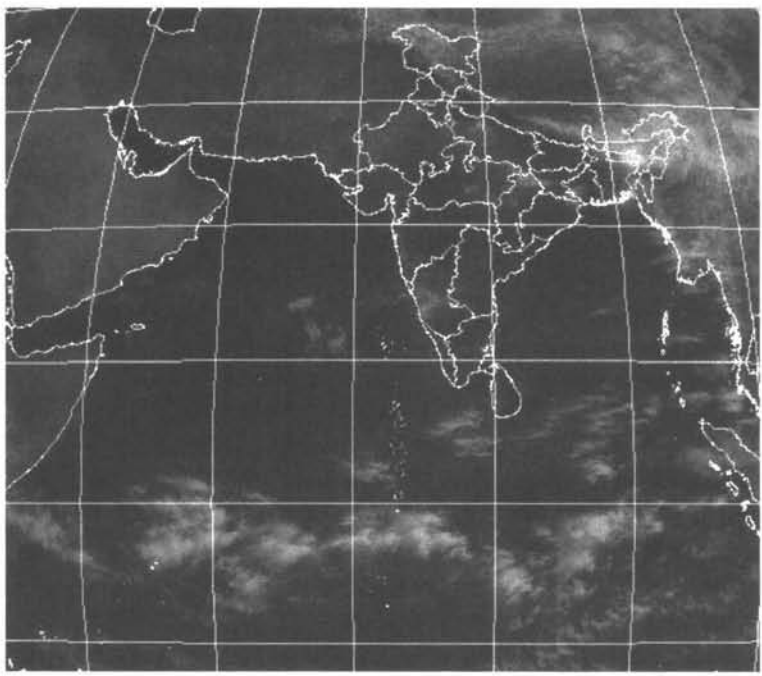

Figure 2.3.5.2 Kalpana-1 VIS image of 11 June 2006 showing the reappearance of the SHET in during the weak phase of the monsoon (Source: IMD)

Figure 2.3.5.3 shows the southwest monsoon in an active phase once again on 3 July 2006. There is a monsoon depression over eastern India, flanked on either side by areas of intense convection on the Arabian Sea and Bay of Bengal, and an off-shore trough along the west coast.

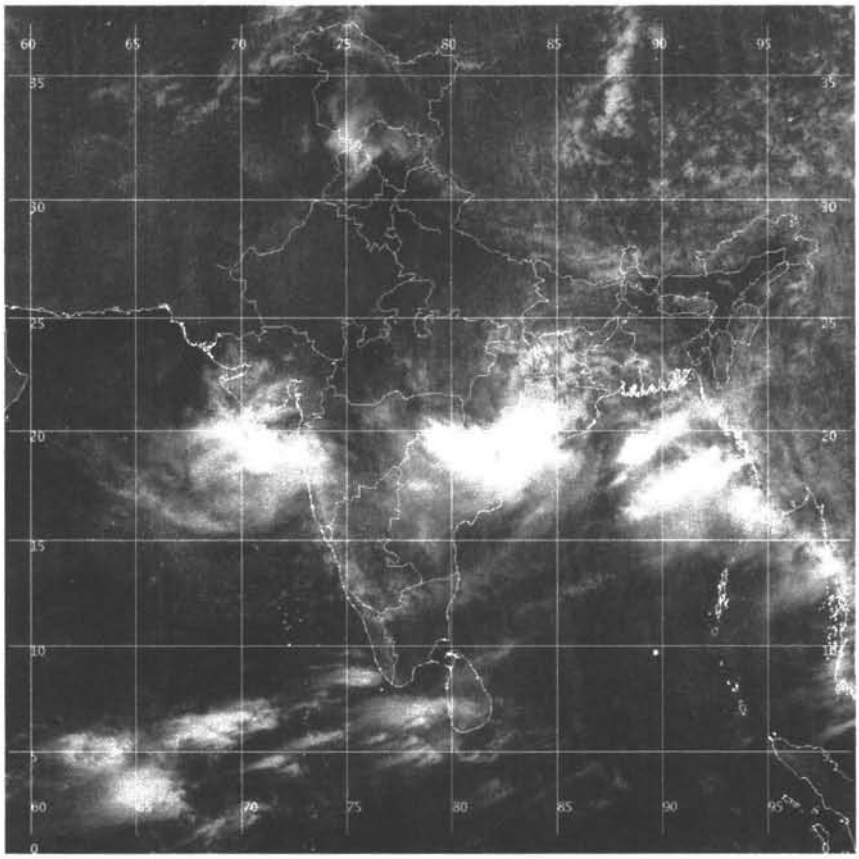

Figure 2.3.5.3 Kalpana-1 VIS image of 3 July 2006 showing a monsoon depression over eastern India flanked by intense convection on the Arabian Sea and Bay of Bengal and an off-shore trough along the west coast. The lower portion shows the cirrus blow-off due to the strong TEJ winds. (Source: IMD)

2.3.6 Breaks in the Monsoon

The southwest monsoon is in its most intense phase during July and August and these are the months of peak rainfall activity over India. However, the monsoon does not maintain a uniform strength all throughout this period and the wet spells are interspersed with dry spells over different parts of the country. At times, when the rainfall becomes very subdued over the country as a whole, the situation is described as a break in the monsoon. Breaks can be of varying intensity and duration, but they have certain common characteristic features. The most prominent synoptic development associated

with a break is the shifting of the axis of the seasonal monsoon trough to the foothills of the Himalayas. The large-scale atmospheric flow pattern develops many anomalous features. The north-south pressure gradient along the west coast reduces from 9 to 3 hPa and lower tropospheric westerlies weaken along the west coast. On the other hand, westerlies over the Gangetic plains strengthen and their speeds may reach even 50 knots. These winds are dry and transport dust from Rajasthan into the Gangetic plains. The monsoon trough slopes northward instead of sloping southward.

In the case of shorter breaks in the monsoon, only the western end of the monsoon trough may shift to the foothills of the western Himalayas, while the eastern end remains entrenched in its normal position. In this case there is excess rainfall over western Himalayas and reduced rainfall over the plains of northwest India. Such a break may be induced by the passage of a western disturbance. The monsoon activity recovers after the western disturbance has moved away.

When the entire monsoon trough migrates to the Himalayan foothills, there is a prolonged break, which may last for 4 to 5 days or even longer. There is excess rainfall all along the Himalayan foothills, especially on the eastern side, leading to a flooding of the Himalayan rivers, but rainfall is deficient over large parts of the country.

Breaks are most common in July and August. If a break-like situation develops in June, it is not called a break, as the monsoon has not established itself by then. Likewise, in September, a weakening of the monsoon is not called a break, as it may lead to a withdrawal of the monsoon and it may not revive.

As the breaks in the monsoon strongly modulate the All-India Summer Monsoon Rainfall (AISMR), they have been the subject of several studies, in which different definitions of a break are also to be found (Gadgil et al 2003, De et al 2002, Webster et al 1998). The most prolonged break was in July 2002 when AISMR was deficient by 19 %. There is a declining trend in the number of break days and their time of occurrence is seen to be shifting from August to July. However, the year 2005 was an exception. There were long breaks during August 2005 and rainfall was deficit by 28 % for the country as a whole in that month. This has happened only twice before in 1901 and 1920.

In most cases, there are no clear advance synoptic indications of an impending break in the monsoon or its cessation, but satellite images provide some signals. A break may be caused by a monsoon low or depression moving from the head Bay towards Assam. The monsoon usually recovers

gradually to a normal pattern. The cessation of the break may sometimes be induced by the formation of a monsoon depression in the Bay or the passage of a low pressure wave across south Indian peninsula that builds up the pressure gradient along the west coast.

In a recent work (Jenamani 2004), two intermediate phases, one in which the monsoon trough is migrating from its normal position to the foothills and another in which the monsoon trough is returning from the foothills to its normal position have been defined in detail with respect to rainfall, pressure and circulation features. He has concluded that in the pre-break phase, there is large negative pressure anomaly and excess rainfall over north India and large positive pressure anomaly and deficient rainfall over peninsular India. In the post-break revival phase, the opposite conditions prevail. He also found that in the pre-break phase, monsoon disturbances form over extreme north Bay of Bengal and in the revival phase, they form over south Bay of Bengal. If these disturbances move northward or northwestward the monsoon revives, but if they move westward the break only gets prolonged and intensified.

Satellite imagery is of great value in monitoring the migration of the monsoon trough from its normal position to the foothills and back. Satellite images during break situations have a conspicuous absence of clouds over a large part of the country.

2.3.7 Withdrawal of Southwest Monsoon

Although the period 1 June to 30 September is commonly regarded as the southwest monsoon season, it is more so because of the convenience of generating climatological statistics of rainfall and other atmospheric parameters than for sound physical reasons. While the onset of monsoon over Kerala occurs around 1 June, northwest India may not get its monsoon rains until the end of June. However, this pre-monsoon rainfall gets clubbed with the rainfall associated with monsoon for climatological purposes. Likewise, the southwest monsoon starts losing its strength in early September over northwest India, where the monsoon season is effectively of only two months duration. On the other hand, over large parts of central and southern India, rains persist much beyond the date of 30 September.

The withdrawal of the southwest monsoon from northwest India is an event that is in no manner comparable to its onset over Kerala. While the onset over Kerala has been a subject of great scientific interest, there have been very few studies of the withdrawal of the monsoon. The withdrawal process is associated with the establishment of anticyclonic flow over northwest

India, a reduction in the atmospheric moisture content and of course the cessation of rainfall. This is the beginning of the transition to the winter circulation pattern, and the return of the ITCZ to its southerly position.

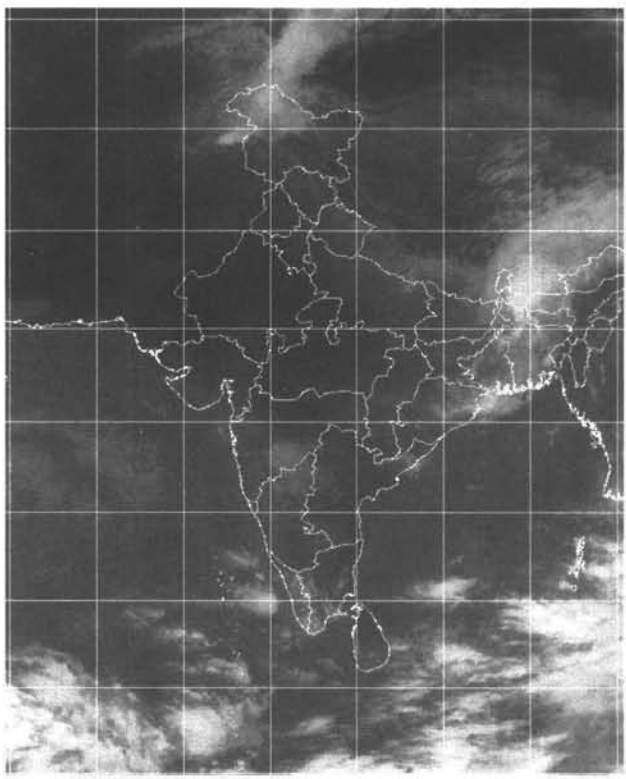

Figure 2.3.7.1 Kalpana-1 IR image taken on 4 October 2005 showing the southwest monsoon in its withdrawal phase. Also seen in the upper portion are the meridional cloud bands of a western disturbance. (Source: IMD)

There is no clear definition of the withdrawal, however, and there is no rule as to how long to wait before declaring that the monsoon rains have come to an end. There are many instances when the monsoon withdrawal has been followed by rains in north India as a result of the passage of a western disturbance or over peninsular India because of strong thunderstorm activity.

Generally, by 15 October, the southwest monsoon withdraws from the country (Figure 2.3.7.1) except from the southern peninsula, where the northeast monsoon continues to bring more rains as described in the next section.

2.3.8 Northeast Monsoon

Even after the withdrawal of the southwest monsoon, rainfall continues until mid-December over southern parts of India, and up to the first week of January over Sri Lanka. This rainfall is produced by the northeasterly winds in the lower troposphere associated with the northeast monsoon. Compared with the southwest monsoon, the northeast monsoon is a phenomenon of a much smaller scale, and it affects only the southern parts of the Indian peninsula during the months of October to December.

The mean date of onset of the northeast monsoon over Tamil Nadu is 20 October with a standard deviation of a week. However, there have been years of very early onset (5 October 1943) as well as extremely delayed onset (11 November 1915). The onset of the northeast monsoon is not rigidly defined, but it is known to be associated with several distinguishing features like the withdrawal of southwest monsoon up to coastal Andhra Pradesh, persistence of easterly/northeasterly winds up to 850 hPa in the lower troposphere and the occurrence of fairly widespread rainfall over coastal Tamil Nadu and adjoining areas. The onset is also marked by a reversal of north-south pressure gradient with the lowest pressure being over the extreme southern peninsula, strengthening of upper tropospheric westerlies over north India and increase in moisture content over the southern peninsula.

The northeast monsoon gets intensified with the passage of easterly waves and low pressure areas across the Bay of Bengal, some of which may grow into tropical cyclones (Figure 2.3.8.1). As the northeast monsoon season advances, the cyclones move at relatively lower latitudes. In November and December, cyclones have a tendency to move towards Tamil Nadu.

For Tamil Nadu, northeast monsoon rainfall is more plentiful than southeast monsoon rainfall. The annual normal rainfall of Tamil Nadu is 100 cm, out of which 35 cm is received during the southwest monsoon and 48 cm in the northeast monsoon season. The northeast monsoon rainfall has a standard deviation of 14 cm making it highly variable.

The northeast monsoon season ends in December. Again there is no specific definition of withdrawal of northeast monsoon. After December, the near-equatorial trough moves further south and the formation of tropical cyclones near the equator is inhibited.

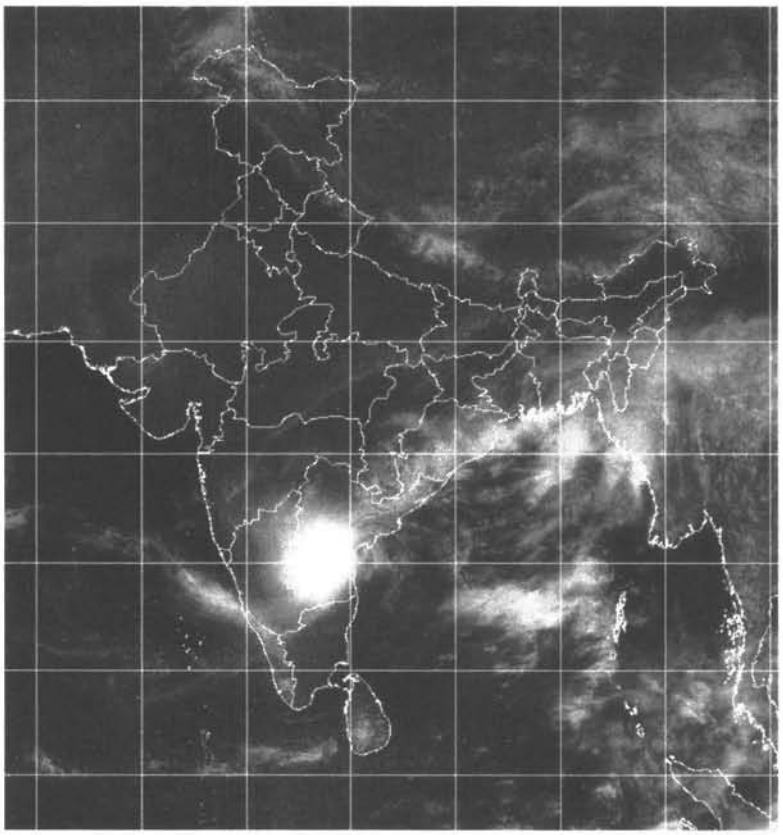

Figure 2.3.8.1 Kalpana-1 VIS image of 28 October 2005 showing the northeast monsoon (Source: IMD)

Khole et al (2003) have composited the area-weighted rainfall for the five meteorological sub-divisions of India forming the core region of the northeast monsoon and found that it is 11 % higher than the long period average in El Nino years and 6 % lower in La Nina years.

Raj (1996) has studied the thermodynamical aspects such as precipitable water vapour, upper air temperatures and moisture fluxes during different phases of the northeast monsoon. Suresh et al (2001) made a similar analysis based upon TOVS-derived outgoing longwave radiation (OLR) and precipitable water vapour for 1996-1998 over the northeast monsoon domain. They found that in the active phase of the northeast monsoon, the lower and upper atmosphere is warmer and the middle atmosphere cooler than in the weak phase. The OLR distribution suggests that during the active phase, the rainfall is maximum over south coastal Tamil Nadu and decreases towards

the Bay of Bengal, while in the weak and post-withdrawal phases, there is higher rainfall over the Bay than over Tamil Nadu. Suresh et al (2002) have also made a study based on TOVS data of atmospheric boundary layer parameters during the northeast monsoon.

2.3.9 Easterly Waves

During the monsoon season, low pressure systems move from east to west across Myanmar into south and central Bay of Bengal and they help in the formation of monsoon depressions. During the pre-monsoon and post-monsoon seasons, some remnants of west Pacific Ocean typhoons travel across southeast Asia, enter into the Bay of Bengal and trigger the formation of tropical cyclones. Easterly waves can be easily tracked through satellite imagery (Figure 2.3.9.1)

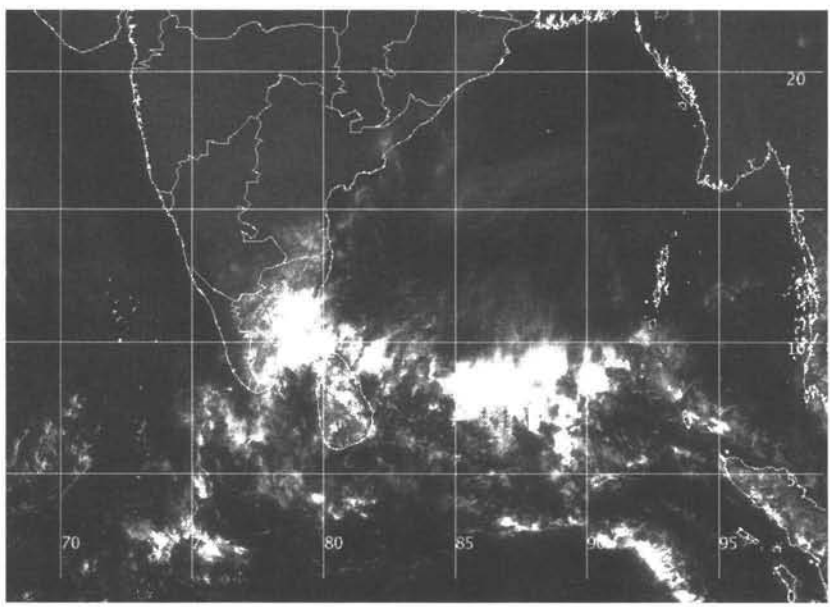

Figure 2.3.9.1 Kalpana-1 VIS image of 5 January 2006 showing an easterly wave over the Bay of Bengal (Source: IMD)

Easterly waves are observed over other parts of the world also. These are waves of relatively feeble intensity. They have smaller amplitudes compared to troughs and ridges and cannot be easily identified on synoptic charts as usually the data is inadequate. They lack a uniform structure as they change with the nature of the zonal current which itself has varying regional and seasonal characteristics. In our region, easterly waves lie between the

sub-tropical ridge and the ITCZ, both of which slope towards the equator with increasing height. Hence at any given latitude, there is considerable difference in the depth of the easterlies. In the Bay of Bengal, easterly waves give rise to closed lows which then move independent of the easterly waves themselves.

2.4 Tropical Cyclones

Getting caught in violent storms at sea has always been a common hazard associated with sea voyages. However, our earliest scientific information about tropical cyclones came from the distress signals sent out by ships and the experiences and observations recorded by mariners in their logs that were scanned by meteorologists when the ships berthed at the ports. It was only in the mid-twentieth century, that a cyclone could be caught in the view of a weather radar as it approached the coast, its structure examined and intensity estimated. Afterwards, in the U.S., dare-devil aircraft reconnaissance missions were flown into tropical cyclones, enabling the *in situ* measurement of atmospheric parameters within and around them. After the launch of the world's first weather satellite in 1960, meteorologists got their first glimpse of a tropical cyclone from space. Initially, only one satellite image of a tropical cyclone was available in a day, and night-time observations became possible later. Early satellite imagery, though quite primitive by present standards, provided a new insight into the structure of tropical cyclones (Fett 1964) and ushered in a new era of tropical cyclone observations and forecasting.

Subsequently, with the launch of geostationary satellites like GOES, Meteosat and GMS, and that of the first INSAT in 1982, tropical cyclones came under a global round-the-clock surveillance right from their genesis up to landfall. Satellite imagery is most useful at all stages of development of tropical cyclones, for first detecting their formation far out at sea, then following their movement, determining their intensity and observing changes in their characteristics.

It has been known for long that there are three basic pre-requisites for the formation of a tropical cyclone, or cyclogenesis, over the tropical oceans. These are (a) the Coriolis force which produces the rotation effect, (b) a warm ocean that provides energy to the cyclone, and (c) relatively moist layers in the middle troposphere. Because of the requirement of the Coriolis force to provide for near-gradient wind balance to occur, a minimum distance of about 500 km away from the equator is required. Without the Coriolis force, the low pressure of the disturbance cannot be maintained. The sea surface temperature should be least 26.5°C, and temperature should be high

enough to a sufficient depth of the order of 50 m below the surface. The atmosphere should cool rapidly with height so that it is potentially unstable to moist convection. It is the thunderstorm activity which allows the heat stored in the ocean waters to be released for the tropical cyclone development. Dry mid-tropospheric levels are not conducive for allowing the continuing development of widespread thunderstorm activity.

Besides the three conditions mentioned above, another condition for cyclogenesis is a pre-existing low-level disturbance. Tropical cyclones do not form on their own, and they require at least some weakly organized system at the surface with sufficient vorticity and low level inflow or convergence. What is also required is a low vertical wind shear between the surface and the upper troposphere. Large values of vertical wind shear work contrary to cyclogenesis. If a tropical cyclone has already formed, large vertical shear can weaken or destroy the tropical cyclone by interfering with the organization of deep convection around the cyclone centre.

While all these conditions are necessary, they are not always sufficient. Many disturbances that seem to be in the midst of a favourable environment, do not develop into tropical cyclones. Also, all cyclones do not have devastating effects. Those which form close to the coastline and have no scope for intensification may even turn out to beneficial as they may give just the badly needed precipitation over the coastal areas. Some systems may move into colder waters and dissipate there without making a landfall. Then there are storms which recurve in the middle of a long path and move away from the coast, some times even after having almost reached it. As a result of all these possible situations, full-blown killer storms are, thankfully, not that common.

A tropical cyclone transports large amounts of sensible and latent heat energy from the sea surface to the atmosphere. As the cyclone moves away, SST falls by several degrees due to upwelling of colder waters from deeper layers, vertical mixing, and cooling due to evaporation at the sea surface because of strong winds. While high SSTs are favourable for cyclogenesis, a tropical cyclone can itself cool down the sea in its wake. This acts as a partial brake on the intensification of cyclones. Hence, one tropical cyclone is not immediately followed by another, and at least a few days must elapse in between.

2.4.1 Nomenclature of Low Pressure Systems

Generally speaking, a tropical weather system that crosses the 64 knots or 118 kmph wind speed threshold gets identified as a major storm. However,

different meteorological agencies responsible for tropical cyclone forecasting use different nomenclature practices to describe the evolution of the system through sccessive stages. The India Meteorological Department uses the term "Very Severe Cyclonic Storm" to categorise a tropical cyclone with wind speeds exceeding 64 knots over the Arabian Sea and the Bay of Bengal (Table 2.4.1.1). In the eastern and central Pacific Ocean and north Atlantic Ocean, such a system is called a "Hurricane" and in the northwest Pacific Ocean it would be termed as a "Typhoon". These differences, however, are only in the nomenclature and not in the characteristics of the storm, and it is at this stage that it gets a name identifier like Katrina or Rita as per naming conventions.

Table 2.4.1.1 Nomenclature of Tropical Weather Systems Used in India

System Category	Wind Speed (knots)	Wind Speed (kmph)
Low Pressure Area	Less than 17	Less than 31
Depression	17-27	31-51
Deep Depression	28-33	52-61
Cyclonic Storm	34-47	62-87
Severe Cyclonic Storm	48-63	88-117
Very Severe Cyclonic Storm	64-90	118-167
Very Severe Cyclonic Storm	91-119	168-221
Super-Cyclone	Greater than 119	Greater than 221

In the U. S., hurricanes are further ranked on the 5-point Saffir-Simpson scale ranging from Category 1 which has the lowest damage potential, to Category 5 which denotes the most powerful hurricane. In India, the term "Super-Cyclone" is used for cyclones in which the winds are stronger than 119 knots or 221 kmph, which roughly corresponds to a Category 4 hurricane on the Saffir-Simpson scale.

2.4.2 Tropical Cyclone Basins

On an average, about 80 tropical cyclones form every year over seven major oceanic basins around the world (Table 2.4.2.1).

Over the south Atlantic Ocean, cyclones are the rarest, with the solitary exception of the one that hit Brazil in March 2004. Over the western north Pacific Ocean, cyclones are the most frequent, their number being as high as

30% of the storms occurring annually over the entire globe. Over the Arabian Sea and Bay of Bengal, we get an average of only 4 to 6 cyclones per year, but historically some of them have been the world's deadliest. They are most frequent in the months of April-May (summer season) and October-November (post-monsoon season). Arabian Sea storms are comparatively fewer than Bay of Bengal storms.

Table 2.4.2.1 Formation of Tropical Cyclones over Different Ocean Basins

Basin	Area	Percentage of Annual Global Number	Main Storm Season	Period of Peak Activity
Western North Pacific Ocean	From the dateline to Asia including the South China Sea	30	July-November, but storms occur throughout the year	Late August/early September
Eastern North Pacific Ocean	From Mexico to about the dateline	11	May-October	Late August/early September
South Western Pacific Ocean	From 142 °E to about 120 °W	11	October-May	February-March
North Atlantic Ocean	Including the Gulf of Mexico, and the Caribbean Sea	12	June-November	September
Northern Indian Ocean	Including the Bay of Bengal and the Arabian Sea	15	April-June and October-December	Double peak in May and November
Southeastern Indian Ocean	From 100 °E to 142 °E	7	October-May	January-March
Southwestern Indian Ocean	From Africa to about 100 °E	14	October-May	January-March

Sikka (2006) has made a historical review of major advances in the understanding and prediction of tropical cyclones over the north Indian Ocean. Two excellent reviews of the use of radar and satellite imagery in India for tropical cyclone analysis and forecasting have been made by Raghavan (1997) and Kalsi (2002) respectively.

2.4.3 Structure of Tropical Cyclones

The life cycle of a tropical cyclone consists of four phases, the formative phase, the developing phase, the mature phase and the dissipating phase.

(a) Formative Phase: In the neighbourhood of the ITCZ, relative cyclonic vorticity is already present. An easterly wave helps in the formation of a weak 'cold core' low in which there is relatively colder air at the lower levels and relatively warmer air at the higher levels. Cyclonic vorticity induces horizontal inflow in the frictional layer and makes the air to rise dry adiabatically. Satellite pictures show spiraling clouds interspersed with open spaces.

(b) Developing Phase: The rising air, after reaching the condensation level, is saturated and warmer than the environment. Release of latent heat of condensation is a source of heat. This releases the convective instability of the lower and middle troposphere. Vertical acceleration of air induces inward spiralling of air. The warm core descends down to the sea level and the entire vortex becomes a warm core system.

(c) Mature phase: The winds strengthen, pressure falls and there is heavy rain at the surface. Descending motion starts at the top of the warm core and penetrates gradually downwards. This leads to the formation of the eye. The cyclonic vortex drifts in the general air current but also interacts with it and even modifies it.

(d) Dissipating Phase: After landfall, being deprived of warm moist air and encountering rough terrain, it again becomes a cold core system. It weakens into a depression and dissipates gradually. In rare cases, a cyclone which has dissipated over land may once again emerge into the ocean. For example a Bay of Bengal storm may weaken after crossing into the Indian peninsula, but continue to move westward and eventually emerge over the Arabian Sea, to re-intensify. Some storms may move to higher latitude and take on the characteristics of an extra-tropical cyclone. The total life span of a tropical cyclone may range from 5 to 15 days.

A typical satellite view of a fully mature tropical cyclone is shown in Figure 2.4.3.1. The characteristic features are explained below:

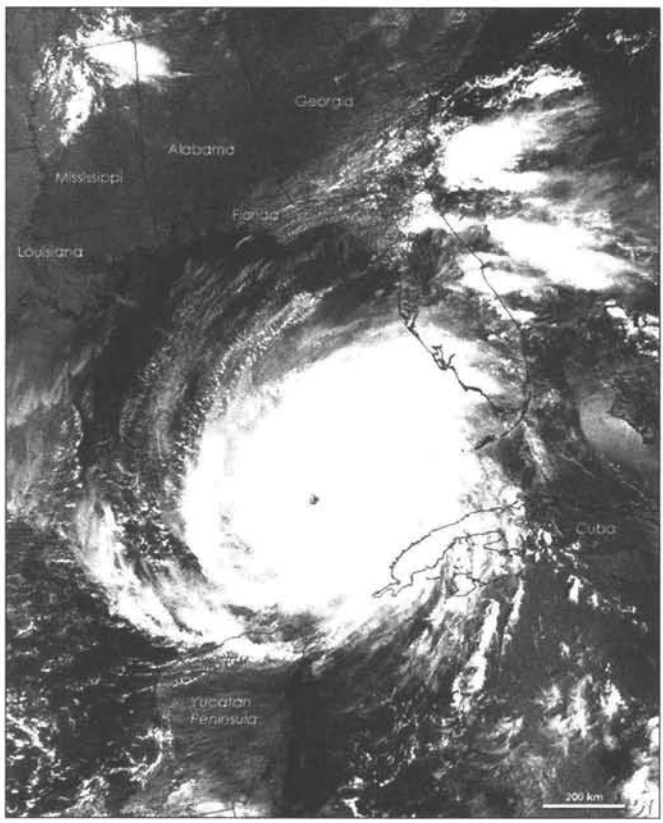

Figure 2.4.3.1 MODIS image of Hurricane Rita taken on 21 September 2005, when the storm was out at sea and in its full fury (Source: http://earthobservatory.nasa.gov/)

(a) Eye and eyewall: At the centre of the pattern is the eye, which is a roughly circular area characterised by fair weather, comparatively light winds, lowest surface pressure and warmest temperatures aloft. Eyes range in size from 8 to 200 km, but most commonly have a 30-60 km diameter. The eye is surrounded by the eyewall which is a roughly circular ring of deep convection. It is the area of highest surface winds in the tropical cyclone. The eye is composed of air that is slowly sinking while the eyewall has a net upward flow as a result of many strong updrafts and downdrafts. The high temperatures of the eye are due to compressional warming of the subsiding air.

The appearance of an eye is indicative of the strengthening of the storm. It increases the dynamical stability. As the storm intensifies, the eye shrinks in size and the eye area becomes more cloudfree. In very intense systems, there may be two cloudfree regions surrounded by two cloud walls, resulting in a double eyewall structure. The eye is mostly round, but occasionally eyes have been seen to have polygonal shapes as a result of instability of the wind structure near the radius of maximum winds. Polygonal eyewalls do not always have clear sky and calm winds but they can have small vortices associated with tall clouds and high winds.

(b) Spiral bands: Convection in tropical cyclones is organized into long, narrow rain bands which are oriented in the same direction as the horizontal wind. Because these bands seem to spiral into the centre of a tropical cyclone, they are also called spiral bands. Along these bands, low level convergence and upper level divergence are most pronounced. The width of the rain bands is about 100 km near the outer periphery of the storm but it reduces inwards. Severe convective rain rates of 3 cm/hr or more are associated with the rain bands. They move along with the system but also move around the centre in the direction of the tangential wind of the cyclone but much slower. Spiral bands persist for a few days but individual cells within the bands are very short-lived.

(c) Central dense overcast: Between the eyewall and the outer bands is the central dense overcast or CDO, which is a shield of cirrus clouds. This cirrus cloud shield results from the thunderstorms in the eyewall of a tropical cyclone and its rain bands. Before the storm reaches hurricane strength of 64 knots the CDO looks uniform. After that an eye may be seen in either the infra-red or visible channel images. Circular CDOs are indicative of favourable, low vertical shear environments.

(d) Moat: This term usually refers to the region between the eyewall and an outer rain band and signifies a region of relatively light rain.

2.4.4 Dvorak's Technique

The advent of meteorological satellites in the 1960's made an immediate impact on the detection and monitoring of tropical cyclones and their track prediction (Sikka 1971a, 1971b, Kulshrestha 1971). Soon thereafter, the technique formulated by Dvorak (1975) for intensity estimation of tropical cyclones from VIS satellite imagery available once a day gained widespread acceptance. The scope of the technique was later enlarged to include IR

imagery which became available at night-time also (Dvorak 1984). Dvorak's technique is basically a pattern recognition process which assumes that certain characteristics or features of the cloud organization are indicators of the intensity. The current satellite picture of a tropical cyclone has to be matched against a number of possible pattern types or analogues. The features, however, may not always be clearly defined or they may appear differently or be uncharacteristic of the standard patterns. Such a complexity can be dealt with through a set of systematic procedures, quantifiable and measurable cloud pattern descriptions and models of storm development with time, which are stipulated in Dvorak's technique.

Table 2.4.4.1 Intensity of Tropical Storms as per Dvorak's Technique

CI-Number or T-Number	Maximum Sustained Wind (knots)	Central Pressure (hPa)	
		Atlantic Ocean	NW Pacific Ocean
0.5	25	----	----
1.0	25	----	----
1.5	25	----	----
2.0	30	1009	1000
2.5	35	1005	997
3.0	45	1000	991
3.5	55	994	984
4.0	65	987	976
4.5	77	979	966
5.0	90	970	954
5.5	102	960	941
6.0	115	948	927
6.5	127	935	914
7.0	140	921	898
7.5	155	906	879
8.0	170	890	858

The application of Dvorak's technique has been discussed in detail by Kalsi (2006) in a case study of the Orissa super-cyclone of 29 October 1999.

Dvorak's model of cyclone development is built in terms of what is called the T-Number (T = Tropical). This has a range of values of 1 to 8 is steps of 0.5, associated with increasing wind speed and decreasing sea level pressure (Table 2.4.4.1).

T1 stands for a nascent disturbance, T2 for a pre-storm situation and T2.5 for a marginal tropical cyclone. T3.5 is a severe cyclonic storm, T4 - T6 a very severe cyclonic storm and T6.5 or higher a super-cyclone. T8 would describe the most extreme case. The T-Number would normally increase by 1 per day during intensification but departures from the model rate are possible. Figure 2.4.4.1 shows a satellite image of three tropical storm systems co-existing in close proximity over the western Pacific Ocean, but at different stages of evolution, each pattern corresponding to different T-numbers on Dvorak's scale.

Dvorak's technique of tropical cyclone intensity estimation has the nature of a complex decision tree with several branches. Since it was intended for operational use by duty forecasters working in meteorological centres, it was the form of a detailed rule-book. Only the 10 basic steps of the decision making process are described below:

Step 1 - Locating the Cloud System Centre (CSC): The first step is to locate the CSC which is the focal point of all curved lines or bands of the cloud system, or it is the geometric centre of the eye if present. A disturbance showing signs of reaching tropical cyclone intensity is classified as T1 if it has persisted for 12 hours or more, if it has a CSC defined within an area having a diameter of 2.5° lat or less, which has persisted for 6 hours or if it has an area of dense, cold (<-31° C) overcast greater than 1.5° lat in extent that appears less than 2° lat from the centre. The overcast may also appear in cumulonimbus lines that curve around the centre. A considerable variability of cloud patterns is often observed during the T1 stage. These weak systems do not involve deep tropospheric circulations. They are short-lived and prone to diurnal and non-periodic oscillations in convection. Kalsi (1993) examined several time sequences of INSAT-1B images and observed that initially there may not be a perceptible difference between developing and non-developing mesoscale cloud clusters over the ocean, but the persistence of convection as a prelude to cyclogenesis is a feature common to many Bay of Bengal tropical cyclones.

Step 2 - Determining the Pattern Type: The manner in which the CSC is defined determines which of the following pattern types would be used: (2a) Curved Band Pattern, (2b) Shear Pattern, (2c) Eye Pattern, (2d) Central Dense Overcast or CDO Pattern, (2e) Embedded Centre Pattern or

(3) Central Cold Cover Pattern. When the cloud pattern being analysed does not conform to any of these patterns, Step 3 is used.

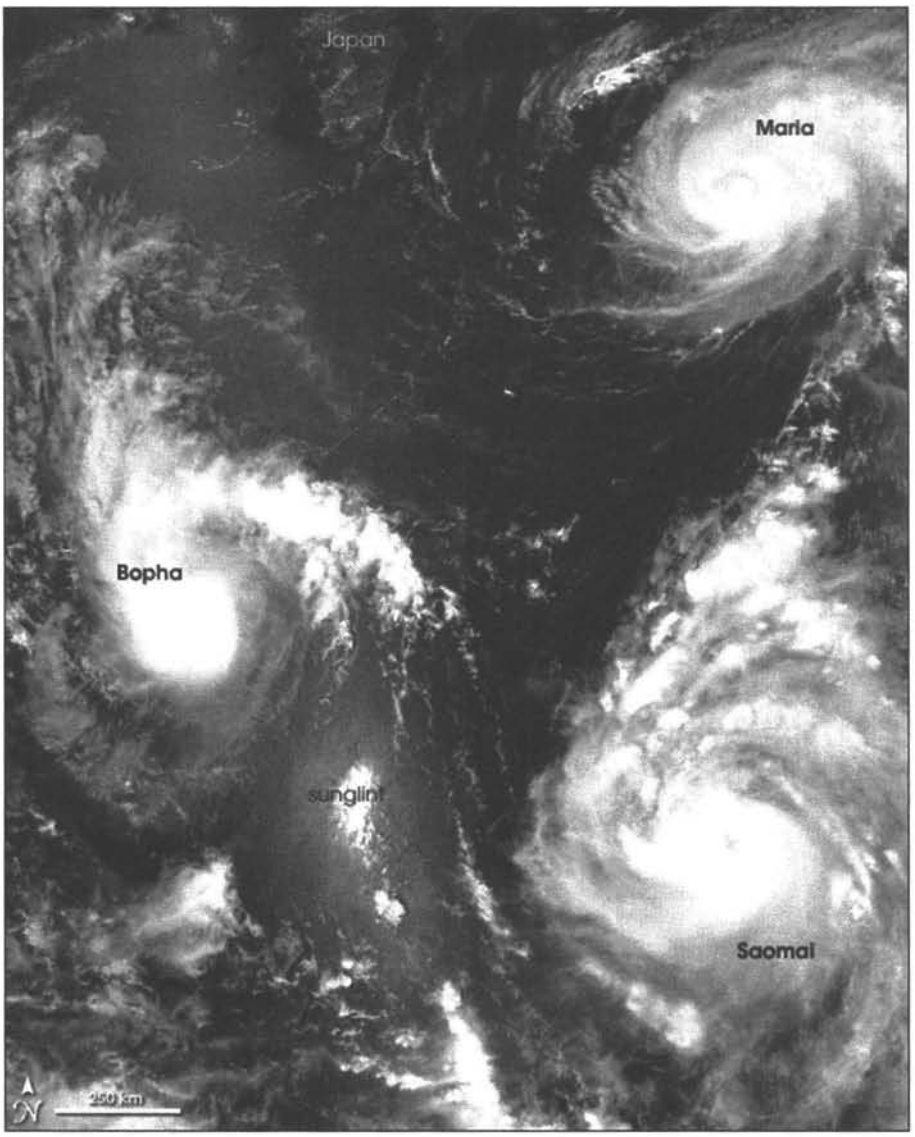

Figure 2.4.4.1 MODIS image of 7 August 2006 showing three different typhoons over the western Pacific Ocean: Saomai, Maria and Bopha with strengths in decreasing order
(Source: http://earthobservatory.nasa.gov/Newsroom/NewImages/)

Step 2a - Curved Band Pattern: This pattern is very commonly observed in both VIS and IR satellite imagery in the development stage of a tropical cyclone (Typhoon Bopha in Figure 2.4.4.1). The intensity estimate is derived from the extent to which the cloud band encircles the storm centre, which is measured as the arc length of the curved band fitted to a 10° logarithmic spiral overlay. The spiral overlay is fitted to the axis of the coldest gray shade (most dense clouds) within the cloud band. Depending on the fit, the associated Data T-Number (DT) is obtained from the chart, either VIS or IR.

During the first two days of development (T1 to T2), the band curvature may increase, remain unchanged or even decrease for some time. So, on the first day, the T-Number is increased from T1 to T2 unless there are clear signs of weakening. It is also important to allow at least 24 hr to pass between a T2 and a T3 classification as even though the coiling process may be rapid, the surface pressure may not fall accordingly.

Step 2b - Shear Pattern: The curved cloud bands may sometimes get obliterated due to strong vertical wind shear. In such a case, the dense upper level clouds get separated from the low level circulation. The dense cloud mass appears to be distant from the centre defined by the cumulus lines (Figure 2.4.4.2). Shear patterns most commonly occur during early development and weakening. They are identified by the cold clouds moving to one side of the cyclone and developing a sharp edge. The DT is derived from both the method of defining the CSC and the distance between the low cloud centre and the dense, cold overcast.

For tropical storm intensity (T2.5 - T3.5), the centre will be defined by parallel, circularly curved low cloud lines with a diameter of 1.5° lat or less near or under the edge of a dense, cold (<-31° C) overcast cloud mass. For weaker systems (T1.5 - T2.5), the low cloud centre will either be poorly defined in spiral lines within 1.25° lat of the cold overcast clouds, or circularly defined near a small, dense overcast (< 1.5° lat diameter).

Step 2c - Eye Pattern: At T2.5, the cloud band may curve half-way around the centre. As the intensity increases, the band widens and coils to form a gap or hole in the centre which is called a banded eye (Figure 2.4.4.3). When the cyclone develops an eye embedded in the CDO (Figure 2.4.3.1), the intensity can be estimated from the size, shape and appearance of the eye and the smoothness of the CDO. Eye patterns are analysed for systems which have been at T2 or greater for 24 hours and have an eye. The DT is derived from the Eye Number E, Eye Adjustment Number EA and Banding Feature Number BF for which there are separate rules.

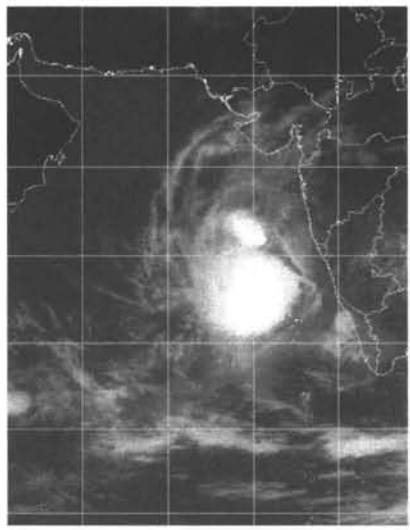

Figure 2.4.4.2 Kalpana-1 IR image of 7 May 2004 showing shear pattern in an Arabian Sea tropical cyclone (Source: IMD)

Step 2d - CDO Pattern (VIS imagery): CDO patterns consist of a dense, solid-looking mass of clouds covering the cloud system centre (Figure 2.4.4.4). Generally, well-defined CDOs of at least 1° lat width are associated with tropical storm intensities and those measuring 2° lat or more are associated with hurricanes. Banding features (BF) and central features (CF) terms are added to get the DT.

Step 2e - Embedded Centre Pattern (IR imagery): Embedded centre patterns are analysed when the tropical cyclone has been T3.5 or stronger and when the CSC is clearly indicated to be within a cold overcast (<9° C). Curved cloud lines or bands within the cold overcast as well as the outer curved bands will indicate the location of the CSC within the overcast. The analysis of this pattern is similar to the eye pattern analysis except that no eye adjustment factor is added.

The non-availability of VIS images at night presents many additional difficulties in the operational use of the Dvorak's technique. Firstly, IR sensors generally have a poorer resolution than VIS sensors. Secondly, thin cirrus clouds which are transparent to VIS radiation, show up in IR pictures prominently, blocking the view of underlying cloud features. Thirdly, the low cloud lines which are clearly seen in VIS pictures and help to locate the centre are not noticeable in IR images. However, the digital brightness data, if used directly, can be of great value in quantitative analysis and digital

enhancement procedures can be applied to bring out many of the storm features.

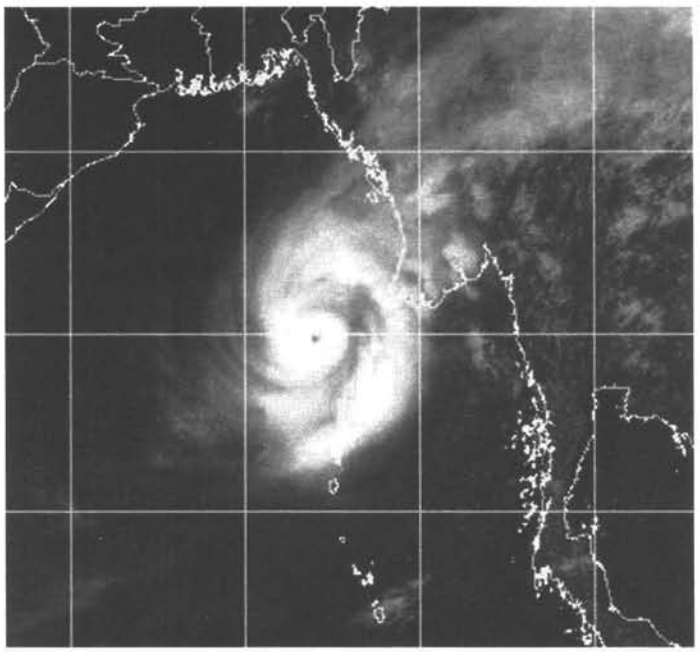

Figure 2.4.4.3 Kalpana-1 VIS image of 28 April 2006 showing a banded eye in a Bay of Bengal tropical cyclone (Source: IMD)

Kalsi (2006) has applied the digital gray scale enhancement technique to the sequence of images of the Orissa super-cyclone of 29 October 1999 and has brought many additional features which cannot be seen in VIS and un-enhanced IR images. The details of the enhancement scheme have been given earlier in Section 1.4.2 and Figures 1.4.2.1 to 1.4.2.3.

Step 3 - Central Cold Cover (CCC) Pattern: The CCC pattern consists of a near-circular, cold or dense overcast covering the cyclone centre or comma head and obscuring the expected signs of pattern evolution. It is usually associated with arrested development and is to be confused with a very cold comma pattern, which has smooth texture and an indication of a wedge and has curved cirrus lines around it.

Step 4 - Past 24-hour Trend: The trend of the past 24-hr intensity change is determined by other observations, or by comparing the current and 24-hr past cloud features. Development is generally associated with increased organisation and better defined central features.

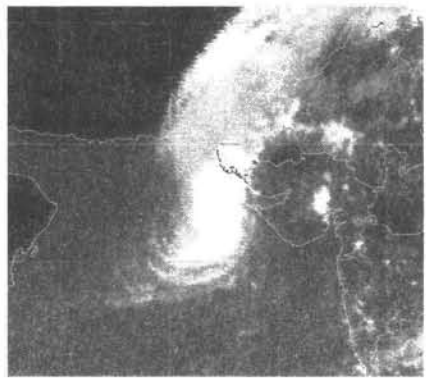

Figure 2.4.4.4 Kalpana-1 IR image of 2 October 2004 showing CDO pattern in an Arabian Sea cyclone (Source: IMD)

The signs of development are: (D1) curved band coils tighter around the CSC, (D2) CDO becomes larger or an increase in banding features is noted, (D3) CSC becomes more tightly defined in curved cloud lines or appears closer to the dense overcast, (D4) eye is more embedded, more distinct (warmer), less ragged, or is surrounded by colder (smoother textures) clouds, or more banding features, and (D5) no significant (non-diurnal) warming of the cloud system is noted. The signs of weakening (W) are exactly the opposite of signs D1 - D5.

Signs of steady state are: (W1) a central cold cover appears in a T3.5 or stronger tropical cyclone or has persisted for more than 12 hr in a weaker cyclone, (W2) the CSC's relationship to the cold clouds has not changed significantly, and (W3) there are conflicting indications of both development and weakening.

Step 5 - Model Expected T-Number (MET): MET is determined by using the 24-hr old T-Number, the D, S, or W, decision in Step 4, and the past amount of intensity change of the cyclone. When the growth rate has not been established in the case of new developments or reversals in trend, a past rate of change of one T-Number per day is assumed. Rapid or slow past rates of change are established when two consecutive analyses showing rapid or slow pattern evolution are observed at 6 hr or longer intervals, or when one observation of strong intensification or weakening is made.

Step 6 - Pattern T-Number (PT): The pattern T-Number is used primarily as an adjustment to the MET.

Steps 7 and 8 - Final T-Number: The final T-Number is determined from the rules stipulated in the technique. Constraints are applied to hold the T-Number within acceptable bounds and avoid misinterpretations of marked changes.

Step 9 - The Current Intensity (CI-Number): The CI-Number relates directly to the intensity of the tropical cyclone and is determined from the T-Number by the rules. After each intensity analysis, the previous analysis of the tropical cyclone has to be reviewed for consistency. If the previous day's analysis was erroneous, the T-number has to be corrected to provide a more accurate model-expected intensity. This correction may at times alter the current intensity analysis.

When the storm begins to weaken, the CI-Number is used to indicate the storm intensity in place of the T-Number. The CI-Number is held higher than the T-Number for weakening storms, otherwise they are the same. This is done as a precaution as indications of weakening may sometimes only be temporary.

Step 10 - Forecasting the intensity: Forecasts of change in cyclone intensity are made using the Dvorak model development curve, statistical methods, and subjective assessment of satellite imagery and environmental conditions. It is necessary to consider whether the cyclone is entering or leaving an environment of strong vertical wind shear or approaching land.

It is important to note here that tropical cyclones show a lot of diurnal variation and the cloud patterns change accordingly from morning to evening. Heavy rain follows the same diurnal cycle as convection. The maximum occurs between local midnight and dawn over the ocean, but there is no preferred time over land, especially when orographic effects dominate.

Extensive use of Dvorak's technique has brought to light many of its limitations and subjectivity. Dvorak's technique was initially calibrated with reference to aircraft observations over the Atlantic and Pacific Oceans and basin to basin differences in storm evolution and structure are not accounted for. New types of satellite data in microwave and WV channels have become available operationally in recent years and they provide additional information to cyclone forecasters in making a judicious use of Dvorak's technique (Velden et al 1991).

In an attempt to eliminate subjectivity in the application of Dvorak's technique and resulting discrepancies, Velden et al (1998) have designed an objective Dvorak's technique. This is a computer-based algorithm that operates on digital IR data and incorporates selected Dvorak rules, additional

constraints and a time averaging scheme. It is applicable to tropical cyclones which have attained tropical storm or hurricane intensity and not to weak systems.

Veldens's objective Dvorak technique (ODT) extracts two temperatures from the IR data in order to obtain an intensity estimate. The ODT first determines if the storm has an eye. If so, it uses the warmest pixel temperature within a 40 km radius of the chosen storm centre. This value is retained as the 'eye temperature'. In the absence of an eye, the value of the pixel at the user-defined storm centre location is used as the eye temperature. Next, ODT analyses temperatures on concentric rings (1 pixel wide) centred on the eye between 24 and 136 km from the eye location. For GOES data with 4 km pixel resolution, this results in a total of 28 rings that are analyzed to determine the surrounding temperature. This parameter is a proxy for the vigour of the eyewall convection which is associated with storm intensity. After identifying the eye and surrounding temperatures, the intensity is determined by matching them with standard cloud patterns objectively by examining areal histograms of cloud top temperatures and corresponding Fourier Analysis for the eye region and surrounding cloud region.

The ODT has been refined periodically and an advanced version (AODT) which also makes use of microwave and WV data is now available (Olander et al 2002). In a case study of three cyclonic storms over the Arabian Sea, Loe et al (2006) have applied the AODT to recompute the T-Numbers at various stages of the storms and compared them with those obtained subjectively by operational forecasters.

2.4.5 Movement of Tropical Cyclones

While a tropical cyclone is characterised by strong winds of the order of 100 to 200 km/hr, the cloud system as a whole moves only at about 20 km/hr along with the large-scale atmospheric flow around it. Usually the system moves towards the west, but has some northward movement as well, because of the existence of an east-west axis of high pressure called the sub-tropical ridge to the north of the system. If the subtropical ridge is weak, the system turns northward rather than westward, and as a result, away from the coastline and ultimately, it may turn fully eastward. This behaviour is called recurvature. The problem is to predict if the storm will recurve or go straight ahead and make landfall. Recurvature is the cause of many tropical cyclones over the Bay of Bengal first heading towards Andhra Pradesh, then turning towards Orissa and finally making landfall over Bangladesh or Myanmar. Occasionally, a cyclone may even perform a loop in its path.

The movement of a tropical cyclone can be predicted in two ways. One is by reference to the climatology of storms for that region and time of the year. If it is assumed that a cyclone will follow the same track as the past storms, a "climatological" forecast can be made for its direction and speed of movement. The other way is to view successive satellite images over the previous 24 hours and assume that the cyclone will continue to move in the same direction and average speed. This is called a "persistence" forecast. The so-called CLIPER technique employs a combination of climatology and persistence.

Because of the wealth of data that the new generation of satellites are making available, the ability of meteorologists to make predictions of cyclone tracks has been consistently improving. In order to forecast what path a tropical cyclone will traverse over the ocean, it is necessary to first predict the steering current in which the tropical cyclone is embedded, and how the cyclone will interact with it. Numerical weather prediction models require appropriate data on the initial conditions of the atmosphere. However, even the most advanced models are constrained by the availabilty of initial data about the cyclone's internal structure and its external environment. The accuracy of cyclone track prediction by operational numerical weather prediction centres has steadily increased over the past ten years, but even now, track predictions made 5 days in advance can be wrong by as much as 600 km and the 3-day predictions by more than 300 km. Even the 24-hour predictions could be in error by up to 150 km. As such, the CLIPER technique shows a relative higher skill than 48 hr numerical model forecasts.

Kelkar (1997) has discussed various satellite-based methods developed or attempted for cyclone track prediction. Velden et al (1984) used the satellite-derived mean layer wind as the steering current for forecasting hurricane movement. In spite of the difficulties in deriving cloud motion winds over cloudy regions, by combining them with microwave data, a fair approximation of the steering current can be derived.

Changes in upper level moisture patterns as seen from WV satellite imagery have also been used to forecast cyclone motion (Dvorak et al 1992). Two features of WV imagery are indicators of recurvature of northeast Pacific hurricanes. One is a curved moisture band about 10° northeast of the hurricane, and bowed cyclonically towards it. Another is an increasing north-south orientation of the moisture cloud pattern of the system. The WV imagery also helps in forecasting a westward turn in the track of the cyclone as it shows up a drying or darkening of the moisture pattern to the north prior to the turn.

2.4.6 Impact of Tropical Cyclones

The real impact of tropical cyclones depends on several factors. While the scale of destruction of property depends upon the intensity of the system and the associated wind speeds, rainfall amounts and rain rates, the loss of human life is more often caused by the storm surge and inundation. While the winds and rainfall are related to the degree of organization of the cyclonic system, the storm surge depends to a great extent on the nature of the coastline at the place of landfall, the slope of the sea bed and the land use pattern.

Table 2.4.6.1 gives a detailed summary of how the impact of tropical cyclones on the coastal belt goes on building up, for a stepwise increase in the T-Number or intensity of the storm. This information, which has been compiled and made available to the public by the India Meteorological Department, is based upon the prevailing scientific knowledge of tropical cyclones and over a century of its own experience of dealing with them. It also gives suggested mitigation actions that can be taken to minimize loss of life and property in the face of an approaching cyclone.

Table 2.4.6.1 Impact of Cyclonic Storms and Suggested Mitigation Actions

---

Category: Deep Depression
T.No.: T 2.0
Wind Speed: 28 – 33 Knots (52 – 61 Kmph)

Structures: Minor damage to loose/unsecured structures.
Road/Rail: Some breaches in kutcha road due to flooding.
Communications: Minor
Agriculture: Minor damage to banana trees and near-coastal agriculture due to salt spray. Damage to ripe paddy crops.
Marine Interests: Very rough seas. Sea waves about 4-6 m high.
Coastal Zone: Minor damage to kutcha embankments.
Overall Damage Category: Minor
Suggested Actions: Fishermen advised not to venture into sea.

Category: Cyclonic Storm
T.No.: T 2.5-T3.0
Wind Speed: 34 –47 Knots (62 –87 Kmph)

Structures: Damage to thatched huts.
Road/Rail: Major damage to kutcha and minor damage to pucca roads.

Communications: Minor damage to power and communication lines due to breaking of tree branches.
Agriculture: Some damage to paddy crops, banana, papaya trees and orchards.
Marine Interests: High to very high sea waves about 6 – 9 m high.
Coastal Zone: Sea water inundation in low lying areas after erosion of kutcha embankments.
Overall Damage Category: Minor to Moderate
Suggested Actions: Fishermen advised not to venture into sea.

Category: Severe Cyclonic Storm
T.No.: T3.5
Wind Speed: 48 –63 Knots (88 –117Kmph)

Structures: Major damage to thatched houses/huts. Roof tops may blow off. Unattached metal sheets may fly.
Road/Rail: Major damage to kutcha and some damage to pucca roads. Flooding of escape routes.
Communications: Minor damage to power and communication lines.
Agriculture: Breaking of tree branches, uprooting of large avenue trees. Moderate damage to banana and papaya trees. Large dead limbs blown from trees.
Marine Interests: Phenomenal seas with wave height 9-14 m. Movement in motor boats unsafe.
Coastal Zone: Major damage to coastal crops. Storm surge upto 1.5m (area-specific) causing damage to embankments/salt pans. Inundation upto 5 Km in specific areas.
Overall Damage Category: Moderate
Suggested Actions: Fishermen advised not to venture into sea. Coastal hutment dwellers advised to move to safer places. Other people in the affected areas to remain indoors.

Category: Very Severe Cyclonic Storm
T.No.: T4.0-T4.5
Wind Speed: 64 –90 Knots (118 –167Kmph)

Structures: Total destruction of thatched houses/ extensive damage to kutcha houses. Some damage to pucca houses. Potential threat from flying objects.
Road/Rail: Major damage to kutcha and pucca roads. Flooding of escape routes. Minor disruption of railways, overhead power lines and signalling systems.
Communications: Bending/ uprooting of power and communication poles.

Agriculture: Widespread damage to standing crops, plantations, orchards, falling of green coconuts and tearing of palm fronds. Blowing down of bushy trees like mango.
Marine Interests: Phenomenal seas with wave heights more than 14m. Visibility severely affected. Movement in motor boats and small ships unsafe.
Coastal Zone: Storm surge upto 2 m. Inundation upto 10 Km in specific areas. Small boats, country crafts may get detached from moorings.
Overall Damage Category: Large
Suggested Actions: Fishermen not to venture into sea. Evacuation from coastal areas needs to be mobilized. People advised to remain indoors. Judicious regulation of rail and road traffic needed.

Category: Very Severe Cyclonic Storm
T.No.: T5.0-T6.0
Wind Speed: 91 – 119 Knots (168 –221 Kmph)

Structures: Extensive damage to all types of kutcha houses, some damage to old badly managed pucca structures. Potential threat from flying objects.
Road/Rail: Disruption of rail/road link at several places.
Communications: Extensive uprooting of communication and power poles.
Agriculture: Extensive damage to standing crops, plantations, orchards. Blowing down of palm and coconut trees. Uprooting of large bushy trees.
Marine Interests: Phenomenal seas with wave heights of more than 14 m. Movement in motor boats and small ships not advisable.
Coastal Zone: Storm surge of 2 – 5 m. Inundation may extend upto 10-15 Km over specific areas. Large boats and ships may get torn from their moorings.
Overall Damage Category: Extensive
Suggested Actions: Fishermen not to venture into sea. Evacuation from coastal areas essential. Diversion / suspension of rail traffic may be required.

Category: Super Cyclonic Storm
T.No.: T6.5 and above
Wind Speed: 120 Knots and above (222 Kmph and above)

Structures: Extensive damage to non-concrete residential and industrial buildings. Structural damage to concrete structures. Air full of large projectiles
Road/Rail: Extensive damage to kutcha roads and some damage to poorly repaired pucca roads. Large scale submerging of coastal roads due to

flooding and sea water inundation. Total disruption of railway and road traffic due to major damages to bridges, signals and railway tracks. Washing away of rail/road links at several places.
Communications: Uprooting of communication and power poles. Total disruption of communications and power supply.
Agriculture: Total destruction of standing crops/ orchards, uprooting of large trees and blowing away of palm and coconut crowns, stripping of tree barks.
Marine Interests: Phenomenal seas with wave heights of more than 14 m. All shipping activity unsafe.
Coastal Zone: Extensive damage to port installations. Storm surge more than 5m. Inundation upto 40 km in specific areas and extensive beach erosion. All ships torn from their moorings. Flooding of escape routes.
Overall Damage Category: Catastrophic
Suggested Actions: Fishermen not to venture into sea. Large scale evacuations needed. Total stoppage of rail and road traffic needed in vulnerable areas.

(Source: IMD http://www.imd.ernet.in, http://www.imd.gov.in/)

2.4.7 Cyclones in the Southern Hemisphere

Much fewer tropical cyclones develop in the southern Indian and Pacific oceans compared to the ocean basins in the northern tropics (Table 2.4.2.1). The southern Atlantic Ocean basin does not even find a mention in global statistics of tropical cyclones.

On 28 March 2004, a rare tropical cyclone in the South Atlantic Ocean crossed the coast of Santa Catarina and Rio Grande do Sul, in the extreme southern parts of Brazil. This was a Category 1 hurricane with central winds of 125 km/hr, making it the first hurricane in the South Atlantic in recorded history.

Southern hemisphere cyclones have not been studied with as much interest as northern hemispheric cyclones, probably because many of them dissipate over the ocean and do not cause great destruction over land. Structurally speaking, tropical cyclones of both northern and southern hemispheres are in no ways different, but the characteristic feature so obvious in satellite images is the clockwise rotation of southern hemispheric cyclones compared with the anticlockwise rotation of northern hemisphere cyclones

(Figure 2.4.7.1.1). This is the effect of the Coriolis force, which is associated with the rotation of the earth and causes the wind to deflect to the right in the northern hemisphere and to the left in the southern hemisphere.

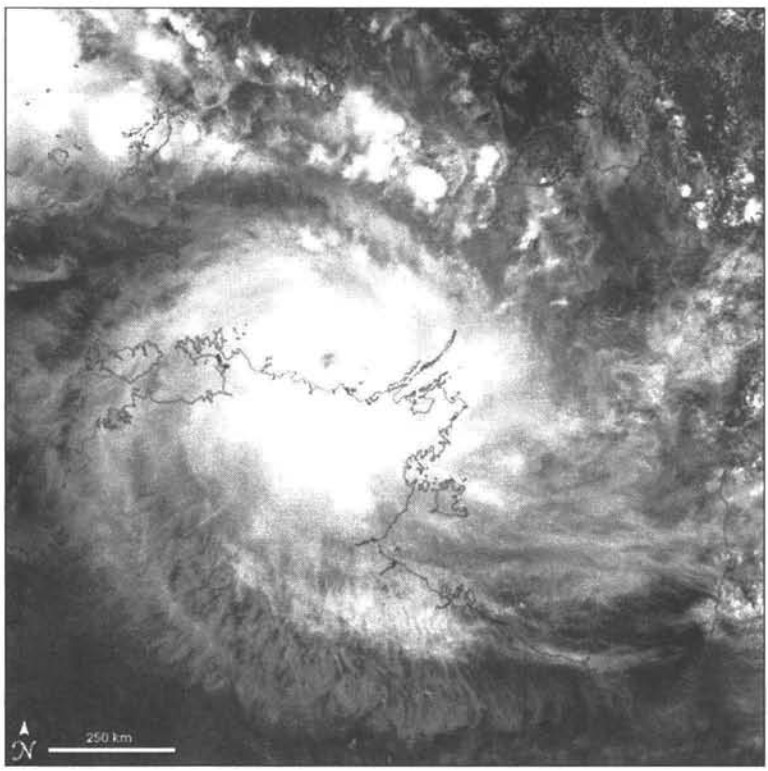

Figure 2.4.7.1.1 Tropical Cyclone Monica in the Southern Hemisphere (Source: http://earthobservatory.nasa.gov/Newsroom/NewImages/)

2.4.7.1 Tropical Cyclone Monica

Tropical Cyclone Monica formed off the northeastern coast of Australia on 17 April 2006. On 20 April, the storm had crossed Cape York Peninsula with weak winds, but it later gathered size and power in the Gulf of Carpentaria and reorganised into a Category 5 storm. Monica grazed across the top of the Northern Territory of Australia, threatening the city of Darwin with heavy rains and very high winds.

The MODIS image of the cyclone acquired by the Aqua satellite on 24 April 2006 (Figure 2.4.7.1.1) shows Cyclone Monica as an impressively large and powerful storm of Category 5. Sustained peak winds in the storm system

were 285 km/hr, and gusts reached as high as 350 km/hr. The eye of the storm appears like a deep whirlpool hovering just off the Australian coastline.

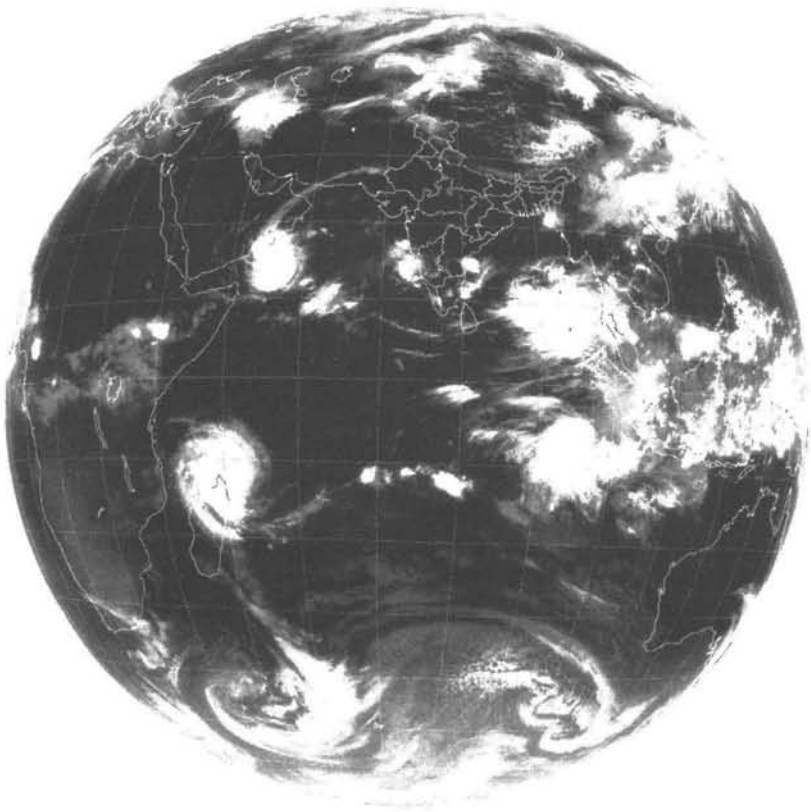

Figure 2.4.7.2.1 INSAT-1D IR image of 9 May 2002 showing cyclone pairs on either side of the equator (Source: IMD)

2.4.7.2 Cyclone Pairs

Full-disc geostationary satellite images quite often show the presence of two cyclonic vortices on either side of the equator at the same longitude. Particularly, when cyclones form over the Bay of Bengal and Arabian Sea, cyclonic storms are seen to develop in the manner of a mirror image on the same longitude in the southern hemisphere.

An interesting situation prevailed in early May 2002 when there was a strong westerly wind burst along the equator in the western Indian Ocean. The westerly wind burst, which is associated with the development of a large

cluster of deep convective clouds along the equator, led to the formation of tropical cyclone twins, on either side of the equator, one over the Arabian Sea and another (Kesiny) in the southern Indian Ocean (Figure 2.4.7.2.1). This area of strong westerlies and convective activity propagated further eastwards as the Madden-Julian Oscillation (MJO) and later spawned another cyclone pair, one in the Bay of Bengal and the other (Errol) in the southern Indian Ocean at the same longitude. Over the next two weeks, the MJO activity continued eastwards into the Pacific Ocean, where super-typhoon Hagibis and hurricane Alma made a third cyclonic pair. Interestingly, Figure 2.4.7.2.1 also shows the formations of extra-tropical low pressure systems in both the hemispheres at the same longitudes as the tropical storms.

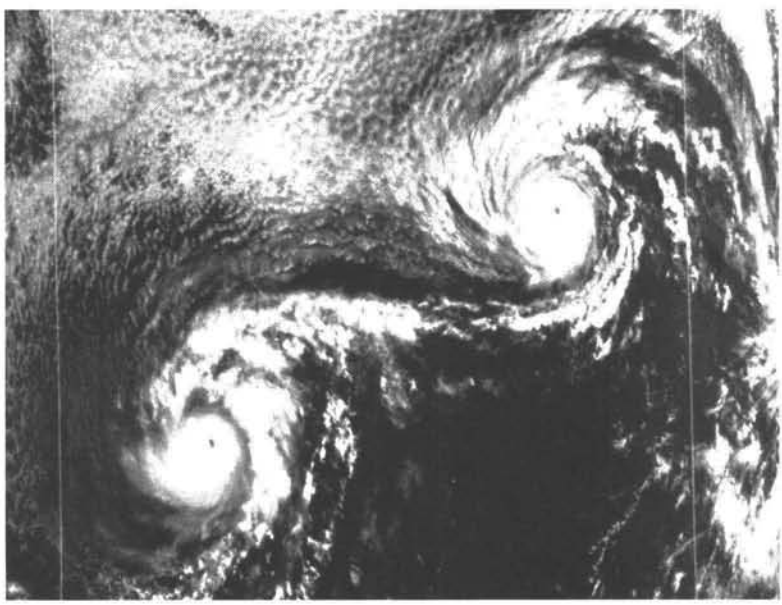

Figure 2.4.7.2.2 NOAA-3 VHRR image 24 August 1974 showing Fujiwhara effect in two interacting hurricanes
(Source: http://www.photolib.noaa.gov/space/spac0280.htm)

There is another type of cyclone pairs that are located on the same side of the equator and not on either side of it (Figure 2.4.7.2.2). When two such cyclones approach each other, their centres begin to rotate in an anticlockwise manner about a virtual point lying somewhere between them. The two cyclones tend to come closer and spiral into this point, and may even get merged into a single vortex. If one of the vortices is stronger than the other, it will tend to dominate the interaction, and the weaker vortex will

orbit around it. This type of interaction is called as the Fujiwhara effect, after the scientist who first described it in 1921 but in a different context.

2.5 Winter Systems over India

In the northern hemispheric winter season, low pressure systems originate over the Mediterranean Sea at frequent intervals and travel across Iran, Afghanistan and Pakistan into extreme northwest India. Because they enter India from the west, these migratory systems are referred as western disturbances or western depressions (WDs), depending upon their intensity. Forecasting the approach of WDs is important, as they bring the much-needed winter precipitation over north and northwest India after the southwest monsoon has withdrawn. The stronger WDs also bring in snowfall in the higher mountain regions of Jammu and Kashmir, Himachal Pradesh and Uttaranchal, and trigger cold waves that penetrate into central and more southern parts of India. Because of the lack of data and the shallowness of the disturbances, WDs may not always show up clearly in synoptic weather charts except in the case of stronger systems. Satellite cloud imageries therefore are a valuable source of information on the origin and movement of western disturbances.

Bhaskara Rao et al (1971) and Agnihotri et al (1982) have studied the approach of WDs into northwest India with the help of satellite cloud pictures. The cloud patterns associated with WDs can be categorized into four broad types: (a) Systems that develop into extra-tropical depressions have an organised clouding with a banded structure and vortex. (b) Broad shallow troughs in the westerlies show up as latitudinal bands which extend in a WSW-ENE direction from central Arabia to India and slowly progress eastwards. They form in association with long waves in the upper tropospheric westerlies or jet streams and some of them may even extend from eastern Sahara to Kashmir. (c) On rare occasions, meridional cloud bands may be seen, but their movement is erratic and they dissipate on encountering mountain barriers. (d) All other weaker disturbances are seen as broken amorphous or overcast cloud masses approaching from the west. These cloud masses can be detected in the region 25-35 °N and 40-55 °E from where they move eastwards at an approximate rate of 10° longitude per day. Figures 2.5.1, 2.5.2 and 2.3.7.1 show how the cloud patterns of types (a), (b) and (c) appear in satellite images.

Winter-time fog is common over northern India, particularly in the wake of a western disturbance that has moved away, and can be seen in VIS satellite images as an extensive white patch with its northern boundary at the foothills of the Himalayas (Figure 2.5.3).

Several interesting case studies of individual western disturbances based upon satellite pictures are found in the literature. Sharma et al (1983) have discussed the linkage of a WD with a low in the Arabian Sea lower tropospheric easterlies off the west coast of India, explaining the occurrence of precipitation far to the south.

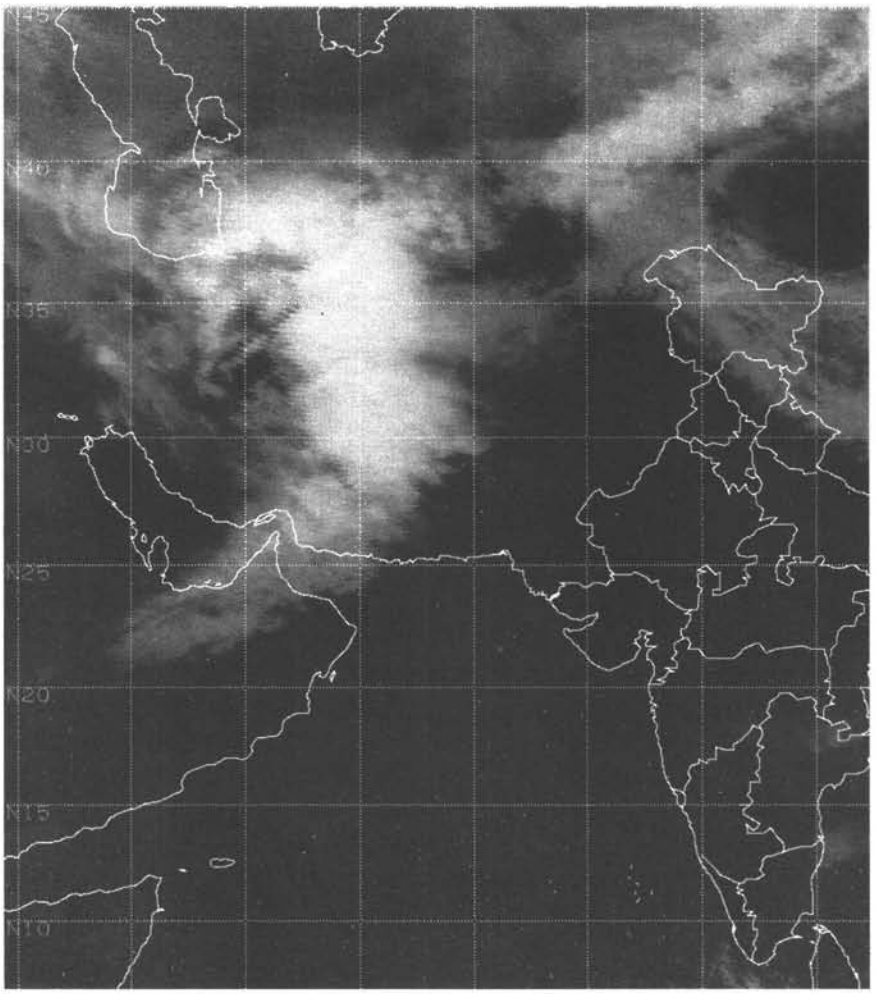

Figure 2.5.1 INSAT-3A IR image of 27 January 2004 showing comma-shaped cloud and vortex associated with an intense western disturbance approaching north India (Source: IMD)

Veeraraghavan et al (1989) studied an active WD that occurred in the month of November and produced widespread precipitation. They also attempted to

correlate the satellite-observed cloud top temperatures with the distribution of precipitation produced by the WD.

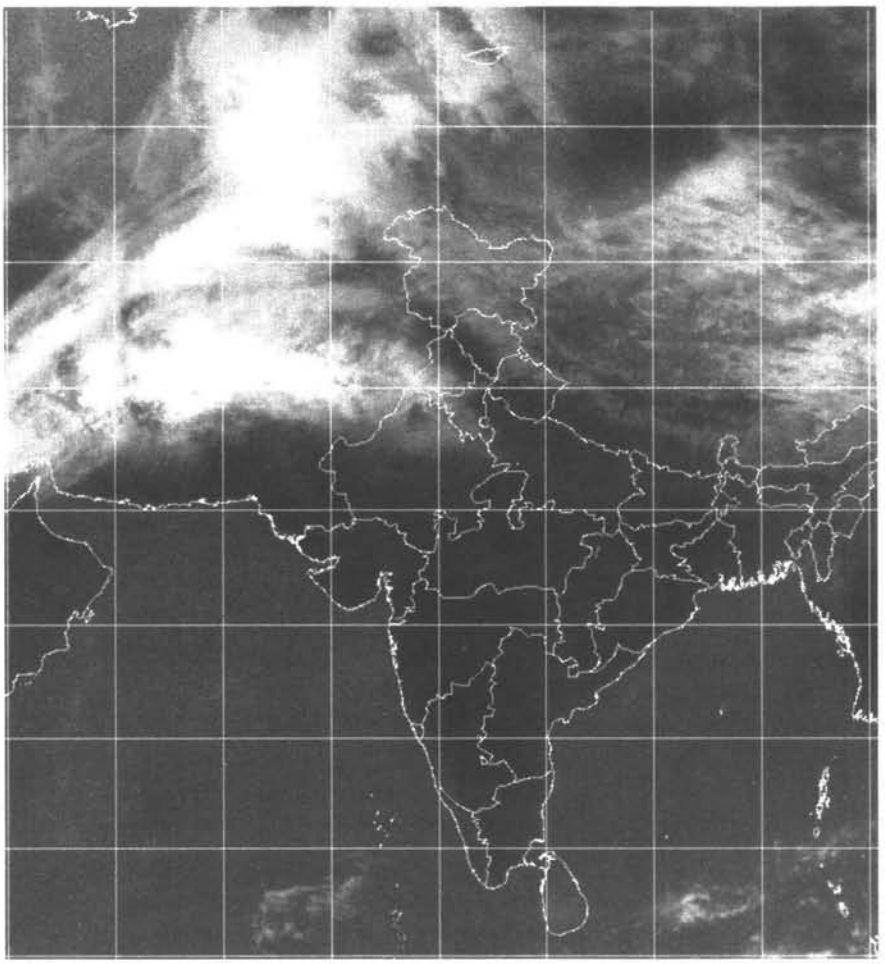

Figure 2.5.2 Kalpana-1 IR image of 17 February 2006 showing latitudinal bands associated with a western disturbance over north India and adjoining region (Source: IMD)

During the winter months, satellite imagery may show extensive formations of high and medium clouds over large parts of north and central India in association with the sub-tropical jet stream (Srinivasan 1971). These clouds are organized into longitudinal bands when the lapse rate is high and wind shear is small, or into transverse bands when the lapse rate is small and there is large wind shear. The clouds are not found on all the days but only when large amplitude troughs are present and moisture advection can occur.

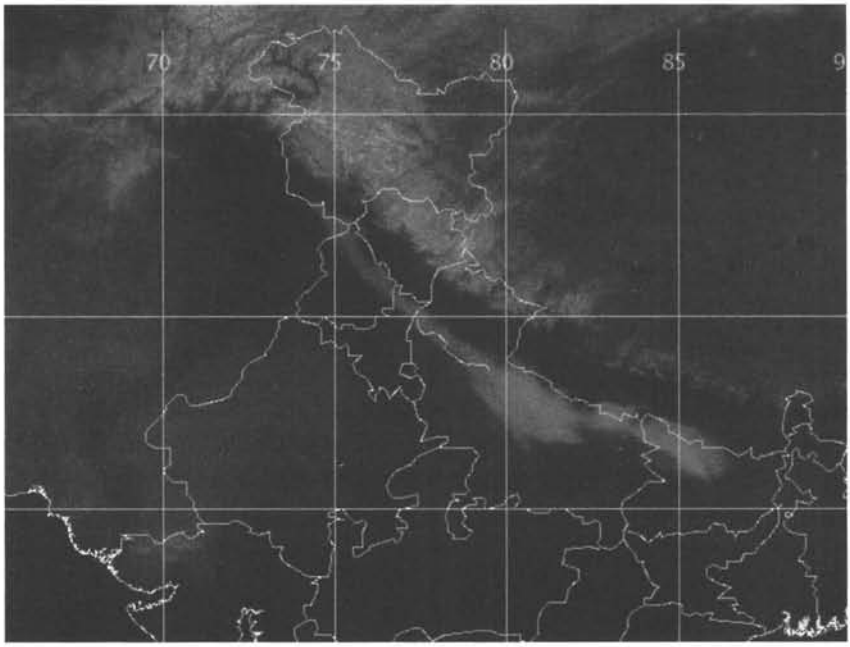

Figure 2.5.3 Kalpana-1 VIS image of 5 January 2006 showing Himalayan snow cover and extensive morning fog over the plains of northern India south of the Himalayan foothills (Source: IMD)

2.6 Extra-tropical Weather

The weather patterns that prevail over the tropical and extra-tropical regions of the globe have significant differences. The main reason is that the quasi-geostrophic approximation which works on the synoptic scale in the extra-tropics does not hold good in the tropics. This means that in the extra-tropical regions, the wind field quickly adjusts itself to the pressure field and can therefore be inferred from it, but this is not so in the tropics where independent analyses of wind and pressure have to be carried out.

Another distinguishing factor is that extra-tropical regions have very strong meridional temperature gradients, resulting in the existence of different kinds of air masses separated by frontal surfaces. The pressure gradients are also steep and there are significant 24 hr changes in the surface pressure. Extra-tropical cyclones keep developing throughout the year as against the preferred seasons of tropical cyclones. The air masses and fronts migrate in an orderly manner and can be tracked on synoptic weather charts and satellite cloud imagery.

2.6.1 Air Masses

An air mass is an extensive body of air that has uniform temperature and moisture properties throughout it in a horizontal plane. Air masses have a source region associated with them, where they acquire their properties. The best source regions for air masses are large flat areas where air can be stagnant long enough to take on the characteristics of the surface below. Large snow-covered polar areas, deserts and tropical oceans, all serve as source regions of air masses. The two most conservative properties of air masses which serve to trace their origin, movement and modification, are the dew point temperature at the surface and the wet bulb potential temperature in the free atmosphere.

Air masses can be classified in several ways. The primary division is with respect to their geographical source region: Arctic (A), Polar (P) or Tropical (T). There is a further sub-division according to the nature of the source region: maritime (m) or continental (c). The resulting combinations are: continental Arctic (cA), continental Polar (cP), continental Tropical (cT), maritime Arctic (mA), maritime Polar (mP) and maritime Tropical (mT). However, cA, cP, mP and mT type of air masses are more predominant than the others.

As air masses move from one region to another they may undergo modifications or acquire additional attributes. Air masses of cA and cP type originate in polar anticyclones, while those of cT and mT originate in subtropical anticyclones. As air masses of the type cA and cP move over oceanic areas, they pick up moisture from the ocean and get modified into become maritime air masses mA and mP. If a polar air mass mP moves southward, say from Canada into the southern U. S., it will get warmed over the ground, but it will still remain very dry and get modified into a continental polar air mass cP. The U. S. Gulf Coast region commonly has a tropical air mass in summer. If a dry continental tropical air mass cT moves and stagnates over the mid-western U. S., drought conditions may develop. Maritime tropical air masses mT have their origin in the tropical and subtropical oceans, but move northward transporting heat and moisture. In contrast, continental polar air masses cP originate over the northern plains, and move southward carrying colder and drier air with them.

2.6.2 Cold, Warm, Stationary and Occluded Fronts

As per its traditional definition, a front is a sharp transition zone between two air masses of different density, temperature and humidity conditions. The warm air boundary of the maximum temperature gradient is considered as the

actual frontal surface. As fronts extend in horizontal as well as vertical directions, the frontal surface has both horizontal and vertical components. Fronts are named after the type of air mass that is replacing the other. The most commonly observed fronts are the continental Arctic front, maritime Arctic front and the Polar front, separating the cA-mA, mA-mP and mP-mT air masses respectively.

Fronts can be classified into four types: (a) A cold front is a front that demarcates the leading edge of a cold air mass displacing a warmer air mass. (b) A warm front is the leading edge of a warm air mass displacing a cold air mass. (c) A stationary front is one in which the air masses are not in motion. If such a front begins to move again, it will once again be called a cold or warm front as the case may be. A noticeable temperature change or shift in wind direction is commonly observed across a stationary front. Cold fronts typically move faster than warm fronts, so they eventually catch up with warm fronts. (d) An occluded front forms when the two fronts get merged. The cold air undercuts the cooler air mass associated with the warm front, further lifting the already rising warm air.

Fronts can be detected on surface weather charts in many ways. Winds usually converge at the fronts and there are noticeable differences in temperature and pressure on either side of a front. However, fronts extend to higher atmospheric levels as well and they have a vertical structure and slope. Warm fronts typically have a gentle slope, so the air rises gradually along the frontal surface. This usually favours the development of widespread layered or stratiform cloudiness and precipitation along and to the north of the front. Cold fronts have a steeper slope and air is forced upward more abruptly. This usually leads to a narrow band of showers and thunderstorms along or just ahead of the front, especially if the rising air is unstable.

A dry line is a boundary that separates a moist air mass from a dry air mass. It is also called a dew point front, as sharp changes in dew point temperature can be observed across a dry line.

Frontal clouds are a combination of various cloud types such as Cb, Ns, As and Ci. Active frontal zones appear in both VIS and IR satellite imagery as long, multilayered cloud bands extending across thousands of kilometres and having a width of up to a few hundred kilometres depending on their intensity. There are apparent differences in the cloud patterns on both sides of the front.

An active cold front can be easily located in a satellite picture as it lies along the outer segment of the spiral band which forms a cloud vortex. The band

narrows down away from the vortex. Cold fronts that are less active, have isolated Cb clouds and appear as narrow, fragmented cloud bands, which look bright in VIS but gray in IR images.

Warm front clouds come in different sizes and patterns and a warm front can be clearly identified in satellite images only in the initial stages of vortex development.

In VIS imagery, an occluded front appears as a wide spiral band of bright clouds with a sharp inner boundary. The leading edge of the cloud spiral is more diffuse or ragged. In IR imagery, however, the brightness reduces towards the centre of the cloud spiral where the clouds do not develop to great heights.

The cloud band associated with a stationary front is only 200-300 km in width and it does not exhibit any curvature. The cloud mass has an irregular shape and broken boundaries in both VIS and IR imageries.

2.6.3 Mid-latitude Cyclones

A cyclone, whether in the tropics or in the extra-tropics, is an area of low pressure around which the winds flow counterclockwise in the Northern Hemisphere and clockwise in the Southern Hemisphere. However, the characteristics of mid-latitude cyclones are significantly different from those of a tropical cyclone that we saw in the preceding sections.

A mid-latitude cyclone in its developing stage is typically accompanied by a warm front pushing northward and a cold front pulling southward, marking the leading edges of air masses coiling around a centre of low pressure, or the centre of the cyclone. The counterclockwise winds around the low pressure area transport warm moist air to its north and cold, dry air to its south. In satellite images, mature mid-latitude cyclones are easily identifiable by the characteristic comma-shaped configuration of the cloud bands associated with them. However, satellite images show four different stages in their life cycle:

(a) Leaf stage: During the initial development of a mid-latitude cyclone, the satellite cloud pattern takes the shape of a leaf because of the jet stream pushing into the western edge of the cloud system and spreading the cloud downwind. The highest cloud tops are over the eastern portion of the leaf and middle-level clouds are over the westward portion. The western edge of the leaf is well-defined.

(b) Open comma stage: A comma-shaped cloud pattern appears in satellite images when the mid-latitude cyclone has well-developed warm and cold fronts. This is a sign of falling surface pressure. The back edge of the comma cloud represents the position of the cold front where the clouds and thunderstorms form because of the frontal lifting. The front edge of the comma cloud pattern is more diffuse as upper level winds make the clouds to spread out.

(c) Occluded stage: As the occlusion forms, the low-pressure circulation separates from the jet stream and the central pressure stops falling. The point at which the occluded, cold and warm fronts come together is referred to as the triple point, and it is often seen in satellite imagery where the jet stream cuts across the system. The cloud pattern is still in the shape of a comma, and the clouds spiral around the centre of the storm located in the comma head (Figure 2.6.3.1).

(d) Dissipating stage: As the storm weakens, upper level winds tend to destroy it. The cloud system loses its organised pattern and the comma head gets cut off from the tail, creating cut-off lows that may persist for a long time.

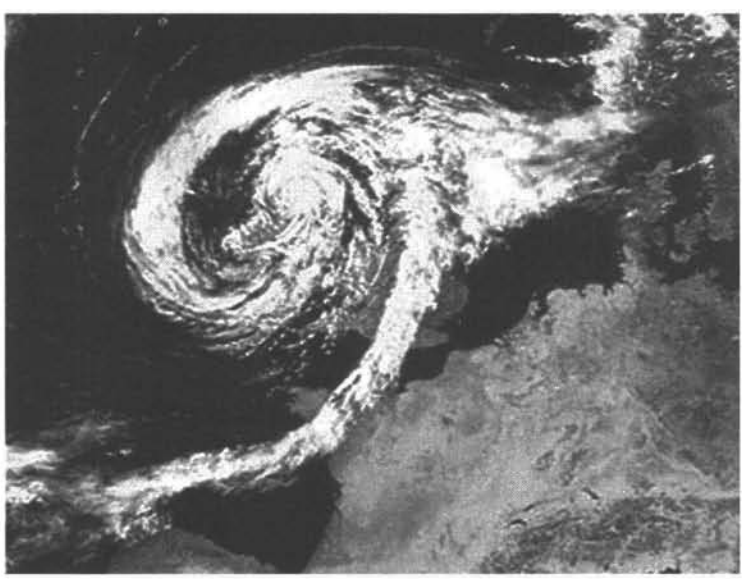

Figure 2.6.3.1 Satellite image showing a mature mid-latitude cyclone (Source: http://rst.gsfc.nasa.gov/)

2.6.4 Sub-tropical Jet Stream

A jet stream in the atmosphere is defined as a strong narrow current 1000 km long, 100 km wide and 1 km deep with wind speed greater than 60 knots concentrated along a quasi-horizontal axis. It has wind shears of the order of 10-20 knots/km in the vertical and 10 knots/km in the horizontal direction, featuring one or two vorticity maxima (Berggren et al 1958).

Five types of jet streams are observed commonly in the atmosphere: (a) the polar night stratospheric westerly jet streams, (b) QBO jet in the lower equatorial stratosphere, (c) polar front westerly jet stream, (d) sub-tropical westerly jet stream, (d) tropical easterly jet stream, and (e) low level jet stream.

In a non-rotating earth, the warm air rising at the equator will move poleward on both sides. Because of the earth's rotation, the air moving poleward conserves its eastward momentum. The regions around 30° N/S and 50-60° N/S are areas of the highest temperature gradients and also therefore the regions of formation of the polar jet stream and the subtropical westerly jet stream.

The sub-tropical westerly jet stream is generally found at 30 °N latitude at 200 hPa or 12 km height, but it fluctuates widely in its position and is most intense in winter when the air masses have a stronger surface temperature contrast.

The sub-tropical jet stream is almost a permanent feature of the 300 and 200 hPa level Indian synoptic charts in the winter months of December to February, its mean location being along 27°N at 12 km height and the mean wind being 100 knots. However, winds as high as 150 and 200 knots may be observed in the jet core and there as instances of the jet stream migrating to a far lower latitude (Joseph 1967).

In IR satellite images, the location of the sub-tropical jet can be identified from the cirrus clouding which predominates on its equatorial side and has a sharp poleward boundary. The cirrus may take various shapes and sizes such as large shields associated with large amplitude troughs, long bands, narrow streaks along the jet axis or transverse bands due to shear.

Satellite images commonly show large masses of cirriform clouds originating in the tropics or the ITCZ and extending poleward. These clouds are usually situated to the south of the wind maximum and represent the meridional transport of momentum and high level moisture from the tropical region.

2.7 Interaction between Tropical and Mid-latitude Systems

The sub-tropical highs insulate the easterly flows in the tropics from the westerly flow of the middle latitudes. However, extra-tropical migratory systems sometimes induce the formation of cold lows in the tropical latitudes to their south. There are occasions when large amplitude troughs develop in the westerlies and extend into the tropical latitudes, which manifest themselves in satellite imageries as long bands surging northeastwards from the tropics. Such an interaction between the tropical and mid-latitude weather systems (abbreviated hereafter as ITML) can occur in many different synoptic settings throughout the year. ITML can lead to an intensification of weather disturbances in winter, outbreak of convection in the pre-monsoon season, oscillations of the monsoon trough and deformation of circulations including cyclonic storms

Kalsi et al (1992) have shown examples of how satellite imagery provides a means of monitoring ITML in relation to these developments, particularly where the short waves cannot be resolved in conventional weather analysis. In the case of an ITML during a western disturbance, an extension of low level warm and moist easterly flow extends to northwest India and Pakistan, where it meets the mid-latitude cold and dry westerly flow. Though the temperature contrast between the two flows may not be significant, the humidity contrast could be striking. A baroclinic leaf pattern associated with a surface trough of low pressure can be seen in satellite imagery.

In the case of an ITML in the pre-monsoon season, the presence of a westerly trough is noticed by the bands of medium and high clouds forming ahead of it. As it meets the low level southeasterlies over central India, the short waves induce a sub-tropical cyclogenesis over Pakistan which can be seen as comma cloud system. Such an interaction can cause a lot of precipitation over India, mostly in association with thunderstorms.

During the monsoon season, ITML can produce different effects like causing intensification of low level lows or troughs, enhancing rainfall in pre-existing systems, causing recurvature of depressions and lows and even causing a break in the monsoon. It can disturb the orientation of the monsoon trough and alter the regions of heavy precipitation.

Although there have been many cases of tropical cyclones having been sheared off by mid-latitude westerlies, Kalsi et al (1992) have given an example of a marginal cyclone in the Bay of Bengal in October 1988 that got

deformed northeastwards as a result of ITML. They have also given a case of abnormally rapid movement of a tropical vortex in the Bay in November 1988 on account of another vortex to its north and its intensification after a merger with it.

2.8 References

Agnihotri C. L. and Singh M. S., 1982, "Satellite study of western disturbances", *Mausam*, 33, 249-254.

Ananthakrishnan R. and Soman M. K., 1988, "The onset of the south-west monsoon over Kerala 1901-1980", *J. Climatology*, 8, 283-296.

Asnani G. C., 2005a, "ITCZ (Inter-Tropical Convergence Zone)", *Tropical Meteorology*, Vol. 1, Chapter 2, 126-144.

Asnani G. C., 2005b, "Subsidence over equator", *Tropical Meteorology*, Vol. 2, Chapter 5, 42-68.

Asnani G. C., 2005c, "Special features of tropics, monsoons", *Tropical Meteorology*, Vol. 1, Chapter 1, 16-37.

Berggren R., Gibbs W. J. and Newton C. W., 1958, "Observational characteristics of the jet stream – a survey of the literature", *WMO Tech. Note No. 19.*

Bhagat D. K. U. R., 2005, "Balance of kinetic energy in the field of mid-tropospheric cyclone", *Mausam*, 56, 473-500.

Bhan S. K., Paul S. and Kharbanda K. L., 2004, "Cloudbursts in Himachal Pradesh", *Mausam*, 55, 712-713.

Bhaskara Rao N. S. and Moray P. E., 1971, "Cloud systems associated with western disturbances: A preliminary study", *Indian J. Meteor. Geophys.*, 22, 413-420.

Bunker A. F., 1965, "Interaction of the summer monsoon air with the Arabian Sea", *Proc. Symp. Meteorological Results of the IIOE,* WMO, Geneva, 3-16.

Chowdhury A. and Gaikwad S. D., 1983, "On some characteristic features of rainfall associated with monsoon depression over India", *Mausam*, 34, 33-42.

Chowdhury A., Urankar P. S. and Upadhye C. U., 1985, "Cloud characteristics of monsoon depressions as viewed by meteorological satellites", *Mausam*, 36, 491-498.

De U. S., 1970, "Lee waves as evidenced by satellite cloud pictures", *Indian J. Meteor. Geophys.*, 21, 637-642.

De U. S., 1970, "Mountain waves over northeast India and neighbouring regions", *Indian J. Meteor. Geophys.*, 22, 361-364.

De U. S. and Mukhopadhaya R. K., 2002, "Breaks in monsoon and related precursors", *Mausam*, 53, 309-318.

Dvorak V. F., 1975, "Tropical cyclone intensity analysis and forecasting from satellite imagery", *Mon. Wea. Rev.*, 103, 420-430.

Dvorak V. F., 1984, "Tropical cyclone intensity analysis using satellite data", *NOAA Tech. Rep. NESDIS 11,* 47 pp.

Dvorak V. F. and Mogil H. M., 1992, "Tropical cyclone motion forecasting using satellite water vapor imagery", *NOAA Tech. Rep., NESDIS 83.*

Fassulo J. and Webster P. J., 2003, "A hydrological definition of Indian monsoon onset and withdrawal", *J. Climate*, 16, 3200-3211.

Fett R. W., 1964, "Aspects of hurricane structure and new model considerations suggested by TIROS and Project Mercury observations", *Mon. Wea. Rev.,* 92, 43-60.

Findlater J., 1966, "Cross-equatorial jet streams at low level over Kenya", Meteor. Mag., 95, 353-364.

Findlater J., 1969, "A major low-level air current near the Indian Ocean during the northern summer," *Quart. J. Royal Meteor. Soc.,* 95, 362-380.

Findlater J., 1974, "An extreme wind speed in the low level jet stream of western Indian Ocean", *Meteor. Mag.*, 103, 201-205.

Gadgil S. and Joseph P. V., 2003, "On breaks of the Indian monsoon", *Proc. Indian Acad. Sci. (Earth Planet. Sct.)*, 112, 529-558.

Golder R. N., Banerjee S. K. and Debnath G. C., 2001, "Tornado in India and neighbourhood", *Pre-published Sci. Rep. No. 2/2001*, RMC Kolkata, India Met. Dept.

Gupta G. R. and Onkari Prasad, 1991, "Activity of southern Indian Ocean convergence zone as seen in satellite cloud data during pre-monsoon months", *Mausam*, 42, 145-150.

Gupta H. N. and Ghosh S. K., 1980, "North Delhi tornado of 17 March 1978", *Mausam*, 31, 93-100.

Gupta H. N. and Ghosh S. K., 1982, "Reported cases of tornadoes in Indian sub-continent", *Vayu Mandal*, 12, 57-60.

Grossman R. L. and Friehe C. A., 1986, "Vertical structure of the southwest monsoon low-level jet over the central and eastern Arabian Sea", *J. Atm. Sci.*, 43, 3266-3272.

Jenamani R. K., 2004, "Distinct synoptic patterns associated with pre-break onset phase and revival of normal monsoon phase", *Mausam*, 55, 591-598.

Joseph P. V., 1967, "A case of very low latitude occurrence of the subtropical jet stream over the India region", *Indian J. Meteor. Geophys.*, 18, 217-226.

Joseph P. V., Raipal D. K. and Deka S. N., 1980, " 'Andhi', the convective duststorm of northwest India", *Mausam*, 31, 431-442.

Joseph P. V., 1982, "A tentative model of *Andhi*", *Mausam*, 33, 417-422.

Joseph P. V., 1990, "Monsoon variability in relation to equatorial trough activity over Indian and west Pacific Oceans", *Mausam,* 41, 291-296.

Joseph P. V., Fishchild J. K. and Pile R., 1994, "Interannual variability of onset of Indian summer monsoon and its association with atmospheric features, El Nino and sea surface temperature anomalies", *J. Climate*, 7, 81-105.

Joseph P. V. Sooraj K. P. and Rajan C. K., 2003, "Conditions leading to monsoon onset over Kerala and the associated Hadley cell", *Mausam*, 54, 155-164.

Joseph P. V. and Sijikumar S., 2004, "Intraseasonal variability of the low-level jet stream of the Asian summer monsoon", *J. Climate*, 17, 1449-1458.

Joseph P. V., 2006, "SW monsoon convective clouds along the west coast of India associated with the low level jet stream", *National Workshop on Cloud Physics, CESS, Thiruvananthapuram*, 24-25 March 2006.

Joseph P. V., Sooraj K. P. and Rajan C. K., 2006, "The summer monsoon onset process over south Asia and an objective method for the date of monsoon onset over Kerala", *Int. J. Climatol.*, 26.

Joshi P. C. and Simon B., 1994, "NOAA/TOVS derived upper tropospheric temperature changes associated with the onset of southwest monsoon over Kerala coast", *Mausam*, 45, 155-160.

Kalsi S. R. and Halder S. R., 1992, "Satellite observations of interaction between tropics and mid-latitudes", *Mausam*, 43, 59-64.

Kalsi S. R., 1993, "INSAT image analysis of tropical cyclone development in the Bay of Bengal", *Advances in Tropical Meteorology (Ed. Keshavamurty R. N. and Joshi P. C.),* Tata McGraw Hill, 289-300.

Kalsi S. R., 2002, "Use of satellite imagery for tropical cyclone intensity analysis and forecasting", *Met. Monograph, Cyclone Warning Div., No. 1/2002, India Meteor. Dep.*, 83 pp.

Kalsi S. R., 2006, "Orissa supercyclone – a synopsis", *Mausam*, 57, 1-20.

Karmakar S. and Mahbub Alam Md., 2005, "On the sensible heat energy, latent heat energy and potential energy of the troposphere over Dhaka before the occurrence of nor'westers in Bangladesh during the pre-monsoon season", *Mausam*, 56, 671-680.

Kelkar R. R., 1997, "Satellite-based monitoring and prediction of tropical cyclone intensity and movement", *Mausam*, 48, 157-168.

Khole M. and De U. S., 2003, "A study of north-east monsoon rainfall over India", *Mausam*, 54, 419-426.

Khole M. and De U. S., 2004, "Association between the monsoon onset over Kerala (MOK) and sea surface temperature (SST) over north Indian Ocean", *Mausam*, 55, 495-496.

Koteswaram P., 1958, "The Asian summer monsoon and the general circulation over the tropics", Proc. *Symp. Monsoons of the World, New Delhi, 19-21 February 1958*, 105-110.

Krishnamurti T. N. and R. S. Hawkins, 1970, "Mid-tropospheric cyclones of southwest monsoon", *J. Appl. Meteor.*, 9, 442-458.

Krishnamurti T. N., Ardanuy P., Ramanathan Y. and Pasch R., 1984, "On the onset vortex of the summer monsoon", *Mon. Wea. Rev.*, 109, 34-363.

Kulshrestha S. M., 1971, "A satellite study of the Orissa cyclonic storm of October 1967", *Indian J. Meteor. Geophys.*, 22, 313-316.

Loe B. R., Giri R. K., Verna B. L., Bali S. and Sen Roy S., 2006, "Comparative analysis of subjective/advanced objective technique of tropical cyclone intensity estimation", *Mausam*, 57, 159-164.

Mahajan P. N., 2003, "Satellite data for diagnostics of monsoon disturbances", *Mausam*, 54, 165-172.

Mahajan P. N. and 5 others, 2004, "Proper depiction of monsoon depression through IRS-P4 MSMR", *Proc. Indian Acad. Sci. (Earth Planet. Sci.)*, 113, 223-243.

Manohar G. K. and Kesarkar A. P., 2003, "Climatology of thunderstorm activity over the Indian region: Part I A study of east-west contrast", *Mausam*, 54, 819-829.

Manohar G. K. and Kesarkar A. P., 2004, "Climatology of thunderstorm activity over the Indian region: Part II Spatial distribution", *Mausam*, 55, 31-40.

Manohar G. K. and Kesarkar A. P., 2005, "Climatology of thunderstorm activity over the Indian region: Part III Latitudinal and seasonal variation", *Mausam*, 56, 581-592.

Miller F. R. and Keshavamurty R. N., 1968, "Structure of an Arabian Sea summer monsoon system", *IIOE Meteor. Monograph No.1,* East-West Press, Honolulu.

Mishra D. K., Gupta G. R., Onkari Prasad and Nath T., 1991, "Some aspects of southwest monsoon as seen in satellite cloud imagery", *Mausam*, 42, 261-264.

Ngara T. and Asnani G. C., 1978, "Five day oscillations in east African low level jet", *Nature*, 272, 708-709.

Olander T. L., Velden C. S. and Turk M. A., 2002, "Development of the Advanced Objective Dvorak Technique (AODT) – current progress and future directions", *25th Conf. Hurricanes Tropical Meteor.*, Amer. Meteor. Soc., San Diego, pp. 585-586.

Pant M. C., 1982, Some characteristic features of the low-level jet field over the Arabian Sea during the Indian summer monsoon, *Mausam*, 33, 85-90.

Pearce R. P. and Mohanty U. C., 1984, "Onsets of the Asian summer monsoon 1979-1982", *J. Atmos. Sci.*, 41, 1620-1639.

Prasad K., Kalsi S. R. and Datta R. K., 1990, "Wind and cloud structure of monsoon depressions", *Mausam*, 41, 385-370.

Raghavan S., 1997, "Radar observations of tropical cyclones over the Indian seas", *Mausam*, 48, 169-188.

Raj Y. E. A., 1996, "Inter- and intra-seasonal variation of thermodynamic parameters of the atmosphere over coastal Tamilnadu", *Mausam*, 47, 259-268.

Rajeev V. K., Parameswaram K. and Raju C. S., 2006, "Satellite-based Cloud Studies: KALPANA1-VHRR and NOAA-AVHRR", *National Workshop on Cloud Physics,* CESS, Trivandrum, 24-25 March 2006.

Rajeevan M., Pai D. S. and Das M. R., 2001, "Asymmetric thermodynamic structure of monsoon depression revealed in microwave satellite data", *Current Sci.*, 81, 448-450.

Rajeevan M., Bhate J., Kale J. D. and Lal B., 2006, "High resolution daily gridded rainfall data for the Indian region: Analysis of break and active monsoon spells", *Current Sci.*, 91, 296-306.

Rao R. R., 1990, "Observed variability in the thermal response of the upper north central Arabian Sea to the forcing of onset vortex during summer monsoon experiments", *Mausam*, 41, 439-444.

Rao R. R. and Sivakumar D. ,1999, "On the possible mechanism of the evolution of a mini-warm pool during the pre-summer monsoon season and the genesis of onset vortex in the southeastern Arabian Sea", *Quart. J. Royal Meteor. Soc.*, 125, 787-809.

Ray T. K., Sinha D. and Guhathakurtha P., 2001, "Landslides in India", Pre-published *Sci. Rep. No. 1/2001*, India Met. Dept., Pune.

Saha K. R., 1971, "Cloud distribution over equatorial Indian Ocean as revealed by satellites", *Indian J. Meteor. Geophys.*, 22, 389-396.

Sarkar R. P. and Chowdhary A., 1988, "A diagnostic structure of monsoon depression", *Mausam*, 39, 9-18.

Sharma R. V. and Subramanian D. V., 1983, "The western disturbance of 22 December 1980: A case study", *Mausam*, 34, 117-120.

Shenoi S. S., Shankar D., and Shetye S. R., 1999, "The sea surface temperature high in the Lakshadweep sea before the onset of the southwest monsoon", *J. Geophys. Res.*, 104, 703-712.

Sikka D. R., 1971a, "Evaluation of the use of satellite photography in determining the location and intensity changes of tropical cyclones in the Arabian Sea and the Bay of Bengal", *Indian J. Meteor. Geophys.*, 22, 305-312.

Sikka D. R., 1971b, "Development of tropical cyclones in the Indian Seas as revealed by satellite radiation and television data", *Indian J. Meteor. Geophys.*, 22, 317-324.

Sikka D. R. and Gadgil S., 1980, "On the maximum cloud zone and the ITCZ over Indian longitudes during the southwest monsoon", *Mon. Wea. Rev.*, 108, 1840-1853.

Sikka D. R., 2006, "Major advances in understanding and prediction of tropical cyclones over north Indian Ocean: a perspective", *Mausam*, 57, 165-196.

Simon B. and coauthors, 2001, "Monsoon onset-2000 monitored using multi-frequency microwave radiometer on-board Oceansat-1", *Current Sci.*, 81, 647-651.

Singh J. and Hem Raj, 1982, "A satellite study of the tropical easterly jet stream during Monsoon-77", *Mausam*, 33, 113-120.

Sinha Ray K. C., 1988, "Satellite observations of mountain waves over northwest India and neighbouring regions and their theoretical verification", *Mausam*, 39, 257-262.

Soman M. K. and Krishna Kumar K., 1993, "Space-time evolution of meteorological features associated with the onset of the Indian summer monsoon", *Mon. Wea. Rev.*, 121, 1177-1194.

Srinivasan V., 1971, "Some case studies of cirriform clouds over India during the winter period", *Indian J. Meteor. Geophys.*, 22, 421-428.

Srinivasan V., Raman S. and Ramakrishnan A. R., 1971, "Monsoon depression as seen in satellite pictures", *Indian J. Meteor. Geophys.*, 22, 337-346.

Suresh R. and Raj Y. E. A., 2001, "Some aspects of Indian northeast monsoon as derived from TOVS data", *Mausam*, 52, 727-732.

Suresh R., Sankaran P. V. and Rengarajan S., 2002, "Atmospheric boundary layer during northeast monsoon over Tamilnadu and neighbourhood - a study using TOVS data", *Mausam*, 53, 75-86.

Veeraraghavan K. and Nath T., 1989, "A satellite study of an active western disturbance", *Mausam*, 40, 303-306.

Velden C. S., Smith W. L. and Mayfield M., 1984, "Applications of VAS and TOVS to tropical cyclones", *Bull. Amer. Meteor. Soc.*, 65, 1059-1067.

Velden C. S., Goodman B. M. and Merrill R. T., 1991, "North Pacific tropical cyclone intensity estimation from NOAA polar-orbiting satellite microwave data", *Mon. Wea. Rev.*, 119, 159-168.

Velden C. S., Olander T. L. and Zehr R. M., 1998, "Development of an objective scheme to estimate tropical cyclone intensity from digital geostationary satellite infrared imagery", *Weather and Forecasting*, 13, 172-186.

Waliser D. E. and Gautier C., 1993, "A satellite-derived climatology of the ITCZ", *J. Climate*, 6, 2162-2174.

Wang B., LinHo, Zhang Y. and Lu M. M., 2004, "Definition of South China Sea monsoon onset and commencement of the east Asia summer monsoon", *J. Climate*, 17, 699-710.

Webster P. J. and coauthors, 1998, "Monsoons: processes, predictability and the prospects for prediction", *J. Geophys. Res.*, 103, C7, 14451-14510.

Chapter 3

Estimation of Atmosphere, Ocean and Land Parameters

The basic objective of meteorological satellites is to observe clouds, and as we have seen in the previous chapter, cloud imagery is their most popular and extensively used product that can reveal a lot of information at a glance. It is, however, further possible to use the satellite-measured radiances to indirectly estimate several atmosphere, ocean and land parameters from either physical considerations or by developing suitable statistical techniques. Satellites essentially intended for non-meteorological applications can also be made to provide useful meteorological information. Satellite retrievals afford two distinct advantages over *in situ* measurements in that the oceans can be covered very well and that fresh retrievals can be made with every satellite pass.

3.1 Cloud Motion Winds

Wind cannot be seen, but it can be made to move objects and its energy can be harnessed. The wind vane and anemometer were two of the earliest meteorological instruments to be developed. In 1806, Admiral Sir Francis Beaufort developed a rating system for an accurate visual estimation of wind speed just by closely observing the movement of objects that we may commonly see around us. This system was originally developed for use by sailors but it was later modified and extended for use on land. It became well-known as the Beaufort Scale, and what is important about it is that it has stood the test of time. In fact, the 64 knots wind speed that occupied the highest place on the 12-point Beaufort Scale is regarded as the hurricane speed threshold even in today's satellite age.

Early in the previous century, pilot balloons came into widespread use for measurement of upper air winds. They are simple and easy to deploy. A small balloon is filled with gas and released and as it ascends, its azimuth and elevation are measured with an optical theodolite by an observer. The track of the pilot balloon is plotted and the winds at various standard levels are computed from its horizontal displacement. The balloon moves very fast initially, hence it is difficult to make measurements in the boundary layer which are required for many applications. If the balloon gets into a cloud, it

is lost from view, which is a serious constraint during the monsoon season because the sky is generally cloudy. At very high levels, the balloon may burst or the observer may lose its track. Night-time ascents are possible by attaching Chinese lanterns to the balloons, but tracking is not easy.

The rawinsonde is similar in principle to the pilot balloon but it employs a large balloon with an attached reflector which is tracked with a radio-theodolite. As the balloon does not burst easily, winds can be obtained up to a height of 30 km or higher.

In the radiosonde, an electronic package with a transmitter is attached to the balloon. The sensors measure the pressure, temperature and humidity at various levels as the balloon rises. The signals are received at a ground station and decoded to retrieve the vertical profiles of temperature, humidity and other parameters.

Most upper air stations take 2 to 4 pilot balloon ascents and 2 radiosonde ascents per day. The observations are expensive as manpower and consumables are involved. The radiosonde packages are usually lost and the few that are retrieved are generally not in a reusable condition. The global upper air observation network is therefore not easy to maintain. Further, it is essentially a land network as radiosonde ascents over the sea are made by very few ships, and upper air data is absent over most parts of the oceans.

Beaufort's method of estimating the speed of wind at the surface from the movability of objects around us, is no longer in vogue as we have anemometers and wind vanes to do that job. However, his basic principle is still used for deriving upper air winds by tracking the movement of balloons. After satellites started sending images of clouds over the earth, the application of Beaufort's principle got further extended to the extraction of winds at various levels by calculating the displacement of clouds and their direction of movement between two successive satellite images. How this is actually done is explained in the following sections.

3.1.1 Extraction of CMWs

The ATS series of geostationary satellites, launched in the late sixties, provided for the first time, an opportunity to determine wind velocities by tracking cloud movements over a time series of satellite pictures (Fujita 1969). Since then, techniques for derivation of Cloud Motion Winds (CMW) have undergone great refinement and CMWs are now being derived operationally over extensive areas within the coverage of geostationary satellites GOES, Meteosat, INSAT and MTSAT. Menzel (2001) and

Le Marshall et al (2003) have given a brief history of how the CMW derivation techniques have evolved over the years and the discussed the present state of art.

The derivation of CMWs with satellite imagery can be done best with geostationary satellite imagery. Generally a set of three consecutive half-hourly images is used to track the motion of clouds, either visually by an expert or by subjecting the images to an automated procedure on an image processing system.

In the manual method, suitable clouds or cloud features, called targets or tracers, are visually identified and their movement is monitored across successive images. In the automated method, an array of pixels is selected in the first image instead of a single cloud or feature. The target is defined in terms of characteristics such as brightness temperature gradients and spatial coherence. An auto-correlation technique is employed to search subsequent images to identify cloud patterns similar to the target (Kelkar et al 1986, Kelkar et al 1993).

In both the methods, the cloud displacement is measured and divided by the time interval between images to get the wind speed, and the direction is obtained from the geometric orientation of the displacement vector. The derived CMW has to be assigned to a proper height and this is usually done with reference to the cloud top temperature, which is obtained from the IR images.

The manual method is very time-consuming but an analyst can derive very accurate vectors and eliminate spurious ones because of personal experience and knowledge of the synoptic situation. On the other hand, automatic pattern-matching techniques can yield thousands of vectors in a much shorter time, but they have to be subjected to stringent quality control in which a large number gets eliminated.

Automated wind extraction methods are based upon statistics (Holmlund 1998). Correlations between target and search patterns can never be very high because of various factors such as navigation and registration errors, brightness changes because of change in solar illumination or vertical growth of cloud, or changes in the cloud form and size. Many cloud features may get altered over successive images.

Image enhancement techniques can be employed to mask noisy signals and isolate a particular level or area. Filter functions can be used to detect distinctive signals and the pattern peaks can then be tracked. The quality control process involves checking for consistency over successive pairs of

images, continuity with the previous retrievals and conformity with nearby vectors within the set. Additional checks are carried out by cross-checking with *in situ* wind observations if available, comparing with numerical model forecasts, or by reference to climatology. Quality control is a vital part of the operational CMW extraction process (Holmlund et al 2001).

All types of imagery can be used for CMW derivation but they have their relative advantages and disadvantages. Visible images have higher resolution compared to other channels and the cloud features are sharply defined. The low clouds and thunderstorms are predominant but their brightness changes with time. In IR images, the resolution is not as good and the cloud features are not sharply defined. High clouds are predominant and they mask the middle and lower clouds. The cloud top temperature may change during the derivation if the cloud grows vertically. In WV images, large-scale moisture patterns can be tracked, but these are mainly in the middle troposphere.

One of the difficult parts of the CMW derivation is the assignment of a proper height to the vector although various methods have been tried for this purpose (Nieman et al 1993). An appropriate height is usually found with reference to the cloud top temperature and applying a vertical temperature profile. Such a profile may not be available, particularly over the ocean. Other difficulties arise from the fact that the target pattern may consist of a mixture of clouds at different levels or the target cloud could also be gaining height or dissipating. In case of low level cumulus clouds seen more in visible images, the CMW usually corresponds to the cloud base at 900 or 850 hPa. Middle level clouds are still more difficult to handle.

The assumption that a cloud is drifting with the prevalent wind may itself be invalid under certain conditions, for example over mountains. Therefore, all cloud movements cannot be assumed as being wind-driven.

The basic requirement of CMW retrievals is of course the presence of clouds and their suitability to serve as tracers. However, over areas of clear skies, CMWs can be retrieved by tracking the movement of moisture patterns in WV imagery, usually above the 400 hPa level. The same height assignment method that is used in IR can be applied to WV tracking also, but not if the areas are totally cloudfree.

Generally, VIS imagery produces better low level winds, and IR or cloudy WV imagery gives better high level winds. VIS imagery gives a clearer distinction between the ocean surface and the low level clouds than does IR imagery. It is obviously not possible to derive CMWs right on the sea surface. This can be obtained only from scatterometers (see Section 4.3).

Attempts are being made to overcome the limitations in the derivation of night-time CMWs when VIS images are not available, by using the GOES SWIR 3.9 μ channel as a new alternative (Velden et al 2005). This is a slightly cleaner window channel than the TIR, making it more sensitive to warmer or lower tropospheric temperatures and it is less sensitive to cirrus clouds. Both these factors make it possible to extract as much as 40 % more low level CMWs at night.

A limitation of geostationary satellites is that they do not see the polar regions and cannot be used to extract winds poleward of about 65° latitudes. Velden et al (2005) have described an initiative for deriving CMWs at such high latitudes from polar orbiting satellite imagery. Polar orbiters have orbital periods of about 100 min, but they can see the polar regions in every orbit, providing overlapping images, from which CMWs can be extracted by the same technique as that used for geostationary satellites images. MODIS IR 11 μ and WV 6.7 μ band images have been successfully used for tracking clouds and cloud features in the polar regions (Key et al 2003).

There have been constant improvements in the quality and volume of CMW data produced by all operational centres. Khanna et al (2000) and Bhatia et al (2002) have discussed the recently introduced improvements in the technique used in deriving CMWs from INSAT imageries and their utilization.

In a very exciting development, an algorithm to derive clear-sky, altitude-resolved wind vectors is being developed and evaluated using simulated hyperspectral data (Velden et al 2004). The simulated datasets are based on the Geosynchronous Imaging Fourier Transform Spectrometer (GIFTS) instrument (see section 6.6). The method utilizes the constant level moisture analyses derived from the hyperspectral sounding information. In clear sky regions, vertical profiles of moisture can be derived from the simulated multiple GIFTS WV channels. Sequences of retrieved water vapour fields become the simulated imagery for tracking winds. Because the moisture fields will already be analyzed to constant pressure surfaces by the retrieval, the heights of the wind vectors will be predetermined. The height assignment error that contemporary satellite winds suffer should be minimized, and improved WV-tracked winds should result. Furthermore, the hyperspectral information allows analyses of moisture at multiple vertical levels, which can then be used to attempt winds tracking to create vertical profiles of wind.

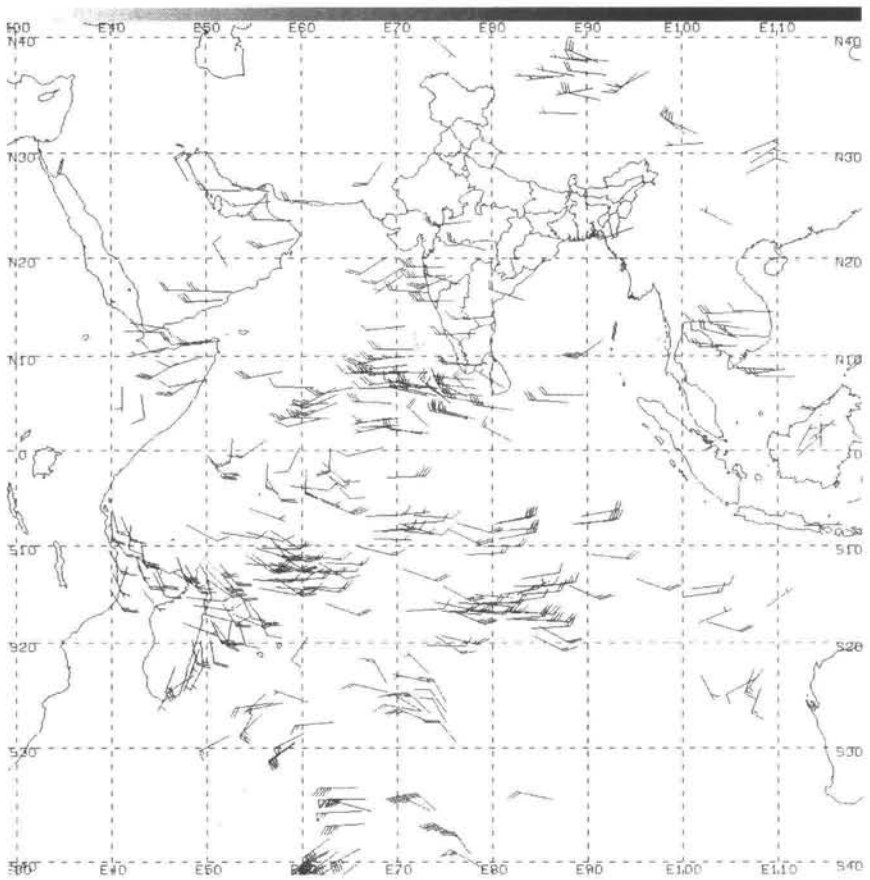

Figure 3.1.3.1 Low Level CMWs derived from Kalpana-1 imagery on 10 July 2006 (Source: IMD)

3.1.2 Use of Rapid-Scan Imagery

Successful tracking of features such as cumulus clouds over land, which have lifetimes that can be considerably less than 30 min, demands the use of imagery with time intervals of the order of 5-15 min. In the U. S., rapid-scan GOES satellite imagery has been used in operational forecasting since the 1980s. Forecasters can utilize the additional detail that can be captured from more frequent imaging in events associated with rapidly changing cloud structures. A study by Velden et al (2000) showed that the more frequent image sampling improved the VIS and IR vector field density and quality, and the optimal tracking time interval was 5 min for VIS, 10 min for IR and 30 min for WV winds.

GOES imagery can now be updated every 15 min over the continental U. S. or every 7.5 min over a smaller area, and even every minute for monitoring severe weather and tropical cyclones. New strategies have been developed for operational CMW derivation to take advantage of such rapid- and super rapid-scans from GOES (Velden et al 2005). Use of the 1 min super rapid-scan requires sophisticated image processing and tracking in order to remove navigation and registration errors (Hasler et al 1998). Extraction of CMWs from rapid scan imagery is not restricted to GOES alone, but Meteosat and GMS imagery is also being used for this purpose.

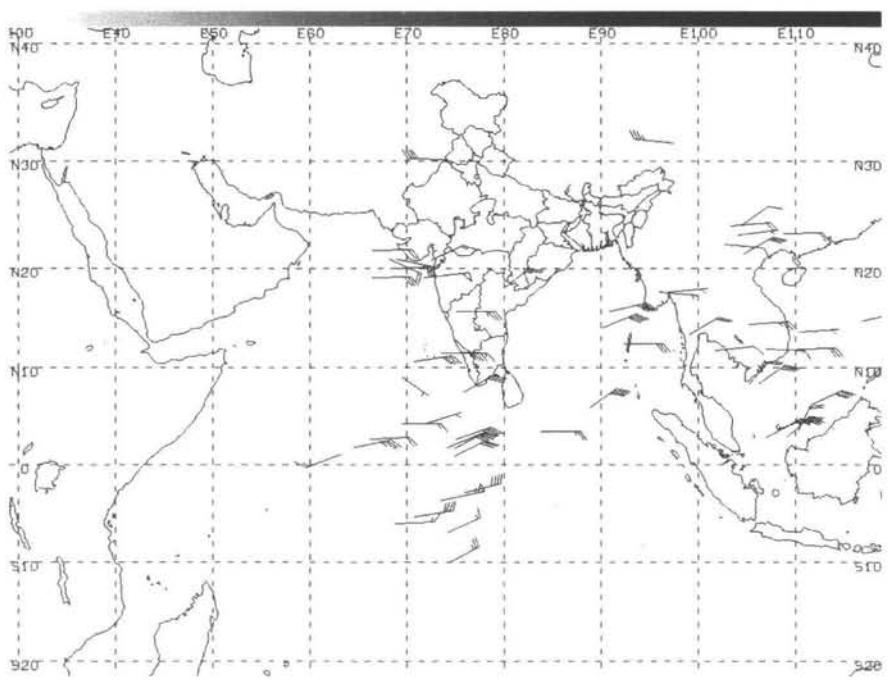

Figure 3.1.3.2 High Level CMWs derived from Kalpana-1 imagery on 29 June 2006 (Source: IMD)

3.1.3 Applications of CMWs

CMWs have direct applications in aircraft flight planning as they provide upper wind data at regular time intervals globally, whereas conventional radiosonde observations are sparse in both space and time, particularly over the oceans. Satellite winds are now used operationally for purposes of initialization of global numerical models especially over oceanic areas. A lot of research and development work goes on at numerical weather prediction

centres towards the assimilation of new satellite wind products and improving the way the CMW data is used.

CMWs over the north Indian Ocean have been found to be particularly valuable for understanding the low level air flow at the time of the Indian summer monsoon. They are able to capture vital information on the formation of eddies, cross-equatorial flow, approach of the southwest monsoon towards the west coast of India, off-shore vortices and the activity of the two branches of the monsoon over the Arabian Sea and the Bay of Bengal (Yadav et al 1989), which cannot be obtained from conventional data. Sant Prasad et al (1990) compiled average monthly mean patterns of INSAT CMWs that bring out the evolution of the wind flow from the pre-monsoon to the monsoon months. The cross-equatorial flow and the low level jet, and the upper level tropical easterly jet, all typical of the monsoon season, are clearly seen in the Kalpana-1 CMW fields in Figures 3.1.3.1 and 3.1.3.2 respectively.

3.2 Outgoing Longwave Radiation

In the past, the Outgoing Longwave Radiation (OLR) at the top of the atmosphere was regarded as just one amongst the many components that made up the radiation budget of the earth-atmosphere system (see Section 1.1.4). Although the importance of OLR in the planetary radiation budget had been well-accepted, in recent years there has been an increasing emphasis on the use of satellite-derived OLR as a proxy for other meteorological parameters which cannot otherwise be observed globally. In the process of derivation of OLR the minor variations in cloudiness get averaged out, and the OLR values can be plotted as a field and subjected to a spatial and temporal analysis which is not possible with simple cloud imagery. Most important is the strong relationship that has been found to exist between OLR and convective activity and large-scale precipitation over the globe. Low OLR usually indicates cold surface temperatures or presence of clouds, while high OLR indicates warm surface temperatures and absence of convection. The Inter-Tropical Convergence Zone (ITCZ), a region of persistent thunderstorms in the vicinity of the equator is marked by low values of OLR. Major deserts and oceanic subtropical highs have the largest OLR during summer.

3.2.1 ERBE and GERB Measurements

Since 1978, various satellites have carried instrument payloads for measurement of both solar and longwave radiation, Nimbus-7 being the first

satellite to carry an Earth Radiation Budget (ERB) payload. A composite Earth Radiation Budget Experiment (ERBE) was designed around three orbiting satellites, ERBS, NOAA-9 and NOAA-10 over the period 1984-1990. The first ERBE instrument aboard the NASA Earth Radiation Budget Satellite (ERBS) was launched from the Space Shuttle Challenger in October 1984. Two more ERBE instruments were launched on NOAA-9 and NOAA-10 satellites in 1984 and 1986 respectively. The main objective of the ERBE mission was to provide accurate measurements of incoming solar energy and shortwave and longwave radiation reflected or emitted from the earth back to space. The other goals of ERBE were to understand the radiation balance between the sun, earth, atmosphere and space which drives our weather and climate system and to establish an accurate, long-term baseline dataset for studying climate system changes (Ramanathan et al 1989, Wielicki et al 2002).

The ERBE Scanner had three scanning detectors of the thermistor bolometer type, in the shortwave 0.2-5 μ, longwave 0.5-50 μ and total 0.2-50 μ wavelength regions. ERBE also included a non-scanning instrument which had five detectors. Of these, four operated in a nadir staring mode and one was a solar monitor that was used only for solar calibration measurements. Two of the detectors had a wide field of view and two had a medium field of view, one each for the total and shortwave bands. The Solar Monitor detector was an active cavity pyrheliometer sensitive to all incident irradiance.

Solar and longwave radiation measurements have also been made by other instruments like the Active Cavity Radiometer Irradiance Monitor (ACRIM-I) during 1980-1989 and ACRIM-II which flew on the Upper Atmosphere Research Satellite (UARS) during 1991-1997.

Until 2002, earth radiation budget observations were made from instruments flown in low earth orbit, which provide good spatial resolution because of the proximity to the surface, but have a relatively coarse temporal sampling. This limits their usefulness for studying short-lived events and features such as convective clouds, frontal systems, and release of aerosols associated with dust storms or volcanoes. The aim of the Geostationary Earth Radiation Budget (GERB) project (Harries et al 2005) is to provide the accurate, rapid measurements that are required to study the forcing and feedback mechanisms on the shorter time scales that are important in many cases, and in turn, to use improved understanding of these mechanisms to determine inter-annual and longer-term climate variability. The Meteosat Second Generation (MSG) satellites are carrying a GERB instrument on board.

The GERB instrument (Harries et al 1999) consists of an optics unit and an electronics unit. The optics unit contains the imaging optics and detector

system, a de-spin mirror, and a quartz filter, along with two onboard calibration targets comprising the thermal blackbody source and the shortwave calibration monitor. The electronics unit controls the instrument and provides data handling. Because the 3 m diameter satellite platform spins at a rate of 100 rpm, the de-spin mirror is a key element in GERB's sampling procedure in counteracting the spacecraft rotation by spinning in the opposite direction. The linear, 256-element detector array is aligned north-south parallel to the satellite's axis of rotation, and the mirror-pointing direction is moved by one pixel in the east-west direction after every spacecraft rotation, building up a complete scan of the earth in 256 × 282 pixels in about 3 min. The blackened detector array is sensitive to radiation at all wavelengths, though only wavelengths longer than about 0.32 μ carry significant energy in the reflected sunlight, due to absorption by ozone. Alternate scans observe either the TOTAL spectrum 0.32-100 μ of radiation from the earth, or are measured through a quartz filter, which transmits only wavelengths that are shorter than 4.0 μ (SW). The longwave (LW) measurement is obtained as a difference between coincident TOTAL and SW measurements during ground processing. The aim is to measure the radiances with an accuracy of 99% of higher. GERB samples the earth's disc at a 50 km ground resolution. Previous ERBE satellites were covering the entire globe, but many regions were visited only once a day because of their polar orbits.

The first two GERB instruments have been in operation since 2002 and 2005 on board the MSG-1 and MSG-2 satellites respectively and are providing radiation data over Africa, Europe and adjoining land oceans every 15 minutes. Data is merged with data from other research satellites in polar orbits.

3.2.2 OLR Estimation

It is possible to estimate OLR from narrow-band thermal infra-red (TIR) window measurements made by polar orbiting as well as geostationary meteorological satellites. Although OLR is by definition a broad band parameter (4-80 μ), and meteorological satellites measure the radiance in a very narrow window (10.5-12.5 μ, for example in the INSAT VHRR), it is possible to fit a statistical regression between the satellite radiance and OLR. While physically this amounts to inferring the whole from a part, in practical terms the method has been found to yield useful information (Ohring et al 1984).

In terms of temperature and assuming a nadir view, the relationship between OLR and radiance relationship is of the form

$$T_f = T_r (a + b\ T_r)$$

where T_r is the brightness temperature in °K measured by the satellite, T_f is the computed flux temperature in °K, and quantities a and b are constants.

OLR is then computed from T_f as σT_f^4, where σ is the Stefan-Boltzmann constant (see Section 1.1.2).

The regression equation for the INSAT VHRR which has an IR channel 10.5-12.5 μ was derived using the spectral response characteristics of this window channel. The constants a and b have the values 1.1889 and 0.000989 /°K respectively for zero zenith angle. For increasing zenith angle, both a and b decrease in magnitude (Rao et al 1989). For obtaining the regression equation, radiative transfer computations were performed on an array of atmospheric profiles to simulate the radiances measured by the satellite radiometer within its wavelength range at different viewing angles. The process was repeated for the entire longwave region to obtain the total flux at the top of the atmosphere. The two sets of flux data were then subjected to regression analysis which yielded the values of the constants a and b.

The procedure for the computation of OLR assumes a knowledge of the brightness temperature of each individual pixel in an INSAT image. The mean OLR can then be obtained in two ways, either by calculating the OLR for each pixel as per its brightness temperature and then averaging the OLR values over a 2.5 × 2.5 ° latitude/longitude box, or by calculating the mean brightness temperature for the box and getting the corresponding OLR. However, the two approaches return very similar values of the OLR.

Arkin et al (1989) found that NOAA OLR values systematically exceeded those derived from INSAT-1B by 5-10 w m^{-2} over land, but were lower than or equal to the INSAT-1B values over cloudy ocean regions. One of the reasons is that the INSAT-1B OLR averages were calculated from radiances sampled every three hours while NOAA OLR averages were based on only two satellite passes with equator crossing times of 0230 and 1430 local time. Kelkar et al (1993) have examined the diurnal cycle of OLR by computing the average INSAT-1B OLR values separately at eight different hours of the day. Thus while the OLR derivation methodology is the same whether the radiometer is on a polar or geostationary satellite, the sampling frequency of the radiometer is much higher in a geostationary satellite and its OLR average will be more representative and realistic.

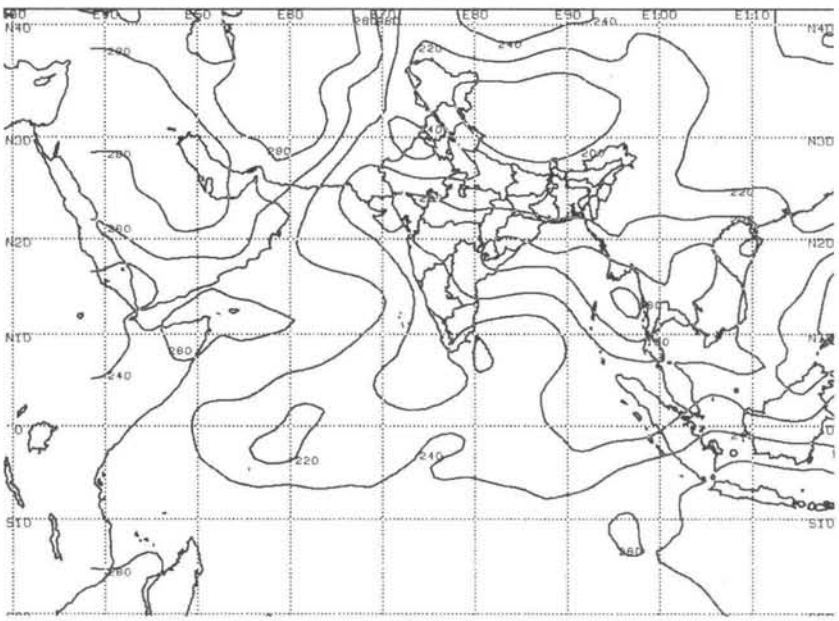

Figure 3.2.3.1 Mean OLR (in w m^{-2}) for the month of August 2006 (Source: IMD)

3.2.3 Applications of OLR

The satellite-derived OLR is a composite parameter that is modulated by four factors: (a) land or sea surface temperature, (b) cloudiness, (c) vertical temperature structure of the atmosphere and (d) optical depth of atmospheric water vapour. It can therefore be used as a proxy for convection and large-scale precipitation and has found application in many areas. Global OLR data sets are now available over periods long enough for means and anomalies to be computed.

Figure 3.2.3.1 shows the distribution of OLR over India and adjoining regions derived from Kalpana-1 IR radiance data for the month of August 2006 in which the monsoon was in an active phase. The isopleth of 240 w m^{-2} generally delineates the region of monsoon rains and the lowest OLR values are found over the region of the monsoon trough extending across India into the Bay of Bengal.

Pattanaik et al (2005a) studied the contrasting features associated with an early and late onset of the monsoon over Kerala. In 2004, the southwest monsoon arrived over Kerala on 18 May, 14 days ahead of normal, while in 2003, it had arrived on 8 June, a week late. Using NOAA OLR anomalies,

they found that in the early onset year of 2004, the pre-monsoon convective activity was stronger over the Indian region than over the South China Sea and western Pacific, while in the late onset year of 2003, the situation was quite opposite. The development of a strong cross-equatorial flow off the Somali coast in early may was associated with early onset, whereas the cross-equatorial flow remained throughout May and early part of June in the year of late onset.

Srivastava et al (2002 and 2004) who analysed NOAA OLR data over the period 1979-2000 found a significant negative correlation between the OLR anomaly over north Atlantic Ocean in the month of May and the monsoon rainfall over northwest India in June-September. When May OLR anomalies are positive over the north Atlantic Ocean, June-September sea level pressure anomalies are positive and anomalous 850 hPa easterlies prevail over peninsular India, characteristic of a weak monsoon.

In a similar study, Pattanaik et al (2005b) attempted to derive a relationship between the Indian summer monsoon rainfall and convective anomalies during the pre-monsoon and preceding winter seasons over the Indo-Pacific region based upon NOAA OLR data for 1975-2004. They observed that winter-time convection anomalies over the western Pacific slowly move northwestwards and get established over the Indian Ocean and southeast Asia by May in a year of excess monsoon rainfall, while in years of deficient rainfall, such a migration does not occur.

In an attempt to bring in more objectivity into the definition of the dates of withdrawal of the southwest monsoon, Shyamala et al (1999) used INSAT-derived OLR values, daily as well as pentad, for the month of September for the years 1987-1993 over the area covering northwest India and north Arabian Sea. They found that the OLR increases steadily towards the end of the monsoon season and when it crosses the threshold of 260 w m^{-2}, and persists at that value for 3 days, it is a signal of monsoon withdrawal. However, they have cautioned that this objective criterion should be applied only within a week of the normal date of withdrawal to eliminate spurious signals due to temporary breaks or weak monsoon conditions. Shyamala (1997) found OLR data to be useful in a similar manner for tracking the onset of the southwest monsoon and evolving objective criteria for determining the onset.

Krishnan et al (2000) have classified break monsoon days in terms of OLR anomalies over the Bay of Bengal and central and northwest India.

In a comparison of the radiative fluxes at the top of the atmosphere OLR derived from INSAT and ERBE, Chakraborty et al (2003) found that the

errors in the monthly mean INSAT OLR are within 15 w m^{-2}, and are dependent on the number of images available per month. They also computed broad band albedo from the INSAT VIS channel data and derived the radiation budget parameters over the Indian region.

Gadgil et al (2003) found that during rain breaks, the OLR anomalies from the July-August OLR mean over the Indian region are positive over most of the Indian region, exceeding 30 w m^{-2} over a large area. They also identified a unique feature associated with the breaks in the monsoon whether they are defined in terms of rainfall or circulation. This is a so-called quadrupole in the OLR anomaly pattern over the Asia-west Pacific region, arising from OLR anomalies having opposite (same) sign as anomalies over the Indian region occurring over the equatorial Indian Ocean and northern tropical (equatorial) parts of the west Pacific. This suggests that convection over the Indian region is linked to that over the east Pacific not only on the inter-annual scale but on the intra-seasonal scale as well.

Joseph et al (2004) have studied the intra-seasonal variability of the low level jet stream (LLJ) over the Arabian Sea associated the southwest monsoon using NCEP 850 hPa wind reanalysis and NOAA OLR data for 1979-1990. They constructed a OLR-wind composite for the pentad around the date of onset of the monsoon over Kerala. Similar composites were also pepared for active and break spells of monsoon activity. They concluded that in active monsoon conditions the core of the LLJ runs across peninsular India at 15 °N but during a break it moves southward to 10 °N.

Using April-September monthly NOAA OLR data for the years 1979-1992, Pai (1997) examined composite OLR anomaly patterns over the tropical region between 50° - 130° W and 30° S - 30° N, in respect of good and bad southwest monsoon years over India. There were significant differences in the OLR anomalies indicative of spatial and temporal changes in the pattern of organized convection. In good monsoon years, persistent negative anomalies were observed over the Indonesian region and large positive anomalies over equatorial west Pacific. In normal monsoon years, the patterns were similar but the anomalies were weaker. However, in deficit monsoon years, above-normal convection was observed over the Pacific region in an ENSO year and over the equatorial Indian Ocean in a non-ENSO year. He also found that OLR anomalies in the pre-monsoon months had strong signals of the nature of the subsequent monsoon activity.

Loe et al (2006) found that the analysis of OLR data around tropical cyclones provides a quantitative assessment of the ongoing deep convection during various stages of cyclone development. Their analysis of the Orissa super-cyclone of October 1999 showed that the OLR value was as low as 82 w m^{-2}

when the system was at its peak intensity of T7. Rao et al (1989) had in an earlier study of a Bay of Bengal cyclone in February 1987 observed a low OLR value of 105 w m^{-2}.

3.3 Large-Scale Precipitation

In the early years of satellite meteorology, there were many attempts to derive some kind of rainfall information from the clouds seen in satellite imagery, particularly from the point of view of forecasting flash floods. The basic problem here is that knowing only the reflectivity or temperature of the top of a cloud, is not sufficient to infer what kind of vertical structure it would be having below it, and it is all the more difficult to assign a rain rate to it. Then again, in images with large pixel sizes, the estimated rainfall cannot be compared to point measurements made by raingauges. Many of the techniques that were developed initially were quite empirical and had location-specific applications. Some techniques were more useful for climatological purposes. A critical survey of the early satellite-based rain estimation algorithms has been made by Adler et al (1988).

3.3.1 GOES Precipitation Index

The GOES Precipitation Index (GPI) is derived from a simple technique which uses only the cloud top temperature measured by geostationary satellites like GOES (Arkin and Meisner, 1987). It has also been applied to INSAT (Arkin et al 1989, Rao et al 1989) and other geostationary satellites. The technique uses IR images taken every three hours and assigns the pixels to 2.5° × 2.5° lat/long boxes. Several hundred pixels fall in a given 2.5° × 2.5° box and the temperatures of all the pixels in a box are distributed over a 16-class histogram covering temperature ranges of less than 190 °K, 191-200, 201-210, 211-215, 216-220, ...,261-265, 266-270 and higher than 270 °K. The mean temperature of the box and variance are computed. In the original method, the histograms were accumulated over a month, but the accumulation can as well be done over a day, pentad or week if the number of pixels is sufficient for statistical analysis.

The GPI rainfall estimate over the period is derived as

$$R = F \times C \times T$$

where R is the areal rainfall estimate in mm,
F is the fractional coverage of IR pixels colder than a certain threshold (typically 235 °K) within each 2.5° × 2.5° box,

C is an assumed constant rain rate of 3 mm/hr or 72 mm/day and
T is the number of hours over which F was compiled.

The GPI technique was originally developed for the north Atlantic region during the GATE experiment of 1979 and the value of the constant C was derived empirically as the result of a linear regression between GOES IR data and co-located radar observations, which is essentially location-specific. The threshold temperature of 235 °K was also chosen empirically. Besides these inputs, the technique does not incorporate any physical processes related to precipitation or clouds.

The GPI technique has been widely used for rainfall estimation in the tropics and parts of the extra-tropics where the surface temperature is relatively warm and the rainfall is mostly convective in nature. The estimates are not always accurate over land and particularly the mountain regions, where rainfall is more orographic than convective. The value of the constant 71.2 mm/day may also need to be recalibrated for land regions using radars and dense raingauge networks that may be available. The method does not work well in regions of persistent non-precipitating cirrus clouds colder than the threshold of 235 °K. The threshold may also not hold good where the rainfall is originating predominantly from warm clouds. Finally, it must be remembered that the method is meant only for large-scale averaged rainfall and cannot be adapted for purposes of short-period heavy rainfall or mesoscale analysis where the flattening out of rainfall maxima is not desirable.

In spite of all such weaknesses in the GPI technique, the great advantage of the technique is in its simplicity and in the use of only IR data which is available frequently over most areas of the globe from geostationary and polar orbiting satellites. Moreover, many studies (Janowiak 1992, Kelkar et al 1990) have shown that the GPI technique does in fact yield useful information about rainfall over the oceans and other land regions where radar and raingauge data are sparse or not available.

Figure 3.3.1.1 shows the distribution of the Quantitative Precipitation Estimate (QPE) over India and adjoining region derived from Kalpana-1 IR radiance data for the month of August 2006 in which the monsoon was in an active phase. A comparison with the OLR distribution of Figure 3.2.3.1 shows that the isopleth of 240 w m^{-2} generally demarcates the raining region in Figure 3.3.1.1. Highest QPE values are found over the Bay of Bengal.

Estimations of large-scale monthly rainfall over the Indian region using INSAT-VHRR data have also been made by Bhandari et al (1995).

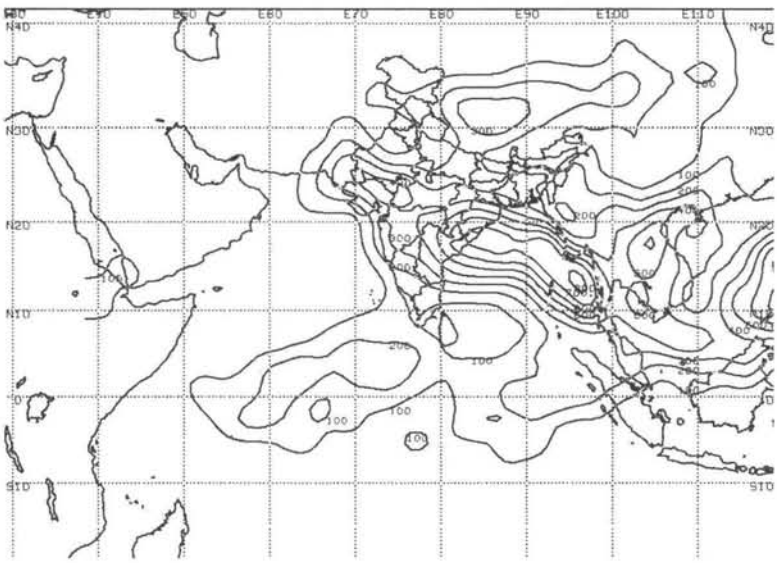

Figure 3.3.1.1 Satellite-derived precipitation total (in mm) for the month of August 2006 (Source: IMD)

Roy Bhowmik et al (2005) made a daily rainfall analysis for June 2001 raingauge data and INSAT-derived daily rainfall estimates over a 1° × 1° lat/long grid. They found that the analysis was able to capture large-scale as well as mesoscale features of monsoon precipitation systems and to bring out the asymmetric rainfall pattern associated with monsoon depressions. This has potential use in initialization of numerical models and their validation.

3.3.2 Rainfall Estimation from Microwave Sensors

Passive microwave channel measurements from satellites provide another means for estimation of large-scale rainfall. Microwaves, on account of their longer wavelengths, are able to penetrate clouds and interact strongly with the raindrops present in clouds. Therefore, while techniques like GPI that use TIR channel data are primarily statistical, the process for rainfall estimation from microwave data has a physical basis.

Nimbus-5 and Nimbus-7 were the earliest satellites to carry passive scanning microwave radiometers and clearly demonstrated the potential of microwave measurements. The Special Sensor Microwave Imager (SSM/I), was first flown on the DMSP satellite in 1987. Three DMSP satellites are carrying it now in a sun-synchronous polar orbit with a 1400 km swath and different

equatorial crossing times. The TRMM Microwave Imager (TMI) on board the TRMM satellite, is another passive microwave instrument operating at 5 microwave frequencies (see Section 1.3.8).

As the microwave emissivity of water is about 0.5, ocean surfaces look very cold to a passive microwave radiometer. Raindrops, on the contrary, appear to have a temperature that is almost equal to their physical temperature and so can be easily distinguished against the cold water surfaces. Land emissivity on the other hand is in the range of 0.9 to 1 and it becomes difficult to differentiate between land and rain as both have almost the same brightness temperature. Moreover, land surface emissivity has a geographical variation because of the changing vegetation, presence of snow cover and variations in topography. Certain properties of rainfall, however, can still be inferred even over land.

There are different approaches to microwave rain estimation which make use of three particular properties of microwave radiation. First, compared to the background atmosphere and ocean, the emission of rain clouds is much higher and it increases with the rain rate. Second, high frequency microwaves (85.5 GHz) are strongly scattered by ice nuclei present in many raining clouds. This reduces the microwave signal at the satellite and offers a contrast against the warm land background. Third, the polarization diversity in microwave measurements, arising due to polarization from the surface and de-polarization from hydrometeors, can be used to advantage.

The largest single source of error in microwave measurements is beam filling. Other limitations are introduced by the low sampling frequency of orbiting satellites and the discontinuous nature of precipitation. It is further difficult to place passive microwave sensors at geostationary height. Even then, because of their all-weather capability, passive microwave data are being used not only for precipitation estimation but in a variety of applications to retrieve geophysical parameters like ocean surface wind speed, area covered by ice and characteristics of ice, snow cover, cloud liquid water, integrated water vapour, soil moisture, land and sea surface temperature (Gairola et al 2003).

3.4 Vertical Profiles of Temperature and Water Vapour

Knowledge of the temperature and humidity distribution in the vertical is essential for obtaining a complete three-dimensional representation of the atmosphere. The conventional method of measuring vertical profiles of temperature, water vapour or any other atmospheric parameter is to release a balloon carrying a suitable instrument package that would sense the

parameter and transmit the data to a ground station. In a radiosonde, which is the most widely used instrument for this purpose, an electronic package with a transmitter is attached to the balloon and the sensors measure pressure, temperature and humidity at various levels as the balloon rises. The signals received at a ground station are decoded to obtain the vertical profiles of temperature, humidity and other parameters. Most upper air stations take two radiosonde ascents per day at the synoptic hours of 00 and 12 UTC.

Radiosonde data also have their own inherent errors due to solar radiation during daytime and infrared cooling at night. The time lag between the temperature and humidity measurements and errors in pressure measurement add further to the overall errors and uncertainties (McMillin et al 1988). In addition, national meteorological services use radiosonde instruments of different makes and designs, and employ different ground computation procedures. This requires them to undertake rigorous inter-comparisons periodically so as to maintain compatibility amongst the instruments and uniformity in the global synoptic analyses.

In an attempt to make use of data from INSAT satellites which did not have a sounder, Prasad et al (1998) developed a technique to estimate tropospheric moisture profiles from INSAT IR digital data to generate moisture fields at various levels for purposes of initialization of numerical models. Such information can be used a proxy for direct satellite soundings.

Polar orbiting satellites and some geostationary satellites can now provide a repetitive, globally consistent sounding capability on land and oceanic areas alike. The soundings are available on a finer grid but they differ from the radiosonde in the scale on which they sample the atmosphere in both horizontal and vertical dimensions. While the radiosonde measures the local environment, satellite profiles are averages of horizontal and relatively deeper layers of the atmosphere. Absolute accuracy of satellite soundings is difficult to establish. With every satellite pass, a fresh retrieval is possible, hence more frequent profiles can be obtained compared to radiosondes. However, elaborate systems are required to receive the satellite data and complex software is needed to process it.

Khanna et al (1993) have described the early attempts at retrieving the temperature soundings of the atmosphere over the Indian region by processing NOAA satellite data received at New Delhi with the International TOVS Processing Package. They have also explained the basic principles of the method adopted for the retrieval, which are summarized below.

The narrow band radiance measurements made by a satellite depend upon the surface skin temperature and the vertical profiles of temperature and

absorbing gases. In the simplest case, it can be assumed that there are no clouds in the atmosphere, there is no scattering, the viewing geometry is vertical and the earth's surface is a black body. The outgoing radiance R_ν at frequency ν reaching the satellite can then be expressed as a sum of two terms:

$$R_\nu = (I_0)_\nu \tau_\nu(z_0) + \int_{z_0}^{\infty} B_\nu\{T(z)\} \frac{d\tau_\nu(z)}{dz}\, dz$$

In this Radiative Transfer Equation (RTE), the first term on the right hand side is the spectral radiance I_0 at frequency ν emitted by the earth's surface, denoted by z_0, and attenuated by the atmosphere. The second term is the integrated spectral radiance at frequency ν emitted by various layers of the atmosphere and attenuated by the atmosphere above them. B_ν is the Planck function for frequency ν and temperature T at height z, and τ_ν is the transmittance from the level z to the top of the atmosphere.

R_ν can be regarded as a sum of the radiance emanating from the earth's surface and the contributions to the upward flux from various atmospheric layers. If we know the vertical profiles of temperature and optical depths of the absorbing gases, and the absorption and emission characteristics of the atmosphere, we can compute the value of the radiance R_ν. This can be accomplished in a relatively straightforward manner and is aptly called the forward problem.

On the other hand, if we measure R_ν at several frequencies in an absorption band, it should be possible to compute either the vertical profiles of temperature or the optical depths of atmospheric gases or both. This is called the inverse problem and it is a much more complicated process. The functions multiplying B_ν in the integral term of the RTE indicate the layer which contributes the maximum to the radiance sensed by a given satellite channel. However, for each channel a considerable depth of the atmosphere contributes to the radiance. Further, satellite instruments sense radiation over a small range of frequencies rather than monochromatic radiation. It is therefore necessary to perform an integration over frequency to obtain radiances of adequate accuracy as measured by the satellite instrument. The inverse problem is again complicated by the fact that the transmittances are not known as a function of the optical depth and temperature as accurately as required. It is not, therefore, possible to infer both temperature and humidity profiles from the same set of satellite measurements. In order to obtain accurate temperature soundings it is necessary to make simultaneous

measurements in the water vapour and ozone absorption bands. It is also desirable to make additional measurements in the short wave spectral region.

Radiance measurements in the absorption bands of CO_2 centred at 15 and 4.3 μ, water vapour at 6.7 μ and ozone at 9.6 μ provide the capability to derive temperature and moisture profiles and total ozone respectively. Sampling at the centre of the band yields radiation from the upper levels of the atmosphere, as radiation from below has already been absorbed by the atmospheric gas. Sampling away from the centre of the absorption band yields radiation from successively lower levels of the atmosphere. In the wings of the absorption band are the windows that view the bottom of the atmosphere.

The RTE can be written in a different form as

$$R_v = (I_0)_v \tau_v(z_0) + \int_{z_0}^{\infty} B_v\{T(z)\} K_v(z)\, dz$$

where K is what is called a "weighting function". The normalised weighting functions for NOAA TOVS/HIRS channels in the CO_2 band are shown in Figure 3.4.1.

A weighting function is used to multiply or weight the Planck function in the atmospheric component of the emitted radiation. It indicates the relative contribution from a given level of the atmosphere to the radiance received by the satellite through a given channel. In order to understand better the nature of the weighting functions, we may consider three air parcels at different heights. For the lowest parcel, the atmospheric density is high and so the amount of radiation emitted is high, but almost all of it is absorbed by the atmosphere above and only a small residual amount reaches space. For the highest parcel, the transmittance to space is high, but comparatively little radiation is emitted because atmospheric density is very low at that height. The result of these opposing effects is that, at some intermediate height, the contribution of a parcel to the radiance is maximum. Most of the radiance originates in a layer around the peak of the weighting function. From a knowledge of the vertical distribution of atmospheric constituents and their spectroscopic properties measured in the laboratory, the variation of the weighting function with height can be calculated. Since the weighting function is the derivative of the transmittance profile, it will peak higher in the atmosphere for the frequency at which the absorption is stronger. In this way, a carefully selected family of frequencies will be able to sense radiation from different layers in the atmosphere.

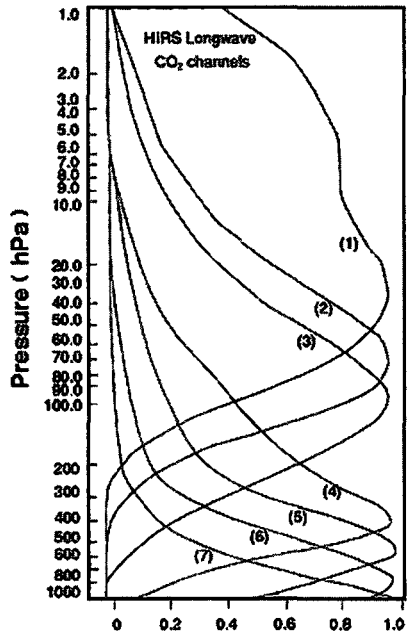

Figure 3.4.1 Normalised weighting functions for NOAA TOVS/HIRS channels in the CO_2 band

Many problems are, however, encountered when dealing with weighting functions. Firstly, weighting functions do not have sharp peaks, so the radiance can be attributed only to the mean properties of thick layers and not to those of single levels. Secondly, successive weighting functions have a high degree of overlap, so although the instrument may make measurements at N separate frequencies, we obtain fewer than N pieces of independent information. Both these factors have implications in the inversion procedure.

The basic problem, however, is that we are trying to retrieve T(z) from a finite number of measurements. T(z), however, is a continuous function of height z and ideally requires an infinite number of parameters to represent it fully. This means that theoretically speaking, an infinite number of atmospheric profiles can lead to the same radiances being measured by the satellite. The aim of a good retrieval scheme is to find out the best or the most reasonable profile.

There are three types of retrieval algorithms, statistical, physical and hybrid, none of which can be said to have a clear superiority over the others.

The statistical retrieval method is the simplest as it does not involve the RTE at all. This approach uses a statistical knowledge of the properties of the atmosphere. A large data set of observations from radiosonde ascents and satellite radiances, co-located as closely as possible in time and space, is first compiled. These are subjected to a regression analysis and a set of correlation coefficients is generated. The regression relationship is then applied to the actual radiances to get the vertical temperature profiles. The procedure is simple and requires minimum computer power and time. In fact it does not make use of either the RTE or the transmittance functions. However, the large training data set needs to be periodically updated, say once a week, to account for any gradual changes in the channel characteristics or air mass composition. As the satellite viewing geometry may vary during different passes over the same area, the radiance may have to pass through varying depths of the atmosphere, in contrast to near vertical radiosonde ascents, and hence a limb correction has to be applied. Some error will also arise if the emissivity of land, which depends upon soil moisture, is not parameterized realistically.

Physical retrieval algorithms attempt to solve the RTE in just one step in perturbation form or iteratively in a number of steps. In the one-step method, the RTE is solved to get simultaneous temperature and moisture profiles using all available radiation information. The iterative process starts with a first guess temperature profile which is judiciously chosen from a model prediction or climatology. The weighting functions are calculated and the RTE is solved to get estimates of the radiance in each channel. If the computed radiances match the observed ones within an acceptable margin, the current profile is accepted as the solution. If the computation diverges, the current profile is adjusted and the computations are repeated until a convergence is achieved. This is a good approach because the physical processes are clearly evident at each stage. However, the method is computationally intensive and it requires an accurate knowledge about the transmittances, which have to be tuned for view angle, cloudiness and air mass variations.

Physico-statistical or hybrid retrieval algorithms are a compromise between the two approaches. They use the inversion technique to make retrievals but the initial guess is made using the statistical approach. They do not use a large training data set. They also use weighting functions like in physical retrievals, but they do not directly perform an integration of the RTE. The 3I method (Improved Initalisation Inversion) is based upon the TIGR (Thermodynamic Initial Guess Retrieval) data set which is generated as a

one-time effort. The nearest profile can be chosen from this voluminous set of 80,000 radiosonde ascents, made over 2,000 locations in tropical as well as extra-tropical regions covering land and sea at different viewing angles.

Khanna et al (1993) found that satellite retrievals over the Indian region were in agreement with radiosonde-measured temperatures between 700 and 150 hPa. Large differences are noticed, however, below 850 hPa and above 150 hPa levels due to excessively high surface temperatures in summer and large seasonal variations in atmospheric moisture. There are particular problems while dealing with thick persistent cloudiness during the monsoon season.

3.4.1 NOAA TOVS

The NOAA-6 satellite first carried an instrument called the TIROS Operational Vertical Sounder (TOVS) and satellites up to NOAA-14 continued to carry the same (Smith et al 1979). TOVS consisted of three separate parts: High Resolution Infrared Radiation Sounder Version 2 (HIRS/2), Microwave Sounding Unit (MSU) and Stratospheric Sounding Unit (SSU). The system as a whole provided atmospheric temperature profiles from the surface to 10 hPa, water vapour content at three levels of the atmosphere and total ozone content. The HIRS/2 was a step-scanner 20-channel spectrometer with 19 IR channels and one VIS channel.

Later satellites of the NOAA series from NOAA-15 onwards, have been flying a higher version of TOVS called the Advanced TOVS (ATOVS) system. In this new system, HIRS/2 has been replaced by an advanced IR aounder called HIRS/3. MSU has been replaced by the Advanced Microwave Sounding Unit-A (AMSU-A), and SSU by the Advanced Microwave Sounding Unit-B (AMSU-B).

HIRS/3 is a discrete stepping, line-scan instrument designed to measure scene radiances in 20 spectral bands to permit the calculation of the vertical temperature profile from the earth's surface to about 40 km. Multi-spectral data are obtained from a single telescope and a rotating filter wheel containing 20 individual filters from 1 VIS channel (0.69 μ), 7 SWIR channels in the CO_2 band (4.57, 4.52, 4.47, 4.45, 4.13, 4.00, 3.76 μ), 7 TIR channels in the CO_2 band (14.95, 14.71, 14.49, 14.22, 13.97, 13.64, 13.35 μ) and 5 TIR channels in the H_2O and ozone bands (12.47, 11.11, 9.71, 7.33, 6.52 μ).

HIRS/3 has an elliptical scan mirror which provides cross-track scanning in 56 increments of 1.8° each. The mirror steps rapidly in less than 35 msec, then holds at each position for 100 msec for the 20 filter segments to be sampled. The IFOV for each channel is approximately 1.4° in VIS and SWIR and 1.3° in the TIR band which, from an altitude of 833 km, covers a ground area of 20.3 km × 18.9 km at nadir.

3.4.2 NOAA AMSU

Beginning with NOAA-15, all subsequent NOAA satellites have flown the 20-channel Advanced Microwave Sounding Unit (AMSU) which consists of two parts: 15-channel AMSU-A for temperature and moisture retrievals and 5-channel AMSU-B for moisture retrieval. AMSU weighting functions spread out much better than the earlier instruments.

AMSU-A is designed to measure not only the vertical temperature profiles but to derive many atmospheric and surface parameters, such as precipitable water vapour, rain rate, cloud liquid water, sea ice and snow cover.

AMSU-A is a cross-track, line-scan instrument designed to measure scene radiances in 15 discrete frequency channels. There are three channels at 24, 31 and 89 GHz, and 12 channels between 50 and 57 GHz. These measurements permit the calculation of the vertical temperature profile from the surface to about 3 hPa or 45 km height. The ground resolution is 48 km at nadir and the swath width is 2,343 km from the 833 km nominal orbital altitude.

AMSU-B is another cross-track, line-scan instrument that measures scene radiances in 5 channels. Of these two are at 89 and 150 GHz, and three near 183 GHz. The AMSU-B channels are numbered 16 to 20, following the 15 channels of AMSU-A. Channels 18, 19 and 20 span the strongly opaque water vapour absorption line at 183 GHz to provide data on atmospheric humidity. Channels 16 and 17 penetrate through the atmosphere to the earth's surface. The ground resolution is 16 km at nadir which is much higher than that of AMSU-A.

Singh et al (2003) attempted to retrieve temperature and humidity profiles over the Indian region from AMSU data and compared them with ECMWF analysis. They found that the Inversion Coupled Imager (ICI) scheme performed better than the Neural Network (NN) approach.

3.4.3 GOES Sounders

Although the physical principle of atmospheric sounding is the same for a polar orbiting or geostationary satellite, sounding instruments on geostationary satellites demand far greater sensitivity and precision because of the small amount of radiances that they have to measure at geostationary height in the same spectral bands. Out of the many geostationary meteorological satellites located around the globe, only GOES has so far been carrying a sounder. The first GOES sounder was the VISSR Atmospheric Sounder (VAS) which was rather a more advanced version of the Visible Infrared Spin Scan Radiometer (VISSR) carried by earlier GOES satellites.

In VAS, west-east scan lines were generated by the rotation of the spinning spacecraft. The lines were moved by stepping the mirror to scan north-south. The resolution was 13.8 km for channels. For atmospheric sounding, VAS had a filter wheel for measuring radiances in 7 bands in the region of CO_2 absorption, 3 in the region of water vapour absorption, and two in the IR window regions.

The GOES I-M sounder, launched on the 3-axes stabilized GOES satellites between 1994 and 2001, is a scanning radiometer with filter wheel selection. It has 18 IR bands plus a low-resolution VIS band, some of which have never been used before in geosynchronous orbit and are sensitive to temperature, moisture and ozone. While VAS had to share scanning time with the imager, the GOES I-M sounder works independently, enabling operational soundings with a resolution of 10 km between 60 °N and 60 °S latitudes. The area and frequency of scan are fully programmable. The scanning mirror steps in 10 km increments, with a step and dwell time of 0.1 sec. Initially, the GOES I-M sounder spectral selection was patterned after the NOAA HIRS sounder channels but subsequently many modifications were introduced.

The GOES-N satellite was launched on 24 May 2006. The GOES N-P Sounder is a 19-channel discrete-filter radiometer covering the spectral range from the visible channel wavelengths to 15 μ. It has 7 channels in TIR, 5 in MWIR, 6 in SWIR and 1 VIS channel for which there are four sets of detectors. Approximately one-fourth of the wheel has no filters. While this dead zone is rotating in front of the detectors, the scanning mirror is stepped to the next location then stopped while the channels are sampled. The mirror scanning sequence takes places by sweeping in alternate east-west and west-east directions, similar to the imager. Details and updates can be found at http://goespoes.gsfc.nasa.gov/goes/instruments/n_p_sounder.html.

3.4.4 DMSP SSM/T

The DMSP satellites carry, in addition to the SSM/I imager, a temperature profiler called SSM/T. This is a 7-channel microwave sounder that measures atmospheric emission in the 50-60 GHz oxygen band. The SSM/T is a cross-track scanning radiometer having a field of view of 14.4°. There are 7 total cross-track scan positions with an angular separation of 12° and with a maximum cross-track scan angle of 36°. While the ground resolution at nadir is about 174 km, it degrades at the far ends of each scan to 213 x 304 km. The SSM/T data swath is about 1500 km and there is a data coverage gap between successive orbits.

One more payload that DMSP satellites carry is the SSM/T-2 water vapour profiler, which is a 5-channel cross-track scanning microwave radiometer. Three out of the five channels are situated symmetrically about the 183.31 GHz water vapour resonance line and the remaining two are window channels. SSM/T-2 is designed to provide global monitoring of the concentration of water vapour in the atmosphere under all sky conditions by taking advantage of the reduced sensitivity of the microwave region to cloud attenuation.

The SSM/T and SSM/T-2 scan mechanisms are synchronized to make their measurements coincident. The swaths have the same width of 1500 km. The SSM/T-2 completes 7.5 scans per minute. There are 28 observations or beam positions per scan for each of the five channels, with each observation having a spatial resolution of about 48 km.

SSM/T-2 data have been found to provide excellent signatures of mid-latitude weather phenomena such as fronts and extra-tropical cyclones. Other phenomena such as tropical cyclones, and the extent of sea ice and snow cover can also be identified. The retrieval of vertically integrated water vapor is also possible due to the strong sensitivity of the 183.31 GHz water vapour absorption line.

3.4.5 INSAT-3D Sounder

The INSAT-3D satellite which is likely to be launched in 2007, will carry for the first time a sounder payload. This will make it much easier to get the data in real time and process it faster, enabling its quick assimilation by numerical models. Since INSAT-3D will be a geostationary satellite, many soundings can be made at small time intervals over the region covered by the INSAT full disc than what are currently available from other means.

The INSAT-3D sounder instrument will be capable of making soundings at 10 km ground resolution every 3 hours for a full frame scan. Derivation of vertical profiles of temperature and humidity over 30 x 30 km areas will be possible. Besides these vertical profiles, there are many other parameters than can be derived such as atmospheric stability indices, total precipitable water, and total column ozone. The INSAT-3D 19-Channel Sounder characteristics are given in Table 3.4.5.1.

Table 3.4.5.1 Characteristics of INSAT-3D Sounder Channels

Channel Number	Central Wavelength (μ)	Main Absorbing Gas
1	14.71	CO_2
2	14.37	CO_2
3	14.06	CO_2
4	13.96	CO_2
5	13.37	CO_2
6	12.66	H_2O
7	12.02	H_2O
8	11.03	Window
9	9.71	O_3
10	7.43	H_2O
11	7.02	H_2O
12	6.51	H_2O
13	4.57	N_2O
14	4.52	N_2O
15	4.45	CO_2
16	4.13	CO_2
17	3.98	Window
18	3.74	Window
19	0.695	Visible

3.5 Sea Surface Temperature

The oceans together occupy three-fourths of the surface area of the globe and play a major role in determining the earth's weather and climate. However, compared to the atmosphere, the ocean has been very poorly observed. It is only with the advent of satellite remote sensing that we have been able to substantially increase our knowledge of the ocean and to monitor it extensively and continuously.

Oceans and climate have a connection through complex exchanges of heat and mass. Oceans are the dominant heat reservoirs of the complete land-

atmosphere-ocean system and play a critical role in our climate and its variability. Ocean currents transport heat from the tropics to higher latitudes. Poleward heat transport by the oceans is of comparable magnitude with that of the atmosphere and shows large inter-annual variability.

It was known since long that oceans influence weather patterns over large regions and that they have close linkages to phenomena like the monsoons. It was back in the 1920's that Sir Gilbert Walker, after whom the Walker circulation has since been named, had discovered three large oscillations in which pressure in one region varies inversely with that in another region. These were the North Atlantic Oscillation, North Pacific Oscillation and the Southern Oscillation (Walker 1923). However, the real impetus to monitoring the El Nino and studying its global impacts came only in the late 1980s, when a reliable time series of global sea surface temperatures derived from NOAA satellites became available. For much of what we know today about the El Nino phenomenon, the genesis of El Nino and La Nina events, their intensity, their evolution, spread and retreat, ocean-atmosphere interactions, and El Nino's impacts on the global climate, due credit has to be given to the extensive as well as intensive monitoring of SST that has been done by satellites (Figure 3.5.1 – Colour Plate-2). Long-term monitoring of the oceans is now considered essential for detecting signals of climate change and for understanding the processes that trigger and maintain inter-annual and longer time scale variability of climate. Ocean observations are equally important for weather forecasting and other practical applications like marine industries and fisheries.

3.5.1 Properties of Ocean Water

Temperature, salinity and density are the three basic characteristics of ocean water. However, unlike the atmosphere, the ocean is horizontally stratified, as these basic ocean characteristics vary much more with the ocean depth than in the horizontal direction. The temperature may drop by 5 °C from the sea surface to a depth of 1 km, but the horizontal temperature gradient may be of the order of only 5 °C in 5000 km. The annual mean temperature of the global oceans is 3.5 °C.

Sea water is a complex solution of positively and negatively charged ions, and non-ionized organic and inorganic compounds. Although the concentration of the dissolved salts varies from place to place, the percentage of abundant elements remains almost a constant. The total quantity of solid material contained in sea water when all the material is completely oxidized, is called its salinity and is expressed in ppt (parts per thousand) or as a percentage. The average salinity of sea water is 35 ppt or 3.5 %. As very

small changes in salinity can significantly alter the density of sea water, salinity has to be measured with an extremely high accuracy. The most precise and widely used method for salinity determination is by measurement of its electrical conductivity. Salinity is expressed as the ratio of the electrical conductivity of sea water to the electrical conductivity of a solution of potassium chloride of a standard concentration.

The distribution of salinity at the sea surface is again basically zonal in nature. Average surface salinity is lowest just north of the equator and highest in the sub-tropical regions. It again decreases rapidly at higher latitudes. Higher values of salinity are observed where evaporation exceeds precipitation. Lower values of salinity are found near the coastlines, in regions of fresh water influx from rivers, and also in the polar regions where ice freezing discards salt to lower waters and melting leads to addition of fresh water.

The vertical profile of salinity exhibits a marked minimum at depths between 600 m and 1 km, and then an increase to about 2 km depth. In the tropics, a sharp maximum is found at around 100 m depth just above the thermocline. In high latitudes, the surface value of salinity is low but it increases with depth to about 2 km and thereafter assumes a constant value.

The density of ocean water is an important parameter as many oceanic movements are driven by differences in density. The density ranges from about 1021 kg m^{-3} at the surface to 1070 kg m^{-3} at 10 km depth and it is a function of salinity, temperature and pressure.

3.5.2 The Layered Thermal Structure of the Ocean

Most of the solar radiation incident on the ocean is absorbed very close to the surface. Wind blowing on the ocean stirs the upper layers, producing a warm thin layer at the top of the ocean having a uniform temperature and salinity. This upper layer of the sea extending from the surface down to a depth of about 10 to 200 m is called the mixed layer. The sea water below about 1 km depth also has a uniformly cool temperature and it is called the deep layer. The region of transition between the mixed layer and this deep layer is called the thermocline and it is characterised by a steep temperature gradient.

The thermocline is also defined as the depth at which the temperature gradient is maximum. However, it is difficult to mark the depth of the thermocline very precisely. In low and middle latitudes the thermocline is always present at depths between 200 and 1000 m, but at higher latitudes where the SSTs are lower, the thermocline is present only seasonally.

The distribution of temperature and salinity at the ocean's surface is influenced by several factors such as heat fluxes, rate of evaporation, rainfall, fresh water inflows, and freezing and melting of sea ice. The mixed layer tends to be more saline than the thermocline between 10° and 40° latitudes, where evaporation exceeds precipitation. At higher latitudes, the mixed layer is less saline because of rain and melting ice.

3.5.3 Remote Sensing of Ocean Parameters

In situ measurements of ocean parameters are very important but it is extremely difficult to cover the vast expanse of the oceans, that too in three dimensions. The cost of operating and maintaining meteorological and oceanographic research vessels is high, and there are only a few of such dedicated vessels. There is a voluntary observing fleet of merchant navy ships which undertake to carry out the additional responsibility of reporting weather observations and keeping weather logs, but a major constraint in this effort is that such observations are confined to narrow designated shipping lanes in which the merchant vessels sail. As a result, vast areas of oceans still continue to remain uncharted.

Against the backdrop of these problems and limitations, satellite remote sensing now provides us with the capability to monitor four important parameters over the global oceans (Pearce et al 2001):

(a) Sea Surface Temperature (SST), which has certainly been most extensively mapped by satellite remote sensing techniques, shows up ocean circulation features, thermal fronts, eddies and upwelling zones and is a basic tool for monitoring the El Nino phenomenon,
(b) Ocean colour, which is an indicator of the presence of phytoplanktons, particulates and suspended sediments in the top layer and surface foam, reveals the properties of the seabed, and shows ocean circulation patterns, fronts and upwelling regions,
(c) Sea surface elevation, which is a product of satellite altimetry, helps to study the shape of the marine geoid, and provides information on tides, and
(d) Sea surface roughness, which is a measure of the effect of wind on the sea surface, is estimated by scatterometers and synthetic aperture radars.

We will be discussing the first two parameters in the following sections and the other two parameters in the next chapter. All the four ocean variables have a direct bearing on both oceanic and atmospheric processes.

3.5.4 Satellite-derived Sea Surface Temperature

Sea Surface Temperature (SST) is an important geophysical parameter, providing the boundary condition used in the estimation of heat flux at the air-sea interface. On the global scale, it is important for building global climatologies, in weather and climate modelling, in studies of the earth's heat balance and for gaining an insight into atmospheric and oceanic circulation patterns such as the El Niño (Figure 3.5.1 – Colour Plate-2). On a more local scale, SST can be used operationally to assess eddies, fronts and upwellings for marine navigation, detection of cyclogenesis and measuring biological productivity.

A satellite radiometer measures radiation over finite wavelength bands. The radiance measured has an associated brightness temperature, or the temperature at which a black body would emit the same radiation. From this the body's true surface temperature can be computed if the emissivity is known. As the emissivity of the sea surface can be assumed to have a value of 1, which is a very close approximation, the satellite-measured TIR window radiance can be inverted to get the temperature of the sea surface. This is the basic principle of satellite SST retrievals.

It is important to consider what exactly is meant by the sea surface. Because of the existence of vertical temperature gradients in the upper layer of the ocean, the SST will be different depending upon the depth at which measurements are made. If we imagine the sea surface to have a thickness of just of one or two molecules, we should ideally measure an interface SST, but it cannot be done in actual practice. Just below this, at a depth of 10 μ, we will get what is called the skin SST. This is what a satellite measures in the TIR channel. The sub-skin SST is at a depth of 1 mm and is what a satellite measures in the microwave channel. A measurement further down is commonly referred to as the bulk SST or near-surface SST. This is measured by a ship or buoy. The different SSTs will have different values at any time or place. The diurnal temperature cycle will cause these differences to be greatest during the afternoon and smallest just before sunrise. Comparisons of SSTs measured by ships or buoys with satellite SSTs are, therefore, not a straightforward matter. Effects of depth, diurnal heating and evaporative cooling may lead to differences as large as 1 °C. These differences have to be properly parameterised when blended SST data sets are compiled from various data sources

NOAA AVHRR channels 1 (0.58-0.68 μ) and 2 (0.725-1.1 μ) measure reflected solar radiation in the VIS and NIR regions, respectively. Channels 3 (3.55-3.93 μ), 4 (10.3-11.3 μ), and 5 (11.5-12.5 μ) are dominated by IR radiation emitted from the surface and the earth's atmosphere. Channel 3 has

the advantage that it is less sensitive to atmospheric water vapour. However, channel 3 will admit a substantial amount of reflected solar radiation. It is, therefore, primarily used at night. Channels 4 and 5 are more affected by water vapour, but are not substantially contaminated by reflected solar radiation. It is the judicious combination of radiance measurements from channels 3, 4 and 5 that permits extraction of SST.

There are two major limitations of satellite SST retrievals. Firstly, clouds block infrared radiation from the earth's surface from reaching the satellite and if cloudy regions are not appropriately identified, SST retrievals would turn out to be incorrect. A cloud filtering scheme is therefore required. Secondly, there is a residual attenuation of the emission from the sea surface on its upward path and scattering by aerosols and atmospheric water vapour. This has to be compensated by applying an atmospheric correction. The correction is a function of location and season and may be as large as 4-8 °C.

These problems can be largely circumvented by adopting certain procedures, but not totally eliminated. Maps of SST compiled from TIR measurements are often made as weekly or monthly composites which allow enough time to capture cloudfree pixels over a region. The effects of the intervening atmosphere, being wavelength-dependent can be further corrected for by resorting to multi-channel measurements. In single window radiometers like the INSAT VHRR, this is not possible.

Considering that two different window channels will have different attenuations and therefore different brightness temperatures, for nadir measurements in cloudless regions the sea surface temperature, T_b, should be of the form

$$T_b = a_0 T_i + a_1 (T_i - T_j) + a_2$$

where T_i and T_j are the brightness temperatures determined from the radiance values in two different infra-red window channels i and j. The constant a_0 is close to 1 suggesting that the infra-red temperature measured in any one of these channels is close to the sea surface temperature. The temperature difference term makes a small correction to this temperature for atmospheric transmittance. The a_2 term is a small correction factor associated with the different atmospheric brightness temperatures at different channels.

In general there are three different classes of SST derivation algorithms. (a) The split-window algorithm uses the T_{11} brightness temperature as the lowest order estimate of sea surface temperature and the difference $T_{11} - T_{12}$ to correct for the atmosphere. (b) The dual-window algorithm uses the T_{11} brightness and the difference $T_{37} - T_{11}$ to correct for the atmosphere. (c) The

triple-window algorithm uses the T_{11} brightness and the $T_{3.7} - T_{12}$ difference to correct for the atmosphere. In addition, there are correction terms that must be applied to adjust the measurements made off nadir. If we define θ to be the sensor zenith angle, then the three algorithms have the form:

(Night-time – Triple)

$$SST_{3/4/5} = a_0 T_{11} + a_1 (T_{3.7} - T_{12}) + a_2 (T_{3.7} - T_{12}) (\sec \theta - 1) + a_3 \sec \theta + a_4$$

(Night-time - Dual)

$$SST_{3/4} = a_0 T_{11} + a_1 (T_{3.7} - T_{11}) + a_2 (T_{3.7} - T_{11}) (\sec \theta - 1) + a_3 \sec \theta + a_4$$

(Daytime - Split)

$$SST_{4/5} = a_0 T_{11} + a_1 (T_{11} - T_{12}) + a_2 (T_{11} - T_{12}) (\sec \theta - 1) + a_3 \sec \theta + a_4$$

The retrieval process involves three steps: (1) Exclusion of data at large zenith angles since experience has shown that the SST retrievals degrade as the sensor zenith angles increases, (2) Finding cloud-free pixels for which there are several cloud detection techniques, (3) Applying an appropriate SST extraction algorithm.

A large albedo in channel 2 is indicative of the presence of highly reflective clouds. In the visible threshold technique, a maximum permissible threshold is used for the channel 2 albedo and pixels with albedo higher than the threshold are flagged as cloud contaminated. A large local variation in the albedo in channel 2 also indicates clouds. If the difference between the maximum and minimum albedo in a region around the pixel under consideration is more than a preset limit, the centre pixel is assumed to contain clouds.

Since clouds are generally cooler than the sea, if the channel 4 and 5 temperatures are too low, the pixels are considered cloud contaminated. Also, channels 3, 4 and 5 absorb significantly different proportions of water vapour. Hence a large difference in the brightness temperatures in these channels beyond a certain threshold is considered as an indication of cirrus cloud contamination. As channel 3 may contain reflected sunlight, this test is used only at night. The presence of sub-pixels clouds can also change the apparent brightness temperature of channels 4 and 5. If the range of their brightness temperature variation in a region is above a prescribed value, the centre pixel is again flagged as cloud contaminated.

3.5.5 Microwave SST Retrievals

SST retrievals from passive microwave measurements suffer from degraded spatial resolution. This is due to the inherent problem of the low energy associated with radiation in the microwave region of the spectrum compared with that in the TIR region. However, microwave retrievals have an advantage over TIR in that radiation at these longer wavelengths is largely unaffected by clouds. As clouds and aerosols are essentially transparent to microwave radiation at frequencies below about 12 GHz, microwave remote sensing has the potential to eliminate the atmospheric contamination problems that vitiate TIR SST retrievals (Chelton et al 2005).

The atmospheric contribution to the microwave brightness temperatures measured by a satellite at these frequencies is only 2-5 per cent. Microwave estimates of SST are possible because the surface radiance is proportional to SST at frequencies between about 4 and 12 GHz. However, microwave signal returns are affected by wind-generated roughness at the ocean's surface and precipitation. The resulting changes in the surface emissivity can usually be accounted for by using multiple frequencies.

Since microwave emission from the sea surface is weak, accurate satellite microwave observations of SST require a highly calibrated and sensitive radiometer. High quality microwave SST data first became available in December 1997 from measurements at 10.7 GHz by the TRMM Microwave Imager TMI (Wentz et al 2000). Individual TMI observations of SST have an accuracy of 0.5 °C and a footprint of 46 km. This is very large compared with the 1 km resolution of satellite IR observations but the advantage lies in that microwave SST retrievals are available in all non-raining conditions. Rain-contaminated measurements from TMI are identified and eliminated from further analysis using co-located measurements at 37 GHz. A limitation in coastal regions is that the TMI brightness temperatures are contaminated by land in the antenna side lobes within about 50 km of land. Another limitation of TMI is that its geographical coverage is limited to the latitude band of 40°S-40°N.

An attempt has been made to eliminate all the limitations of the TMI mentioned above in the Advanced Microwave Scanning Radiometer (AMSR-E), which has been orbiting the earth on the NASA Aqua satellite in a sun-synchronous, near-polar orbit since June 2002. The AMSR-E covers 89% of the globe each day and 98% of it every two days. AMSR-E retrievals of SST are based on measurements of brightness temperature at 6.9 GHz, which is more sensitive to SST than the 10.7 GHz channel. The AMSR-E footprint size for SST measurements is 56 km, and the accuracy is estimated to be about 0.4°C.

3.6 Potential Fishing Zones

An important example of how meteorological satellite data can be used for non-meteorological applications is the delineation of potential fishing zones in the oceans. Oceanic features like fronts, eddies, gyres and upwelling areas play a major role in the supply of nutrients in oceanic waters. Most of the productive fishing grounds of the world are located in the areas where upwelling is found to occur. SSTs derived from NOAA-AVHRR data serve as a very useful indicator of prevailing and changing environmental conditions from the point of view of fish aggregation.

In India, satellite-based estimates of chlorophyll concentrations and retrievals of SSTs are extensively used for identification of potential fishing zones in the Arabian Sea and Bay of Bengal. SST data are composited over 3-4 days and relative thermal gradients are worked out. The thermal front areas where fish are expected to congregate are delineated as Potential Fishing Zones (PFZ). The information on PFZ is then disseminated to more than 100 fishing centres located along the Indian coast regularly and through different media. The information communicated specifies the distance of the PFZ from a known coastal point, bearing and the depth of water at the zone. Adequate training is imparted to the fishermen in the utilisation of the information including the guidance for reaching the PFZ location in the sea.

Solanki et al (2001) used near-synchronous SeaWiFS-derived chlorophyll concentrations and NOAA-AVHRR SSTs to understand patterns, persistence and inter-relationship between ocean colour and thermal features. An inverse relationship between chlorophyll concentration and SST features was observed. The frontal zone positions on the chlorophyll concentration images coincided with temperature boundaries at some locations. In a subsequent study by Solanki et al (2003), validation of the PFZ forecasts was carried out with the help of fishing trawlers plying in the PFZ regions.

3.7 Ocean Colour

The colour of the sea is not a parameter that is of direct interest to meteorologists and atmospheric scientists. However, satellite observations of ocean colour have brought out the fact that it has a strong bearing on the structure of the thermocline. The penetration of the blue component deeper into the water and the absorption of the red component in the sea can alter the depth of the mixed layer and cause perturbations in the ocean circulation. Thus ocean colour has an indirect linkage with atmospheric processes.

The colour of the sea varies from deep blue to green or even greenish yellow due to scattering of short wave radiation by the water molecules. In clear waters, most of the red and yellow wavelengths in sunlight get absorbed in the upper few metres of sea water, and only the blue wavelengths are scattered, imparting an overall blue colour to the water. In the presence of particulate matter in the sea water, other wavelengths are also scattered, creating a different hue. When marine organisms called phytoplanktons are present in the water, the chlorophyll content absorbs the blue light and alters the colour to green. This is also seen in coastal waters where vegetation is dense and rivers bring in dissolved organic substances. Subtle changes in ocean colour can therefore be used as proxy indicators of chlorophyll concentration and primary production by phytoplanktons.

Phytoplankton cells contain dissolved CO_2 and therefore represent a key element of the carbon cycle in the ocean. They also control the optical turbidity of the oceans and the development of ocean ecosystems. Ocean colour information is important for the management of marine resources and protection of the coastal zone.

The Coastal Zone Colour Scanner (CZCS) instrument, which was launched on the Nimbus-7 satellite in October 1978, was the first such instrument that was solely dedicated to the observation of ocean colour and it worked until June 1986. The SeaStar (OV-2) satellite launched on 1 August 1997, carried an ocean colour sensor called SeaWiFS (Wide Field of View Sensor).

The Indian Remote Sensing Satellite IRS-P4 (named Oceansat-1), was launched on 26 May 1999 from Sriharikota, using ISRO's Polar Satellite Launch Vehicle (PSLV). The satellite is carrying two payloads, the Ocean Colour Monitor (OCM) and a Multi-frequency Scanning Microwave Radiometer (MSMR). OCM is a multi-spectral CCD camera (see Section 1.3.3) operating in eight narrow spectral bands in the VIS, NIR and IR range of the electromagnetic spectrum between 402 and 885 nm (Table 3.7.1). The camera is being used to collect data on chlorophyll concentration, detect and monitor phytoplankton blooms and obtain data on atmospheric aerosols and suspended sediments in the water. It has a spectral resolution of 360 m × 236 m and a swath of 1420 km. The satellite is in a polar sun-synchronous circular orbit at an altitude of 720 km. It has a repeat cycle of two days with an equator crossing time around noon. There is a provision to tilt the camera by ± 20° in the along-track direction to avoid sunglint.

Table 3.7.1 Oceansat-1 OCM Spectral Bands

Spectral Band Number	Wavelength Range (nm)
1	402-422
2	433-453
3	480-500
4	500-520
5	545-565
6	660-680
7	745-785
8	845-885

The successor satellite, Oceansat-2, which is planned to be launched in 2007, will carry three payloads: another OCM, a Wind Scatterometer and an Italian payload called ROSA.

The 36-channel Moderate Resolution Imaging Spectroradiometer (MODIS) on board the Terra and Aqua satellites offers twice-daily coverage and simultaneous measurements of ocean colour, sea surface temperature and ocean primary production at a moderate spatial resolution of 250 m to 1 km (see Section 1.3.4). The Terra spacecraft has a 10:30 am equator crossing and the Aqua spacecraft has a 1:30 pm equator crossing time. Thus, MODIS data are available for two overpasses per day. Improved atmospheric products will enable better correction for atmospheric effects in the ocean signals. The products will be used to investigate ocean circulation, ocean biology and ocean chemistry, including the ocean carbon cycle. In addition to ocean measurements, simultaneous measurements of land vegetation, cloud characteristics, temperature and moisture profiles, snow cover, and sea ice, will be made.

In an interesting application of OCM data, Prasad et al (2000) used sequential data of IRS-P4 OCM to retrieve sea surface current velocities over parts of both east and west coast of India. The method was based on matching suspended sediment dispersion patterns across two sequential atmospherically corrected and geo-referenced images by using the maximum cross-correlation technique.

3.8 Sea Surface Salinity and Soil Moisture

While sea surface salinity and soil moisture are two apparently unconnected parameters, it so happens that both of them can be measured by a common satellite technique.

Microwave radiometry at low frequencies in the L-band (1.4 GHz, 21 cm wavelength) is now being regarded as a promising technique for estimating both sea surface salinity and soil moisture. However, when deployed on a space platform, large antennas of the dimensions of several metres are required for achieving an adequate spatial resolution. To overcome this problem, the principle of aperture synthesis has been adopted in the Soil Moisture and Ocean Salinity (SMOS) satellite, which is planned for launch in 2007 as a French mission.

The SMOS instrument is a dual-polarized L-band microwave radiometer that will achieve a ground resolution of 50 km and will enable frequent and global coverage of these two important parameters. A two-dimensional interferometer with a set of elementary antennas that are uniformly distributed along a Y-shaped structure, will sample the Fourier transform of the scene. At the ground, an inverse Fourier transform will be performed to retrieve the image. Updates on the SMOS mission are available at http://smsc.cnes.fr/SMOS/GP_satellite.htm.

3.8.1 Sea Surface Salinity

The global distribution of sea surface salinity is currently derived from the limited measurements made by ships and buoys and it is quite different from that of sea surface temperature. High values of salinity are found near the centre of the ocean basins, away from the mouths of rivers, and in sub-tropical oceans, where evaporation exceeds precipitation. At high latitudes, salinity is low because of the melting of ice that dilutes sea water.

Fresh water is light and floats on the surface, while salty water is heavy and sinks. Greater salinity, like colder temperatures, results in an increase in ocean density with a corresponding depression of the sea surface height. In warmer, fresher waters, the density is lower resulting in an elevation of the sea surface. These height differences are related to the circulation of the ocean. The ocean stores more heat in its top 3 m layer than in the entire atmosphere. Salinity is therefore a key factor in the global thermohaline circulation and needs to be measured globally by satellite.

Aquarius is another mission that is planned for measurement of global sea surface salinity. Aquarius is a joint U. S. - Argentina venture planned for a 2009 launch and will carry an L-band polarimetric radiometer operating at a frequency of 1.413 GHz which is sensitive to salinity, and a polarimetric scatterometer operating at 1.26 GHz that will correct for the ocean's surface roughness. The footprints will have sizes of 76 × 94, 84 x 120 and 96 × 156 km. Latest information on the Aquarius mission would be available at http://aquarius.gsfc.nasa.gov/.

3.8.2 Soil Moisture

Soil moisture measurements on different spatial and temporal scales have many applications ranging from agricultural meteorology and operational hydrology to atmospheric modelling. Frequent *in situ* measurements of soil moisture on a global scale is extremely difficult because of the heterogeneity of soil and the time consuming nature of the traditional measurement process which involves drying and weighing soil samples. Hence data from satellite-based passive microwave radiometers have been used to make an indirect estimation of this important land parameter and to compensate for the absence of a good ground network (Rao et al 2001).

The relationship between the physical temperature of the surface T_s and its brightness temperature T_b measured by a satellite radiometer, is of the form $T_b = \varepsilon T_s$, where ε is the surface emissivity. In the microwave region, the emissivity is strongly dependent on the moisture content of the soil, varying between 0.6 for wet soils and 0.3 for dry soils. For a surface temperature value of 300 °K, the microwave brightness temperature may vary as much as between 180 and 270 °K for wet and dry soils respectively. This large range of variation of T_b provides a good signal-to-noise ratio and makes it possible to retrieve the soil moisture indirectly. Ideally, microwave estimates of soil moisture can be made with an accuracy as high as 99 %. However, in practice such an high accuracy can not be attained because several other factors such as surface roughness, vegetation cover, or soil temperature, also influence the brightness temperature that is measured by the satellite.

Thapliyal et al (2003, 2005) derived regression relationships between the Oceansat-1 MSMR 6.6 GHz channel data and soil moisture at various locations in India where *in situ* observations were available and found very good correlations between them.

3.9 Vegetation Index

The first widespread application of meteorological satellite data for a non-meteorological purpose was perhaps in the derivation of what came to be known as the vegetation index. The pigment in plant leaves, chlorophyll, strongly absorbs sunlight (VIS 0.4-0.7 μ) and makes use of it in the process of photosynthesis. The cell structure of the leaves, on the other hand, strongly reflects radiation in the near infrared region (NIR 0.7-1.1 μ). Healthy plants with a high leaf density will absorb most of the incident visible light, and will reflect a large portion of the near infrared radiation. Plants which have not had a proper growth or have been struck by disease, will behave in an opposite manner, and reflect more of VIS and less of NIR radiation.

If a satellite radiometer has channels suitable for measuring radiation in VIS and NIR wavelengths and the view of the land is clear, the above properties of vegetation enable the derivation of a vegetation index that gives a gross idea of the state of the vegetation. There are many ways of defining a vegetation index, but the commonly used index is the Normalized Difference Vegetation Index (NDVI) expressed as

$$NDVI = (NIR - VIS)/(NIR + VIS)$$

where VIS and NIR are the radiances or brightness temperatures measured simultaneously for a given pixel in the VIS and NIR channels of a satellite radiometer.

Theoretically, NDVI can range between −1 and +1, with the value 0 signifying the total absence of vegetation, and an index of +1 indicating the maximum possible density of green leaves. The NDVI values derived in practice commonly lie between 0.1 and 0.7, the higher values of the index being associated with healthy vegetative cover. NDVI is best obtained under clear sky conditions, but this may not always be possible. In India, for example, the main agricultural season is during the monsoon when there is extensive cloud cover present most of the time. The presence of cloud and snow does vitiate the computations and may result in an under-estimate of the NDVI, creating the impression of a less green vegetation.

The vegetative index NDVI has been most widely derived parameter from the data from the Advanced Very High Resolution Radiometer (AHVRR) on board the NOAA polar-orbiting satellites for over 20 years now on a global scale. Long-term averages of NDVI patterns have been compiled and anomalies can be computed. Comparing the NDVI pattern for a given year or month with the 20-year average can reveal whether the productivity in a

given region is normal or anomalous. The net photosynthesis is directly related to the amount of photosynthetically active radiation (PAR) that a plant can absorb. If it absorbs more PAR during the growing season, the photosynthesis will be higher and the more productive it will be. If it absorbs less PAR, it will be less productive. These scenarios get reflected in the value of the NDVI which can be used to monitor the health and productivity of the vegetation and the incidence and spread of agricultural drought.

In addition to NOAA AVHRR data, data from other remote sensing satellites are also used for computing the vegetation index. The difference is that while NOAA satellites pass over a region every day, the other satellites have a repeat cycle which is 10-20 days long and the vegetation can not be monitored in the intervening periods. The various spectral bands used for derivation of NDVI are:

- NOAA AVHRR - bands 1 (0.58-0.68 μ) and 2 (0.72-1.0 μ)
- Landsat MSS - bands 5 (0.6-0.7 μ) and 6 (0.7-0.8 μ) or 7 (0.8-1.1 μ)
- Landsat-4 and Landsat-5 - bands 2 and 3 or 4
- Landsat TM - bands 3 (0.63-0.69 μ) and 4 (0.76-0.90 μ)
- Landsat ETM - bands 3 (0.63-0.69 μ) and 4 (0.75-0.90 μ)

A new data product called the Enhanced Vegetation Index (EVI) is being developed for using MODIS data in bands 1 (0.62-0.67 μ) and 2 (0.841-0.876 μ). EVI is calculated similarly to NDVI, but it corrects for some distortions in the reflected light caused by aerosols. The EVI data product also does not become saturated as easily as the NDVI when viewing rainforests and other areas of the earth with large amounts of chlorophyll.

Prasad et al (2004) assessed the spatial distribution of NDVI for the period 1990-1999 over India and they found a good positive correlation between anomalies in rainfall and NDVI especially for monsoon season. They have prepared a climatic classification map of India based on NDVI and rainfall data and their temporal variation, and made an assessment of drought-affected regions.

3.10 Snow Cover

Snow cover has many different effects on atmospheric and soil processes. Because of its high albedo, it reduces the fraction of solar radiation that can penetrate the soil. Due to its small heat conductivity, snow cover acts as a thermal insulation between the atmosphere and land surface. Melting of snow

causes it to act as a heat sink and a water source. That the Eurasian snow cover has a dominant and inverse relationship with the all-India summer monsoon rainfall, has been known since long, but this continues to be a topic of study (Bamzai et al 1999, Dash et al 2003). Conventional methods of measuring snowfall do not have the high accuracy or the spatial resolution required for quantifying such teleconnections. Therefore, remote sensing of snow cover assumes great importance for monsoon forecasting as well as climate studies (Kulkarni et al 2002).

There are three main long-term data sets of remotely sensed snow cover: (a) Nimbus-7 SMMR, (b) DMSP SSM/I and (c) EASE-Grid. The Nimbus-7 data set consists of monthly global 1° × 1° snow cover and snow depth derived from the Scanning Multi-channel Microwave Radiometer (SMMR) measurements over the period 1978-1987. SSMR was a 10-channel passive radiometer operating at 5 microwave frequencies of 6.63, 10.69, 18, 21 and 37 GHz, all with V and H polarization. Since the emission from the surface at these frequencies gets modified differently by the overlying snow, the snow cover and depth can be derived indirectly. At 37 GHz, microwave radiation gets scattered by the snow in proportion to the snow depth whereas at 18 GHz, it is mainly absorbed by the snow. By using this differential response of the 18 and 37 GHz channels, the snow depth can be empirically computed from the difference in the brightness temperature of the two channels. The method works better with dry snow than wet snow and when the snow depth is more than a minimum threshold value.

The DMSP data set consists of monthly global 1° × 1° and 2.5° × 2.5° snow cover derived from measurements made by the Special Sensor Microwave/Imager (SSM/I) on successive DMSP satellites over the period beginning 1987 to date. SSM/I is a 7-channel passive radiometer operating at 4 microwave frequencies of 19.35, 37 and 85.5 GHz, all with V and H polarization and 22.235 GHz with only V polarization (see also Section 1.3.8). Snow cover scatters the microwave radiation and can be indirectly estimated from the difference in the brightness temperatures of lower (19.35 or 22.235 GHz) and higher frequency channels (37 or 85.5 GHz). Snow can be differentiated from rain by reference to the temperature of the surface. The DMSP data set provides snow cover information in terms of the fractional area of a 1° × 1° or 2.5° × 2.5° grid box covered by snow.

The Northern Hemisphere Equal Area SSM/I Earth (EASE) Grid Weekly Snow Cover and Sea Ice Extent data set covers the period 1978 to date. Prior to 1978, data for snow alone is available from 1966. This data set includes monthly climatology of average snow cover and sea ice, probability of occurrence and variance. The grid size is 25 × 25 km. Besides estimations from SSM/I and Nimbus SMMR, early snow cover values derived from a

manual interpretation of VIS and IR imagery from NOAA and GOES satellites has also been incorporated in the EASE data set.

Mapping of snow cover can be carried out from VIS and NIR imagery manually by visual estimation or in an automated manner by using a suitable algorithm based on the marked contrast in albedo of snow and surrounding land surface. However, when clouds are present, and that happens quite frequently, either the surface may not be seen at all or the clouds may vitiate the scene and reduce the accuracy of the snow cover estimation. INSAT VHRR and CCD imagery has been routinely used to compute the extent of the Himalayan snow cover. The VIS channel has a resolution of 2 km while the CCD channels have a resolution of 1 km. In view of the meteorological and hydrological importance of the Himalayan snow cover, as many Indian rivers have their origin there, data from other satellite sensors like IRS-LISS, WiFS, NOAA-AVHRR, MODIS, etc, have also been used for this purpose. There are, however, many difficulties and likely errors in the snow estimation process. The reflectance and temperature characteristics of the clouds in the Himalayan region are such that they can easily be confused with snow (Kulkarni et al 2003). In winter moths, the sun's inclination is such that the tall mountains cast shadows. Clouds can also cast shadows. Hence multi-spectral analysis has to be done to reduce errors arising from such situations.

3.11 Land Temperature

Compared to SST, the land temperature could be said to be a poorly retrieved satellite parameter, with the main constraint lying in the large geographical variation in the properties of the land and soil surface. It is however required for many purposes such as in atmospheric models for the computation of sensible heat flux from the difference between the land surface temperature and the air temperature near the surface. SST is retrieved from satellite radiance measurements assuming an emissivity of 1, which is quite a valid assumption most of the time. In a similar manner, the Land Surface Temperature (LST) can, theoretically speaking, be derived from AVHRR radiances if the surface emissivity is known or assumed. However, unlike SST, LST has a high diurnal range and even if the emissivity problem is solved, it is another great challenge to interpolate the diurnal cycle from the twice daily values that can be obtained from AVHRR. Moreover, the need for correcting the retrieved temperature for atmospheric attenuation and cloud contamination applies to LST retrievals as well (Sobrino et al 1994).

The conventional screen temperature measured at a ground observatory, is not the soil temperature but the air temperature at the screen height. It is a

thermodynamically defined quantity. LST, as may be measured by a radiometer mounted above the ground surface is, however, a radiatively defined quantity. Although these two parameters are quite related to each other, they differ in value and and physical meaning. There are several other major problems that prevent NOAA AVHRR data from being used to develop a long-term LST data set, such as orbit drift, uncertainties in skin temperature retrieval due to unknown surface emissivity, unknown cloud occurrence during a day other than at observing time, or lack of LST diurnal cycle measurement.

Jin (2004) has made a serious attempt to overcome these problems and produce an LST Diurnal-averaged (LSTD) dataset of monthly skin temperature, monthly maximum skin temperature (T_{max}) and monthly minimum skin temperature (T_{min}), from 1981 to 1998 at 8 km resolution. The dataset is scaled up to a $0.5° \times 0.5°$ latitude/longitude grid, and is comparable to other surface temperature data sets. LSTD can be used to study the climatology of land skin temperature and its diurnal, seasonal, and inter-annual variations on both global and regional scales. Snow screening is done through AVHRR Channel 1 and Channel 2 albedo information.

Global LSTD is useful because it spatially samples more areas than the global observation network and help to reduce any errors in the data-sparse regions. Another advantage of LSTD is that its uniformly high resolution makes it easier to study regional climate particularly over mountains, deserts or regions like the Tibetan plateau.

Singh et al (2006) have proposed a new method to determine near-surface air temperature from satellite observations.

3.12 Atmospheric Ozone

The ozone layer that resides in the earth's stratosphere acts as a natural shield that protects living beings on earth from the harmful effects of the ultraviolet radiation of the sun. A depletion of stratospheric ozone will reduce this protection that we now have, and ozone concentrations therefore need to be monitored carefully on a global scale. There is an extensive global network of spectrophotometer stations that make ground-based measurements of total column ozone and surface ozone levels. At some locations, vertical ozone profiles are being obtained with ozonesondes. As with most other networks, the availability of data is confined to land regions.

The earliest satellite measurements of atmospheric ozone began in 1978 with the Total Ozone Mapping Spectrometer (TOMS) sent on Nimbus-7 satellite,

and they continued aboard the Russian Meteor-3 satellite until December 1994. Another TOMS instrument was launched in July 1996 on the NASA Earth Probe. The total ozone amount is computed by comparing the incoming solar energy and the backscattered UV radiation measured by TOMS at six different wavelengths. This series of TOMS instruments is going to be continued with another TOMS on board the next Japanese ADEOS satellite. It will fly at an altitude of 800 km and complement the TOMS on the Earth Probe which is at a 500 km altitude. This height differentiation is expected to result in a better separation of stratospheric and tropospheric ozone measurements from satellites.

Satellite measurements of stratospheric ozone have greatly helped to generate detailed maps of the global ozone distribution and resulted in startling revelations about what has come to be popularly known as the Antarctic ozone hole. Every year, as spring returns to the southern hemisphere, a series of chemical reactions is set off that result in a depletion of ozone in the stratosphere. The Antarctic ozone hole is an area of exceptionally low concentrations of stratospheric ozone, which begins to develop in August and continues to spread in September and October (Figures 3.12.1 – Colour Plate-2).

On 21 April 1995, the European Space Agency (ESA) launched the Global Ozone Monitoring Experiment (GOME) aboard the second European Remote Sensing satellite (ERS-2). GOME is the first European passive remote sensing instrument whose primary objective is the determination of the amounts and distributions of atmospheric trace constituents. It has four spectral channels 237-316, 311-405, 405-611 and 595-793 nm in the UV, VIS and NIR wavelength regions respectively, with a spectral resolution of 0.20 to 0.33 nm. The ERS-2 satellite moves in a retrograde, sun-synchronous, near-polar orbit at a height of about 795 km. The maximum scan width in the nadir viewing is 960 km and global coverage is achieved within three days. The local crossing time at the equator is 10:30 am.

GOME is a precursor to a more comprehensive mission known as SCIAMACHY, an acronym for Scanning Imaging Absorption Spectrometer for Atmospheric CHartographY. This is a spectrometer designed to measure solar radiation and its reflection and scattering by the earth's surface and atmosphere or surface, in eight channels in the UV, VIS and NIR wavelength regions between 240 and 2380 nm at moderate spectral resolution of 0.2-1.5 nm. SCIAMACHY was launched on the ENVISAT-1 platform in 2002 and it will make a variety of measurements of trace gas concentrations and aerosols in the atmosphere and cloud cover. A special feature of SCIAMACHY is the combined limb-nadir measurement mode, which enables the tropospheric column amounts of several trace gases to be determined.

The NOAA TOVS system which has a 9.7 μ channel that peaks at the wavelength of maximum absorption by stratospheric ozone, has also been providing global total ozone measurements. Using TOVS data, Suresh (2002) studied the variability of total ozone over peninsular India and adjoining ocean. Shyam Lal et al (2003) have made a comprehensive review of various space-based instruments used for atmospheric ozone measurements.

3.13 References

Adler R. F. and Mack R. A., 1988, "Thunderstorm cloud height - rainfall rate relations for use with satellite rainfall estimation techniques", *J. Climatol. Appl. Meteor.*, 23, 280-296.

Arkin P. A. and Meisner B. N., 1987, "The relationship between large-scale convective rainfall and cold cloud cover over the western hemisphere during 1982-84", *Mon. Wea. Rev.*, 115, 51-74.

Arkin P. A., Rao A. V. R. K. and Kelkar R. R., 1989, "Large-scale precipitation and outgoing longwave radiation from INSAT-1B during the 1986 southwest monsoon season", *J. Climate*, 2, 619-628.

Bamzai A. and Shukla J., 1999, "Relation between Eurasian snow cover, snow depth and the Indian summer monsoon: an observational study", *J. Climate*, 12, 3117-3132.

Bhandari S. M. and Varma A. K., 1995, "Estimation of large-scale monthly rainfall over Indian region using minimal INSAT-VHRR data", *Int. J. Remote Sensing*, 16, 2023-2030.

Bhatia R. C., Singh D., Prasad S. and Mukharjee S. K., 2002, "Current status of operationally derived INSAT AMVs quality: details of recent improvements and utilization of derived products", *Proc. Sixth Int. Winds Workshop,* Madison, WI, WMO, 33–43.

Chakraborty A. and Srinivasan J., 2003, "Comparison of radiative fluxes at the top of the atmosphere from INSAT and ERBE", *Mausam*, 54, 299-314.

Chelton D. B. and Wentz F. J., 2005, "Global microwave satellite observations of sea surface and sea surface temperature for numerical weather prediction and climate research", *Bull. Amer. Meteor. Soc.*, 86, 1097-1115.

Dash S. K., Singh O. P., Shekhar M. S. and Vernekar A. D., 2003, "Influence of Eurasian snow depth anomaly on the Indian summer monsoon circulation", *Mausam,* 54, 427-442.

Fujita T., 1969, "Present status of cloud velocity computation from the ATS-I and ATS-III satellites", *Space Research*, IX, North Holland Pub. Co., Amsterdam, 557-570.

Gadgil S. and Joseph P. V., 2003, "On breaks of the Indian monsoon", *Proc. Indian Acad. Sci. (Earth Planet. Sct.)*, 112, 529-558.

Gairola R. M., Varma A. K. and Agarwal V. K., 2003, "Rainfall estimation using spaceborne microwave radar and radiometric measurements", *Mausam*, 54, 89-106.

Gupta H. V., Rengarajan S., Suresh R. and Gupta R. C., 1996, "Reception of HRPT data from NOAA satellites at IMD, Madras", *Vayu Mandal*, 26, 56-59.

Harries J. E. and Crommelynck D., 1999, "The geostationary earth radiation budget experiment on MSG-1 and its potential application", *Adv. Space Res.*, 24, 915–919.

Harries J. E. and coauthors, 2005, "The geostationary earth radiation budget project", *Bull. Amer. Meteor. Soc.*, 86, 945-960.

Hasler A. F., Palaniappan K., Kambhammetu C., Black P., Uhlhorn E. and Chesters D., 1998, "High-resolution wind fields within the inner core and eye of a mature tropical cyclone from GOES 1-min images", *Bull. Amer. Meteor. Soc.*, 79, 2483–2496.

Holmlund K., Velden C., and Rohn M., 2001, "Enhanced automated quality control applied to high-density satellite-derived winds", *Mon. Wea. Rev.*, 129, 517-529.

Holmlund K, 1998, "The utilization of statistical properties of satellite-derived atmospheric motion vectors to derive quality indicators", *Wea. Forecasting*, 13, 1093-1104.

Janowiak J. E., 1992, "Tropical rainfall: a comparison of satellite-derived rainfall estimates with model precipitation forecasts, climatologies and observations", *Mon. Wea. Rev.*, 120, 448-462.

Jin M., 2004, "Analysis of land skin temperature using AVHRR observations", *Bull. Amer. Meteor. Soc.*, 85, 587-600.

Joseph P. V. and Sijikumar S., 2004, "Intraseasonal variability of the low-level jet stream of the Asian summer monsoon", *J. Climate*, 17, 1449-1458.

Joseph P. V., Sooraj K. P. and Rajan C. K., 2006, "The summer monsoon onset process over south Asia and an objective method for the date of monsoon onset over Kerala", *Int. J. Climatol.*, 26.

Kelkar R. R. and Khanna P. N., 1986, "Automated extraction of cloud motion vectors from INSAT-1B imagery", *Mausam*, 37, 495-500.

Kelkar R. R. and Rao A. V. R. K., 1990, "Interannual variability of monsoon rainfall as estimated from INSAT-1B data", *Mausam*, 41, 183-188.

Kelkar R. R., Rao A. V. R. K. and Bhatia R. C., 1993, "Recent improvements in cloud motion vector derivation from INSAT", *Second International Winds Workshop*, Tokyo.

Kelkar R. R., Rao A. V. R. K. and Prasad S., 1993, "Diurnal variation of outgoing longwave radiation derived from INSAT-1B data", *Mausam*, 44, 45-52.

Kerr Y. H. and coauthors, 2001, "Soil moisture retrieval from space: the Soil Moisture and Ocean Salinity (SMOS) mission", IEEE *Transactions on Geoscience and Remote Sensing,* 39, 1729-1735.

Key J. and coauthors, 2003, "Cloud-drift and water vapor winds in the polar regions from MODIS", *IEEE Trans. Geosci. Remote Sens.*, 41, 482-492.

Khanna P. N., Bhatia R. C. and Singh D., 2000, "Recent improvements in the quality of INSAT-derived AMV and their use in NWP". *Proc. of the Fifth Int. Winds Workshop,* Lorne, Australia, WMO, 103-108.

Khanna P. N. and Kelkar R. R., 1993, "Temperature sounding of the atmosphere over the Indian region using satellite data", *Mausam*, 44, 167-174.

Krishnan R., Zhang C. and Sugi M., 2000, "Dynamics of Breaks in the Indian summer monsoon", *J. Atmos. Sci.*, 57, 1354-1372.

Kulkarni A. V., Mathur P., Rathore B. P., Alex S., Thakur N. and Manoj Kumar, 2002, "Effect of global warming on snow ablation pattern in the Himalayas", Current Sci., 83, 120-123.

Kulkarni A. V. and Rathore B. P., 2003, "Snow cover monitoring in Baspa Basin using IRS WiFS data", *Mausam,* 54, 335-340.

Le Marshall J., Leslie L. M., Seecamp R. and Rea A., 2003, "High resolution space based wind observations estimation and application", *Mausam*, 54, 39-50.

Loe B. R., Verma B. L., Giri R. K., Bali S. and Meena L. R., 2006, "Recent very severe tropical cyclones over the Bay of Bengal: analysis with satellite data", *Mausam*, 57, 37-46.

McMillin L. M., Gelman M. E., Sanyal A. and Sylva M., 1988, "A method for use of satellite retrieval as a transfer standard to determine systematic radiosonde errors", *Mon. Wea. Rev.*, 16, 1091-1101.

Menzel W. P., 2001, "Cloud tracking with satellite imagery: from the pioneering work of Ted Fujita to the present", *Bull. Amer. Meteor. Soc.*, 82, 33-47.

Nieman S., Schmetz J., and Menzel P., 1993, "A comparison of several techniques to assign heights to cloud tracers", *J. Appl. Meteor.*, 32, 1559-1568.

Ohring G., Gruber A. and Ellingson R., 1984, "Satellite determination of the relationship between total longwave radiation flux and infrared window radiance", *J. Clim. Appl. Meteor.*, 23, 416-425.

Pai D. S., 1997, "A diagnostic study of interannual variability of Indian summer monsoon using outgoing longwave radiation (OLR) data", *Mausam*, 48, 55-64.

Pattanaik D. R., Jayanthi N. and Mazumdar A. B., 2005a, "Contrasting pre-monsoon features associated with early and late onset of southwest monsoon over Kerala", *Mausam*, 56, 617-626.

Pattanaik D. R., Kalsi S. R. and Hatwar H. R., 2005b, "Evolution of convection anomalies over the Indo-Pacific region in relation to Indian monsoon rainfall", *Mausam*, 56, 811-824.

Pearce A. and Grundlingh M., 2001, "Applications of satellite remote sensing in the southern Indian Ocean", The Indian Ocean – a perspective", Vol. 1, Oxford IBH Pub., 95-158.

Prasad A. K. and coauthors, 2004, "Inter-annual variability of vegetation cover and rainfall over India", *Proc. 35th COSPAR Scientific Assembly*, 18-25 July 2004, Paris, 1015.

Prasad O., Prasad S., Prasad K. and Kelkar R. R., 1998, "Some applications of humidity profiles estimated from INSAT infra-red digial cloud imagery data", *Proc. Indian Acad. Sci., (Earth Planet. Sci.)*,107, 5-18.

Prasad S., Rajawat A. S., Pradhan Y., Chauhan O. S. and Nayak S. R., 2000, "Retrieval of sea surface velocities using sequential Ocean Colour Monitor (OCM) data", *Current Sci.*, 80.

Ramanathan, V., Cess R. D., Harrison E. F., Minnis P., Barkstrom B. R., Ahmad E. and Hartmann D., 1989, "Cloud-radiative forcing and climate: results from the earth radiation budget experiment", *Science*, 243, 57–62.

Rao B. M. and coauthors, 2001, "Large scale soil moisture estimation using microwave radiometer data", *J. Agrometeor.*, 3, 179-187.

Rao A. V. R. K., Kelkar R. R. and Arkin P. A., 1989, "Estimation of precipitation and outgoing longwave radiation from INSAT-1B radiance data", *Mausam*, 40, 123-130.

Roy Bhowmik S. K., Joardar D., Sen Roy S. and Hatwar H. R., 2005, "Mesoscale features of monsoon precipitation system as revealed by the objective analysis of rainfall from the use of high dense land rainfall observations", *Mausam*, 56, 543-548.

Sant Prasad, Khanna P. N., Rao A. V. R. K. and Kelkar R. R., 1990, "Satellite-derived monthly average wind fields over the Indian Ocean in April-July 1988", *Mausam*, 41, 445-450.

Shyam Lal, Sheel V. and Patra P. K., 2003, "Satellite techniques for trace gas measurements", *Mausam*, 54, 315-326.

Shyamala B., 1997, "Satellite studies of monsoon processes", *Proc. First Int. Workshop on Monsoon*, Bali, Indonesia.

Shyamala B and Sudevan S., 1999, "Objective criteria for withdrawal of southwest monsoon based on OLR data", *Mausam*, 50, 406-408.

Singh D., Bhatia R. C., Srivastav S. K. and Singh B., 2003, "Retrieval of atmospheric parameters from NOAA-16 AMSU data over Indian region – preliminary results", *Mausam*, 54, 107-110.

Singh R., Joshi P. C. and Kishtwal C. M., 2006, "A new method to determine near surface air temperature from satellite observations, *Int. J. Remote Sensing*, 27, 2831-2846.

Smith W. L. and coauthors, 1979, "The TIROS-N operational vertical sounder", *Bull. Amer. Meteor. Soc.*, 60, 1177-1187.

Sobrino, J. A., Li Z.-L., Stoll M. P. and Becker F., 1994, "Improvements in the split-window technique for land surface temperature determination", *IEEE Trans. Geosci. Remote Sens.*, 32, 243–253.

Solanki H. U., Dwiwedi R. M. and Nayak S. R., 2001, "Synergistic analysis of SeaWiFS chlorophyll concentration and NOAA-AVHRR SST features for exploring marine living resources", *Int. J. Remote Sensing,* 22, 3877-3882.

Solanki H. U. and coauthors, 2003, "Fishery forecast using OCM chlorophyll concentration and AVHRR SST: validation results off Gujarat coast, India", *Int. J. Remote Sensing,* 24, 3691-3699.

Srivastava A. K. and Rajeevan M., 2004, "Prediction of summer monsoon rainfall over northwest region of India using an OLR index", *Mausam*, 55, 583-590.

Srivastava A. K., Rajeevan M. and Kulkarni R., 2002, "Teleconnection of OLR and SST anomalies over Atlantic Ocean with Indian summer monsoon", *Geophys. Res. Letters*, 29, 125.1-4.

Suresh R., 2002, "On forecasting cyclone movement using TOVS data", *Mausam*, 53, 215-224.

Suresh R., 2002, "On variability of total ozone derived from TOVS data over peninsular Indian sub-continent and adjoining oceanic area", *Mausam*, 53, 503-514.

Suresh R. and Raj Y. E. A., 2001, "Some aspects of Indian northeast monsoon as derived from TOVS data", *Mausam*, 52, 727-732.

Suresh R., Sankaran P. V. and Rengarajan S., 2002, "Atmospheric boundary layer during northeast monsoon over Tamilnadu and neighbourhood - a study using TOVS data", *Mausam*, 53, 75-86.

Thapliyal P. K., Rao B. M., Pal P. K. and Das H. P., 2003, "Potential of IRS-P4 microwave radiometer data for soil moisture sstimation over India", *Mausam,* 54, 277-286

Thapliyal P. K., Pal P. K., Narayanan M. S. and Srinivasan J., 2005, "Development of a time series based methodology for estimation of large area soil Wetness over India using IRS-P4 microwave radiometer data", *J. Appl. Met.*, 44, 127-143.

Velden C., Stettner D. and Daniels J,, 2000, "Wind vector fields derived from GOES rapid scan imagery", Preprints, *10th Conf. on Satellite Meteorology*, Long Beach, CA, Amer. Meteor. Soc., 20–23.

Velden C. and coauthors, 2004, "Determination of wind vectors by tracking features on sequential moisture analyses derived from hyperspectral IR satellite soundings", Preprints, *20th IIPS Conf.,* Seattle, WA, Amer. Meteor. Soc.

Velden C. and coauthors, 2005, "Recent innovations in deriving tropospheric winds from meteorological satellites", *Bull. Amer. Meteor. Soc.*, 86, 205-223.

Walker G. T., 1923, "Correlation in seasonal variations of weather VIII: A preliminary study of world weather", *Memoirs India Meteor. Dept.*, 24, 75-132.

Wentz F. J., Gentemann C., Smith D., and Chelton D., 2000, "Satellite measurements of sea surface temperature through clouds", *Science*, 288, 847–850.

Wielicki, B. A. and coauthors, 2002, "Evidence for large decadal variability in the tropical mean radiative energy budget", *Science*, 295, 841–844.

Chapter 4

Measurement of Parameters by Active Sensors

For many centuries, meteorological observations were made with sensors that respond to the environment in a passive manner. A revolutionary change in this traditional method of observation came about after the Second World War in mid-twentieth century, when radars which had been deployed for spotting enemy targets and airplanes were offered to meteorologists as disposal items. Radars have since come into use in a wide variety of applications in everyday life, and the weather radar has become the operational forecaster's primary tool for viewing rapidly evolving local weather and storms out at sea.

A radar (an abbreviation of RAdio Detection And Ranging) sends out pulses and integrates the return energy over a large volume as a function of range, beam width or spreading, and beam elevation above ground. The transmitted pulse is reflected back to the radar by an object, which is also called a target. The time taken by the pulse to return to the radar is a measure of the distance of the target, called its range. The transmitted pulse may get modified by the target and the characteristics of the returned pulse, or echo, indicate the size and nature of the target. In a Doppler radar the speed of movement of the target can also be measured from the Doppler frequency shift.

Weather radar echoes from clouds are very weak, but rain and hail are very easily detected by most radars and quantitative estimation of rain is possible. They are extremely useful is observations of local severe storms, mesoscale convective complexes, tornadoes and tropical cyclones near the coast. Clear air returns depend on the particulate matter in the atmosphere. As atmospheric refractive index gradients are dependent on the vertical profiles of temperature and humidity, it is possible to estimate wind speeds, wind shear and turbulence.

Radars enable the computation of the precipitation through what are known as 'Z-R Relationships'. Their general from is $Z = A R^b$, R being the rainfall and Z is the radar reflectivity factor or the power returned. The constant b has values in the range 1-2 and constant A in the range 100-300. The best known relationship is $Z=200 R^{1.6}$ (Raghavan 2003). The numerous Z-R relationships are the result of the use of different assumptions with regard to micro-

physical characteristics like drop size distribution, presence of hail, coalescence of drops and evaporation of drops below the cloud base. The relationships are also different because different statistical methods have been used for averaging gauge data over an area. The relationships show a general bias towards larger rain drop sizes and they may be affected by radar errors like beam blockage in hilly terrain and attenuation due to intervening rainfall.

Raingauges on the other hand provide cumulative rainfall amount added over time. For rain rate and intensity measurement, we need to take frequent raingauge readings or have automatic stations. Because of high variability, rainfall averaging over large areas requires a very dense raingauge network. Radars give areal rainfall and frequent measurement is possible making them particularly useful for flood forecasting. However, because of their long and widespread use, raingauges continue to remain as the standard for measuring surface rainfall or "ground truth".

The growth of both radar technology and radar meteorology over the last few decades has indeed been phenomenal, and we now have various types of atmospheric radars operating in different frequencies and serving different areas of applications, in research as well as operations (Raghavan 2003). The X-, C-, and S-band microwave radars are used for purposes of storm detection and measurement of rain drop size and rain rate. Sodars, which use acoustic or sound waves, have applications in studies of atmospheric turbulence in the boundary layer. Lidars operate with optical or light waves and are coming into increasing use for measurement of atmospheric aerosols. Millimetre wave radars provide measurements of cloud physical properties and vertical structure.

UHF/VHF Radars like the MST Radar have been established at many locations around the globe for obtaining vertical profiles of winds and other atmospheric parameters. The name MST radar indicates that its strong beam penetrates the mesosphere, stratosphere and troposphere. India has an MST radar located at Gadanki, near Tirupati. It operates at a frequency of 53 MHz or 6 cm wavelength. It uses the Doppler beam swinging technique to get the three-dimensional wind field. The vertical resolution is as high as 150 m and the time resolution is between 1 and 2 min (Rao et al 1995). The MST radar gives direct measurements of vertical velocities in the atmosphere. Asnani et al (2000) have discussed how in MST radar profiles the vertical velocities change sign every few kilometres of height above ground, and how this leads to the formation of thin layered cirrus clouds particularly over the tropopause.

While the possibility of launching radars on satellites was considered since long, there were great difficulties in realizing it and meteorological remote sensing worked essentially in a passive mode. The fast motion of satellites in low elevation orbits, the extremely long range at geostationary height, and considerations of radar power, weight and antenna size, posed daunting challenges in the way of putting a weather radar in space. The concept of a space-borne precipitation radar mooted way back in 1984 was realized thirteen years later with the launch of the TRMM satellite in 1997. With this development, a new era of active meteorological remote sensing has begun and active sensor technology is now proliferating. Many satellites are already making new types of measurements demanded by meteorological, oceanographic and climate change related applications that passive sensors are unable to cater to, and more satellites are planned to be launched in the near future. These developments are covered in the subsequent sections of this chapter.

4.1 Precipitation

Prior to the satellite era, we did not have a comprehensive understanding of the global rainfall distribution as it is not possible to make routine raingauge measurements over the wide oceans. There is also a sparse density of raingauges over many land areas like mountains and deserts because of logistic problems and there very few precipitation radars around the globe than what are required, because of their very high cost.

The estimation of large-scale precipitation from geostationary IR radiances was a major breakthrough in improving our knowledge of global rainfall patterns, particularly over the oceans, but this method is essentially statistical and does not work on smaller space and time scales and has additional errors over land. Statistical techniques were also developed for deriving rainfall from measurements made by passive microwave sensors, but it was found that different algorithms produced very diverse rain estimates.

The classical view regarding the diurnal variation of precipitation has been that over continental stations, rainfall is maximum in the afternoon and has a convective nature, and that over coastal and island stations, it is maximum at night or in the early morning. However, this has many exceptions and terrain irregularities cause intense mesoscale diurnal circulations which alter the pattern (Asnani 2005). *In situ* observations over the oceans are too sparse to arrive at any firm conclusions and only satellite studies can throw light on the diurnal precipitation variation over the oceans (Murakami 1983).

In summary, although meteorological satellites have greatly helped us to improve our knowledge of the global distribution of rainfall, many aspects such as rainfall amounts over the tropical oceans, the diurnal cycle of precipitation, the rain rate and its vertical profile, have continued to remain largely uncertain and unvalidated. At the same time, since a major contribution to the energy that drives the atmospheric circulation comes from the latent heat released by tropical precipitation, climate prediction modellers are demanding a far greater accuracy in the precipitation measurements that go as inputs into their models.

The idea of measuring rainfall from a satellite having a combination of passive sensors and a microwave radar instrument was mooted in the early 1980s and it took the shape of a proposal to launch a Tropical Rainfall Measuring Mission (TRMM). Several orbits and altitudes were considered from among which an inclined orbit extending between 35°N and 35°S at 350 km altitude was chosen. The inclined orbit precessed in such a manner that the satellite would fly over a given location at a different time every day with a repeat cycle of about 2 days. This orbit would allow the measurement of the large diurnal variation of tropical rainfall.

The TRMM project went through a long process of evolution and eventually took the form of a joint mission between NASA and the Japan Aerospace Exploration Agency (JAXA). TRMM became the first satellite to have an on-board radar to measure precipitation quantitatively from space.

TRMM satellite was launched on 27 November 1997 in a low earth orbit at a height of 350 km and an inclination of 35° that views the tropical region viewed many times a day (Kummerow et al 2000). The TRMM science objectives are to map the 4-dimensional structure of latent heat, understand the role of latent heat in the weather and climate of the tropics, obtain monthly average rainfall over the tropics and examine the diurnal cycle of tropical rainfall and timing of heaviest rainfall. In line with these objectives, TRMM data are being used to quantify the relative contributions of convective and stratiform rain, develop a better understanding of the hydrological cycle, study the latent heat inputs global energy and water cycles, study how tropical rainfall influences global circulation, and to improve modelling and prediction.

4.1.1 TRMM Precipitation Radar

For a radar on board a geostationary satellite, the range will be enormous while polar orbiting satellites move at high speed with respect to earth and there is less dwell time. The beam width has to be narrow enough to be fully

filled with precipitation (Varma et al 2004). The swath has to be wide enough to eliminate gaps in coverage. A space-borne radar should be able to discriminate the weak precipitation echo over the strong return from the earth's surface. It is desirable to use wavelengths shorter than 3-10 cm, which are used in conventional weather radars, as at shorter wavelengths the return echo is stronger.

The basic payload of TRMM is the Precipitation Radar (PR). It also carries a 9-channel passive TRMM Microwave Imager (TMI) which is similar to the SSM/I, and a Visible Infrared Scanner (VIRS) which makes measurements in the VIS and IR channels like the AVHRR. Besides these three primary payloads, TRMM has two other instruments, the Clouds and the Earth's Radiant Energy System (CERES), and the Lightning Imaging Sensor (LIS). PR, TMI and VIRS are designed to obtain rainfall and other relevant information such as rain type, height of the bright band, cloud type and cloud top height individually and complement each other's functions.

A detailed description of the three primary TRMM payloads, PR, TMI and VIRS, has been given by Kummerow et al (1998). The PR is a 128-element phased array system operating at two frequencies, 13.796 and 13.802 GHz. The PR has a horizontal resolution of 4.3 km at nadir and a swath width of 215 km. One of its most important features is its ability to provide vertical profiles of rain and snow from the surface up to a height of 20 km at a vertical resolution of 250 m. The PR can perceive rain through clouds and detect even light rain rates of the order of 0.5 mm/hr. At intense rain rates, where the attenuation effects can be strong, new methods of data processing have been developed that help correct for this effect. The power requirement of the PR is incredibly low, just 224 watts.

Several algorithms have been developed to derive estimates of rainfall rate and vertical rainfall profiles from the PR data (Iguchi et al 2000). The TRMM 2A25 algorithm produces an attenuation-corrected estimate of the vertical rainfall rate profile for each radar beam. The rainfall rate estimate is given at each resolution cell of the PR radar. To compare with ground-based radar data, the attenuation-corrected Z factor profile is also given. The estimated near-surface rainfall rate and average rainfall rate between the two predefined altitudes of 2 and 4 km are also calculated for each beam position. Other output data include parameters of Z-R relationships, integrated rain rate of each beam, range bin numbers of rain layer boundaries and many intermediate parameters.

There is an extensive plan for validation of TRMM rainfall under which a large number of validation sites have been set up globally to generate ground truth. Radars and gauge networks are involved.

The first attempt to use TRMM rainfall information to estimate the four-dimensional latent heating structure over the global tropics for one month, February 1998, was made by Tao et al (2001). Adler et al (2003) have analysed three years of TRMM monthly estimates of tropical surface rainfall to document and understand the differences among the TRMM-based estimates and compare them with pre-TRMM estimates and current operational analyses. Variation among the TRMM estimates is shown to be considerably smaller than with pre-TRMM collection of passive microwave-based products. TRMM estimates are shown to have a range of about 20% for the tropical ocean as a whole and 30 % over heavily raining ocean areas of the ITCZ. In mid-latitude ocean areas the differences are smaller. Over land there is a distinct difference between the tropics and middle latitudes.

The diurnal variation of precipitation has been studied by Nesbitt et al (2003) using three years of TRMM data. Over the oceans, the diurnal cycle of rainfall has a small amplitude, with the maximum contribution to rainfall coming from mesoscale convective systems (MCSs) in the early morning. Land areas have a much larger rainfall cycle than over the ocean, with a marked minimum in the mid-morning hours and a maximum in the afternoon, slowly decreasing through midnight. They also found that non-MCS features have a significant peak in afternoon convective intensities, which differs from previous studies using rain rates derived from hourly rain gauge data. MCSs over land have a convective intensity peak in the late afternoon. However, all land regions have MCS rainfall peaks that occur in the late evening through midnight due to their longer life cycle. The diurnal cycle of MCS rainfall over land and convective intensity varies significantly from one region to another.

Hirose et al (2005) investigated the spatial and diurnal variation of rainfall over Asia using TRMM PR data for 1998-2003. Small precipitation systems occurred most frequently around early afternoon over land. The south-facing slopes of the Himalayas, especially the upper portion of the Brahmaputra valley, are the most obvious region of the daytime genesis of the convective systems over the Asian landmass. Over the Tibetan Plateau the occurrence of the small systems was larger than over inland India and the foothills. Large systems developed mostly in the evening over nearly flat landmasses. Widespread systems with intense rain pixels developed over the foothills of the Himalayas in the late night to early morning period, which was distinct from the daytime convection.

The TRMM Precipitation Radar is the first space-borne instrument to provide three-dimensional maps of tropical storm structure. The measurements yield invaluable information on intensity, distribution and type of the rain and the height at which the snow melts into rain. The TRMM Microwave Imager (TMI) measures the amount of energy scattered by the ice particles. The more ice there is, the more energy is scattered, meaning smaller amounts of energy are received by TRMM and lowest values of returned energy (200° K) represent the most intense clouds. By following a sequence of TRMM images, changes in the structure of the eyewall and rain bands with time can be analysed. Many times the evolution of a double eyewall can be clearly seen. These signals help in estimating whether a storm will intensify or weaken.

Cecil et al (2002) documented 261 overpasses of 45 hurricanes by the TRMM satellite during 1997-98, with the observed radar reflectivity values, passive microwave ice scattering magnitudes, and total lightning. Properties of the three regions of the hurricane, eyewall, inner rain band, and outer rain band were treated separately and compared to other tropical oceanic and tropical continental precipitation systems. Reflectivity profiles and ice scattering signatures are found to be fairly similar for both hurricane and non-hurricane tropical oceanic precipitation systems, although the hurricane inner rain band region yields the weakest of these convective signatures. When normalized by the area experiencing significant convection, the outer rainband region produces more lightning than the rest of the hurricane or non-hurricane tropical oceanic systems. As a whole, the tropical oceanic precipitation systems, both hurricane and non-hurricane, are dominated by stratiform rain and relatively weak convection.

Hurricane Katrina which became a Category 5 hurricane in the central Gulf of Mexico, began as a tropical depression in the central Bahamas on the afternoon of 23 August 2005. The TRMM PR image (Figure 4.1.1.1-Colour Plate-3) shows a three-dimensional perspective of Katrina with a cross-section through the eye. Two isolated tall towers (in red) are seen, one in an outer rain band and the other in the northeastern part of the eyewall. This area of deep convection in the eyewall extending to 16 km is associated with the area of intense rainfall. Such tall towers near the core are often an indication of intensification as was true with Katrina.

Figure 4.1.1.2 (Colour Plate-4) is a TRMM image centred on the west coast of India at 10:09 UTC on 26 July 2005 and clearly showing the exceptionally heavy rainfall over the city of Mumbai. Rain rates in the centre part of the swath are measured by the TRMM PR, and those in the outer swath are from

the TMI. The image brings out the highly localized nature of the rainfall event.

4.2 Cloud Properties

For over four decades, satellite meteorology had focused on the observation of global cloud cover and interpretation of cloud patterns as indicators of the development and movement of weather systems. That clouds are not just passive tracers or end products of atmospheric processes, but that they play an independent and dominant role in them is, however, a comparatively recent realization. It is now accepted that even small changes in the global cloud distribution are more likely to affect the future climate than what greenhouse gases and anthropogenic aerosols may do (Wielicki et al 1995, Glecker et al 1995).

Clouds occupy a crucial place in the hydrological cycle, acting as the link between the condensation of atmospheric water vapour and occurrence of precipitation. Clouds develop in regions of high relative humidity and in turn affect the moisture distribution. As clouds form, condensation releases latent heat. Clouds are also a major component of the earth's radiation budget as they reflect solar radiation back to space, and absorb and emit terrestrial thermal radiation. Any long term change in cloud distribution will therefore result in modifying the redistribution of heating within the atmosphere. It is further possible that changes in climate may in turn give rise to changes in clouds and these feedbacks could be either positive or negative. At the same time, many of the climate models currently in use suffer from large discrepancies in the poleward transport of heat due to a poor resolution of cloud layers and inadequate representation of their radiative properties (Stocker et al 2001). For overcoming these difficulties, the type of observations of clouds that current meteorological satellites are able to provide and the vertically integrated products that can be derived from them are not sufficient. What is required is an entirely new type of satellite instrument that would make measurements of the vertical structure of clouds.

While the three-dimensional geometrical properties of clouds like fractional cloud cover and cloud boundaries directly enter the process of solving the radiative transfer equations, microphysical properties of the hydrometeors they contain, like ice or water phase, particle size, shape, non-sphericity and orientation, and fall velocity of cloud particles, are no less important. The cloud feedbacks produced by atmospheric general circulation models differ both in magnitude and sign depending on the manner in which the cloud optical properties are treated (Yao et al 1999). The following sections describe the recent advances in space-based measurements of cloud

properties by dedicated satellite missions that complement the general imaging capabilities of meteorological satellites.

4.2.1 POLDER

The visible solar radiation coming from the sun is not polarized, but certain physical processes on earth result in generating polarized light. Satellite imageries in the VIS channel show bright areas called sunglint over calm oceans at certain times. They are less apparent when the sea surface is rough (see section 1.4.3). However, in addition to reflection, polarization also takes place, which can be measured by a satellite.

The measurement of polarization which is not done by the operational meteorological satellites, helps to clearly identify the cloud phase, because liquid droplets have a highly specific signature in a preferred viewing direction. Polarization data, when combined with directionality, helps to determine the physical and optical properties of aerosols and clouds and their influence on the earth's radiation budget (Bellouin et al 2003).

An instrument for measuring the POLarization and Directionality of the Earth's Reflectances (POLDER) was flown on two Japanese satellites, ADEOS-I (August 1996 to June 1997) and ADEOS-II (December 2002 to October 2004). It had a camera comprising a two-dimensional CCD detector array, wide field of view optics and a rotating wheel carrying spectral and polarized filters. Both the satellites were in a sun-synchronous orbit with a 10:30 am descending node, flying at an altitude of 800 km and having a repeat cycle of 4 days. POLDER had a total of 9 spectral bands, out of which three bands, 443, 670 and 865 nm, had polarized filters (Buriez et al 1997, Deuze et al 2000). Currently, POLDER is flying on the PARASOL satellite which was launched on 18 December 2004 for a 2-year mission. PARASOL is an acronym for Polarization and Anisotropy of Reflectances for Atmospheric Sciences coupled with Observations from a Lidar.

For updates on the POLDER mission and latest results and images, the reader is referred to the CNES web site http://smsc.cnes.fr/POLDER/.

4.2.2 CloudSat Cloud Profiling Radar

The basic premise of remote sensing is that by viewing the same object or surface in different bands or regions of the electromagnetic spectrum, different properties of the object come to light. A VIS image of a cloud indicates the reflection of solar radiation from its top, whereas an IR image

indicates the temperature and so the height of the cloud top. Likewise if a cloud could be scanned simultaneously by a radar and a lidar, different regions of the cloud would respond with different sensitivity to the centimetre or millimetre wavelength of the radar and the nanometre wavelength of the lidar. The relatively wider beam of the radar would be more sensitive to large particles, while finer particles would be better observed by the narrow beam of the lidar. The radar and lidar can thus be used together so as to complement each other's capabilities and provide a more complete description of the cloud top, base and depth with a higher precision than they can do individually.

The drop size distribution of a cloud depends on several factors such as the updraft velocity, concentration of cloud condensation nuclei and the height above the cloud base. The optical depth and albedo of a cloud are a function of the water content and effective radius. Formation of precipitation by the warm cloud process requires that some drops grow large enough for efficient coalescence.

Satellite measurement of cloud properties became a reality with the successful launch of two satellites, CloudSat and CALIPSO, on 28 April 2006. CloudSat carries a mm-wave radar and CALIPSO has on board a backscattering lidar. The pair of satellites forms a unique combination of radar and lidar in space. The CloudSat mission has been designed to serve for two years to enable more than one seasonal cycle to be observed, although there are high expectations that the radar would last for another year. Stephens et al (2002) have given an excellent overview of the CloudSat mission, onboard instruments, data processing and validation plans.

The science objectives of CloudSat are to observe the vertical structure of clouds, measure the profiles of cloud liquid water, ice water content and optical properties. They will help to determine how clouds affect both the local and large-scale environment, and to validate the results of cloud process models and cloud parameterizations in global scale models.

Ground-based weather radars generally operate at wavelengths of 2 to 15 cm in the X, C and S bands to enable the detection of raindrop-sized particles. Radars operating at 3 or 8 mm (94 or 35 GHz) can detect the much smaller particles of liquid water and ice that constitute the large cloud masses. Many millimetre-wave radars have been in use on ground since long and have also been flown on NASA DC-8 aircraft since 1998. The CloudSat Cloud Profiling Radar (CPR) which was developed jointly by NASA/Jet Propulsion Laboratory and the Canadian Space Agency is, however, the first mm-wavelength cloud radar to fly in space. The CPR is a 94 GHz nadir-looking

radar which measures the power backscattered by clouds as a function of distance from the radar. The orbit of CloudSat is identical to the sun-synchronous, 705 km altitude, polar orbit of the Aqua satellite.

The choice of the radar frequency is a critical consideration in the CPR design and applications. The sensitivity and antenna gain increase with frequency while atmospheric transmission and transmitter efficiency decrease with frequency. In order to achieve sufficient cloud detection sensitivity, a relatively low frequency (<94 GHz) radar would require an enormous antenna and high peak power. At frequencies much greater than 100 GHz, a large antenna and high peak power are also needed due to rapid signal attenuation through cloud absorption. Furthermore, technologies at such high frequencies are less developed. The choice of frequency means that a small percentage of the time when very thick clouds or heavy precipitation is present, CPR will not be able to penetrate to the cloud base. The 94 GHz frequency chosen for CPR offers the best compromise, meeting performance within the spacecraft resources. It is a trade-off between sensitivity, antenna gain, atmospheric transmission and radar transmitter efficiency.

The design of the CPR is driven by the science objectives of the CloudSat mission. The antenna diameter is 1.95 m, the pulse width is 3.3 μsec, and the pulse repetition frequency is 4300 Hz. The minimum detectable reflectivity factor is -26 dBZ, and the dynamic range is 70 dB. The CPR has an along-track resolution of 3.5 km and cross-track resolution of 1.2 km, and a vertical resolution of 500 m.

Besides the CPR, the CloudSat spacecraft also carries several other instruments including the dual-wavelength lidar system of CALIPSO, and the Aqua instrument suite comprising CERES, AIRS, AMSR and MODIS.

At the time of writing this book, the CloudSat CPR has already started sending images. Figure 4.2.2.1 (Colour Plate-5) shows two images of Hurricane Ileana over the east Pacific Ocean on 23 August 2006. The GOES image at the top gives a view of the hurricane from above. The CloudSat image below it is a sideways view of the same system. The CloudSat image is a slice through the hurricane along the line marked AB. The region of the eye appears empty or dark in the CloudSat image. The red and purple areas indicate large amounts of cloud water. The blue areas along the top of the clouds indicate cloud ice. The wavy blue lines on the bottom center of the image indicate intense rainfall. Further information, latest images and updates, are available at the web sites http://www.nasa.gov / mission_pages/cloudsat/ and http:// cloudsat.atmos.colostate.edu/.

4.2.3 CALIPSO Cloud-Aerosol Lidar

The Cloud-Aerosol Lidar and Infrared Pathfinder Satellite Observation (CALIPSO) mission was launched on 28 April 2006 simultaneously with CloudSat as mentioned in the preceding section. CALIPSO is a joint U.S.-French (NASA-CNES) enterprise and the satellite has an expected life of three years during which it will provide a new insight into the role that clouds and atmospheric aerosols play in regulating the earth's weather, climate and air quality.

Detailed information is available in the literature (Reagan et al 2002 and Winker et al 2003, 2004), and at the NASA CALIPSO portal http://www.nasa.gov/mission_pages/calipso/ which the reader is advised to visit for viewing the latest images and knowing the current status of the mission.

The CALIPSO payload consists of three co-aligned nadir-viewing instruments. The primary payload is the Cloud-Aerosol Lidar with Orthogonal Polarization (CALIOP), which is a dual-wavelength polarization-sensitive Nd YAG lidar that provides high resolution vertical profiles of aerosols and clouds. CALIOP measures the 1064 nm backscatter intensity and has two more receiver channels for measuring orthogonally polarized components of the 532 nm backscattered signal. The receiver telescope is 1 m in diameter. Measurement of the linear depolarization of the backscattered return allows discrimination of the cloud phase and detection of non-spherical aerosols.

The second payload on CALIPSO is the Imaging Infrared Radiometer (IIR) that provides calibrated IR radiances at wavelengths of 8.65, 10.6 and 12.0 μ. IIR is a nadir-viewing, non-scanning imager having a 64 × 64 km swath with a pixel size of 1 km. The CALIOP beam is nominally aligned with the centre of the IIR image. The three wavelengths were selected to optimize joint CALIOP/IIR retrievals of cirrus cloud emissivity and particle size.

CALIPSO also has a high-resolution Wide Field Camera (WFC) that acquires high spatial resolution imagery. It is a fixed, nadir-viewing imager with a single spectral channel covering the 620-670 nm region, selected to match Band 1 of the MODIS instrument on Aqua.

The CALIOP lidar operates on the same principle as a radar except that the laser transmits pulses of green light and IR energy to the target instead of microwave energy. The transmitted light interacts with and is changed by the target. Some of this light is reflected or scattered back to the instrument. The change in the properties of the light enables some property of the target to be

determined. The time for the light to travel out to the target and back to the lidar is used to determine the range to the target.

CALIOP has a basic vertical resolution of 30-60 m and a horizontal resolution of 333 m. However, the atmosphere becomes more spatially uniform with increasing altitude, and signals from higher levels in the atmosphere tend to be weaker. Therefore, an altitude-dependent on-board averaging scheme was developed which provides full resolution in the lower troposphere, where the spatial variability of cloud and aerosol is greatest, and lesser resolution in the upper atmosphere.

The fundamental science objective of the CALIPSO mission is to provide vertically resolved information on aerosol distribution, extinction coefficient, hydration state, discrimination of large and small particles, and cloud masking, in order to enable climate models to estimate direct as well as indirect aerosol forcing and reduce uncertainty. Another science objective of CALIPSO is to provide comprehensive observations of cloud height, thickness and multi-layering, for more accurate computation of surface and atmospheric radiative fluxes in global climate models. Modelling of cloud-radiation feedbacks and interactions, which involves the prediction of cloud properties and then using them to compute radiative fluxes, is also expected to benefit from the simultaneous observations of clouds, radiation, and atmospheric state that CALIPSO and other satellites will provide. CALIPSO began its lidar operations on 7 June 2006 and has already proved its ability to detect cloud layers, aerosols and volcanic plumes.

4.2.4 A-Train

The CALIPSO and CloudSat satellites have highly complementary functions. They will together provide totally new 3-dimensional perspectives of clouds and aerosols. Flying in formation (Stephens et al 2002), CALIPSO and CloudSat provide a direct overlap of the lidar footprint within the footprint of the radar more than 70% of the time and within 1.5 km of each other at all times.

So far, the term "formation flying" has been commonly used to describe the disciplined and orderly flying of birds and aircrafts that results in exhibiting a geometrical pattern in the sky. This concept has now been extended to satellites. Satellites in a formation flying mode, are made to fly in matched orbits, keep a certain distance from each other and maintain a predetermined relative geometry. Between 2006 and 2008, six satellites will be flying in a formation that has been named as the "A-Train" (Anderson et al 2005). The six-element constellation comprises Aqua, Aura, PARASOL, CloudSat,

CALIPSO and OCO, in which CloudSAT is the satellite which is subjected to the adjustments required to keep the formation in order.

The A-Train concept provides for the first time, a synergy among different sensors, overlapping footprints and complementary capabilities in terms of retrieved quantities, sensitivity, resolution, coverage, and joint product retrievals. It now makes it possible to obtain an ensemble of near-simultaneous measurements of aerosols, clouds, temperature, relative humidity and radiative fluxes over the globe during all seasons. All satellites in the constellation have a nominal orbital altitude of 705 km and inclination of 98° with a repeat cycle of 16 days. The Aqua satellite leads the constellation with an equatorial crossing time of about 1:30 pm. CloudSat and CALIPSO trail behind it by just a couple of minutes and the two satellites themselves are separated from each other by just 10-15 seconds (Vincent et al 2004). PARASOL lags behind CALIPSO by a minute. Aura trails Aqua by about 15 minutes but it crosses the equator 8 minutes behind Aqua due to its different orbital track which allows for synergy with Aqua. The sixth satellite, the Orbiting Carbon Observatory (OCO), which is yet to be launched, is designed for making measurements of carbon dioxide concentrations and will precede Aqua by 15 minutes. Detailed and updated information on the configuration of the A-Train and the instruments and payloads carried by the various satellites is available at the NASA web site http://www-calipso.larc.nasa.gov/about/atrain.php.

4.3 Sea Surface Winds

While winds can be estimated from cloud motion as viewed in successive images of geostationary satellites, the wind vectors cannot be derived at the surface level by this technique for obvious reasons. Hence for knowing the wind patterns at the ocean surface with high accuracy, alternative means such as a scatterometer have to be used.

A scatterometer is an active microwave sensor, or a kind of radar, that can measure the reflection or scattering effect produced while scanning the surface of the earth from an aircraft or a satellite. The measurements can be made equally well in cloudy and clear conditions. A rough ocean surface returns a stronger signal because the waves reflect more of the radar energy back toward the scatterometer antenna. A smooth ocean surface returns a weaker signal because less of the energy is reflected. The principle of the scatterometer is that since the radar backscatter returned to the satellite is modified by waves or ripples on the ocean surface, by measuring the backscatter the surface wind velocity can be retrieved.

Scatterometers have significantly enhanced the ability to detect and track severe storms and cyclones by providing direct measurements of winds at the sea surface. Scatterometer data have vital applications in various fields such as studies of air-sea interaction, ocean circulation, deforestation or changes in polar sea ice masses. Scatterometer measurements of ocean surface wind speed and direction have also been proved useful in improving the forecast accuracy of numerical weather prediction models by providing the initial fields particularly in the region of tropical storms.

4.3.1 ERS Scatterometers

The first space-borne scatterometer was flown on the Seasat satellite in 1978, but the mission was very short-lived. In recent times, four scatterometers have been launched on satellites, two by the European Space Agency (ESA) and two by NASA. One scatterometer was launched by ESA on the European Remote Sensing Satellite (ERS-1) in August 1991, followed by an identical instrument on ERS-2, which was launched in April 1995. The ERS scatterometers operate at 5.3 GHz frequency in the C-band with a resolution of 50 km.

The ERS scatterometer is designed with three antennas that generate radar beams with vertical polarizations looking 45° forward, sideways and backward with respect to the flight direction of the satellite. These beams continuously illuminate a 500 km wide swath as the satellite moves along its orbit. Thus three backscatter measurements of each grid point are obtained at different viewing angles and separated by a short time delay. These measurements which are called triplets, are fed to a mathematical model which calculates surface wind speed and direction.

At a given angle to the flight path of the satellite, the amount of backscatter depends on the size of the surface ripples of the ocean, i.e. surface roughness, and their orientation with respect to the direction of propagation of the pulse of radiation transmitted by the scatterometer. The first factor is dependent on the surface wind stress while the second is related to the wind direction. Hence both wind speed and direction can be derived. The root mean square errors of the wind speed and direction retrievals are of the order of 1.4 m/sec and 19° respectively (Freilich et al 1999), the wind direction ambiguity being a major limitation.

4.3.2 NSCAT and QuikSCAT

The NASA Scatterometer (NSCAT) was launched in August 1996 on the first Japanese Advanced Earth Observing Satellite (ADEOS-1) as a joint U.S.-Japan project. The instrument was operated at a Ku-band frequency of 13.995 GHz. The Ku-band is more sensitive to wind variation at low wind speeds but is more subject to rain contamination. Shorter ocean surface waves have a stronger influence on backscatter at higher frequencies.

NSACT had six dual-polarized, 3 m long, fan-beam, stick-like antennas that collected backscatter data at 45°, 115°, and 135° azimuth angles with a resolution of 25 km. NSCAT worked for only nine months as the satellite lost power.

Following the loss of NSCAT, NASA launched another scatterometer named Quick Scatterometer (QuikSCAT) in June 1999 as a quick recovery mission. This is also a Ku-band instrument that uses pencil-beam antennas in a conical scan and has a continuous 1800 km swath that covers 93% of the global ocean in a single day. It operates at a frequency of 13.4 GHz and provides a wind vector resolution of 25 km. Wind speed is measured in the range of 3 to 20 m/sec with an accuracy of 2 m/sec, and wind direction with an accuracy of 20°. The accuracy of QuikSCAT wind measurements exceeds instrument specification, and is better than NSCAT.

Sarkar (2003) has given an exhaustive review of space-based techniques for measurement of sea surface winds, including the use of passive microwave sensors like SSM/I for derivation of sea surface wind magnitude. Another review of the use of scatterometer data over the oceans and its emerging applications over land and ice surfaces, has been made by Liu (2002).

The pulsations of the Somali jet of intense southwesterly surface winds over the Arabian Sea (see Section 2.3.2), were studied by Halpern et al (1998, 1999) using NSCAT and ERS scatterometer data. The data at 2-day intervals clearly revealed the eastward expansion of the jet speed winds and an increase in NSCAT-derived surface wind convergence as well as in the SSMI-derived integrated cloud liquid water content.

Small vortices, in their formative stages, are too small to be resolved by operational numerical weather prediction products, and they have no clear signals in cloud imagery. Scatterometer data therefore have great potential in spotting such vortices and their development into mature tropical cyclones, although there are many problems to circumvent.

Figure 4.3.2.1 (Colour Plate-6) is a composite image showing the surface winds in hurricane Floyd as it approached the Bahamas on 13 September 1999, measured by the QuikScat scatterometer and rain rate as measured by the TRMM precipitation radar at around the same time.

Loe et al (2006) have studied the impact of QuikSCAT scatterometer winds on the intensity estimation and track prediction of two recent cyclones over the Bay of Bengal. They found that the view of the low-level circulation provided by the scatterometer winds was very helpful in determining the outer wind structure during the weak tropical cyclone stage.

4.3.3 Oceansat-2 Scatterometer

The Indian Space Research Organisation (ISRO) has a continuing programme of launching satellites for oceanographic and related atmospheric applications. Oceansat-1 was launched on 26 May 1999 (see Section 3.7) and it carried an Ocean Colour Monitor and a Multi-frequency Scanning Microwave Radiometer (MSMR).

The second Indian satellite in this series, Oceansat-2, is expected to be launched into a near polar sun-synchronous orbit of 720 km altitude by 2007. Oceansat-2 will carry another OCM and for the first time, a Wind Scatterometer. This will be a Ku-band pencil-beam scatterometer, similar to NASA QuickSCAT operating at 13.515 GHz. A conically scanning antenna will transmit microwave pulses and receive the backscattered power from the ocean surface from which wind vector information will be derived. This scatterometer will operate with two beams, the inner beam in horizontal polarization and the outer beam in vertical polarization. The resolution will be 50 km. Both the OCM and the wind scatterometer payloads are also to be carried on the next Indian satellite, Oceansat-3, which may be go into orbit in 2009.

4.4 Sea Surface Height

The term mean sea level refers to the height of the sea surface against a local reference point, averaged over a long period of time to remove the fluctuations due to waves and tides. This term has been popularly used and understood, as the elevation of land is expressed as the height above the mean sea level. In recent times, however, the topic of sea level rise has come into prominence in connection with global warming and climate change. Since the sea level could rise because of thermal expansion of the ocean and

also because of the inflow of water arising from melting of glaciers (Church et al 2001), accurate monitoring of the sea surface height has assumed great importance. Sea level rise will not only have consequences for the ocean-atmosphere system itself, but it also poses a serious threat to the populations residing in coastal regions and islands.

Before the climate change aspects of sea level came into the picture, mapping of the sea surface height was confined to geological and oceanographic interests. The present geological and topographic structures of the ocean floor are the result of plate tectonic activity over millions of years. Although ocean floor geology is much simpler than continental geology, it has remained under-investigated because electromagnetic waves cannot penetrate the sea water. However, the topography of the ocean floor shows up through the undulations of the ocean surface which can be measured globally with a radar altimeter placed on a satellite (Ali 2003).

Data obtained from altimeters can be used to map the geographical variation of sea level change and to validate the predictions of climate models. Altimeter data is also being fed into weather and climate models used to calculate the transport of heat, water mass, nutrients and salt by the oceans, and to better understand the ocean circulation and its seasonal changes. Satellite altimeters have made a revolutionary impact on the estimation of ocean tides. Since tides account for 80 % of the sea surface height variations, it is critical to eliminate their contribution when studying ocean circulation using altimeter data.

A satellite-borne altimeter is basically a microwave radar operating at a frequency in which the sea surface acts as a good reflector. The radar pulse illuminates a spot on the sea surface which is large enough to smooth the effects of local waves and ripples, and a high pulse repetition rate is used to improve the signal to noise ratio, especially when the ocean surface is rough. The two-way travel time gives the height of the satellite above the sea surface. It must be remembered here that the aim is to detect changes in the sea level of the order of millimetres from a satellite altitude of several hundred kilometres. The process demands extreme precision and the satellite position itself has to be tracked by a global network of lasers and Doppler ranging stations. Corrections have to be applied to the travel time of the pulse to account for ionospheric and atmospheric delays, and known tidal corrections are made as well. The sea surface height is calculated as the difference between the distance of the satellite from the centre of the earth and the distance between the sea surface and the satellite as measured by the altimeter.

The slope of the altimeter return pulse is stretched in time because of the delay between reflections from the wave crests and troughs. This helps to estimate the significant wave height which itself is useful in correcting the sea surface height observations. The strength of the return pulse is an indicator of the wind speed. The altimeter is the only instrument that can provide real time information on the sea state and the waves generated by cyclonic storms. However, altimeter measurements have several sources of error and need to be properly corrected before use. The errors could first of all arise from within the instrument itself (Haines et al 1998). Another set of errors could be attributed to the fact that the actual speed of propagation of electromagnetic radiation in the atmosphere may not be the same as that used in the computations. Additional errors may creep in due to ocean tides, inverse barometer effects, and inaccuracies in the modelling of the geoid itself (Ali 2003).

4.4.1 TOPEX/Poseidon

Seasat was the world's oceanographic satellite, launched on 26 June 1978, with very a complex array of advanced sensing instruments, passive as well as active, such as a wind scatterometer, synthetic aperture radar and a radar altimeter. The satellite had an extremely short life of just over three months but it sent down very valuable data (Fedor et al 1982). It may be mentioned that even before Seasat, altimeters had been flown on SkyLab in 1973 and Geos-3 in 1978.

Against this past experience, the first successful radar altimeter mission may be said to be that of Geosat, which was launched by the U.S. Navy in 1985 and worked for more than four years. It had a horizontal resolution of 10-15 km, a vertical resolution of 3 cm and a repeat cycle of 17 days.

TOPEX/Poseidon was launched on 10 August 1992 as a joint NASA-CNES programme. The satellite was positioned at an altitude of 1336 km, in a circular, non-sun-synchronous, 66° inclination orbit covering 95 % of the world's ice-free oceans between 66°N and 66°S latitudes with a 10-day repeat cycle.

The satellite carried two radar altimeters, NASA TOPEX operating at two frequencies 13.6 and 5.3 GHz in the Ku- and C-band respectively, and CNES Poseidon operating at 13.65 GHz in the Ku-band. It also carried a 3-channel NASA microwave radiometer to measure total water vapour along the altimeter path and use it to correct for pulse delay. The NASA Global Positioning System Payload (GPSP) receiver provided precise orbit and

ephemeris data. An essential accompaniment was the CNES DORIS system (Doppler Orbitography and Radio-positioning Integrated by Satellite) which received signals from ground beacons for precise orbit determination, satellite tracking and ionospheric correction data for the CNES altimeter. The NASA Laser Retroreflector Array (LRA) payload served as a target for laser ranging stations on ground stations to track the satellite, calibrate the other satellite location systems and verify altimeter measurements.

The range measurements after correction for atmospheric and instrumental effects, were accurate to 3-4 cm. The range measurements when subtracted from estimates of the satellite orbital height, resulted in ocean height measurements of 4-5 cm accuracy relative to the centre of the earth. This accuracy figure pertained to a spot on the ocean surface of the size of a few kilometres directly beneath the TOPEX/Poseidon satellite. By averaging the thousands of measurements collected by the satellite in the 10 days time that it took to cover the global oceans, global mean sea level could be determined with a precision of the order of millimetres.

The TOPEX/Poseidon mission lasted about 14 years, until the satellite was de-commissioned on 18 January 2006. TOPEX/Poseidon could be said to have revolutionized oceanography as during its lifetime, it has given the longest ever and most complete direct observations of sea level change, including the El Nino event of 1997.

Satellite-determined sea surface height is not affected by vertical land movements as in tide gauge observations and satellite data are in great abundance compared to the sparse tide gauge network observations, enabling global as well as regional sea level change to be determined (Cazenave et al 1997, 1998). An analysis of the first six years of TOPEX/Poseidon data revealed that the rate of global average sea level was around 2 mm/yr. Thus the rate of sea level rise during the 1990s was greater than the mean rate for much of the twentieth century. It is not clear whether this is the result of a recent acceleration, of systematic differences between two measurement techniques, or of the shortness of the record (Church et al 2001).

A comparison of surface wind speed and wave parameters derived from the TOPEX/Poseidon altimeter with ocean buoy data has been made for the Indian Ocean by Kshatriya et al (2001).

4.4.2 Jason and OSTM

On 7 December 2001, the Jason-1 satellite, another joint NASA-CNES venture, was launched as a replacement of the TOPEX/Poseidon mission and

placed in the same orbit with similar instruments. It is continuing to make the same measurements. Parallelly, on 1 March 2002, ESA's ENVISAT satellite was launched with another radar altimeter in an orbit repeating at 35 days instead of 10 days for Jason and sampled the ocean on a smaller spatial scale, complementing the Jason data.

During the period when both Jason-1 and TOPEX/Poseidon were operational, the two satellites were made to fly in tandem, providing twice the coverage of the sea surface. In the tandem mission, Jason-1 was positioned to move along the same ground track as that of TOPEX/Poseidon which was commanded to move onto a parallel ground track so that it was mid-way between two adjacent Jason ground tracks. The near simultaneous measurements from the same altitude of the same sea surface locations by Jason and TOPEX/Poseidon altimeters enabled a rigorous comparison and correlation of their altimetry results. The will allow Jason to continue seamlessly adding to the nine years of TOPEX/Poseidon data. -

The joint U. S. - Europe Ocean Surface Topography Mission (OSTM/Jason-2) is expected to be launched in June 2008. This will extend the time series of ocean surface topography measurements beyond TOPEX/Poseidon and Jason time frames to accomplish two decades of observations.

The OSTM satellite is to be launched into the same orbit as that of Jason-1. It will maintain the same measurement accuracy of Jason (3-4 cm) with a goal of achieving an even better figure of 2.5 cm. It will maintain the stability of the global mean sea level measurement with a drift less than 1 mm/year over the life of the mission and the accuracy of significant wave height to 50 cm or 10% of the value, whichever is greater.

The satellite payloads will include the CNES Poseidon-3 Altimeter (C- and Ku-band) to measure height above sea surface, the NASA Advanced Microwave Radiometer (AMR) with 3 channels to measure total water vapour along the altimeter path to correct for pulse delay, and the other three instruments carried by Jason.

The progress of the OSTM/Jason-2 mission as it moves nearer to its launch in 2008 can be watched on the NASA web site http://sealevel.jpl.nasa.gov/mission/ostm.html.

Around 2009, another altimeter called AltiKa, working in Ka-band at 35 GHz, is likely to be launched aboard the Indian Oceansat-3 satellite as a joint India-France mission and will complement Jason-2.

With the success of the TOPEX/Poseidon and Jason-1 missions, satellite altimeter products have found their way into many research programmes such as WOCE (World Ocean Circulation Experiment), and GODAE (Global Ocean Data Assimilation Experiment. In parallel, ocean models are expected to reach increasing levels of performance and new initiatives like ARGO will enhance the global *in situ* observation network. The next challenge would be use the data in operational oceanography for making seasonal ocean forecasts of currents, temperature and salinity, and short range forecasts of wave height and wind speed. These would be of great benefit to ship routing, and ecosystem and coastal zone management and such other activities.

An extensive overview of the applications of satellite remote sensing to oceanography, specially in the context of the Indian Ocean, is available in the literature (Pearce et al 2001). Another review of the current state and future prospects of satellite oceanography has been made by Gairola et al (2000).

4.5 References

Adler R. F. and coauthors, 2003, "Status of TRMM monthly estimates of tropical precipitation", *Meteor. Monogr., Amer. Meteor. Soc.*, 29, 223 pp.

Ali M. M., 2003, "Satellite altimetry for meteorological and oceanographic applications", *Mausam*, 54, 205-214.

Anderson T. L. and coauthors, 2005, "An "A-Train" strategy for quantifying direct climate forcing by anthropogenic aerosols", *Bull. Amer. Meteor. Soc.*, 86, 1795-1809.

Asnani G. C. and coauthors, 2000, "Patchy layered structure of tropical troposphere", *Indian J. Radio Space Physics*, 29, 182-191.

Asnani G. C., 2005, "Special features of tropics, monsoons", *Tropical Meteorology*, Vol. 1, Chapter 1, 16-37.

Bellouin N., Boucher O., Tanre D. and Dubovik O., 2003, "Aerosol absorption over the clear-sky oceans deduced from POLDER-1 and AERONET observations", *Geophys. Res. Lett.*, 30, 1748-1751.

Buriez J.-C. and coauthors, 1997, "Cloud detection and derivation of cloud properties from POLDER", *Int. J. Remote Sens.*, 18, 2785–2813.

Cazenave A. and coauthors, 1997, "Caspian sea level from Topex-Poseidon altimetry: level now falling", *Geophys. Res. Lett.*, 24, 881-884.

Cazenave A. and coauthors, 1998, "Global mean sea level changes observed by Topex-Poseidon and ERS-1", *Physical Chemical Earth*, 23, 1069-75.

Cecil D. J., Zipser E. J. and Nesbitt S. W., 2002, "Reflectivity, ice scattering, and lightning characteristics of hurricane eyewalls and rainbands. Part I: quantitative description", *Mon. Wea. Rev.*, 130, 769-784.

Church J. A. and coauthors, 2001, "Changes in sea level", *Climate Change 2001 The Scientific Basis, IPCC WG I Third Assessment Report*, Chapter 11, 639-693.

Deuze J. L. and coauthors, 2000, "Estimate of the aerosol properties over the ocean with POLDER", *J. Geophys. Res.*, 105, 15329-15346.

Fedor L. S. and Brown G.S., 1982, "Wave height and wind speed measurements from the Seasat radar altimeter", *J. Geophys. Res.*,87, 3254-3260.

Freilich M. H. and Dunbar S., 1999, "The accuracy of the NSCAT-1 vector winds: comparisons with National Data Buoy Center buoys". *J. Geophys. Res.*, 104, 11231-11246.

Gairola R. M. and Pandey P. C., 2000, "Satellite oceanography: review of the progress and future prospects", *Proc. Indian National Sci. Academy*, 66, 317-365.

Glecker, P. J. and coauthors, 1995, "Cloud-radiative effects on implied oceanic energy transports as simulated by atmospheric general circulation models", *Geophys. Res. Lett.*, 22, 791–794.

Haines B. J. and Bar-Sever Y. E., 1998, "Monitoring the TOPEX microwave radiometer with GPS: stability of columnar water vapor measurements", *Geophys. Res. Lett.*, 25, 3563-3666.

Halpern D., Freilich M. H. and Weller R. A., 1998, "Arabian Sea surface winds and ocean transports determined from ERS-1 scatterometer", *J. Geophys. Res.*, 103, 7799-7805.

Halpern, D. and Woiceshyn P. M., 1999, "Onset of the Somali jet in the Arabian Sea during June 1997", *J. Geophys. Res.*, 104, 18041-18046.

Hirose M. and Nakamura K., 2005, "Spatial and diurnal variation of precipitation systems over Asia observed by the TRMM precipitation radar", *J. Geophys. Res.*, 110, D05106.

Iguchi T. and coauthors, 2000, "Rain-profiling algorithm for the TRMM precipitation radar", *J. Appl. Meteor.*, 39, 2038–2052.

Kummerow C., Barnes W., Kozu T., Shiue J. and Simpson J., 1998, "The Tropical Rainfall Measuring Mission (TRMM) Sensor Package", *J. Atm. Ocean. Technol.*, 15, 809–817.

Kshatriya J., Sarkar A. and Raj Kumar, 2001, "Comparison of TOPEX/Poseidon altimeter derived wind speed and wave parameters with ocean buoy data in the north Indian Ocean", *Marine Geodesy*, 24, 131-138.

Kummerow C. and coauthors, 2000, "The status of the Tropical Rainfall Measuring Mission (TRMM) after two years in orbit", *J. Appl. Meteor.*, 39, 1965–1982.

Liu W. T., 2002, "Progress in scatterometer application", *J. Oceanogr.*, 58, 121-136.

Loe B. R., Verma B. L., Giri R. K., Bali S. and Meena L. R., 2006, "Recent very severe tropical cyclones over the Bay of Bengal: analysis with satellite data", *Mausam*, 57, 37-46.

Murakami M., 1983, "Analysis of the deep convective activity over the western Pacific and southeast Asia, Part I: diurnal variation", *J. Meteor. Soc. Japan*, 61, 60-75.

Nesbitt S. W. and Zipser E. J., 2003, "The diurnal cycle of rainfall and convective intensity according to three years of TRMM measurements", *J. Climate*, 16, 1456-1475.

Pearce A. and Grundlingh M., 2001, "Applications of satellite remote sensing in the southern Indian Ocean", *The Indian Ocean - a perspective*, Vol. 1, Oxford IBH Pub., 95-158.

Raghavan S., 2003, *Radar Meteorology*, Kluwer Academic Publishers, 549 pp.

Rao P. B. and coauthors, 1995, "Indian MST radar I –system description and sample vector wind measurements in ST mode", *Radio Sci.*, 30, 1125-1138.

Reagan J. A., Wang X. and Osborn M. T., 2002, "Spaceborne lidar calibration from cirrus and molecular backscatter returns," *Trans. Geosci. Rem. Sens.*, 40, 2285-2290.

Sarkar A., 2003, "Space based techniques for remote sensing of oceanic winds – a review", *Mausam*, 54, 111-120.

Stephens G. L. and others, 2002, "The CloudSat mission and the A-Train: a new dimension of space-based observations of clouds and precipitation", *Bull. Amer. Meteor. Soc.*, 83, 1771–1790.

Stocker T. F. and coauthors, 2001, "Physical climate processes and feedbacks", *Climate Change 2001 The Scientific Basis, IPCC WG I Third Assessment Report*, Chapter 7, 417-470.

Tao W.-K. and coauthors, 2001, "Retrieved vertical profiles of latent heat release using TRMM rainfall products for February 1998", *J. Appl. Meteor.*, 40, 957-982.

Varma A. K., Liu G. and Noh Y. J., 2004, "Sub-pixel scale variability of rainfall and its application to mitigate the beam filling problem", *J. Geophys. Res.*, 109, D18210.

Vincent M. A. and Salcedo C., 2004, "The insertion of CloudSat and Calipso into the A-Train constellation", *Adv. Astronautical Sci.*, 116, Part II, 1401-1418.

Wielicki B. A. Cess R. D., King M. D., Randall D. A. and Harrison E. F., 1995, "Mission to planet earth: role of clouds and radiation in climate", *Bull. Amer. Meteor. Soc.*, 76, 2125–2153.

Winker D. M., Pelon J. and McCormick M. P., 2003, "The CALIPSO mission: spaceborne lidar for observation of aerosols and clouds," *Proc. SPIE*, 4893, 1-11.

Winker D. M., Hunt W. and Hostetler C., 2004 "Status and performance of the CALIOP lidar", *Proc. SPIE*, 5575, 8-15.

Yao M-S. and Del Genio A. D., 1999, "Effect of cloud parameterization on the simulation of climatec change in the GISS GCM", *J. Climate*, 12, 761-779.

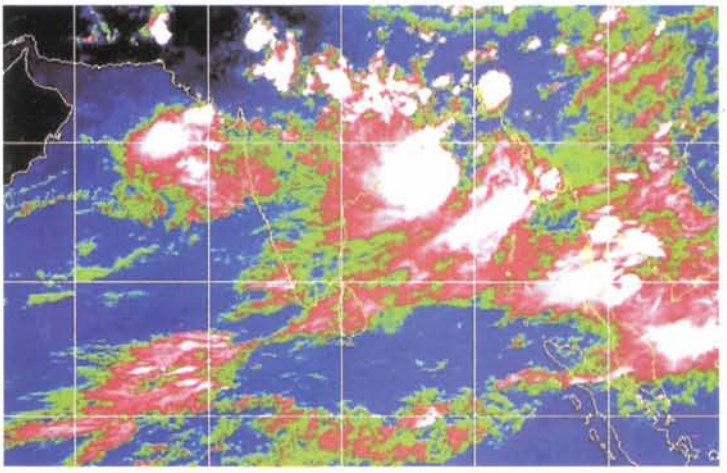

Figure 1.4.2.4 Colour enhancement showing strong convection in red and tallest clouds in gray (Source: http://www.cimms.ssec.wisc.edu/)

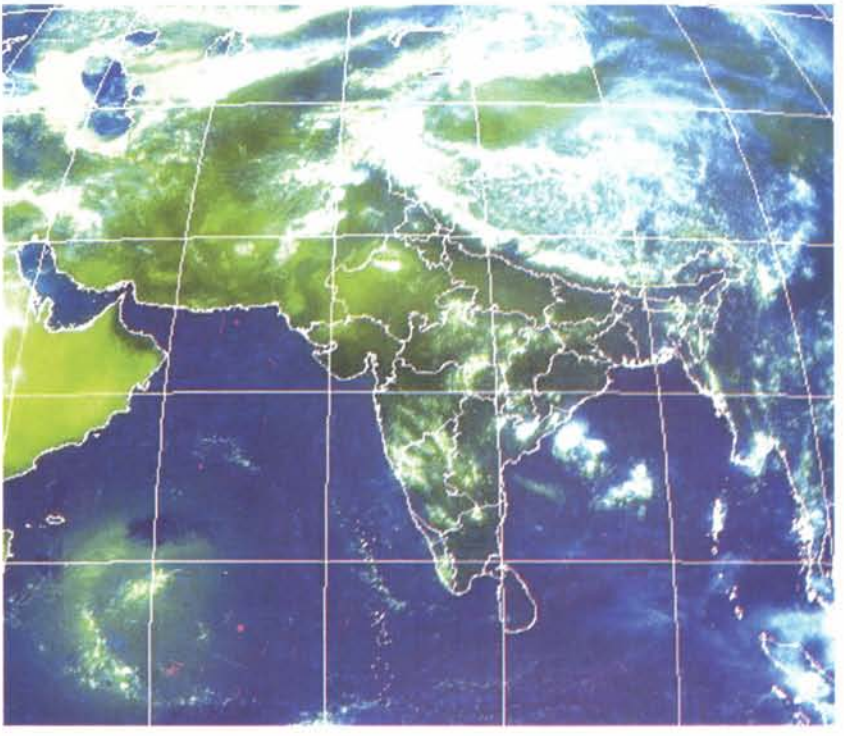

Figure 1.4.2.5 Example of pseudocolour imagery generated by a combination of VIS and IR images (Source: IMD)

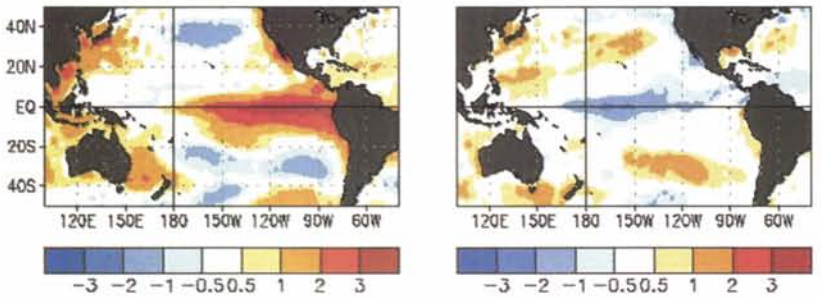

Figure 3.5.1 Satellite –derived SST anomalies over the Pacific Ocean during (left) major El Nino of 1998 and (right) major La Nina 1989 showing opposite signs of the anomaly patterns (Source: http://www.cpc.ncep.noaa.gov/products/analysis_monitoring/ensocycle/)

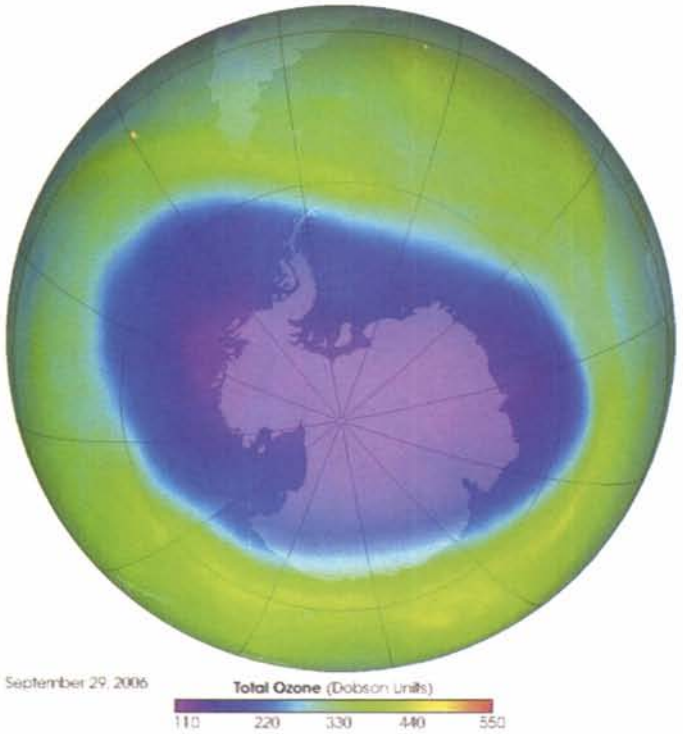

Figure 3.12.1 Image taken on 29 September 2006 by the Ozone Measuring Instrument on NASA's Aura satellite, showing the Antarctic Ozone Hole, as the blue and purple area where ozone amounts are below 220 Dobson Units (Source: http://earthobservatory.nasa.gov/Newsroom/NewImages/)

Colour Plate 2

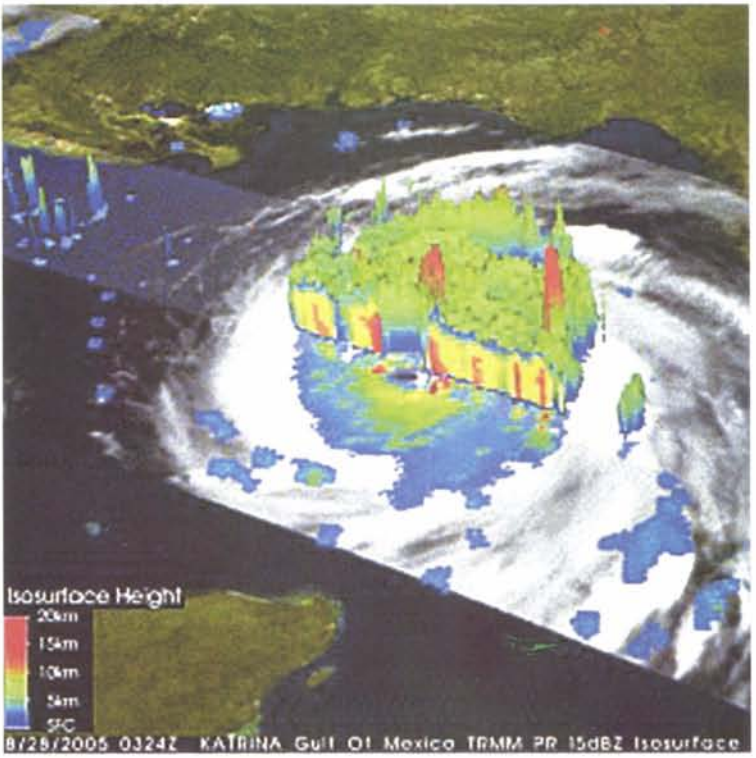

Figure 4.1.1.1 TRMM-PR image of 25 August 2005 showing a cross-section through Hurricane Katrina (Source: http://trmm.gsfc.nasa.gov/trmm_rain/)

Colour Plate 3

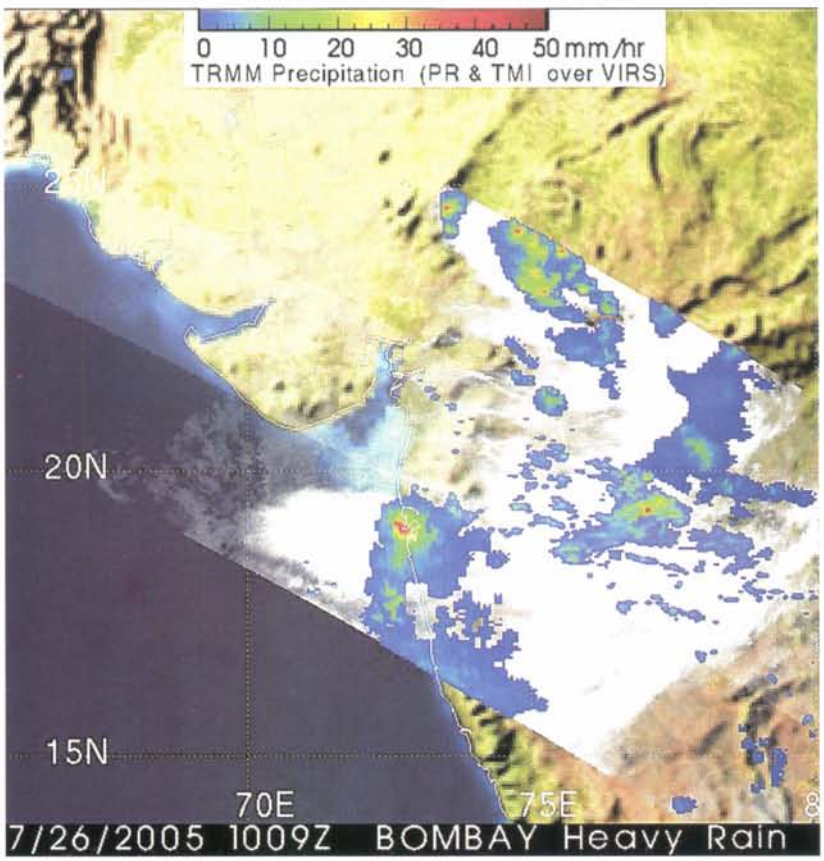

Figure 4.1.1.2 TRMM composite PR/TMI image centred on the west coast of India showing showing the exceptionally heavy rainfall (red area) over the city of Mumbai on 26 July 2005 (Source: http://trmm.gsfc.nasa.gov/trmm_rain/Events/bombay_26july05_1009utc.gif)

Colour Plate 4

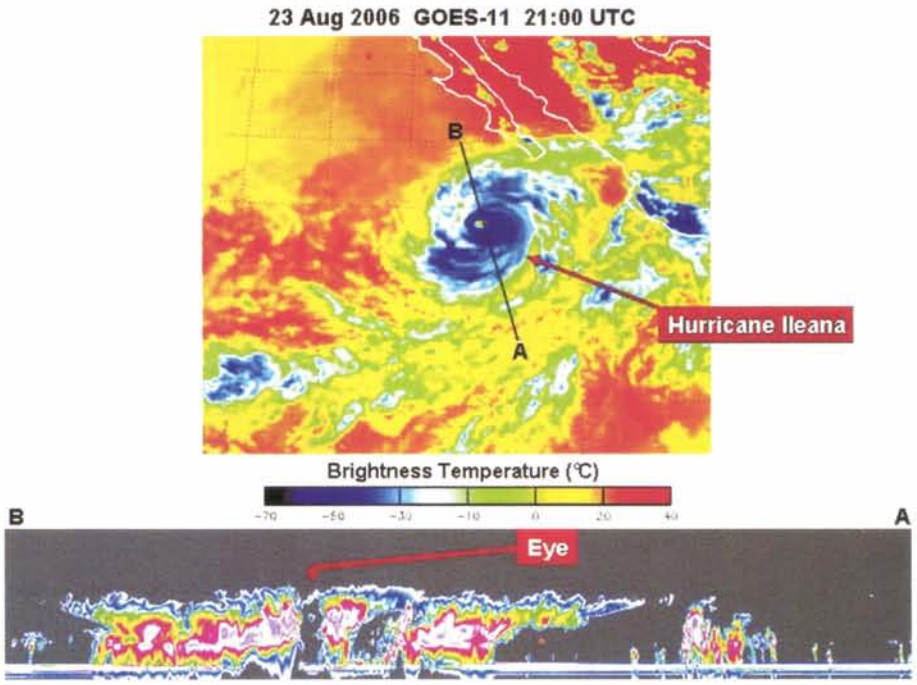

Figure 4.2.2.1 Hurricane Ileana over the east Pacific Ocean on 23 August 2006 as viewed by the GOES satellite from the top and sliced through the hurricane along the line marked AB by the CloudSat CPR. The region of the eye appears dark in the CloudSat image. The red and purple areas indicate large amounts of cloud water.
(Source: http://www.nasa.gov/mission_pages/cloudsat/)

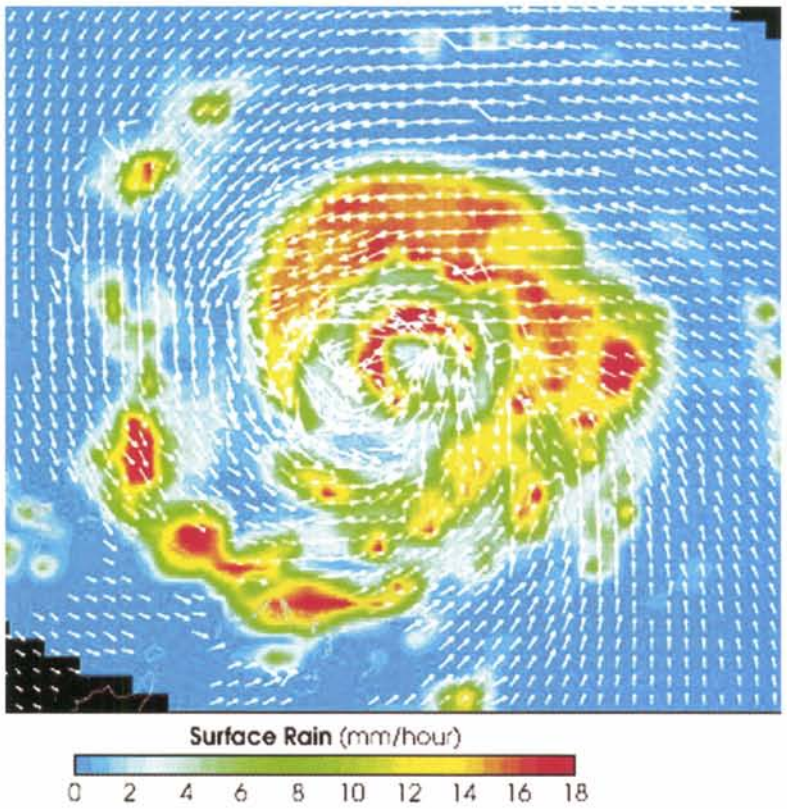

Figure 4.3.2.1 Coincident surface winds in hurricane Floyd on 13 September 1999, as measured by the QuikScat scatterometer and rain rate as measured by the TRMM precipitation radar
(Source: http://earthobservatory.nasa.gov/Newsroom/NewImages/)

Colour Plate 6

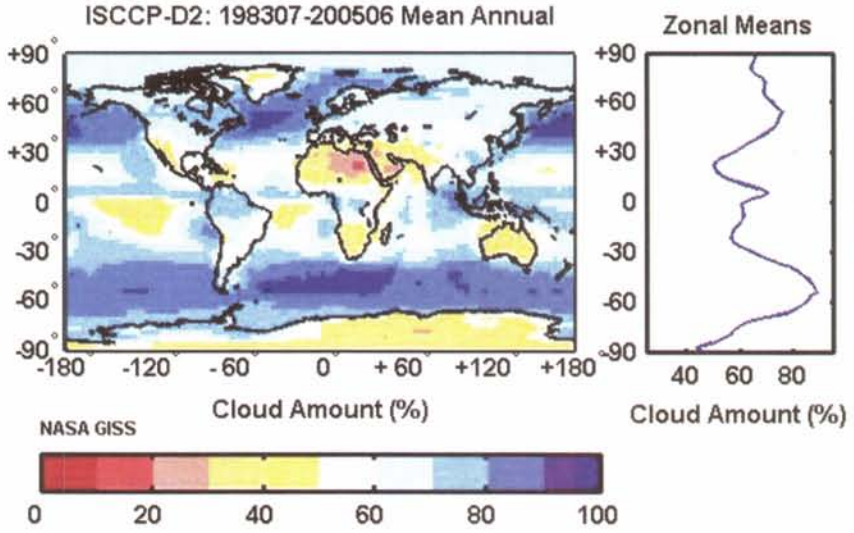

Figure 5.7.2 ISCCP global climatology of mean annual cloud amount for 1983-2005 period (Source: http://isccp.giss.nasa.gov/)

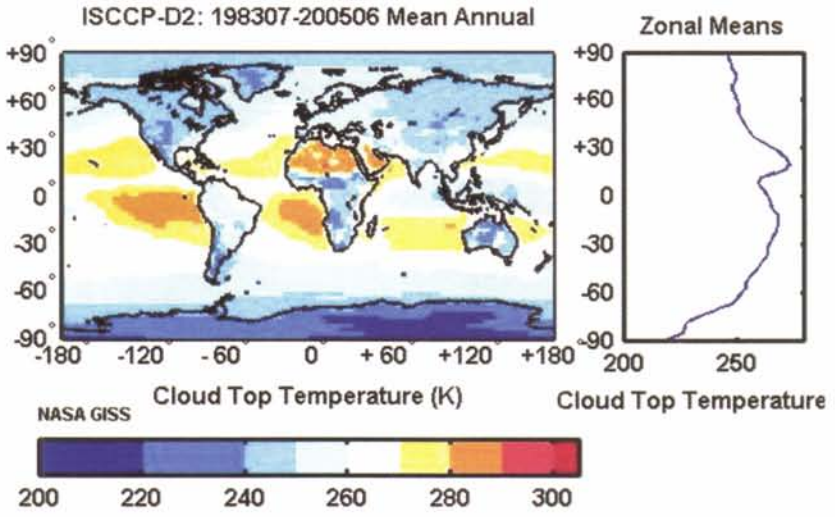

Figure 5.7.3 ISCCP global climatology of mean annual cloud top temperature for 1983-2005 period (Source: http://isccp.giss.nasa.gov/)

Colour Plate 7

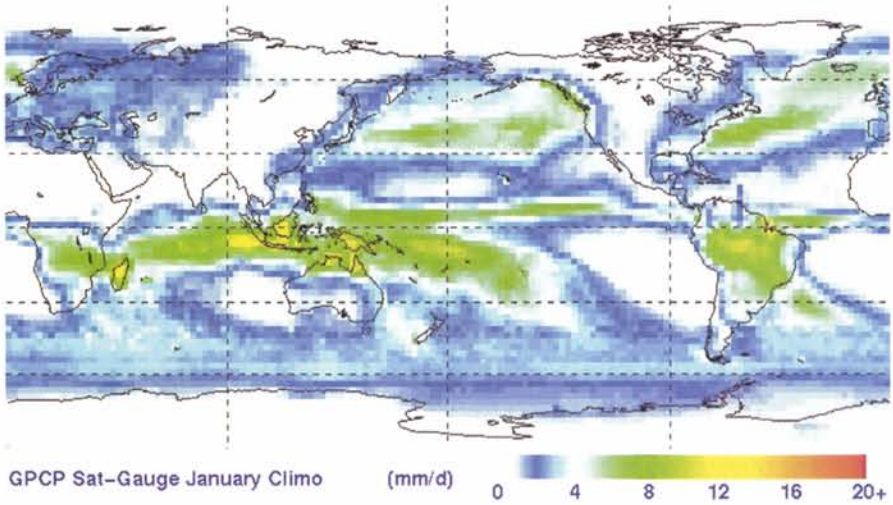

Figure 5.8.1 GPCP global mean rainfall for January
(Source: http://precip.gsfc.nasa.gov/gifs/v2.79-02.climo.0001.gif)

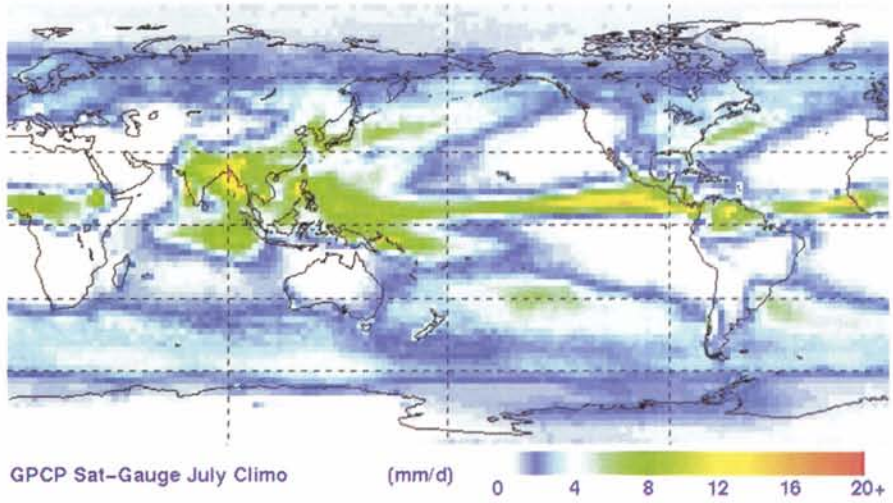

Figure 5.8.2 GPCP global mean rainfall for July (Source: http://
precip.gsfc.nasa.gov/gifs/v2.79-02.climo.0001.gif)

Colour Plate 8

Chapter 5

Satellite Inputs for Numerical Modelling and Climate Studies

The cost of operating and maintaining the global network of meteorological observing stations is increasing continuously and becoming uneconomical for many countries. Many observatories have being replaced by automatic weather stations and some upper air stations making daily radiosonde flights either have been closed down or are under a threat of closure. While methods of weather forecasting based on synoptic charts and analysis require synoptic observations, the demands of numerical weather modeling for observational data are comparatively very stringent as the accuracy of the model predictions depends on the prescription of the initial state. In contrast to the dwindling surface component of the global observation system and the continuing sparseness of data over the oceans and many land regions, the space component of the observing system has made remarkable strides in recent years (Hinsman 2003). Satellite observations and derived products are becoming freely available in real time on a global scale and meteorological satellite systems are being constantly upgraded and improved.

Continuous efforts are therefore being made to assimilate the satellite data and satellite-derived products into the numerical models in order to improve the forecasts. This is not easy because the satellite data are available on time and space scales that are very different from those of synoptic weather observations. Many parameters are not available from the terrestrial network at all, or are not observed over the spatial and temporal resolutions demanded by the models.

There has been a steady improvement in the performance of numerical models over the last decade, especially over the southern hemisphere. The noticeable improvements in the late nineties are, to a significant degree, due to direct assimilation of satellite radiances and derived products. However, there is a substantial scope for further improvement of the performance of the models, and it is obvious that assimilation of future satellite observations will be a deciding factor.

Although the primary objective of the operational weather satellites of various countries has been to augment the conventional inputs available to weather forecasters and modellers, the satellite data are being used in a

manner aiming far beyond these immediate objectives. Many satellite measurements and derived products are being used for validating atmosphere-ocean models, in climate simulation experiments and for diagnostic studies of the climate system (Kelkar 1993). Although the record lengths of these new data are much shorter than conventional data, and there are problems like sensor degradation and calibration errors to overcome, the extensive coverage in space and time compensates for their shortcomings (Kelkar 1994). Thus while it may appear paradoxical that for studying global and climate change, use is being of an observational record that is relatively the shortest, meteorological satellites have even been named as sentinels for the monitoring of climate and global change (Ohring et al 1991).

It is certain that in the years to come, satellite data are going to continue playing a vital role in climate studies and modelling. The World Climate Research Programme (WCRP) has specified that it expects observations from space missions to:

(a) provide for long-term monitoring to detect and attribute climate trends and changes through continuous, systematic, consistent and accurate observations,

(b) allow for short-term studies of specific climate-related processes through experimental observations and long-term statistical studies of the interaction of multiple processes, and

(c) provide global observations to appropriately initialize and validate models for climate prediction from seasonal through decadal to centennial time scales, including prediction of anthropogenic climate change.

The requirements of building up long-term climate data based from space-based observations are thus very stringent compared to those for weather monitoring and they involve strict quality control of satellite data and derived products, corrections for deterioration of sensors on-board, regular calibration and inter-satellite comparisons for merger of data sets obtained from different satellites over different time periods. There is a great need for validation of satellite data and products with ground truth, development of algorithms and software for product derivation and their constant refinement in the light of experience gained.

5.1 Use of Satellite Data for Initialisation of Numerical Models

The earliest impact of satellite data on regional and global NWP was through the assimilation of cloud motion vectors derived from geostationary satellites

routinely using all types of cloud motion vectors derived from IR, high-resolution VIS and WV images and rapid-scan images (Le Marshall et al 2003, Su et al 2003) as they are clearly seen to be beneficial to the forecast process.

The European Centre for Medium-range Weather Forecasts (ECMWF) assimilates a wide variety of satellite data in the 4D-Var analysis system (Courtier et al 1994). Humidity profiles data are assimilated from HIRS, AMSU-B, AIRS and SSM/I on polar orbiting platforms, as well as from the imaging instruments on a number of geostationary platforms. The most recent addition to this observing system is data from the SEVIRI water vapour channels flown on the new MSG satellites (Szyndel et al 2005). All these data, together with data from Meteosat-5, GOES-9, GOES-10 and GOES-12, give a total coverage of the tropics with fine temporal resolution. It has been found that the use of two WV channels from geostationary orbit appear to improve the humidity analysis which in turn improves the geopotential anomaly correlation in the northern hemisphere, as well as the vector winds in the tropics.

A recent observing system experiment conducted by the ECMWF has demonstrated the impact of various satellite observing systems on model forecasts (Kelly 2004) by removing the satellite inputs systematically and assessing how the model performance deteriorates without them. Experimental runs were made for various data scenarios like without any satellite data at all, with only CMWs removed and with only AMSU radiances removed. The OSE covered an 89-day period during 2002. The assimilation of CMWs was found to have a significant impact on the ECMWF forecast performance in the tropics while the impact was not as dramatic in the mid-latitudes of the southern hemisphere.

Several such studies of the impact of assimilation of satellite data and products have been made in India also, by the National Centre for Medium Range Weather Forecasting and the India Meteorological Department. Das Gupta et al (2003) have assessed the impact of assimilation of NOAA ATOVS temperature and moisture profiles at 120 km grid resolution on the NCMRWF global analysis-forecast system. Assimilation cycles were re-run using ATOVS data for the month of September 2001 and the monsoon onset phase of 2002. There was an overall improvement in the 72 hr precipitation forecast over the oceanic areas but not over high precipitation areas over land. ATOVS data were found to be helpful in maintaining the strength of the low level jet and cross-equatorial flow in up to 120 hr predictions.

During the monsoon seasons of 2000 and 2001, sea surface wind speeds and total precipitable water vapour content data from five different microwave

sensors, TRMM TMI, DMSP SSM/I and Oceansat-1 MSMR were assimilated by NCMRWF in several experimental runs (Kar et al 2003). The results were compared with the operational runs in which such data were not used and were found to have had made a significant improvement in the removal of the dry bias and the winds over the oceanic regions.

Roy Bhowmik et al (2005) in another study involving Oceansat-1 showed that MSMR-derived surface winds had a positive impact on the NCMRWF T-80 model runs at the time of the monsoon onset of 2001. The onset vortex was observed as a depression over southeast Arabian Sea on 21 May 2001, which later intensified into a cyclonic storm. The experimental run with MSMR winds was able to capture the strengthening of winds at the time of the vortex formation.

Prasad (2003) has made a quantitative assessment of the impact of high resolution wind vector data in terms of RMSE and objective skill scores on the NCMRWF analysis and prediction during an experimental run for March-April 2002 in which cloud motion vector data from geostationary satellites and QuikSCAT winds were specially assimilated.

Rambabu (2006) analysed several cases of tropical cyclones over the Bay of Bengal using the MM5 mesoscale model and the initial data sets were strengthened with QuikSCAT scatterometer data. He found that the inclusion of scatterometer data made a positive impact in the forecasts up to 48 hr and there was a 50-100 km improvement in the track prediction accuracy compared to the control runs. Basu et al (1997) made an impact study of satellite-derived moisture profiles on numerical models.

Krishnamurti et al (2003) made use of rain rates derived from TMI and SSM/I data for initialization of a super-ensemble of 11 global models, with which they were able to make much better 5-day forecasts of heavy precipitation and flooding events over different regions including northeast India and Bangladesh.

5.2 Direct Assimilation of Satellite Radiances

When global retrievals of temperature and moisture profiles from polar orbiting satellites first became available there was considerable excitement about their use in numerical weather prediction models and the results were promising. However, as both numerical models and data assimilation techniques themselves improved in the 1980s, the positive impacts due to the assimilation of the satellite retrievals over Northern Hemisphere began to fade out in comparison, and in some cases the impact even appeared to be on

the negative side. Research investigations revealed that the procedures that had been adopted for retrieval of various parameters from satellite observations were such that the results had inherent errors, biases and uncertainties, which could not be removed by applying a simple quality control (Kelly et al 1991).

Further, satellite retrievals of vertical temperature and humidity profiles have a relatively poor vertical resolution due to the broad and overlapping nature of the weighting functions used in the retrieval process, and it is not possible to derive a unique profile. Iterative procedures are used which require a realistic first guess that is not always available. This implies that the small-scale features of the vertical structure in the retrieval must come from the prior information and not the sounding instrument (Eyre et al 1989, Goldberg et al 1988). The contribution of errors in the first guess to the final retrieval can turn out to be significant.

All these limitations of satellite data did not really matter when they were used for synoptic analysis in a manner that just conformed to and complemented the available ground-based observations. However, the implications of assimilating them for initialization of numerical models were found to be more serious, and led to the new thinking that it might be better to assimilate the basic satellite radiances themselves rather than products derived indirectly from them.

The process of direct radiance assimilation essentially involves a simulation of the satellite radiances through a forward solution of the radiative transfer equation, assuming a knowledge of the vertical profiles of temperature and absorbing gases, through a series of iterations. The vertical profiles are adjusted until convergence is reached. As a first step towards direct radiance assimilation, a stand-alone one-dimensional variational analysis or 1D-Var scheme is used for the retrieval of different atmospheric variables from the satellite radiances in the vertical direction alone. In the more advanced 3D-Var scheme, the final retrieval step is not performed for single profiles but all available observations and radiances are used together with the background fields and associated error covariances. Arrangements have to made by the operational NWP centres to receive the satellite radiance data of various satellites in near real time from the concerned satellite agencies. The radiance data is voluminous, considering that a single full disc image of a geostationary satellite in one channel may consist of 10 to 100 million pixels or more and an appropriate processing software package is required for handling such data.

The main advantage of 3-D Var assimilation of satellite radiances is that the errors in radiances are much easier to characterize than the errors in the retrievals. However, errors in the background fields will also strongly affect the retrieval solution necessitating quality control and data screening (Eyre 1995).

5.3 Tropical Cyclone Track Prediction

The prediction of tropical cyclone intensity and movement is one of the toughest problems faced by operational forecasters in both scientific and practical sense. Disaster management officials expect the timing and place of the cyclone landfall to be made known to them as early and accurately as possible and they wish to know the intensity with which the storm will strike the coast. Crucial management decisions have to be taken on the basis of the operational forecasts and human lives are at stake. On the other hand, the operational forecasts have two basic limitations. One, in spite of the advances in satellite and radar technology, a complete three-dimensional picture of the tropical cyclone is not always available to the forecaster in real time. Second, it is necessary to first predict the steering current in which the tropical cyclone is embedded, and its likely interaction with the steering current, a process which is also not fully understood. Forecasters at operational tropical cyclone prediction centres, therefore, still have to resort to the use of the CLIPER technique, in which the trend shown by the tropical cyclone is considered against the past history of the behaviour of the cyclones in a given ocean basin in a given season.

The CLIPER technique is to a large extent subjective and intuitive in nature, but it has been proved to be more accurate than numerical models. Therefore, a lot of research effort is currently under way to improve upon the accuracy of numerical cyclone forecasts using newly available satellite inputs.

We have seen before that the genesis of tropical cyclones does not take place on its own but requires some kind of initial disturbance. In numerical models, unless such a disturbance gets picked up from the initial field, the cyclone does not show up in the forecast field. To overcome this limitation, it is common to introduce a 'bogus' vortex made up of synthetic observations, into the numerical analysis to force the cyclone to develop. Because of the wealth of data that the new generation of satellites are making available, through precipitation radars, passive microwave imagers and scatterometers in particular, it is now becoming increasingly possible to introduce synthetic vortices which are closer to reality. Further, advanced satellite-based techniques like the objective Dvorak's technique, and extraction of cloud motion winds from rapid-scan geostationary satellite imagery, have improved

the prescription of the steering current in the numerical model as the storm centre and its direction of movement can be determined more accurately.

Because of advanced data assimilation techniques, continuous model development, higher resolutions, and realistic vortex specification, there has been a progressive reduction in tropical cyclone forecast errors globally over the past three decades. The errors have been on the decline particularly in the case of 48 hr and 72 hr forecasts, which is most desirable, as disaster managers can use them with a higher degree of credibility. While the improvement in tropical cyclone forecasting has been significant, the landfall forecasts made by the operational centres still have an average error in the range of ± 80 km for 24 hr forecasts and ± 250 km for 72 hr forecasts. Over the north Indian Ocean region, the main factor responsible for reduction of errors was the greater use of synthetic vortices by operational NWP centres like India Meteorological Department (IMD) and National Centre for Medium Range Weather Forecasting (NCMRWF) in their regional and global model analyses (Gupta 2006, Rama Rao et al 2006). The current emphasis of international tropical cyclone research is to achieve greater accuracy of cyclone track prediction, especially in the short range, by maximizing the use of non-conventional data, meso-scale analysis, use of synthetic data for vortex specification, and the performance of physical parameterization at higher model resolution.

Scatterometer data on wind speed and direction are being increasingly used for initialization of NWP models especially for prediction of cyclone intensity and track prediction. The beneficial impact of assimilating the ERS-1 scatterometer data in the global analysis was established in several Indian studies (Bansal et al 1994, Rao et al 1998). In an impact study by Das Gupta et al (2002) ERS-2 data was assimilated along with other operational data for the period from 27 May 1998 to 10 June 1998 which covered the onset of the southwest monsoon and a tropical cyclone over the Arabian Sea. It was found that the impact of this kind of data on the NCMRWF global analysis-forecast system was different over data-sparse oceanic regions than that over land regions where plenty of conventional data is available and it is more in the lower levels of the atmosphere.

Singh et al (2005) have also made a study of the impact of introducing a bogus vortex on the accuracy of cyclone track and intensity prediction.

5.4 Monitoring of Aerosols for Climate Modelling

In recent years, an increasing importance is being given to the study and measurement of aerosols in the atmosphere, because of their role in climate

processes which is considered crucial but not yet completely understood. Aerosols are produced as a result of biomass burning or combustion of fossil fuels, and industrial activity and vehicles are their main sources. There are also natural aerosol sources like breaking sea waves or wind-blown dust. Absorption of radiation by aerosols like silicates, sulphates and nitrates, results in a heating of the atmosphere while scattering of radiation by aerosols leads to cooling. The presence of aerosols in the atmosphere therefore not only pollutes the environment locally but also alters the radiative balance and it can directly influence the global climate. Aerosols can also have an indirect effect on climate processes as they modify cloud properties like droplet size. However, our present state of knowledge of the properties of different aerosols and their distribution over land and oceans is full of uncertainties which need to be reduced if the results of climate prediction models are to be made more accurate.

Besides the purposes of climate modelling, the global aerosol distribution is also required to be observed for applying corrections to satellite imagery and products and remove biases. Major volcanic eruptions in the recent years are known to have introduced errors in satellite-derived parameters like SST and vegetation index which had later to be corrected for.

Satellite monitoring of aerosols from space involves conversion of the satellite-measured radiance into different aerosol properties. However, this is not be a straightforward process as the same value of the radiance may be arrived at through different combinations of aerosol properties (Kaufman et al 1997, King et al 1999). Moreover, radiation reaching the satellite would have undergone not only absorption and scattering but also a change in its polarization. Although aerosols are also present in the stratosphere, their concentration there is relatively much smaller than in the troposphere except after occurrences of volcanic eruptions.

The aerosol properties required to be estimated from satellite measurements are the aerosol optical depth (AOD), phase function and single scattering albedo, all as a function of wavelength, the aerosol columnar concentration, aerosol size distribution and chemical composition. While available satellite sensors like NOAA AVHRR and MODIS are being used for this purpose, POLDER is one instrument which is specially designed for aerosol measurements (see Section 4.2.1). Instruments like Stratospheric Aerosol and Gas Experiment (SAGE) were used earlier for monitoring stratospheric aerosols (Kent et al 1995). Vinoj et al (2003) have reviewed the investigations on aerosols using satellite data with emphasis on the Indian region and they have discussed the sensors and algorithms used. Das et al (2003) have demonstrated the use of ocean colour sensors like the Oceansat-1 Ocean Colour Monitor and the IRS-P3 Modular Optoelectronic

Scanner (MOS)-A for an indirect estimation of AOD and size distribution by exploiting the differential absorption properties of oxygen in four narrow band channels around 760 nm.

5.5 Monitoring of Solar Radiation

The energy that drives the entire climate system of the earth comes from a single source, the sun. The annual average solar irradiance received outside the earth's atmosphere on a surface of unit area normal to the incident radiation and at the mean sun-earth distance has been defined as the solar constant. There is a global network of surface observations at which the direct and diffuse components of solar radiation as received at the ground are regularly measured. Obviously, it is not possible to make parallel measurements at the top of the atmosphere. In the absence of data, it has therefore always been a matter of speculation whether the solar constant is indeed a constant and whether variations in the solar constant can cause the earth's climate to change. Ground-based measurements of the solar constant date back to 1913 but the difficulty with such measurements is that they must be corrected for the effect of the intervening atmosphere. Only satellite-based measurements are capable of providing more accurate values of the solar constant since they are made outside the earth's atmosphere.

The Nimbus-6 and later satellites in the series carried the Earth Radiation Budget Experiment (ERBE) instrument. This could view the sun for approximately 3 min and measured the solar irradiance in several spectral channels. The Solar Maximum Mission satellite, launched on 16 February 1980 carried an Active Cavity Radiometer Irradiance Monitor (ACRIM).

The mean Nimbus-7 solar constant, measured over an 11-year solar cycle, was 1372 W m^{-2} with a standard deviation of 0.6 W m^{-2}. The Solar Maximum Mission gave a mean solar constant over a period shorter than a solar cycle of 1367.5 W m^{-2} with a standard deviation of 0.4 W m^{-2}. The value obtained from ERBE measurements is approximately 1365 W m^{-2}. Such differences of the order of 7 W m^{-2} across various satellites are only to be expected because of the difficulty in achieving an absolute calibration. However, the measurements made by the different instruments are highly correlated and the relative variations in the solar constant are in good agreement (Lean et al 1998, Wilson 1997).

The ACRIMSAT satellite was launched in December 1999 and it carried an advanced version of the Active Cavity Radiometer Irradiance Monitor (ACRIM-III). This satellite provided the first data set that clearly demonstrated that the total radiant energy from the sun was not a constant.

The Solar Radiation and Climate Experiment (SORCE) is a NASA-sponsored satellite mission for making highly accurate measurements of incoming solar radiation separately in the x-ray, ultraviolet, visible, near-infrared, and total wavelength bands. SORCE was launched on 25 January 2003 into a 645 km, 40° inclination orbit. It carries four instruments, Total Irradiance Monitor (TIM), Solar Stellar Irradiance Comparison Experiment (SOLSTICE) covering 0.1-0.3 μ, Spectral Irradiance Monitor (SIM) covering 0.2-2 μ and X-Ray and UV Photometer System (XPS). With the sophisticated measurements provided by SORCE in different spectral bands it will be possible to make specific studies of how variations in solar radiation could possibly influence climate change and the data could be incorporated in climate prediction models.

5.6 Generation of Satellite Data Sets for Climate Studies

By the end of the 1970s decade, an operational system of polar orbiting and geostationary satellites had been put into place, and a massive amount of data was being collected by the satellite agencies. Until this time, the main objective that satellite operators had in view was the use of imagery for short-time weather forecasting and the retrieval of parameters in a form that weather forecasters were accustomed to see plotted on their synoptic charts. By the beginning of the 1980s decade, there was a paradigm change in this thinking. It was realized that carefully analyzed and processed satellite data and products had great value from the point of view of long-term climate monitoring, numerical modelling and climate change studies. At that point of time, only passive sensors were in vogue, and it was felt that whatever information that could be gathered from passive sensors about the nature and distribution of clouds and precipitation should be systematically used and processed. Accordingly, two international programmes were conceived and they are described in the following sections.

Compared to the methods adopted in conventional climatology, the generation of long-term satellite data sets for climate purposes is a very demanding exercise. First of all, there is a need for a very strict quality control of the satellite data and the derived products. Sensors on board satellites show a degradation with time, which has to be accounted for and the data corrected accordingly. Unlike meteorological instruments on the ground, satellite sensors are constantly improving and changing. Different types of sensors are used on different satellites. Hence a lot of effort has to be put in to make the data sets compatible across different sensors, and comparable throughout the time series. Merger of satellite derived parameters and their observations on the ground is another difficult problem as the two may not necessarily have the same physical meaning. At the same time, there

is no alternative to the necessity of evaluating and validating of satellite products against what is available as ground truth.

5.7 ISCCP

The International Satellite Cloud Climatology Project (ISCCP) was established as part of the World Climate Research Program (WCRP) in 1982 (Schiffer et al 1983) with several specific objectives, the prime goal being the production of a global, calibrated and normalized data set of visible and infrared radiances along with basic information on the radiative properties of the atmosphere, from which cloud parameters could be derived. A lot of effort was put in towards developing techniques and algorithms. ISCCP was expected to improve parameterizations of clouds in climate models and our understanding of the earth's radiation budget and hydrological cycle.

Operational data collection for the ISCCP began on 1 July 1983 and it is a complex process. For each operational satellite, a Satellite Processing Centre collects the raw satellite data and sends it to the Global Processing Centre which also receives other non-satellite data through the Correlative Data Centre. The Satellite Calibration Centre normalizes the calibration of the geostationary satellites with respect to a polar orbiting satellite standard. All ISCCP data products are archived at the NASA Langley Research Centre.

A primary product of ISCCP is the B3 data set which is a collection of VIS and IR radiance images from all of the operational weather satellites in a common format and normalized to a standard reference calibration. These are basically a reduced (30 km) resolution version of the original images. There are 14 other other ISCCP data sets that provide data on a variety of space and time resolutions and processed differently to serve different application areas. The Climatological Summary Product (FD-MPF) data set provides as many as 81 parameters. Details of the ISCCP data sets are given by Rossow et al (1991) and are also available at http://isccp.giss.nasa.gov/overview.html.

A 3-step procedure is adopted by ISCCP for cloud analysis involving cloud detection, radiative model analysis and statistical analysis. Cloud detection refers to the separation of the image pixels into cloudy and clear scenes. Each scene is then compared to calculations of a radiative transfer model that simulates the radiance that should be measured by the satellite. There are some uncertainties in the detection as well as in the interpretation of the radiances, resulting particularly from the assumption that all image pixels containing cloud are completely covered by a single, homogeneous layer.

The cloud classification scheme adopted by ISCCP is that of two-dimensional frequency distributions or histograms of the cloud top pressure and visible optical thickness of which there are nine different combinations (Figure 5.7.1). The middle and low level cloud types can also be separated into liquid and ice clouds. Each category is given a name that conforms to conventional cloud types (Hahn et al 2001).

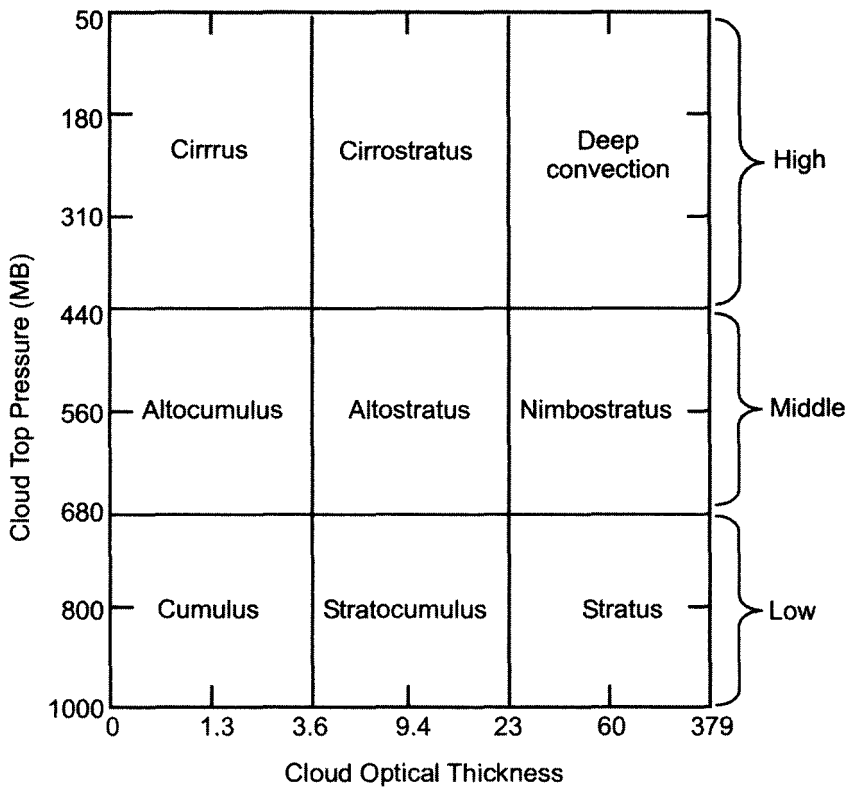

Figure 5.7.1 ISCCP cloud classification

A significant result of the 22-year ISCCP analysis is that the global annual mean cloud amount is about 67%. The mean annual Southern Hemisphere cloud amount is 6% greater than the mean Northern Hemisphere cloud amount because of differences in hemispheric land fractions. The mean annual ocean cloud amount is about 23% larger than the land cloud amount. The mid-latitude zones 30°-60° have the largest mean cloud amount, about 10% larger than the global mean value. Figures 5.7.2 and 5.7.3 (Colour Plate-7) show the 1983-2005 averages of cloud amount and cloud top temperature respectively across the globe and also their zonal means.

In an interesting application of ISCCP C-2 data, Pai et al (1998) used monthly data of cloud parameters for four representative months January, April, July and October for the years 1985-1988 to study the cloud-radiation interaction over the tropical Indian Ocean and its relationship with sea surface temperature. They found that the frequency of occurrence of tropical convection increases dramatically at an SST threshold of about 27-28 °C, specifically 27.6 °C in July for the north Indian Ocean. The ISCCP High Cloud Amount (HCA) data could be used as a proxy for deep convection in this region. In a further study by Pai (2003) for the monsoon months of June-September and an extended ISCCP data set for the period 1984-1990, it was seen that above an SST value of 29.2 °C, the HCA shows a decrease with increase in SST. Over the Bay of Bengal, where SST is always high, the overlying circulation has greater importance in the development of deep convection than the SST itself.

5.8 GPCP

The ISCCP initiative of 1982 was closely followed by the launch of another major international undertaking that would complement the ISCCP. The Global Precipitation Climatology Project (GPCP) was established by the World Climate Research Programme (WCRP) in 1986 to address the problem of quantifying the long term distribution of global precipitation. The initial goal was that of deriving monthly mean precipitation data on a 2.5° × 2.5° latitude-longitude grid. Later, the data sets were expanded so that in addition to the monthly mean product available, the GPCP now has a 2.5° × 2.5° pentad data set (Xie et al 2003) starting from 1979 and a 1° × 1° daily data set (Huffman et al 2001) starting from 1997. The GPCP data sets are being used to validate general circulation and climate models, study the global hydrological cycle and analyze the variability of the global climate system.

Monthly mean precipitation estimates are being produced from 1979 onwards under GPCP. The general approach is to combine the precipitation information available from several sources: microwave estimates from DMSP SSM/I, IR estimates from geostationary satellites of U.S., Europe and Japan, and IR estimates from NOAA AVHRR and TOVS, besides data from more than 6000 raingauges.

The GPCP is intricately organized across many countries and agencies. The Geostationary Satellite Data Processing Centres (GSDPC's) which collect IR data from which precipitation is estimated, are operated by the respective satellite agencies. The Geostationary Satellite Precipitation Data Centre is

operated by NOAA/NWS. It collects histograms prepared by the GSDPC's and creates a merged set of IR precipitation estimates.

The microwave component is handled by the Emission Data Processing Centre at NASA/GSFC which prepares oceanic precipitation estimates from the 19 GHz channel data of SSM/I. The Scattering Data Processing Centre located at NOAA/NESDIS prepares land precipitation estimates from the 85 GHz channel of SSM/I.

The Global Precipitation Climatology Centre located at Deutscher Wetterdienst, Germany collects, checks and analyzes station data from synoptic reports and national climatic summaries. It combines satellite and *in situ* estimates to prepare a global gridded precipitation analysis. The GPCP Merge Development Centre at NASA/GSFC is responsible for developing analysis procedures for merging satellite and gauge estimates of precipitation and providing these merged products on a global grid.

The calibration and validation component is responsible for ensuring that satellite estimates are of high quality. The Surface Reference Data Centre at the University of Oklahoma acquires time series of high density raingauge data from different climatic regions for long-term validation of satellite estimates as well as gridded analyses. An Algorithm Inter-comparison Programme coordinates field campaigns for the validation of satellite algorithms and the development of new ones. The New Technology Programme deals with the development and testing of new oceanic rainfall measuring technology like optical raingauges and acoustic techniques.

The GPCP has promoted the development of an analysis procedure for blending the various estimates together to produce the composite global gridded precipitation fields. This has been used to produce what is known as the GPCP Version 2 Combined Precipitation Data Set covering the period January 1979 through the present (Adler et al 2003). The primary product in the Version 2 dataset is a combined gridded analysis of raingauge measurements and satellite estimates of rainfall. However, the data set has a total of 27 other products that provide the individual and intermediate estimates, including estimates of RMS random error.

The voluminous data collection and processing effort under the GPCP project has culminated in the compilation of the global and seasonal distributions of precipitation which have a sound foundation and authenticity. All available months in the period from January 1979 onwards have been used to compute monthly climatological values. Figures Figure 5.8.1 and 5.8.2 (Colour Plate-8) show the GPCP global rainfall distributions averaged for the months of January and July respectively. In the July climatology, the

Bay of Bengal, northeast India and the west coast of India stand out as the zones of highest rainfall in the world (more than 20 mm/day), matched only by the eastern Pacific Ocean. At the same time, the southwestern Arabian Sea is clearly seen as an almost rainless region. In the January climatology, rainfall does not generally exceed 10 mm/day, and the heavy rainfall belt is seen to be aligned with the ITCZ over the southern hemisphere.

The Goddard Profiling Algorithm (GPROF) is a physical retrieval of hydrometeor vertical profiles that best fit the available 7 channels of microwave data from SSM/I. Each hydrometeor profile is associated with a surface precipitation rate. GPROF retrieves all parameters using the estimated expected value as described by Kummerow et al (1996). Over the ocean, convective/stratiform classification is performed, as described by Olson et al (1999).

5.9 References

Adler, R.F. and coauthors, 2003, "Version 2 Global Precipitation Climatology Project (GPCP) monthly precipitation analysis (1979-present)", *J. Hydrometeor.*, 4, 1147-1167.

Bansal R. K. and coauthors, 1994, "Impact of ERS-1 scatterometer data on the analysis and prediction of a storm in the Bay of Bengal", *Vayu Mandal*, 24, 59-66.

Basu S., Gairola M., Kishtwal C. M. and Pandey P. C., 1997, "Retrieval of moisture profiles using satellite measurements of precipitable water and study of their impact on numerical weather prediction models", *Indian J. Radio and Space Phys.*, 26, 49-76.

Bouttier F. and Kelly G., 2001, "Observing system experiments in the ECMWF 4D-VAR data assimilation system", *Quart. J. Royal Meteor. Soc.*, 127, 1469-1488.

Courtier P., Thepaut J.-N. and Hollingsworth A., 1994, "A strategy for operational implementation of 4D-Var, using an incremental approach", *Quart. J. Royal Meteor. Soc.*, 120, 1367-1387.

Das I. and Mohan M, 2003, "Detection of marine aerosols using ocean colour sensors", *Mausam*, 54, 327-334.

Das Gupta M., Rizvi S. R. H. and Mitra A. K., 2002, "Impact of ERS-2 scatterometer wind data on global analysis-forecast system", *Mausam*, 53, 153-164.

Das Gupta M., Mitra A. K., Prasad V. S. and Rajan D., 2003, "Impact of ATOVS temperature and moisture profiles on NCMRWF analysis and prediction", *Mausam*, 54, 215-224.

Eyre J. R. and Lorenc A. C., 1989, "Direct use of satellite sounding radiances in numerical weather prediction", *Meteor. Magazine.*, 118, 13-16.

Eyre J. R., 1995, "Variational assimilation of remotely-sensed observations of the atmosphere", *ECMWF Tech. Memo.*, 221 pp.

Goldberg M. D., Daniels J. M. and Fleming H. E., 1988, "A method for obtaining an improved initial approximation for the temperature-moisture retrieval problem", *Third Conf. Sat. Meteor. Oceanogr.*, Anaheim.

Gupta A., 2006, "Current status of tropical cyclone track prediction techniques and forecast errors", *Mausam*, 57, 151-158.

Hahn, C.J., Rossow W. B. and Warren S. G., 2001, "ISCCP cloud properties associated with standard cloud types identified in individual surface observations", *J. Climate*, 14, 11-28.

Hinsman D., 2003, "The expanded space-based component of the Global Observing System and the role of the Coordination Group for Meteorological Satellites", *Mausam,* 54, 13-24.

Huffman, G.J. and coauthors, 2001, "Global precipitation at one-degree daily resolution from multi-satellite observations", *J. Hydrometeor.*, 2, 36-50.

Kar S. C., Pattnaik S., Rupa K., Prasad V. S. and Singh S. V., 2003, "Impacts of surface wind and moisture data from microwave sensors in the analysis and prediction of weather in the Indian Ocean region", *Mausam*, 54, 225-236.

Kaufman Y. J. and coauthors, 1997, "Passive remote sensing of tropospheric aerosols and atmospheric correction for the aerosol effect", *J. Geophys. Res.*, 102, 16815-16830.

Kelly G. and coauthors, 1991, "Quality control of operational physical retrievals of satellite sounding data", *Mon. Wea. Rev.*, 119, 1866-1880.

Kelly G., 2004, "Observing system experiments of all main data types in the ECMWF operational system", *3rd WMO Numerical Weather Prediction OSE Workshop*, Alpbach, Austria, WMO, Tech Rep. 1228, 32–36.

Kelkar R. R., 1993, "Applications of satellite data in the study of monsoon variability", *Proc. Indian Acad. Sci. (Earth Planet. Sci.)*, 102, 271-281.

Kelkar R. R., 1994, "Satellites for monitoring climate change: the emerging scenario", Proc. Indian National Sci. Acad., 60 A, 335-348.

Kent G. S., Wang P. H., McCormick M. P. and Skeens K. N., 1995, "Multiyear SAGE-II measurements of upper-tropospheric aerosol characteristics", *J. Geophys. Res.*, 100, 13875-13899.

King M. D., Kaufman Y. J., Tanre D. and Nakajima T., 1999, "Remote sensing of tropospheric aerosols from space: past, present and future", *Bull. Amer. Meteor. Soc.*, 80, 2229-2258.

Krishnamurti T. N., Vijaya Kumar T. S. V., Mackey B., Cubucku N. and Ross R. S., 2003, *Mausam*, 54, 121-140.

Kummerow, C., Olson W. S. and Giglio L., 1996, "A simplified scheme for obtaining precipitation and vertical hydrometeor profiles from passive microwave sensors", *IEEE Trans. Geosci. Remote Sens.*, 34, 1213-1232.

Lean J. and Rind D., 1998, "Climate forcing by changing solar radiation", *J. Climate*, 11, 3069-3094.

Le Marshall J., Leslie L. M., Seecamp R. and Rea A., "High resolution space based wind observations estimation and application", *Mausam*, 54, 39-50.

Ohring G., McClain E. P. and Ellis J. O., 1991 (Eds.), "Operational satellites, sentinels for the monitoring of climate and global change", *Global Planet. Change*, (Special Issue).

Olson, W.S., Kummerow C. D., Hong Y., and Tao W.-K., 1999, "Atmospheric latent heating distributions in the tropics derived from satellite passive microwave radiometer measurements", *J. Appl. Meteor.*, 38, 633-664.

Pai D. S. and Rajevan M, 1998, "Clouds and cloud radiative forcing over tropical Indian Ocean and their relationship with sea surface temperature", *Current Sci.*, 75, 372-381.

Pai D. S., 2003, "Interannual variation in the sea surface temperature threshold for the deep convection over north Indian Ocean", *Mausam*, 54, 595-604.

Prasad V. S., 2003, "Impact of high resolution wind vector data on NCMRWF assimilation and forecasting system", *Mausam*, 54, 237-246.

Rambabu G., 2006, "QuikSCAT scatterometer wind data impact on tropical cyclone forecasts by a mesoscale model", *Mausam*, 57, 141-150.

Rama Rao P. V., Hatwar H. R. and Agnihotri A., "Tropical cyclones prediction by numerical models in India Meteorological Department", *Mausam*, 57, 47-60.

Rao U. R. and coauthors, 1998, "Early prediction of onset of southwest monsoon from ERS-1 scatterometer winds", Proc. *Indian Acad. Sci. (Earth Planetary Sci.)*, 107, 33-43.

Rossow, W.B. and Schiffer R. A., 1991, "ISCCP cloud data products", *Bull. Amer. Meteor. Soc.*, 72, 2-20.

Roy Bhowmik S. K., Joardar D., Rama Rao Y. V. and Hatwar H. R., 2005, "Initialization of monsoon onset vortex from the use of MSMR surface wind", *Mausam*, 56, 477-481.

Schiffer R. A. and Rossow W. B., 1983, "The International Satellite Cloud Climatology Project (ISCCP): the first project of the World Climate Research Programme", *Bull. Amer. Meteor. Soc.*, 64.

Singh R. and coauthors, 2005, "Impact of bogus vortex for track and intensity prediction of tropical cyclone", *J. Earth System Sci.*, 114, 427-436.

Szyndel MDE, Thepaut J.-N. and Kelly G., 2005, "Evaluation of potential benefit of SEVIRI water vapour radiance data from Meteosat-8 into global numerical weather prediction analyses", *Atmos. Sci. Letters*, 6, 105-111.

Su X., Derber J., Lord S., Velden C, and Daniels J., 2003, "Toward improved use of GOES satellite-derived winds at NCEP", *NCEP Tech. Note 440*, 22 pp.

Vinoj V. and Satheesh S. K., 2003, "Observations of aerosols from space: an overview", *Mausam,* 54, 287-298.

Wilson R. C., 1997, "Total solar irradiance trend during solar cycles 21 and 22", *Science*, 277, 1963-1965.

Xie P. and coauthors, 2003, "GPCP pentad precipitation analyses: an experimental dataset based on gauge observations and satellite estimates". *J. Climate*, 16, 2197-2214.

Chapter 6

Future Scenario

The previous chapters have described the many stages of evolution that satellite meteorology has gone through. The first pictures from space of the earth and its cloud cover were taken by astronauts with their cameras through the windows of their space capsules. Then came dedicated weather satellites with television cameras that relayed to the ground the scenes that they viewed. These were soon replaced by scanning radiometers that measured VIS and IR radiances that could be digitally converted into the more familiar image form. As technology advanced, more spectral channels were added and the most significant transition was to the use of passive microwave sensors. The latest advances in satellite meteorology are have been brought by the use of active sensors of various kinds.

In parallel, satellite orbits have improved progressively from random over-passes to sun-synchronised visits, settled down for a long time for a combination of polar orbiting and geostationary orbits, until technology paved the way for placing satellites in tropical orbits at low elevations.

The emerging scenario, as we shall now see, is full of even more innovative ideas and concepts that certainly appear to be realizable in the not too distant future.

6.1 New Techniques in Meteorological Remote Sensing

The following sections describe some new initiatives in meteorological remote sensing. We have seen before how non-meteorological satellites can be used for certain meteorological applications. Another example of this type will be discussed here. We shall also see upcoming attempts to bring in new types of sensors to make measurements that were not possible so far.

6.1.1 GPS-based Soundings

The Global Positioning System (GPS) of satellites was originally developed for meeting the requirements of high-precision navigation and positioning and consists of a constellation of satellites that transmit L-band radio signals

(see Table 1.1.5.4). The present GPS constellation is made up of 29 satellites, all moving in a circular orbit of 26,500 km radius with a 55° inclination and a period of revolution of 12 hr around the earth. However, while their orbital characteristics are identical, the satellites move in six different orbital planes. Each GPS satellite broadcasts signals in two L-band frequencies called L1 and L2, at 1.57542 GHz or 19 cm wavelength, and 1.22760 GHz or 24.4 cm wavelength, respectively.

An exciting application of great potential is in an area that the original GPS concept was never intended to serve, and it has emerged recently. This has come to be known as the GPS radio occultation technique which is now being used to retrieve temperature and humidity profiles in the atmosphere. Various aspects of the GPS radio occultation technique and data processing have been discussed in detail in many papers (TAO 2000), but a concise explanation and description has been given by Anthes et al (2003).

The GPS radio occultation technique is based on the principle that radio waves while passing through the atmosphere undergo refraction, the nature of which is in turn determined by the gradients of temperature, water vapour and electron density. Refraction effects are most pronounced when the radio wave traverses a long atmospheric limb path, and measurements for a series of such paths at different tangent heights contain information on the vertical profile of refractivity. If the refraction effects can be measured, then the atmospheric temperature and humidity elements that produced them can, theoretically speaking, be retrieved.

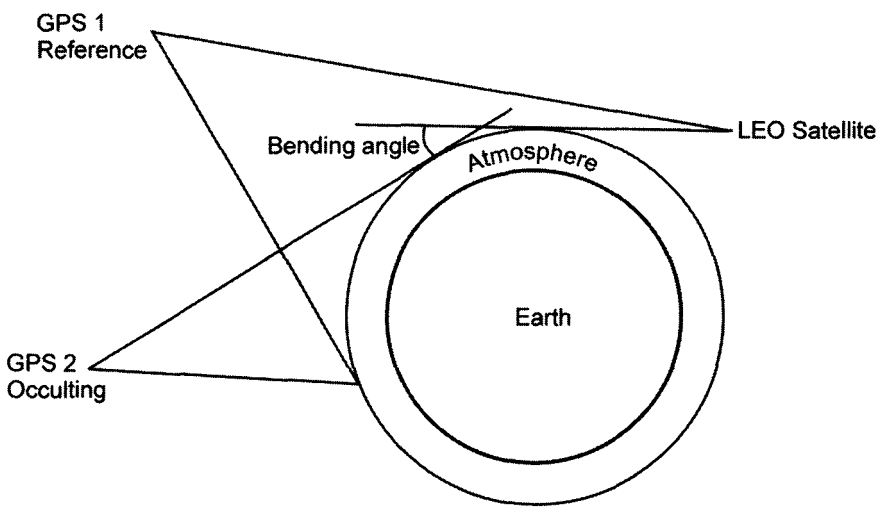

Figure 6.1.1.1 Schematic of the GPS radio occultation technique

In practice, the GPS radio occultation technique involves precise L-band dual-frequency phase measurements by a GPS receiver placed on a low earth orbiting (LEO) satellite which tracks a setting or rising GPS satellite on the horizon (Figure 6.1.1.1). The GPS receiver has to be suitable equipped to detect amplitude, pseudo-range and phase measurements for each of these signals. The LEO satellite uses the GPS signals both to determine its own precise location and to make signal occultation measurements. As the position and velocity of both the LEO and GPS satellites are known, the small increase in the phase path due to the atmospheric refraction during the occultation event can be derived. This information is then converted to the atmospheric bending angles. Assuming a spherically symmetric atmosphere, vertical profiles of refractive index can be determined and converted to lower tropospheric soundings of atmospheric parameters such as pressure, temperature and indirectly water vapour.

The main advantages of the GPS soundings are global coverage, high vertical resolution and all-weather capability combined with high accuracy which make them ideally suited for various applications in atmospheric and ionospheric research, weather forecasting and climate studies. The potential of the GPS occultation technique was first demonstrated in the GPS/MET experiment which was launched on 3 April 1995 and continued for two years (Ware et al 1996). The GPS/MET soundings were used for many applications like study of upper level fronts (Kuo et al 1998). Later the CHAMP satellite which has an advanced GPS receiver, provided thousands of occultation soundings. Currently there are other satellites like SAC-C, GRACE, Sunsat, and Picosat, which are being used for this purpose.

CHAMP (CHAllenging Minisatellite Payload) was launched with a Russian COSMOS rocket on 15 July 2000 in an almost circular (eccentricity 0.004), near polar (inclination 87.2°) orbit with an initial altitude of 454 km. The mission has a life of five years, during which the effects of atmospheric drag will progressively pull down the satellite by 50 to 200 km depending on the actual solar activity. The first occultation measurements with CHAMP were performed on 11 February 2001 (Wickert et al 2001). CHAMP has been providing on an average of more than 200 globally distributed vertical profiles of atmospheric parameters per day up to a height of 50 km. The vertical resolution ranges from 0.5 km in the lower troposphere to 1.5 km in the stratosphere and the resolution along the ray path is around a few hundred km. In the troposphere, vertical profiles of humidity can be derived using independent temperature data from meteorological analyses. The satellite is currently in its sixth year in orbit.

While the GPS radio occultation technique is conceptually quite simple, the accuracy of the derived profiles depends on two major aspects of how the

system actually operates. First is the calibration of the signal, which requires the atmospheric delay induced on the occulted signal to be isolated from all other effects such as geometrical motion of the satellites, clocks and ground troposphere. The other is the process of inversion of the atmospheric delay to obtain physical parameters such as refractivity and other derived products. There is a need for carrying out a proper calibration of the phase delays measured from GPS, correction of measurement errors due to data outages, proper smoothing of the data, and evaluation of errors due to Doppler shift and bending.

For dry air, the density profiles are obtained from the known relationship between density and refractivity. Pressure and temperature are obtained from the hydrostatic equation and the equation of state for an ideal gas. However, when water vapour is present, additional information is required to determine the humidity and density from refractivity profiles, since the refraction of microwave signals is very sensitive to water vapour. For this purpose, temperature profiles from operational meteorological analyses of the European Centre for Medium-Range Weather Forecasts (ECMWF) are used to derive humidity profiles from the calculated refractivity in an iterative procedure. However, more elaborate retrieval methods are required for obtaining water vapour profiles with a higher accuracy.

A statistical comparison between vertical profiles of temperature, derived from early CHAMP measurements and corresponding ECMWF data (Kuo et al 2000) shows that the agreement in temperature values above the tropopause is better than 1 °K with a standard deviation of 1.5 °K or less. At latitudes to the north of 30 °N this temperature bias is even less than 0.5 °K.

The Constellation Observing System for Meteorology, Ionosphere and Climate (COSMIC/Formosat-3) consists of six satellites that were launched on 14 April 2006 as a joint U. S.-Taiwan project. The mission is expected to last for five years. In the first year, the orbital altitude of the satellites will be gradually boosted from 400 to 800 km, and important geodetic/gravity experiments will be carried out during this phase.

Each of the spacecrafts carry three science payloads comprising a GPS occultation receiver, a Tiny Ionospheric Photometer (TIP), and a Triband Beacon transmitter (TBB). Each of the COSMIC satellites will track the GPS satellites as they are occulted behind the earth's limb to retrieve up to 500 daily profiles of ionospheric and atmospheric parameters. Every day the constellation will provide globally about 4000 GPS soundings. TIP will measure electron densities at the peak of the F2 layer along the satellite track. TBB transmissions will be received on the ground for high-resolution tomographic reconstruction of the ionospheric electron density.

The science objectives of the COSMIC mission are to investigate the global moisture distribution, monitor the tropopause, obtain lower stratosphere temperature profiles with high resolution and demonstrate the use of the measurements in operational weather prediction models. COSMIC will provide a global self-calibrating data set for climate monitoring and model evaluation, particularly for studying ozone depletion, volcanic effects and troposphere/stratosphere exchange processes (Anthes et al 2000).

Anthes et al (2003) have discussed three case studies of the application of GPS soundings to a typhoon over the western Pacific Ocean, gravity waves over the Indian Ocean and a monsoon depression over India, which have brought out the high accuracy of the soundings.

For the latest status of the COSMIC mission, readers are referred to the web site http://www.cosmic.ucar.edu/.

6.1.2 Hyperspectral Imaging

As seen in Section 1.3.5, the spectral resolution of a satellite sensor is inversely related to the spectral range covered by it. A higher spectral resolution and an accurate spectral signature can be obtained by having a large number of narrow bands, rather than one continuous broad band. Further, the spectral resolution and spatial resolution are also inversely related, since for registering the small amount of radiance contained in a very narrow spectral band, the sensor must dwell on the ground area for a longer time. However, if the satellite sensors are made to scan the earth at a slow speed they will take longer to complete the scan, thus reducing the temporal resolution or repetivity of observations as well. Remote sensing satellites can have a long repeat cycle of 10-20 days and can therefore make measurements in narrow spectral channels. Meteorological satellites cannot do this and in order to accomplish fast earth scans, they acquire stronger radiances from wider spectral bands such as VIS 0.55-0.75 μ or TIR 10.5-12.5 μ. The sensor response is, however, not uniform over the entire width of the channel and even if many satellite radiometers have nominally the same spectral bandwidths, their spectral response functions across the band are not identical. This is the reason why images of the same region obtained from different satellites look a little different from each other.

Hyperspectral imaging is a new and powerful means for reducing the spectral channels to extremely small widths, even as small as 0.01 μ. With such narrow widths, the spectral range from 0.38 to 2.55 μ for example, can be

divided into as many as 217 intervals. This is made possible by the use of silicon microchips as detectors for the very near IR region, and Indium-Antimony (In-Sb) alloy detectors for the shortwave SWIR region. The radiance values measured by the CCDs for each such narrow interval are plotted as a graph of intensity versus wavelength, that provides a sufficient number of points through which we a meaningful continuous spectral curve can be drawn. Hyperspectral imaging is in principle far superior to multi-spectral imaging, as it provides much more detail about the spectral properties of the features to be identified. The hyperspectral data yields continuous spectral signatures rather than the band histogram plots.

Two satellites that are currently in orbit have been able to demonstrate the capability of hyperspectral imaging. An instrument called Hyperion, is part of EO-1, the first satellite in NASA's New Millenium series, launched in December 2000. It was inserted into an orbit that positions it just about 50 km behind Landsat-7, which allows both satellites to view almost the same scene for making comparative evaluations.

ESA has launched in 2001, as part of the MicroSat program, a satellite called Project for On-Board Autonomy (PROBA). This small satellite of dimensions 40 × 60 × 80 cm and a weight of 94 kg with solar panel collectors mounted on its surface, also has a hyperspectral imaging system with 200 narrow bands.

6.1.3 Lightning Detection

Lightning is a phenomenon that is far more deadly than other severe hazards like hail, squalls and heavy rain associated with a thunderstorm. Hundreds of people lose their life every year across India to lightning strikes particularly in the pre-monsoon summer months. Meteorological satellites are able to monitor thunderstorms but not lightning per se.

By definition, lightning is a high-energy luminous electrical discharge from a cumulonimbus (Cb) cloud to the ground which is accompanied by thunder. Electrical discharges can also occur in the atmosphere in two other ways. Intra-cloud lightning occurs within a Cb cloud and inter-cloud lightning is between two different Cb clouds.

The top of the Cb cloud develops a positive electric charge while its base has a negative charge. As air is a poor conductor of electricity, positive charge accumulates on all objects below the Cb cloud, and tends to concentrate on the highest object in the area. When the potential difference between this positive charge and the negative charge on the cloud becomes large enough

to overcome the electrical resistance of the air, lightning occurs. The heavy electrical discharge of 100 million volts leaves the air heated to about 30,000 °C in a few milliseconds. This generates shock waves whose propagation is heard as thunder.

Since lightning can occur only when there is a thundercloud, data on lightning occurrence can serve as proxy for convective precipitation. Lightning also plays a role in atmospheric chemistry as it produces NO_x in and around Cb clouds. This is carried to the upper troposphere by the convective updrafts and leads to an increase in the ozone concentrations at those levels.

Estimates of the frequency of lightning flashes were first made from space in the early 1980's with optical detectors on the DMSP and ISS-b satellites by observing the atmospherics from lightning discharges at frequencies of 2.5, 5, 10 and 25 MHz.

An instrument called the NASA Optical Transient Detector (OTD) was launched on 3 April 1995 aboard the MicroLab-1 satellite into a 70° inclination orbit at an altitude of 740 km. At any given instant it viewed a 1300 × 1300 km region of the earth at 128 × 128 pixels. The instrument had a spatial resolution of 10 km and a temporal resolution of 2 ms. From an analysis of OTD data it has been found that over 1.2 billion lightning flashes, including both intra-cloud and cloud-to-ground strikes, occur around the world every year (Christian et al 1999, 2003). The highest number is over the land portion of the Inter-Tropical Convergence Zone (ITCZ), and there is generally far more lightning over the continents than over the oceans. This results from the stronger vertical motions that occur in continental clouds than in oceanic clouds.

The OTD detected lightning flashes during both daytime and night-time conditions with a detection efficiency ranging from 40% to 65%, depending upon external conditions such as sunglint and radiation. However, as the OTD never observed a given location for more than a few minutes each day, many lightning occurrences may have gone unrecorded.

The TRMM satellite launched in 1987, carried another lightning detection instrument called the Lightning Imaging Sensor (LIS). While the primary mission of TRMM is to measure rainfall, lightning data can be used to corroborate the rainfall data. LIS has been used to detect lightning in all its three forms, cloud-to-cloud, intra-cloud, and cloud-to-ground, and it has been possible to map out their frequency and distribution over the tropical regions.

LIS consists of a staring imager which is optimized to locate and detect lightning with storm-scale resolution (4 to 7 km) over a large region (600 × 600 km) of the earth's surface. In spite of the fact that the TRMM satellite moves at a speed of 7 km/sec, LIS has an observation time of 90 seconds over any place, which is long enough to estimate the flashing rate of most storms. The instrument records the time of occurrence, measures the radiant energy and determines the location of lightning events within its field of view. LIS uses a wide field of view optics, a narrow band filter and a matrix of highly sensitive CCDs for the detection of the transient lightning signals. Even in the presence of bright sunlit clouds or high background illumination, the lightning signal can be extracted at 90 % efficiency by adopting appropriate filtering and data processing techniques.

Data from TRMM/LIS is being used to study mesoscale phenomena such as storm convection, dynamics and microphysics. These will be related to global rates and amounts and distribution of convective precipitation, as well as to the release and transport of latent heat, which are all influenced by global scale processes.

Because of the small dwell time of orbiting satellites over a given place and the long time interval between their successive passes, efforts are now under way to place a lightning detector on geostationary platforms. The GEO Lightning Mapper (GLM) proposed to fly on the GOES-R satellite in 2012, is a sensor capable of continuously mapping lightning discharges at all times. From this orbit, the sensor will be capable of detecting all forms of lightning with a high spatial resolution and detection efficiency.

In recent times, there has been a growing interest in upper tropospheric water vapour (UTWV) in relation to climate change (Williams 2005). However, it is difficult to measure daily fluctuations in UTWV with high accuracy over an extended period. Operational radiosonde networks do not produce high-quality data above 500 hPa and satellites too have problems observing short-term variability in the upper tropospheric water vapour. In a novel approach, Price et al (2006) have suggested the use of lightning observations as a sensitive indicator of the daily variability of UTWV in tropical continental regions.

6.1.4 Polarimetric Radiometry

As we have seen before, the emissivity of the sea surface can be assumed to be close to 1 in the IR region, but in the microwave region of the spectrum, it is a highly variable function of various factors particularly the roughness of

the sea surface and its temperature and salinity. When the sea is calm, it has a smooth surface and the microwave emissivity is low. When the winds blowing over the sea surface are strong, the sea surface roughness increases and the microwave emissivity also increases. A finer feature of this situation, however, is that the waves on the ocean surface driven by the winds are not isotropic and their distribution varies with the wind direction. The result is that the intensity of the microwave emission from the seas surface is determined not only by the characteristics of the wave structure, but also by the directional orientation of the wind-driven waves.

We saw previously (see Section 4.2.1) that while the visible solar radiation coming from the sun is not polarized, certain physical processes on earth result in generating polarized light. Satellites like POLDER are able to measure this polarization and derive properties of clouds and aerosols which cause the polarization.

A similar principle is made use of in the design of polarimetric radiometers working in the microwave region of the spectrum. A microwave polarimetric radiometer measures both vertical and horizontal polarizations of the radiation reaching the satellite, and in addition measures the cross-correlation between the two. The cross-correlation terms are derived from the microwave radiances at vertical, horizontal, and 45° left hand circular and right hand circular polarizations. The Stokes vector provides a full characterization of the spectral signature of the ocean surface in the microwave region and yields all the independent information that is needed to uniquely determine the wind direction over the ocean (Lahtinen et al 2003).

Wind retrievals from polarimetric radiometers are best made when there is no rain, and the data can also be used to obtain additional information on parameters such as sea surface temperature, rain rate, ice and snow characteristics, water vapour and soil moisture over land.

The first space-borne polarimetric radiometer, with a 1.9 m diameter reflector, was flown on the Coriolis/WindSat satellite, which was launched by the U. S. on 6 January 2003 in a 830 km altitude polar orbit. The satellite has an expected life of three years. This instrument is designed to measure the ocean surface wind field at a 25 km spatial resolution. The Coriolis/WindSat instrument operates in 6.8, 10.7, 18.7, 23.8 and 37.0 GHz microwave bands. The 10.7, 18.7 and 37.0 GHz channels are fully polarimetric. The 6.8 GHz channel has dual-polarization and is more sensitive to SST than to winds. It is therefore useful for removing measurement noise due to variations in SST. The 23.8 GHz channel also has

dual-polarization. This is more sensitive to water vapour absorption, and is used for removing the attenuating effects of atmospheric water vapour on the signal. The horizontal spatial resolution of the different channels varies between 40 × 60 km at 6.8 GHz to 8 × 13 km at 37.0 GHz (St Germain et al 2000).

6.1.5 Lidar-based Humidity Profiling

Satellite soundings of atmospheric humidity are currently obtained from instruments that measure either IR or microwave radiances. In the proposed Megha-Tropiques satellite (see Section 6.5.1) an instrument called SAPHIR will provide humidity soundings, while the INSAT-3D satellite (see Sections 3.4.5) will carry a sounder that will operate in the water vapour absorption bands. Passive microwave sensors are less sensitive to clouds than IR but the surface emissivity problem still has to be taken care of.

In recent times, ground-based and airborne Differential Absorption Lidar (DIAL) systems have been coming into increasing use as an alternative means for atmospheric humidity measurements because of their good vertical resolution, high precision and low bias (Wulfmeyer et al 1998, 2000). The success of these measurements have prompted the use of the DIAL technique in space-based systems. In other words, an attempt is being made to have the first humidity profiling system in space using active remote sensing technique. The initiative towards this goal has come from the European Space Agency (ESA) and has been named the Water Vapour Lidar Experiment in Space (WALES). The project targeted for 2010, aims at achieving unsurpassed data quality. WALES is intended to profile the atmosphere in a nadir-viewing configuration (Gerard et al 2004).

The use of the DIAL technique for humidity profiling basically consists of a comparison of the attenuation of two laser pulses emitted at a pair of closely spaced wavelengths in the 925-940 nm region. The on-line wavelength falls on the centre of a water vapour absorption line, and the off-line wavelength falls on the line wing, where absorption is significantly reduced. The water vapour number density as a function of height is directly derived from these two measurements.

The high vertical resolution of WALES can be regarded as a major advance over present humidity profiling techniques. A further possible extension of the space-based DIAL technique is to use three pairs of wavelengths: the strongest absorption line pair will measure the humidity in the upper troposphere, lower stratosphere and tropopause region, and the weakest pair will probe the lower troposphere.

The proposed WALES instrument is of the non-scanning type. As the satellite moves in its orbit, backscatter signals from consecutive laser shots with a footprint of 40 m, will be averaged over a distance of 50-100 km, but the data downlinked to ground is expected to be supplied at around 1 km horizontal resolution. Assuming an integration length of 100 km, this means that about 6000 profiles would be collected daily. The DIAL technique used by WALES allows for trade-offs between horizontal as well as vertical resolution and precision for serving different types of applications. An advantage of DIAL systems is that they can make precise measurements of cloud tops, and profiling above the cloud tops causes no significant difference in instrument performance.

WALES is not expected to replace the present observation systems but it will provide a new standard against which advanced passive sounding techniques can be evaluated.

6.2 Advanced Geostationary Satellites and Sensors

For all these years, measurements from geostationary satellite sensors have faced severe limitations because of the low radiances reaching up to the height of the satellites and the comparatively low signal-to-ratio ratio of the instruments. Recent advances in sensor technology have, however, helped to overcome these limitations and new sensors of various types are under active consideration for being placed at geostationary altitudes. The likely configuration of the next generation GOES satellite which has been named GOES-R is currently in the formulation phase. The GOES-R satellite that is likely be launched by the U. S. around 2012, is being looked upon as a satellite that would usher in a new era in environmental remote sensing (Gurka et al 2001).

6.2.1 GOES-R

The three main meteorological instruments that have been proposed for the GOES-R satellite are the Advanced Baseline Imager (ABI), Hyperspectral Environmental Suite (HES) and GEO Lightning Mapper (GLM).

The HES instruments are designed to provide vertical profiles of temperature and moisture, monitor mesoscale systems and synoptic scale storm systems, and provide data on ocean parameters. These functions will be carried out, however, by GOSE-R at much higher spatial, temporal, spectral and radiometric resolutions than the present GOES sensors in order obtain the

required accuracies of the products. HES will have the capability of simultaneous vertical soundings, one over the full disc for large-scale phenomena, and the other over smaller space and time intervals for monitoring mesoscale phenomena.

GOES-R is envisaged to be a three-axes stabilized geostationary satellite. The advanced imager ABI on GOES-R will therefore be a multi-spectral, scanning radiometer with alternate east-west and west-east scans. It will be possible to order the scans over desired geographical areas for obtaining rapid scan imagery and products (Schmit et al 2005). ABI will offer 16 spectral bands compared to the 6 channels of the present GOES imager. Some of the new 10 channels will be spectral variants of the present GOES imager channels and some will be similar to those proposed for NPOEES-VIIRS channels. The ground resolution of ABI will be nominally 2 km for IR channels and 0.5 km for the 0.64 μ VIS band.

The ABI data will be used in concert with HES soundings making it possible to derive a host of new products such as hurricane intensities, land and sea temperatures, cloud top temperatures, identification of fires and hot spots, aerosol and smoke detection, precipitation, and fog. ABI represents an exciting expansion in geostationary remote sensing capabilities and will be used for a wide range of weather, oceanographic, climate, and environmental applications.

The GOES-R satellite is planned for launch in the 2012 time frame and the mission concept and design is likely to undergo further modifications by that time. The progress of the GOES-R mission can be followed at the web site http://goespoes.gsfc.nasa.gov/goes/.

6.2.2 IGeoLab Concept

A recent concept which has caught the attention of the meteorological satellite community is that of an International Geostationary Laboratory (IGeoLab) which aims at stimulating proposals and implementation of geostationary demonstration missions by a partnership of space development agencies. It is based on an approach that would facilitate transition to operational status and, ultimately, generalization pertinent to all satellites in geostationary orbit. It offers a test-bed opportunity for demonstrations for future missions. Many different options have been proposed, considering the various practical constraints in the implementation.

An international partnership of space agencies is desired to develop and to facilitate the global operation of the IGeoLab. A major logistical challenge to the exercise is the availability of geostationary orbit slots for operating IGeoLab over different locations of the world. A possible solution to this problem may lie in placing the IGeoLab in equatorial slots already owned by operational weather satellites thus sharing pre-allocated space. This approach would also help the operational geostationary satellite operators to experiment with new capabilities provided by IGeoLab prior to their incorporation on their own operational satellites.

6.2.3 GIFTS

One of the proposals made under the IGeoLab programme is that of the Geostationary Imaging Fourier Transform Spectrometer (GIFTS). This is a new measurement concept that uses a number of advanced technologies, including particularly the Large area format Focal Plane detector Array (LFPA) with the Fourier Transform Spectrometer (FTS). GIFTS will improve the observation of all three basic atmospheric variable of state, temperature, moisture, and wind velocity allowing much higher spatial, vertical, and temporal resolutions than what is now achievable with currently operational geostationary weather satellites. The displacement of the measured water vapour and cloud features will be used as tracers of the transport of atmospheric water as well as other important atmospheric constituents similar to CMW vector derivations. However, a key advance over current geostationary wind measurement capabilities is that it will be possible to resolve the water vapour winds with respect to height throughout the troposphere. GIFTS observations could thus lead to a significantly better understanding of weather and climate processes, including the atmosphere's water cycle and the transport of greenhouse and pollutant gases.

The Large area format Focal Plane Array (LFPA) that GIFTS proposes to use is a 128 × 128 element array of IR detectors in a Fourier Transform Spectrometer (FTS) that will be mounted on a geostationary satellite. The expected spectral resolution is of the order of 0.6 cm^{-1} and the spatial resolution will be 4 km. The IR radiance spectra over a large geographical area (512 km × 512 km) of the earth will be obtained within a time interval of 10 secconds. A visible light camera will provide quasi-continuous imaging of clouds at 1 km spatial resolution. Extended earth coverage is achieved by step scanning the instrument field of view in a contiguous fashion across any desired portion of the full disc. The radiance spectra observed at each time step will be transformed to the vertical temperature and moisture profiles at high vertical resolutions of 1-2 km using rapid profile retrieval algorithms.

The GIFTS programme is yet at the conceptual stage but it has a great promise. When realized, it will provide measurements on the vertical and horizontal space scales and time scale as never before. However, this may happen perhaps only by the year 2015.

6.3 Advanced Polar Orbiting Satellites and Sensors

From the very beginning, the U. S. has maintained an operational system of polar orbiting meteorological satellites in the TIROS, ESSA, and NOAA series. The successive AVHRR instruments have provided continuity in the global coverage of satellite imagery and have been used to generate a long time series of derived products like OLR, SST and NDVI globally. The TOVS and ATOVS instruments have been used to derive temperature and humidity profiles on a global scale. Other countries have not been able to match the U. S. operational system so far. The following sections describe the U. S. plans for launching new polar orbiting satellites with advanced payloads, the new European initiative for their own polar orbiting satellites, and an international effort to bring about a convergence in the two satellite systems.

6.3.1 U. S. NPOESS

The new National Polar-orbiting Operational Environmental Satellite System (NPOESS) of the U. S. and the NPOESS Preparatory Project (NPP) satellite to be launched by 2008, will carry a next-generation payload to be called the Visible-Infrared Imager-Radiometer Suite (VIIRS). The VIIRS instrument will have an unprecedented number of 22 channels and will draw its heritage from the best capabilities of the instruments that are currently flying, such as the NOAA-AVHRR, NASA-MODIS and DMSP-OLS.

Lee et al (2006) and Miller et al (2006) have given complete details of the VIIRS payload, including its characteristic features and the pixel dimensions in the along- and cross-track directions. Out of the total 22 VIIRS channels, 9 are in VIS and NIR (0.4-0.9 μ), 8 are in SWIR and MWIR (1-4 μ), 4 in the TIR (8-12 μ), and one in the low-light VIS. While VIIRS is by all means an ambitious instrument from an operational viewpoint, its primary shortcomings are the absence of the now-familiar WV channel at 6.7 μm and its low saturation temperature at 11 μ.

As far as the resolution is concerned, out of the 22 channels, 7 channels to be used for ocean colour and SST applications will have a ground resolution of 0.742 km × 0.259 km, 9 channels to be used for deriving cloud properties and SST will have a resolution of 0.742 km × 0.776 km, and 5 imaging channels will have a resolution of 0.371 km × 0.387 km. Some of the moderate resolution channels will have dual gains, capable of measurement within two discrete ranges of radiance.

The VIIRS low-light Day/Night Band (DNB) sensor at 0.7 μ will draw its heritage from the DMSP Operational Linescan System (OLS). This sensor will be sensitive at all levels of illumination, including strong daytime reflections of sunlight and low night-time reflections of moonlight, as well as anthropogenic night-time light emissions. To achieve satisfactory radiometric resolution across such an extreme dynamic range, the DNB selects its amplification gain dynamically from three simultaneously collecting stages or groups of detectors residing upon the same focal plane assembly. Out of the low, medium and high radiance scenes, the most sensitive stage is selected in which the pixel is not saturated so that the entire scene will appear as if it were uniformly illuminated.

Currently VIS satellite sensors provide one of the few means to observe and map snow and ice cover operationally. However, they have the capacity for only daytime measurements, and have severe limitations during winter when nights are long particularly over the polar regions. VIIRS DNB will fill this gap by providing moonlit VIS images. DNB will be able to detect snow, ice, low clouds, dust and smoke, city lights, forest fires and lightning.

The NPOESS satellite as well as the intermediate NPP satellite will not be just a higher version of the current weather satellites, but it will have a totally different form of an integrated environmental observing system that is expected to generate as many as 55 geophysical parameters related to the atmosphere, oceans, climate, earth and sun. For fulfilling this requirement of data products, NPOESS and NPP will carry not only the imaging instrument VIIRS, but a host of other instruments. These include microwave and IR sounders, instruments for observing ozone distributions, space environment monitors, polarimetric sensors for retrieving cloud and aerosol properties, radiation budget sensors similar to ERBE and CERES, a radar altimeter and a scatterometer. NPOESS and NPP will also continue to carry payloads that provide a data collection system for gathering data from automatic weather stations and ocean buoys, a search and rescue service, and a satellite laser ranging service. Details of all these payloads are available at http://www.ipo.noaa.gov/Projects/npp.html.

6.3.2 European MetOp

The Meteorological Operational (MetOp) satellite programme is a new European initiative for providing to have their own meteorological polar orbiting satellites like those of the U. S. NOAA series. The MetOp programme comprising a series of three such satellites, has been jointly established by ESA and the European Organisation for the Exploitation of Meteorological Satellites (EUMETSAT). The programme also represents the European contribution to a new international cooperative venture with NOAA. One of the three MetOp satellites is planned to be launched every 5 years, to ensure continuity of high quality global meteorological data until at least 2020.

MetOp-A, the first satellite in this new series, is expected to be launched in 2006. It will replace one of two satellite services currently operated by NOAA and will be Europe's first polar orbiting satellite dedicated to operational meteorology. After its launch, responsibilities for such meteorological satellite services will be shared between the U. S. and Europe. MetOp-A has been designed to work in conjunction with the NOAA satellite system whereby the two satellites fly in complementary sun-synchronous orbits. The MetOp-A s will provide the mid-morning (AM) pass and an existing NOAA (POES) satellite will continue to provide the mid-afternoon (PM) pass.

MetOp-A will carry seven heritage instruments provided by NOAA and the French Space Agency (CNES), and a new generation of five European instruments offering improved sensing capabilities to both meteorologists and climatologists. Several of the instruments will be measuring similar atmospheric parameters but using different techniques for doing so.

The heritage instruments that will be common to both MetOp-A and NOAA satellite payloads include the imager AVHRR/3 (see Section 1.2.3.1), the microwave sounder AMSU (see Section 3.4.2), and the IR sounder HIRS/4 which will be a higher version of HIRS/3 (see Section 3.4.1.2). MetOp satellites will also carry the Advanced Data Collection System (ADCS), also known as Argos, for relaying data from buoys and automatic weather stations, the Space Environment Monitor (SEM-2), the Search And Rescue Processor (SARP-3) and the Search And Rescue Repeater (SARR).

The five European instruments which MetOp will carry are:

(a) Infrared Atmospheric Sounding Interferometer (IASI), which will obtain humidity and atmospheric temperature profiles in the troposphere and lower stratosphere,
(b) Microwave Humidity Sounder (MHS), which will make passive microwave measurements to obtain atmospheric humidity profiles
(c) Global Navigation Satellite System Receiver for Atmospheric Sounding (GRAS), in which is a GPS receiver will be used to derive atmospheric temperature and humidity profiles through the process of GPS radio occultation (See Section 6.1.1),
(d) Advanced Scatterometer (ASCAT) that will be an enhanced follow-on to the scatterometers flown on the ERS-1 and ERS-2 satellites (see Section 4.3.1)
(e) Global Ozone Monitoring Experiment-2 (GOME-2) for measurements of ozone and other atmospheric constituents (see Section 3.12).

Updates on MetOp-A launch and the further progress of the mission would be available at http://www.esa.int/.

6.3.3 Convergence of Polar Orbiting Missions

The U.S. has always been maintaining two separate operational weather satellite systems. These are the Polar-orbiting Operational Environmental Satellite system (POES) operated by NOAA and the Defense Meteorological Satellite Program (DMSP) operated by the U. S. Department of Defense. In 1994, the U. S. decided to work towards a convergence of the two systems into a National Polar-orbiting Operational Environmental Satellite System (NPOESS) that would consolidate both the systems into one. Going a step further, the NPOESS programme will build upon international cooperation between the U. S. and Eumetsat towards the evolution of a Joint Polar System. The European MetOp satellites will complement the NPOESS satellites in orbit, and there will be a commonality of instruments on both of them.

The convergence of the current POES and DMSP programmes to the new NPOESS is expected to take many years to achieve. Currently the U.S. is operating two POES and two DMSP primary satellites. With the expected launch in 2006 of the first European polar-orbiting MetOp satellite, there will be four polar orbiting satellites: one POES, one MetOp and two DMSP satellites with complementary coverage and instruments. The complete

convergence is likely to be achieved only by 2010, after the last of the satellites in the DMSP and POES series have been launched.

As an intermediate step in the process of transition to NPOESS, the U. S. has initiated what is known as the NPOESS Preparatory Project (NPP) and an NPP satellite is likely to be launched in 2008. NPP will also bridge the gap between the end of life of the NASA Aqua and Terra satellites and the launch of the first NPOESS.

The current design concept for NPOESS is a constellation of three sun-synchronous spacecrafts flying at an altitude of 833 km in 98.7° inclination orbital planes with equatorial crossing times of 5:30 am, 9:30 am and 1:30 pm local times. The early morning (5:30 am) and afternoon (1:30 pm) spacecraft will carry the full suite of instruments. The mid-morning (9:30 am) spacecraft will carry fewer instruments which would complement EUMETSAT's MetOp satellite.

Further details of the convergence programme could be seen at the NASA web site http://www.publicaffairs.noaa.gov/grounders/npoess.html.

6.4 Global Precipitation Mission

As seen in the previous chapters, meteorological satellites have contributed immensely to our knowledge and understanding of precipitation processes in many different complementary ways:

(a) Satellite cloud imagery indicates the presence and movement of cloud systems that can give rise to precipitation, and help in short range forecasting of rainfall and floods,
(b) Raining areas can be inferred from low values in satellite-derived OLR fields, below a certain threshold like 240 w m^{-2}, which represent regions of high convective activity,
(c) Large-scale precipitation over space scales of 2.5° × 2.5° grid boxes and time scales of a month can be estimated from the IR radiances measured by geostationary satellites like INSAT and GOES in their coverage areas,
(d) Rain rates and vertical rain profiles are measured quantitatively by the TRMM precipitation radar as the satellite passes over various parts of the tropical region once in two days,
(e) The precipitation data gathered from satellites, either through estimation or measurement, are now of a sufficiently long duration to enable the compilation of a global satellite-based climatology of various precipitation parameters through GPCP.

(f) Recently launched satellites which have an ability to slice through the cloud, will provide further insights into the processes that go on inside precipitating clouds.

The TRMM satellite, launched in 1998 as a joint U.S.-Japan project, is now nearing the end of its highly successful mission. To provide a continuity to the TRMM mission and also to widen the scope of radar-based measurement of precipitation from the tropics to the extra-tropics, a new international follow-on programme called the Global Precipitation Measurement Mission (GPM) is now being planned (Flaming 2005).

While the GPM mission is still getting into final shape, four broad and basic elements of the GPM have been identified:

(a) A core spacecraft that will carry a Dual-frequency Precipitation Radar (DPR) and a GPM Microwave Imager (GMI) to make the primary radar-based rainfall measurements and also serve as a calibration reference for other instruments operating under GPM,
(b) A large constellation of satellites to be provided by various space agencies, equipped with passive microwave radiometers,
(c) A ground validation programme for verification with reference to ground truth over different weather regimes, and
(d) A data processing system to collect, process and disseminate the vast amount of data gathered by the core satellite and other members of the GPM constellation.

The GPM core spacecraft will be launched into a 65° inclination orbit at a 400 km altitude. NASA and the Japanese Aerospace Exploration Agency (JAXA) are working together to build and launch the GPM core satellite. This orbit will exclude the latitudes poleward of 65° N and S, but will cover all the regions where precipitation occurs in the form of rain. As was the case with TRMM, JAXA will provide the weather radar and possibly a launch vehicle while NASA will provide the passive microwave radiometer, the satellite bus, and the ground control segment.

Besides the core satellite, the GPM constellation may have up to eight satellites provided by different agencies, including satellites of opportunity. In response to an invitation from NASA, both ISRO and CNES have agreed to join the GPM mission by making the Megha-Tropiques satellite (see Section 6.5.1) a component of the GPM constellation.

The Dual-frequency Precipitation Radar (DPR) will consist of a Ku-band precipitation radar (KuPR) and a Ka-band precipitation radar (KaPR). The KuPR operating at 13.6 GHz would be an advanced version of the present

TRMM PR. The KaPR would also be basically similar in design to the TRMM PR but will have a frequency of 35.55 GHz in the Ka-band. The phased array antennas of both KuPR and KaPR will be aligned on the GPM spacecraft bus in such a manner that both of them have identical 5 km size footprints on the ground.

Since the precipitation radars operate at two widely separated frequencies, the attenuation and reflectivity of the transmitted pulses would be different. This information would permit a better differentiation of drop size distributions and rain rates. The GPM DPR is expected to be more sensitive than the TRMM PR especially in the measurement of light rainfall and snowfall in the high latitude regions. The variable pulse repetition frequency technique is to be adopted in order to realize a sensitivity of 0.2 mm/hr in the rain rate measurement.

The GPM Microwave Imager (GMI) instrument is a multi-channel, conical-scanning, microwave radiometer that would serve as a precipitation standard as well as a radiometric standard for the other GPM constellation members. The GMI has 13 microwave channels ranging in frequency from 10 to 183 GHz. Besides carrying the same five channels as the TRMM Microwave Imager (TMI), the GMI will also carry four high frequency, millimetre-wave channels in the 166 to 183 GHz range.

The GMI antenna will have a diameter of 1.2 m. This larger reflector will reduce the area of the GMI footprint to about one-fourth of the TMI footprint. There will be a significant reduction in measurement uncertainty arising from inhomogeneous surface conditions, such as in thunderstorm situations. The DPR and GMI swaths will have the necessary overlap required for radiometer-based precipitation retrievals.

Updates on the GPM mission would be available at the NASA GPM web site http://gpm.gsfc.nasa.gov/.

6.5 Future Indian Space Missions

Since 1982, the Indian Space Research Organisation has launched a series of geostationary satellites that have provided a continuous meteorological coverage of the Indian region and the surrounding land and Indian Ocean regions. Four satellites in the INSAT-1 series, three in the INSAT-2 series, the dedicated Kalpana-1 satellite, and the current INSAT-3A satellite, have carried a total of nine VHRR instruments so far, besides the CCD cameras on the more recent satellites. The next satellite, INSAT-3D, to be launched in

2007 will have an advanced 6-channel imager and a 19-channel sounder. These will offer new capabilities for obtaining high resolution images in new channels and deriving vertical profiles of temperature and moisture.

India has an ambitious space programme that includes a lunar mission. While the accent on the INSAT programme has always been on meeting the requirements of operational meteorology, India is now planning to go in a big way in several new directions towards making systematic observations of parameters related to climate studies. This will also involve the use of microwave sensors, both passive and active, and the placement of satellites in non-geostationary orbits, as described in the following sections.

6.5.1 Megha-Tropiques Mission

As seen earlier, geostationary and polar orbiting satellites have their own relative merits and demerits in various aspects. Geostationary satellites provide images every half-hour or even faster for small sectors. However, because of their height, they are not suited for microwave remote sensing as the radiance reaching them is very weak. Orbiting satellites either in polar orbits or tropical orbits like TRMM, can provide a higher spatial resolution but they have a repeat cycle of one or two days and hence many atmospheric developments are lost between scans. The proposed Megha-Tropiques satellite strikes a trade-off among these conflicting requirements by placing passive microwave sensors in a low altitude orbit also having a low inclination with respect to the equatorial plane.

Megha-Tropiques is a joint India-France (ISRO-CNES) mission with a shared responsibility for development of payloads which would be flown on an ISRO IRS bus. A PSLV launcher will launch the satellite from Sriharikota in an orbit with 867 km altitude and a unique 20° inclination in late 2008 or early 2009. The expected mission life is 3 years.

The main scientific objectives of the Megha-Tropiques mission are:

(a) To collect a long-term set of measurements with a good sampling and coverage over tropical latitudes to understand better the processes related to tropical convective systems and their life cycle.

(b) To improve the determination of atmospheric energy and water budget in the tropical region on various time and space scales.

(c) To study tropical weather and climate events like monsoon variability, droughts, floods, and tropical cyclones, and their predictabilty.

Megha-Tropiques will carry a rare combination of three state-of-art payloads, MADRAS, SAPHIR and ScaRaB designed for measurements of radiative fluxes, precipitation, humidity profiles and cloud properties, which are described below.

MADRAS (Microwave Analysis and Detection of Rain and Atmospheric Structures), will be a passive imaging radiometer operating at five frequencies of 18.7, 23.8, 36.5, 89 and 157 GHz in both H and V polarizations except the 23.8 GHz which will have only V polarization. Data from the first three channels will have applications in the retrieval of rain over oceanic regions, liquid water content in clouds and vertical integrated water vapour. Their spatial resolution is expected to be better than 40 km. The 89 GHz channel will be useful in retrieving convective rainfall over both land and ocean at a still better resolution of less than 10 km. The 157 GHz channel will measure the concentration of ice particles in clouds at a resolution as high as 6 km.

SAPHIR (Sounder for Atmospheric Profiling of Humidity in the Inter-tropics by Radiometry) is a microwave sounding instrument. It will have six channels in the frequency region of 183 GHz, having 10 km ground resolution. SAPHIR soundings will complement the temperature and humidity profiles that will be derived from the INSAT-3D sounder that is to be launched in 2007.

The third Megha-Tropiques payload, is a radiation budget instrument. ScaRaB (Scanner for Radiation Budget Measurement) will have four channels: Sc1 - Visible 0.5 to 0.7 μ, Sc2 - Solar 0.2 to 4.0 μ, Sc3 - Total 0.2 to 100 μ, and Sc4 - IR window 10.5 to 12.5 μ. Sc2 and Sc3 are the main channels of the ScaRaB instrument. Longwave irradiance can be calculated from the difference between Sc3 and Sc2 measurements. Images from Sc1 and Sc4 channels will be used for scene identification and will provide the necessary compatibility with operational satellites like INSAT which have radiometers with similar spectral channels.

The time frame of the Megha-Tropiques mission coincides with that of the forthcoming Indian satellite, INSAT-3D, which will have an advanced imager and a sounder, and another Indian satellite, Oceansat-2, which will fly a scatterometer for measurement of surface winds. A synergistic uitlisation of the data gathered from all these satellites is certainly going to lead to a great advancement of the current knowledge of the role of the tropical atmosphere and oceans in the global weather and climate.

The progress of the Megha-Tropiques mission can be seen on the web sites http://meghatropiques.ipsl.polytechnique.fr/ and http://www.isro.gov.in/.

6.5.2 Satellites for Aerosol Measurements

While currently available satellite sensors can provide information on the aerosol optical depth (AOD) and can distinguish between coarse and fine mode particles, their limitation is that they cannot differentiate whether the aerosols are of the absorbing and scattering type, which is important from the standpoint of their impact on climate. It is also not possible for the sensors to delineate unambiguously the contribution from naturally produced particles and anthropogenic aerosols to the total aerosol optical depth.

India is therefore considering making space-borne measurements that will focus on the source apportionment of aerosols and differentiation between natural and anthropogenic, and absorbing and non-absorbing aerosols. The objective is also to get their vertical distributions of aerosols, ozone, water vapour and carbon monoxide, and their regional and seasonal variation. Measurements of cloud top height and its spatial and seasonal variations will additionally help in estimating the radiative forcings at the top of the atmosphere and within it.

There are proposals for launching two small satellites carrying three major scientific payloads:

(a) A nadir-viewing multi-angle polarisation and multi-spectral sensor in the wavelength bands 0.4-1.2, 2-4 and 10.5-12.5 μ,

(b) An instrument for measurements along the earth's limb to obtain the vertical distribution and extinction properties of aerosols in the stratosphere and troposphere,

(c) An IR spectrometer for measurement of concentrations of atmospheric gases in the 2-5 μ range using a Cassegrain telescope and a linear 256 pixel In-Sb detector.

6.5.3 Satellites for Precipitation Measurements

There is another proposal for a launching a comprehensive Indian mission carrying the complement of sensors listed below using a low altitude, low latitude earth orbiting satellite for more frequent coverage of the tropical regions:

(a) A scanning radiometer and a polarimetric radiometer operating at 6.6, 10.6, 18, 23, 37, 89 GHz and 150 GHz with a combination of vertical and horizontal polarisations. These instruments would help to retrieve

various parameters such as atmospheric water vapour, liquid water content and rain.

(b) Synthetic Aperture Radiometer operating at 1.4 GHz in the L-Band for measuring moisture with a high spatial reslution.

(c) Precipitation radars in Ku and Ka bands similar to those in the GPM mission for measurement of rain and rain rate.

Ultimately, the development of the above payloads is expected to converge into the design of a single combined passive microwave imager/sounder. These are exciting proposals and the Indian weather and climate community is looking forward to their realization.

6.6 In Conclusion

The brief history of satellite meteorology is a fascinating account of successes and failures, where the success stories have far outshined the disappointments. Some missions have ended prematurely, while others have lasted and kept working far beyond their expected lifetimes. This is what has kept satellite meteorology growing at a phenomenal rate. The current state of art of satellite meteorology is the result of scientific ingenuity, technical innovation and human enterprise all working together to make our planet a better and safer place to live. Satellite meteorology has reached a stage from where there is no going back. Within the short time that this book was being written, many new satellites have been launched while some have faded into oblivion, and the future is studded with many bright stars on the horizon.

The Third Assessment Report of Working Group I of the Intergovernmental Panel on Climate Change, published in 2001, summarised in its concluding chapter what needs to be done for advancing our understanding of the world's climate (Moore et al 2001). It said that further work was required to be done to improve the ability to detect, attribute and understand climate change, to reduce uncertainties, and to project future climate changes. While additional systematic observations, modelling and process studies were recommended, a particular concern that was expressed was about the decline of observational networks in many parts of the world. The observational foundation for climate studies needs not only to be sustained but expanded into a strategy for integrated global observations that would provide accurate, long-term and consistent data. There is a need for a better understanding of the mechanisms and factors leading to changes in radiative forcing, which calls for an improvement in the observations of the spatial distribution of greenhouse gases, aerosols and CO_2 sources and sinks, and measurement of

precipitation, soil moisture and ocean salinity. Hydrological and energy exchange processes, especially those involving clouds, surface exchanges, and interactions of these with radiation are crucial for further progress in modelling the atmosphere.

The ultimate goal of the weather and climate community is to achieve a completely interactive simulation of the dynamical, radiative, and chemical processes taking place in the integrated atmosphere-ocean-land system. There is no doubt whatever that satellite meteorology has already made, and will continue to make in future, a significant contribution towards achieving this goal.

"What is faith?" is a question posed in the Bible, and the answer that follows says, "Faith gives substance to our hopes and makes us certain of realities we do not see" (NEB 1961). Except for the changing colour of the sky, and the beauty and fury of clouds and rain, there is little else in the atmosphere that we can actually see. It is satellite meteorology that, in the manner of faith, makes us certain of the realities of the atmosphere that we are not able to see with our own vision.

6.7 References

Anthes R. A., Rocken C. and Kuo Y-H., 2000, "Applications of COSMIC to meteorology and climate", *Terrestrial, Atmospheric and Oceanic Sciences,* 11, 115-156.

Anthes R. A., Kuo Y-H., Rocken C. and Schreiner W. S., 2003, "Atmospheric sounding using GPS radio occultation", *Mausam*, 54, 25-38.

Christian H. J., 1999, "Optical detection of lightning from space", *Proc. 11th International Conf. Atmospheric Electricity*, Guntersville, Alabama, June 7-11, 1999, 715-718.

Christian H. J. and coauthors, 2003, "Global frequency and distribution of lightning as observed from space by the Optical Transient Detector", *J. Geophys. Res.*, 108, 4005.

Flaming G. M., 2005, "Global Precipitation Measurement Update", *Proc. Remote Sensing Symp., IGARSS'05.*

Gerard E. and coauthors, 2004, "Major advances foreseen in humidity profiling from the Water Vapour Lidar Experiment in Space (WALES)", *Bull. Amer. Meteor. Soc.*, 85, 237-251.

Gurka, J. J. and Dittberner G. J., 2001, "The next generation GOES instruments: status and potential impact", Preprints, *Fifth Symp. Integrated Observing Systems,* Albuquerque, NM, Amer. Meteor. Soc.

Kuo Y-H. and coauthors, 1998, "A GPS/MET sounding through an intense upper-level front", *Bull. Amer. Meteor. Soc.*, 79, 617-626.

Kuo Y-H., Sokolovskiy S. V., Anthes R. A. and Vandenberghe F., 2000, "Assimilation of GPS radio occultation data for numerical weather prediction", *Terrestrial, Atmospheric and Oceanic Sciences,* 11, 157-186.

Lahtinen J. and coauthors, 2003, "Fully polarimetric microwave radiometer for remote sensing", *Geosci. Remote Sensing IEEE Trans.*, 41, 1869-1878.

Lee T. E. and coauthors, 2006, "The NPOESS VIIRS day/night visible sensor", *Bull. Amer. Meteor. Soc.*, 87, 191-199.

Miller S. D. and coauthors, 2006, "NexSat - previewing NPOESS/VIIRS imagery capabilities", *Bull. Amer. Meteor. Soc.*, 87, 433-446.

Moore B. and coauthors, 2001, "Advancing our understanding", *IPCC WGI Third Assessment Report, Chapter 14*, 769-785.

NEB, 1961, "A letter to Hebrews", Chapter 11, Verse 1, *New English Bible.*

Price C. and Asfur M, 2006, "Can lightning observations be used as an indicator of upper-tropospheric water vapor variability?", *Bull. Amer. Met. Soc.*, 87, 291-298.

Schmit T. J., Gunshor M. M., Menzel W. P., Gurka J. J., Li J. and Bachmeier A. S., 2005, "Introducing the next-generation advanced baseline imager on GOES-R", *Bull. Amer. Meteor. Soc.*, 86, 1079-1096.

St. Germain, K.M. Gaiser, P.W., 2000, "Spaceborne polarimetric microwave radiometry and the CoriolisWindSat system", *Proc. IEEE Aerospace Conf.*, 5, 159-164.

TAO, 2000, *Terrestrial, Atmospheric and Oceanic Sciences,* 11.

Ware R. and coauthors, 1996, "GPS soundings of the atmosphere from low earth orbit: preliminary results", *Bull. Amer. Meteor. Soc.*, 77, 19-40.

Wickert J. and coauthors, 2001, "Atmsopheric sounding by GPS radio occultation: first results from CHAMP", *Geophys. Res. Letters*, 28, 3263.

Williams E. R., 2005, "Lightning and climate: a review", *Atmos. Res.*, 76, 272–287.

Wulfmeyer V. and Bösenberg J., 1998, "Ground-based differential absorption lidar for water-vapor profiling: Assessment of accuracy, resolution, and meteorological applications", *Appl. Opt.*, 37, 3825–3844.

Wulfmeyer V. and Walther C., 2000, "Future performance of ground-based and airborne water-vapor differential absorption lidar. I. Overview and theory", *Appl. Opt.*, 40, 5304–5320.

Subject Index

S

"This page is Intentionally Left Blank"